

POLITECNICO DI TORINO

**Master's degree in
Energy and Nuclear Engineering**

Master Thesis

**Algorithms development for lifetime
estimation of electrochemical devices using
long term on-field experimental data**



Supervisor

Prof. Pierluigi Leone

Co-supervisor

Dott. Philippe Moçoteguy

Candidate

Giovanna Sessa

Matr. S231431

A.A. 2017-2018

Table of contents

Abstract.....	6
Introduction.....	8
Chapter 1: PHM and Prognostics.....	10
1.1 Classification of prognostic approaches.....	11
1.1.1 Data-driven approaches	11
1.1.2 Model-based approaches.....	12
1.1.3 Fusion approaches.....	12
1.2 Prognostics metrics and guidelines	12
1.2.1 Time constant and system granularity	12
1.2.2 Data selection and processing.....	13
1.2.3 Health indicators and End of Life definition	13
1.2.4 Accuracy criteria.....	13
1.3 Prognostics models for Fuel Cells	14
1.3.1 Data-driven methods: approaches for prognostics.....	14
1.3.2 ANFIS: Adaptive Neuro-Fuzzy Inference System	16
1.3.3 ESN: Echo State Network.....	16
1.3.4 SW-ELM: Summation Wavelet - Extreme Learning Machine	19
1.3.5 W-GMDH: Wavelet analysis - Group Method of Data Handling	21
1.3.6 Model-based approach for PEMFC prognostics.....	23
1.3.7 Particle Filtering approach for model-based prognostics	25
1.3.8 Hybrid approach and moving window method.....	28
1.4 Prognostics models for Batteries.....	31
1.4.1 Space state model and Unscented Particle Filter	31
1.4.2 Discharge-rate-dependent prognostic method	32
1.4.3 Iterative Nonlinear Degradation Auto-Regressive model	33
1.5 Conclusions	35
Chapter 2: ANFIS. Method description and applications.....	37
2.1 Artificial Neural Network and Fuzzy Logic systems.....	37
2.1.1 Artificial Neural Networks	37
2.1.2 Fuzzy Inference Systems	39
2.2 ANFIS: Adaptive Neuro-Fuzzy Inference System.....	40

2.2.1 ANFIS architecture	40
2.2.2 Hybrid Learning Algorithm	42
2.3 PEMFC voltage prediction using ANFIS	44
2.3.1 PEMFC voltage prediction at different operational conditions	44
2.3.2 PEMFC voltage degradation prediction	45
2.3.3 PEMFC performance prediction	46
2.4 Conclusions	46
Chapter 3: Profiling algorithm for “event-based” prognosis	48
3.1 “Event-based” prognosis.....	48
3.2 Profiling algorithm.....	49
3.3 Quality evaluation of the average profiles	51
3.4 Conclusions.....	53
Chapter 4: Mafate energy system. Profiling of experimental data for prognostics	54
4.1 System description	54
4.2 Energy balance and power consumption.....	56
4.3 Fuel Cell power profiles	60
4.3.1 Quality evaluation.....	63
4.4 Electrolyser power profiles	66
4.4.1 Quality evaluation.....	69
4.5 Battery power profiles	71
4.5.1 Quality evaluation.....	76
4.6 Solar irradiance profiles	78
4.7 User load power profiles	85
4.7.1 Average procedure for user power profiles	86
4.7.2 ANFIS implementation for load prediction	96
4.7.3 Comparison between the average and ANFIS procedure	106
4.8 Conclusions	110
Chapter 5: Col du Palet energy system. Profiling of experimental data for prognostics	111
5.1 System description	111
5.2 Energy balance and power consumption.....	113
5.3 Fuel Cell power profiles	116
5.3.1 Year 2016 power data	118
5.3.2 Year 2017 power data	123
5.4 Electrolyser power profiles	126

5.4.1 Year 2016 power data	129
5.4.2 Year 2017 power data	134
5.5 Battery power profiles	138
5.5.1 Year 2016 power data	139
5.5.2 Year 2017 power data	149
5.6 Conclusions.....	158
Conclusions.....	159
Nomenclature.....	161
List of symbols.....	163
Figure index	166
Tables index.....	171
References.....	172
Acknowledgements.....	175

Abstract

The usage of electrochemical devices, such as Proton Exchange Membrane Fuel Cells (PEMFC) and Lithium-ion batteries, is currently widespread and common for a large number of different applications. Among the biggest challenges linked to the utilization of these systems, there are the need to extend their life duration and increase their reliability. In this context, an important role is played by the discipline of Prognostics and Health Management (PHM), which aims at monitoring the state of health of the system and at predicting its Remaining Useful Lifetime (RUL). In literature, different kinds of prognostics approaches have been presented, mainly divided into data-driven, based on historical and monitored data, and model-driven, based on physical or empirical models describing the system behaviour.

A new prognostic algorithm was developed by EIFER, based on the identification of several operational modes in the system behaviour, each one corresponding to a different degradation rate of the device, according to its specific features. In order to identify the features associated to each operating condition and to forecast the future operational profile of the system, a profiling and averaging analysis was performed in this work, using the on-field experimental data collected from two different power production systems. In both plants, the power is produced from a renewable primary source, using photovoltaic panels, associated with an energy storage made by a battery pack and a hydrogen system, whose components are a fuel cell for the power production, an electrolyser for the hydrogen production and a reservoir for the hydrogen storage. The experimental data about the solar irradiance, the end user consumptions and the power produced or consumed by the fuel cell, the electrolyser and the batteries were analysed on a daily time window and, according to their specific features, divided into several classes. An average profile was built for each of them, with the aim to represent the different operational modes of the devices.

The accuracy of the obtained results was evaluated by comparing the average daily profiles with the experimental ones and calculating the Percentage Relative Standard Deviation (PRSD) and the Absolute Standard Deviation. In most cases, the approximation was proved to be acceptable, as the associated errors reached low values, but some cases show, on the contrary, very high values of the error. This is linked to the uncertainties of this kind of prognosis, which, being based on the forecasting of daily events, is affected by the randomness of the data, as the daily power requested by the user or produced by the electrochemical devices can be characterized by significant variations. Nevertheless, the proposed averaging procedure allowed to obtain better approximation results, compared with the implementation of an Adaptive Neuro-Fuzzy Inference System (ANFIS) algorithm on the same data.

The future development of this work could be the utilization of the obtained profiles as a database for the prognostic algorithm developed by EIFER, in order to characterize the features of the operational modes of each device and to forecast their future operational profile. This will allow the evaluation of the degradation rate associated to each system state and, finally, the prediction of its expected Remaining Useful Lifetime.

Introduction

According to the International Energy Agency (IEA), the world energy demand is currently interested by a growing trend that could bring, in the next decades, to an increase of 40% of the energy request [1], causing consequently an increment of carbon pollutant emissions [2]. For this reason, many efforts have been devoted to achieve an energy transition from fossil fuels to alternative and renewable power sources [3].

In this context, the use of electrochemical devices, like Proton Exchange Membrane Fuel Cells (PEMFC) or Lithium-ion (Li-ion) batteries, appears as a promising solution [3].

A PEMFC converts the chemical energy of hydrogen directly into electrical energy. At the anode, the hydrogen splits into protons and electrons; the protons reach the cathode through the polymer electrolyte membrane, while the electrons through an external circuit, producing electric energy. At the cathode, the electrons and the protons coming from the membrane combine with the oxygen to form water [4]. Thanks to their advantages, including high efficiency, low emissions, high power density and low operating temperature, fuel cells can be applied in a wide range of stationary or portable power applications [5, 6]. For instance, they can be used in renewable stand-alone power systems, such as solar or wind generators, as an energy storage, combined with electrolyzers and batteries, to supply power in case of intermittence of the renewable source. Moreover, they are used as primary power sources in transportation applications, combined with batteries, in order to reduce carbon dioxide emissions and fuel consumption [7].

Li-ion batteries have been widely applied for consumer electronics, electric vehicles and aerospace systems [8], and they are one of the most diffuse solutions for energy storage, thanks to their high energy and power density, low weight and long life cycle [9].

However, the functionality of these devices degrades during operation, resulting in worse performance, economic losses and system failure [10]. A possible solution to increase their reliability and extend their lifetime could be the process of Prognostics and Health Management (PHM) [11]. It aims at monitoring the state of health of the electrochemical devices and at predicting the evolution of their aging process, in order to perform the preventive maintenance actions needed to preserve the system and increase its lifespan [8].

Prognostics, as a key step of the PHM process, allows the estimation of the Remaining Useful Lifetime (RUL) of a system, defined as the operating time before the device reaches the failure [12]. It requires the knowledge of both the past and future operating conditions of the system [7], and therefore real monitoring data must be used to identify relevant indicators able to describe the current and future state of health of the device [13]. Different kinds of prognostics algorithms have been proposed in the scientific literature; therefore, an update of the current state of the art was first presented in this work. This is useful in order to have

an overview of the different methods and to highlight their specific features that make them suitable for different kinds of applications. Prognostics algorithms can be roughly divided into model-based approaches, which use complex models to describe the real degradation phenomena, and data-driven approaches, which base the prediction on monitored and historical data without modelling the physical phenomena [5].

A new prognostics algorithm was developed by EIFER (European Institute For Energy Research), which can be included in the class of data-driven approaches. This algorithm uses the monitored data of the specific system in order to identify all its possible operating states, named as operational points, and their features. Indeed, as the degradation of the device changes according to the specific operating conditions, each operational point will be characterized by a different aging rate. Therefore, in order to predict the system RUL, the knowledge of its future operational profile is needed, together with the knowledge of its behaviour at each operational point, for the evaluation of the correct aging rate.

The present work was, thus, developed as a part of this research. Two sets of experimental data, gathered from long-term on-field measurements of two power production plants, were analysed and a profiling and averaging procedure was developed and applied to their most relevant quantities (such as power, solar irradiance or user load), in order to identify the different operating modes of the devices and their features.

The first experimental dataset comes from the on-field measurement of a stand-alone power system composed by photovoltaic panels, batteries, fuel cell and electrolysers, located in a village in the Reunion Island. The second experimental dataset comes from a power system having a similar structure, but located in the mountain retreat of Col du Palet, in France.

This work is organized as follows. Chapter 1 is dedicated to the literature analysis performed in order to update the state of the art of lifetime estimation algorithms for fuel cells and batteries. One of the methods proposed in Chapter 1 is, then, described and analysed in depth in Chapter 2, as it can be applied for prognostics purposes on the available experimental data. In Chapter 3, the first power production plant is presented and the on-field measured data are fed to the prognostics algorithm based on the profiling and averaging of profiles, whose features are described in the same Chapter; here, the comparison between the results obtained with the proposed method and the ANFIS one are also presented. Chapter 4 is dedicated to the analysis of the experimental data measured on the second power production system, applying on them the proposed method. Finally, some comments and final considerations about the obtained results are presented in the Conclusions.

Chapter 1: PHM and Prognostics

The performance of electrochemical devices, like Proton Exchange Membrane Fuel Cells (PEMFC), electrolyzers or batteries can be affected by many factors, such as operating conditions, materials aging and mechanical stresses that lead to the degradation of PEMFC system over time (aging) and limit its lifespan. This highlights the interest in its Prognostics and Health Management (PHM) [5]. PHM can be defined as a process whose aim is to enhance the reliability and availability of a system by detecting upcoming failures. It is seen as an architecture integrating seven layers, as shown in Figure 1:

- *Layer 1:* Data acquisition
- *Layer 2:* Data processing - It receives data from the sensors and performs signal transformations and features extraction, reduction and selection.
- *Layer 3:* Condition assessment - It determines the system current State-of-Health (SoH): it compares on-line data with expected values of system's parameters, generating also alerts based on pre-set operational limits.
- *Layer 4:* Diagnostic - It determines if the condition of the system has degraded and allows to identify the component that has ceased to operate (propagation from effects to causes).
- *Layer 5:* Prognostics - It predicts the future condition of the system by acquiring data from all previous modules (propagation from causes to effects).
- *Layer 6:* Decision support - It provides recommended maintenance actions to perform on the system.
- *Layer 7:* Human-machine interface - It receives data from all previous modules and communicates with the user. [13]

The present work focuses on the prognostics phase.



Figure 1 - PHM architecture [14]

Prognostics is defined as the prediction of a system's Remaining Useful Life (RUL). The RUL is the duration between the time at which the prognostics starts and the time at which the failure of the system occurs. Prognostics is divided into two stages: learning and prediction. During the learning phase, the prognostics tool “learns” the behaviour of the system by analysing its current condition and its past operation profile. Then, during the prediction phase, the prognostics tool predicts the future evolution of the system and finally determines its RUL [5].

This Chapter is organized in the following way. Section 1.1 shows the classification of prognostic approaches, highlighting their main features. Section 1.2 presents some metrics and guidelines for prognostics. In Section 1.3 and 1.4, some prognostics algorithms are described, which can be applied, respectively, for fuel cells and batteries. Section 7 presents some final considerations about the analysed approaches.

1.1 Classification of prognostic approaches

The prognostics algorithms on electrochemical systems can be classified in three main approaches, as shown in Figure 2: model-based approaches, data-driven approaches and fusion approaches.

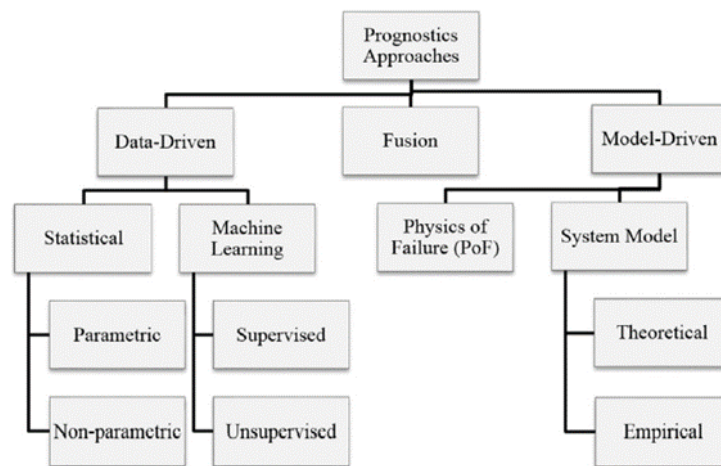


Figure 2 - Classification of prognostics approaches [13]

1.1.1 Data-driven approaches

Data-driven methods are considered as black box approaches as they can be implemented without specific knowledge of the system physical degradation. They are suitable for complex systems, whose behaviour is difficult to be fully understood or modelled. Indeed, no physical models are needed as the system behaviour is learned through monitored and historical data [15].

The main advantage of the data-driven approaches is that they can track and predict the system nonlinear characteristics. The main disadvantage, instead, is that the accuracy of the predictions depends on the available data, which sometimes are difficult to obtain. This happens, for example, in the case of a new device that may require long time to test. However, there are procedures that allow overcoming this drawback:

- *Hardware-in-the-Loop simulation*: the system is tested by connecting it to the hardware that applies simulated loads, as in a real application.
- *Accelerated Stress Test*: the device is operated under accelerated stress conditions in order to reach the failure more quickly than under normal operating conditions.
- *Online Learning (Unsupervised learning)*: the data acquired from the new system are directly used to train the data-driven method. This type of approach is also called “unsupervised” learning, as no reference data are available [15].

1.1.2 Model-based approaches

The model-driven approaches, also known as Physics of Failure (PoF) approaches, use empirical or physical equations to describe the system degradation. The main advantage of the model-based approaches is that they can achieve good RUL predictions on long time horizons. The main disadvantage is that they require a specific knowledge of the failure mechanisms of the system, of the properties of its materials and of the loads applied to it [15].

1.1.3 Fusion approaches

The fusion approaches can be defined as a combination of data-driven and model-driven approaches. Indeed, they require an accurate mathematical model of the system for the model-based failure approach, and enough historical data for the data-driven approach. The aim of the fusion approach is to overcome the disadvantages of both approaches and to benefit from their advantages. Therefore, the prediction accuracy (assessed with the criteria shown in Section 1.2.4.) of the fusion approach should be higher than both approaches used individually, although it may not be suitable for a real-time analysis due to the significant computational cost [15].

1.2 Prognostics metrics and guidelines

Before starting the prognostics procedure to estimate the Remaining Useful Life of a system, regardless of the specific method used to perform prognostics, some preliminary considerations must be done.

1.2.1 Time constant and system granularity

During the operation of the system, the data needed for prognostics are collected and processed continuously for health assessment. Among all the phenomena occurring within the device, the degradation and ageing effects are the main factors that shorten its lifespan. Consequently, as these are slow phenomena, time constants of at least one hour should be considered to perform prognostics.

Degradation occurs at all levels of the system granularity: stack, cells, components and at the interfaces between them. The data acquisition could be performed at the stack level or at the cell level. Working at the cell level could allow to perform prognostics on the most degraded cells, as they are not degrading in a uniform way. However, replacing only these faulty cells would be difficult due to the assembly constraints and could also disturb the stack behaviour, accentuating its degradation. Therefore, the prognostics is usually performed at the stack level [3].

1.2.2 Data selection and processing

The focus of the prognostics process is set on the observation of the degradation phenomena. However, the degradations are mixed with transient phenomena, as some punctual characterizations can disturb the power and create transient stages. As the transient stages have a low duration with respect to the degradation, they should be taken with caution or even removed for prognostics [3].

In order to work only on the degradation phenomena and to remove transient stages, the data can be processed, by reducing and filtering them. The time constant of degradations is at least in hours while the data frequency acquisition is commonly in seconds, so the quantity of data used for prognostics can be reduced. This can enhance the speed of the prognostics algorithms and reduce their computational cost. Then, the data can be filtered in order to remove the transient phenomena, which are not linked to degradation [3].

1.2.3 Health indicators and End of Life definition

Different indicators can be used as prognostics criteria [3]:

- *Voltage*: it can indicate the evolution of degradation phenomena, as it decreases with the increase of the aging of the system.
- *Cumulative energy*: for a PEMFC it is the energy produced during its lifetime and it is calculated by making the integral on time of the product of voltage and current.
- *Efficiency*: for a PEMFC, it is defined as the ratio between the output electrical power and the energy flux of the reactants.

The End of Life (EoL) threshold indicates the condition in which a device is considered as failed. It is generally defined as a loss of a certain percentage of the initial performance, depending on the specific health indicator chosen for prognostics [3].

1.2.4 Accuracy criteria

The accuracy of the predictions can be assessed by using the following statistical criteria: the Root Mean Square Error (RMSE), the Mean Absolute Percent Error (MAPE) and the coefficient of determination (R^2). The RMSE and the MAPE should have low values to indicate a high accuracy. The R^2 values are included between 0 and 1, and values close to 1 indicate a high accuracy. They can be expressed with the following equations [16]:

$$RMSE = \sqrt{\frac{1}{m} \sum_{t=1}^m (\hat{y}_t - y_t)^2} \quad (1)$$

$$MAPE = \frac{1}{m} \sum_{t=1}^m \frac{|\hat{y}_t - y_t|}{|y_t|} \quad (2)$$

$$R^2 = 1 - \frac{\sum_{t=1}^m (y_t - \hat{y}_t)^2}{\sum_{t=1}^m (y_t - \bar{y}_t)^2} \quad (3)$$

Here, y_t is the observed value of the specific health indicator at time t , \hat{y}_t is the predicted value, \bar{y}_t is the average of the observed values at time t , and m is the number of observed values.

The prognostic tool will predict a value of the RUL of the system. If the predicted value is smaller than the actual RUL, it is called an “early prediction”; instead, if the predicted value is higher, it is called a “late prediction”. The acceptable error will not be the same in each case. Indeed, a late prediction is useless in real applications, as it does not allow to perform preventive maintenance actions. On the contrary, early predictions allow more flexibility, as an anticipated maintenance is less disadvantageous, even if it can create some extra costs [3].

1.3 Prognostics models for Fuel Cells

1.3.1 Data-driven methods: approaches for prognostics

As seen in Section 1.1., data-driven approaches are suitable especially in cases where obtaining in-situ data is easier than constructing physical or empirical models. These methods aim at transforming raw monitored data, taken as inputs, into relevant information and predictions about the state of health of the system, given as outputs. Among these methods, neural networks and neuro-fuzzy systems (also known as connexionist networks) perform predictions by approximating an input-output function, so they need to build an approximation model [17].

Let X be an input data set, Y an output data set, and $\Gamma(.)$ the function that links the inputs and outputs:

$$Y = \Gamma(X) \quad (4)$$

This function is generally unknown, so an approximation model must be used to find an approximated function $\hat{\Gamma}(X)$, able to give estimated values of the output set, \hat{Y} .

$$\hat{Y} = \hat{\Gamma}(X) \quad (5)$$

The estimated input-output law is obtained thanks to a learning phase. For that purpose, it is expressed as the combination of a structure $f(.)$ and a set of parameters $[\theta]$, both estimated by using a learning algorithm $La(.)$ that aims at making the residual between the real output data set Y and the estimated one \hat{Y} as close as possible to the null vector [17].

$$\begin{aligned} \{f, [\theta]\} &\leftarrow La(X, Y) \\ \hat{\Gamma}(.) &= f([\theta]) \end{aligned} \quad (6)$$

$$\hat{Y} = f(X, [\theta]) \quad (7)$$

1.3.1.1 Multi-step ahead prediction approaches

In order to perform predictions, different kinds of approaches can be used. Multi-step prediction approaches can be divided into two main categories: those based on the combination of single output tools (Iterative, Direct and DirRec approaches), and those based on multiple outputs tools (Parallel and MISMO approaches).

- *Iterative approach.* It is the most common. Multi-step predictions are provided using a single tool that performs a one-step ahead prediction. The estimated value at each time-step is then used as a new input for the next time-step. This operation is, then, repeated until the prediction horizon H is reached. This approach is the simplest to implement. However, it suffers from error propagation: the accuracy decreases as the length of the prediction horizon H increases [17].
- *Direct approach.* It is a combination of single-output models, each one aiming at predicting a specific time-step. All models use the same observed data and work in parallel, without interactions between them. However, in this way, the dependencies between the predicted values are not taken into account, and this could affect the prediction accuracy. Moreover, this approach is not easy to implement [17].
- *DirRec approach.* It is similar to the Iterative approach except that each prediction step is performed using a distinct model. Each model must be sequentially tuned, using the predicted values obtained in the preceding step. This approach has the same disadvantage as the Iterative approach with respect to the error propagation [17].
- *Parallel approach.* It is a multiple output prediction tool. This approach performs all prediction steps with a single model. It provides all step predictions with less computing time than the Direct approach because there is only one model to tune [17].
- *MISMO approach.* The Multiple-Input Several Multiple-Outputs (MISMO) approach consists in several Multiple-Input Multiple-Output (MIMO) tools, which require several inputs and give as a result several outputs. The user must set a parameter, s , that determines the number of outputs of each MIMO model. If $s=1$, one output is given by each model, as in the Direct approach. Instead, if $s=H$, this means that a unique model is used to provide the predictions for all the time-steps until the prediction horizon H is reached; this corresponds to the Parallel approach [17].

To evaluate and compare the approaches, some criteria should be taken into account [17]:

- *Prediction accuracy:* it can be assessed using the accuracy criteria described in Section 1.2.4. The mean and the standard deviation of the prediction errors are also evaluated.
- *Computational complexity:* it assesses the amount of computing resources or time that are necessary during the learning and prediction phases. The multiple-tools approaches (Direct, DirRec, and MISMO) should take more training time than single-tool approaches (Iterative and Parallel) because several models have to be tuned.
- *Implementation difficulty:* it quantifies the effort in implementing the prediction approach. The simplest are the Parallel and the Iterative approaches, while the most complex are the MISMO, the Direct and the DirRec approaches.

1.3.2 ANFIS: Adaptive Neuro-Fuzzy Inference System

The Adaptive Neuro-Fuzzy Inference System (ANFIS) is one of the Artificial Neural Network (ANN) techniques used for prognostics in data-driven approaches. They do not require complex mathematical models, they are fast and adaptable to different kinds of systems. Their principal drawback is that the performance of the predictions highly depends on the quantity and quality of data [16].

The ANFIS methodology is a fuzzy logic system, where the system parameters are optimized through a training phase. They are constructed from a collection of fuzzy “if-then” rules and Membership Functions (MFs) which define the relationship between input and output variables. Fuzzy rules and MFs are defined by using human knowledge or by using data from the system. Figure 3 shows an example of ANFIS structure. It is generally organized in layers, which contain several nodes that represent the computational units. Nodes within the same layer perform functions of the same type [16].

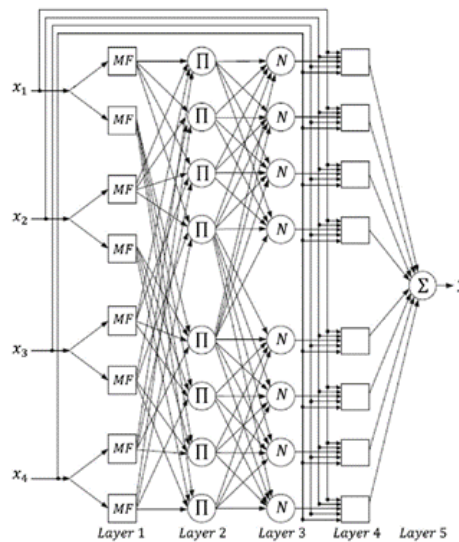


Figure 3 - Example of an ANFIS structure [16]

The ANFIS network uses historical and measured data to generate the rules and the functions that link the inputs with the final outputs. The network must be trained with a set of input and output data, in order to evaluate and adapt the parameters of its functions. The higher the number of training data is, the higher the accuracy of the model will be. An increase in the number of functions could improve the quality of the prediction. However, this also implies an increase in the network complexity and therefore of the computing-time [16, 18].

In the present work, this method was chosen to be applied to perform prognosis on the available experimental data, so it will be described in details and with some application examples in Chapter 2.

1.3.3 ESN: Echo State Network

Among the Artificial Neural Networks techniques, an Echo State Network (ESN) consists in a reservoir of dynamic neurons (randomly connected to each other) which perform predictions through linear regression. It belongs to the category of Recurrent Neural Networks (RNN), which are widely used to evaluate the RUL of complex systems. In

particular, in an Echo State Network, the hidden layers are replaced by a neurons reservoir. The weight matrices between layers, which define the connection between neurons, are created randomly [18].

1.3.3.1 ESN structure

The structure of an ESN is shown in Figure 4. It is divided in three main parts: the first one is the input layer, the second one is the neurons reservoir and the third one is the output layer [18].

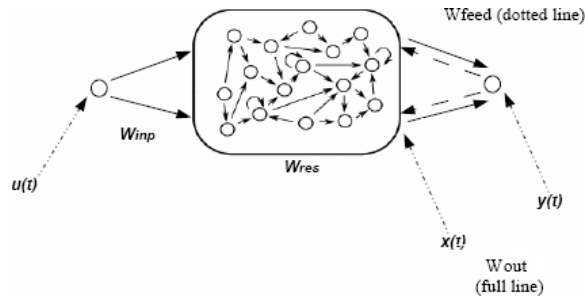


Figure 4 - ESN structure [19]

The learning phase of the algorithm is based on an iteration process. First, the current reservoir state is updated using new input data, the previous reservoir state and the corresponding weight matrices. Then, the ESN output is calculated with the current reservoir state and the output obtained at the previous step.

The design of the ESN reservoir consists in the configuration of several parameters [19]:

- *Number of reservoir neurons*: it is one of the most important parameters. To find a good linear combination in order to obtain good results, it is better to define a large reservoir.
- *Reservoir connectivity*: to obtain the best results, each reservoir neuron should not be connected with all the others. For this reason, a connectivity parameter has to be chosen, in order to define how the neurons should be the connected. It represents the percentage of non-zero weights in the reservoir matrix and its value can vary between 0 and 1.
- *Spectral radius*: the spectral radius of a square matrix corresponds to the maximum value of its eigenvalues. In ESN, the spectral radius is used to scale the non-zero elements of the reservoir weight matrix.
- *Leaking rate*: it defines the influence of the previous time-step reservoir on the new one. Its value has to be in the range [0, 1]; the higher this value is, the less important the reservoir echo becomes.

1.3.3.2 Example: application of ESN for PEMFC prognostics

Morando et al. [19] made experiments on a PEMFC stack operating for 1400 h, choosing the mean cell voltage as health indicator. The experiments were perturbed by the Electrochemical Impedance Spectroscopy (EIS) characterizations, but the data were processed to eliminate these perturbations. The metrics used to check the ESN performance were the RMSE, the MAPE and the R^2 (described in Section 1.2.4.). In order to predict the

RUL, the Iterative approach was used, with time-steps of 1 hour. The results are shown in Figure 5 for the voltage prediction and in Figure 6 for the RUL estimation.

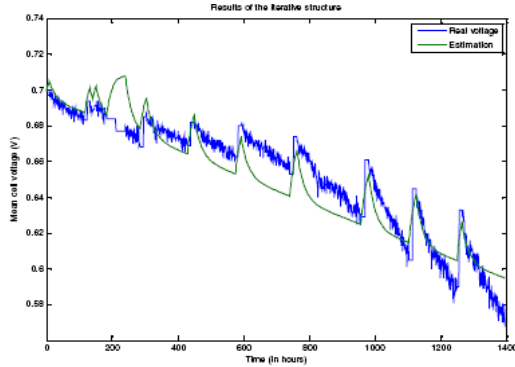


Figure 5 - Voltage prediction results with ESN [19]

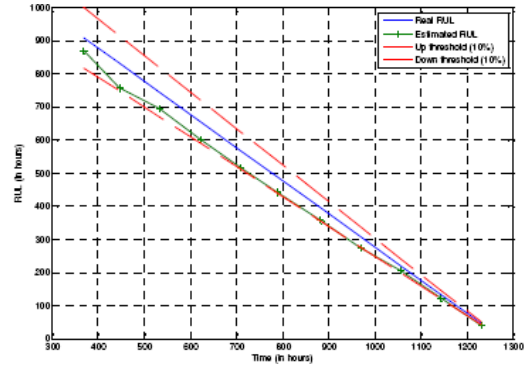


Figure 6 - RUL prediction with ESN [19]

A tolerance interval was set at the 10% of the actual RUL. Figure 6 shows that the estimated RUL does not exceed this interval, so the results were considered as acceptable. The results are really close to the lower bound: this indicates early predictions. Moreover, the RUL prediction accuracy increases as the duration of the learning phase increases [19].

1.3.3.3 Example: improving ESN with ANOVA method

The use of ESN involves the problem of the configuration of its parameters, listed in Section 1.3.3.1. In order to solve this problem, Morando et al. [1] performed a sensitivity analysis, making it possible to quantify the impact of the change in model parameters on the model output. This allows choosing the best set of parameters for the ESN configuration.

In order to perform this sensibility analysis, Morando et al. [1] used an Analysis of Variance (ANOVA) method. The ANOVA is a collection of statistical models and procedures for simultaneous comparisons between several variables, to determine meaningful relationships between them. For example, in a system with two parameters A and B (having different levels) and one output Y , the aim is to compare the different values of the output Y for each possible combination of A and B .

Four parameters were studied (the number of neurons in the reservoir, the spectral radius of the reservoir matrix, the leaking rate and the reservoir connectivity), each one with three different levels (low, medium and high). The experiments were performed on a PEMFC stack, operating for 1100 h at a constant current. 81 different combinations of parameters were tested and for each one the mean results were evaluated on 100 simulations; therefore, 8100 simulations were performed.

The results obtained with the ANOVA method for these simulations showed that the most influential parameter was the spectral radius of the reservoir matrix. Spectral radius defines the scaling of the reservoir matrix, that is the importance given to information that passes between two neurons, meaning that this parameter cannot be dissociated from the number of neurons in the reservoir. The leaking rate and the connectivity had, instead, a low influence on results [1].

This analysis made it possible to optimize the choice of ESN parameters, in order improve the prediction accuracy. The results obtained choosing the best set of parameters are shown in Figure 7 for the voltage prediction and in Figure 8 for the RUL estimation. The RUL

estimations do not exceed the tolerance interval set at the 10% of the actual RUL, so they can be considered as acceptable. Moreover, with respect to the results obtained in Section 1.3.3.2., the estimated RUL values are closer to the actual ones [1].

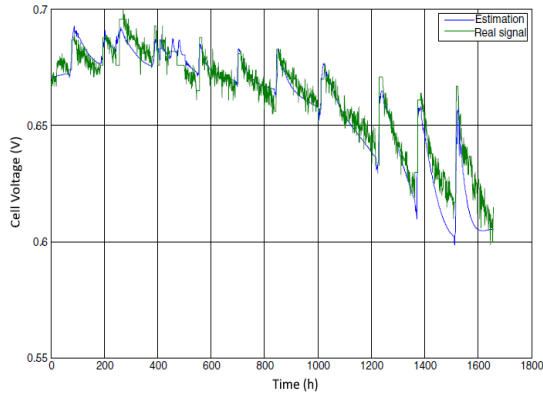


Figure 7 – ANOVA-optimized ESN: voltage results [1]

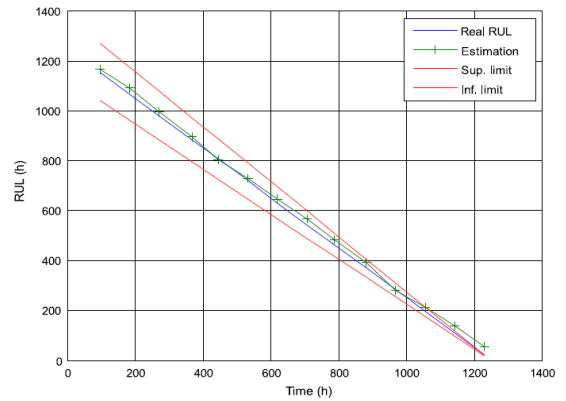


Figure 8 – ANOVA-optimized ESN: RUL results [1]

1.3.4 SW-ELM: Summation Wavelet - Extreme Learning Machine

Among ANN models, the Feed-Forward Neural Networks (FFNN) are those characterized by having connections in the forward direction (not cyclic as in RNN). The Extreme Learning Machine (ELM) algorithm belongs to this group [4].

1.3.4.1 SW-ELM structure

ELM is a single hidden layer Feedforward Network that requires the user to set only the number of neurons in the hidden layer. The input weights and hidden connections are initialized randomly, without prior knowledge. Then, knowing through measurements a certain number of data samples, the ELM links the inputs and the targets with a system of linear equations, and unknown weights between the hidden-output layers are determined analytically [4].

The Summation Wavelet-Extreme Learning Machine (SW-ELM) is an improved variant of ELM, which has the following advantages:

- *Parameter initialization*: it gives a better starting point to initiate the learning phase, reducing the impact of random parameters.
- *Structure*: to encounter non-linear input in a better way, the output from each hidden node is an average value from two distinct activation functions.

The performance of this model can be affected by the randomness of parameters, so a single model would not give an accurate forecast due to uncertainties. To improve the robustness of the prediction, an ensemble of SW-ELM models, each with different parameters, is used. However, models should satisfy three constraints otherwise they are rejected [4].

$$\frac{d}{dt}(\hat{y}_t) \neq 0 \quad (8)$$

$$\hat{y}_t > \hat{y}_{t+1} \quad i \in Z_+ \quad (9)$$

$$\hat{y}_{t+H} \leq FT \quad (10)$$

Being \hat{y}_t the predicted value at a certain time-step and H the prediction horizon, constraints in Eq. (8) and Eq. (9) are based on the assumption that the aging process is an irreversible degradation, while the constraint in Eq. (10) ensures that predictions intersect the Failure Threshold (FT). Finally, the RUL of the ensemble is computed as the median of the RULs estimated by each model [4].

1.3.4.2 Example: application of SW-ELM for PEMFC prognostics

Javed et al. [4] applied the SW-ELM ensemble model on two PEMFC stacks tested at constant current for 1745 h. This model was compared with a simple ELM and an ESN model using two metrics:

- *RUL Offline accuracy*: evaluated with the coefficient of determination (R^2), that measures the prediction accuracy of the learned model. See Eq. (3).
- *RUL Online steadiness*: it indicates the quality of RUL estimates at time t (small values indicate better results):

$$RUL_{OS}(t) = \sqrt{\text{Var}(\overline{RUL}_t)} \quad (11)$$

A first comparison was made on a RUL prediction at two different Failure Thresholds (FT), set at 90% and 85% of the initial voltage value. In both cases, the learning time was fixed at 1000 h. As shown in Figure 9, for both the FTs, the SW-ELM ensemble shows a higher accuracy. The ELM ensemble gives early RUL estimations, while ESN shows very late RUL estimations, which are useless for prognostics. The reasons behind the uncertainty in the ESN are the insufficient learning data and difficulty in parameter settings [4].

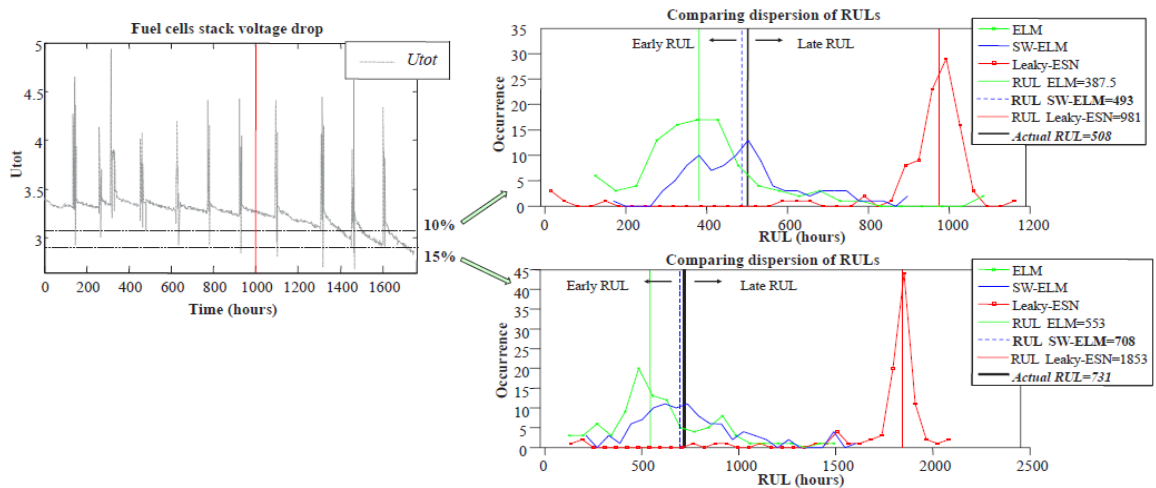


Figure 9 - Comparison of SW-ELM, ELM and ESN on RUL estimation for two different FTs [4]

Another comparison was made, starting the prognostics at 850 h and then estimating a new RUL every 50 h interval. The results in Figure 10 show that for all models the RUL accuracy increases with time, when more data become available. In particular, SW-ELM model is able to give more accurate RUL estimations with respect to ELM and ESN, even when few learning data are available [4].

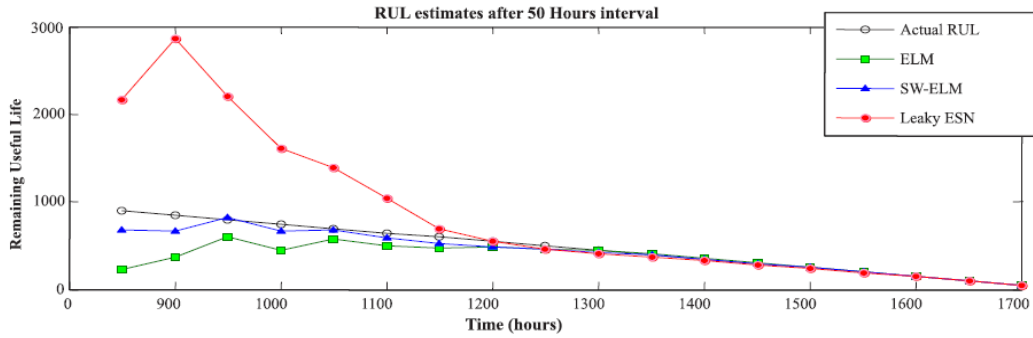


Figure 10 - RUL estimation at frequent intervals for the three approaches [4]

These results are confirmed by the comparison between the offline accuracy and the online steadiness for the three approaches. For both indexes, the SW-ELM ensemble shows the best results, as shown in Figure 11.

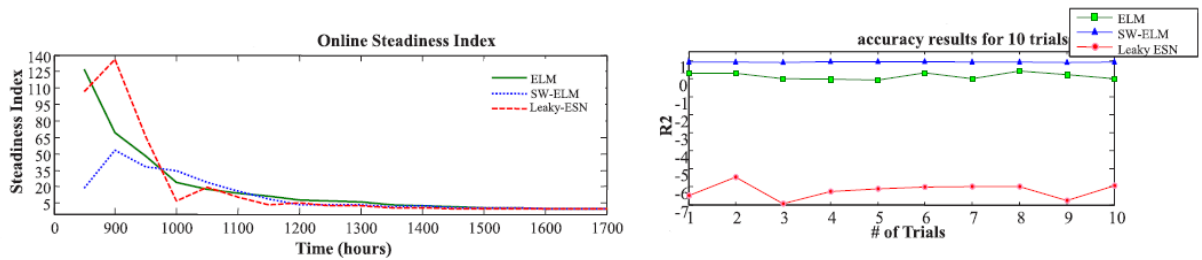


Figure 11 - Accuracy results for the three approaches [4]

1.3.5 W-GMDH: Wavelet analysis - Group Method of Data Handling

1.3.5.1 W-GMDH structure

The Group Method of Data Handling (GMDH) approach belongs to the Feed-Forward Neural Network (FFNN) models. The most important input variables (such as the number of layers and the number of neurons in the hidden layers) are initialized randomly and they are then automatically adapted during training. It learns by building a polynomial function that gets the minimum error between the predictions and the available experimental data samples, used as targets [6].

In order to improve its accuracy, the GMDH approach can be combined with a wavelet analysis. The voltage measurement of a PEMFC exhibits different behaviours during its operation. Indeed, examining the voltage signal in the frequency spectrum, degradation phenomena have low frequencies, while the fluctuations and regeneration phenomena have high frequencies. The aim of the wavelet analysis is to examine the different parts of the signal by adaptively adjusting the focus on the different trends. Therefore, narrow windows are used in high frequency parts to generate the detailed information and wide windows are used in low frequency parts to generate the global information [6].

The W-GMDH model combines the GMDH model and the wavelet analysis. It uses the wavelet analysis to first decompose the voltage signal into several sub-waveforms and then the prognostics is performed on each of them separately using the GMDH. The final prognostics results are evaluated by combining the results obtained on each sub-waveform.

As in the GMDH model the parameters are initialized randomly, an averaging of the results from multiple training should be performed to reduce the impact of the randomness [6].

1.3.5.2 Example: application of W-GMDH for fuel cell prognostics

Liu et al. [6] compared the W-GMDH approach with the simple GMDH to assess its effectiveness. The W-GMDH was tested on two 5-cell PEMFC stacks: Stack 1 was operated at constant current for 991 h and Stack 2 at ripple current for 1020 h. Static and dynamic characterizations (polarization curves and EIS) were performed every 160 h. The accuracy of the method was assessed by using the MAPE, the RMSE and the R^2 .

Figure 12 shows the results obtained with the GMDH model on Stack 1. Most of the predictions were accurate. However, the predictions could not accurately follow the real voltage between 830 h and 890 h due to the local large fluctuations of the voltage [6].

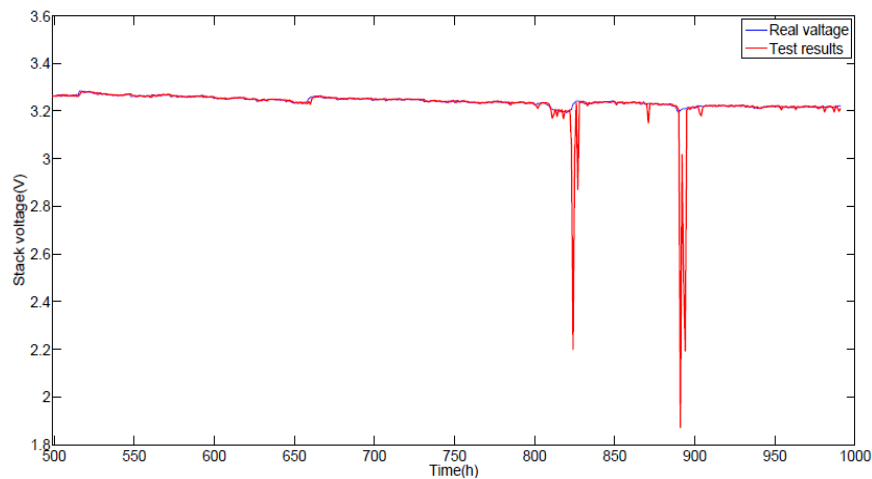


Figure 12 - GMDH prediction results on Stack 1 [6]

In the W-GMDH model, the voltage was decomposed in one approximation wavelet and three detailed ones, as shown in Figure 13. The GMDH model was applied on each of them; then all the sub-waveform predictions were added to get the final results, shown in Figure 14. The W-GMDH prognostics method could get better prediction results, also when dealing with voltage fluctuations [6].

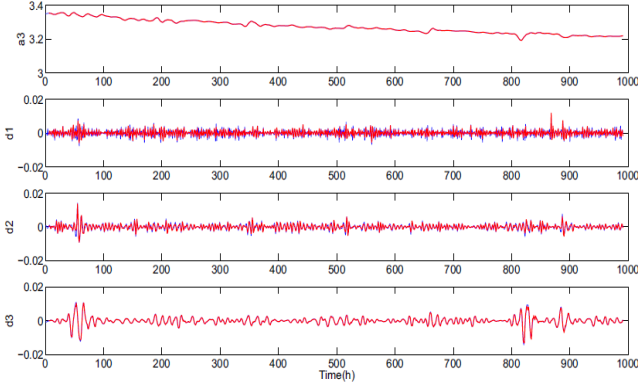


Figure 13 - W-GMDH results on Stack 1 for each waveform [6]

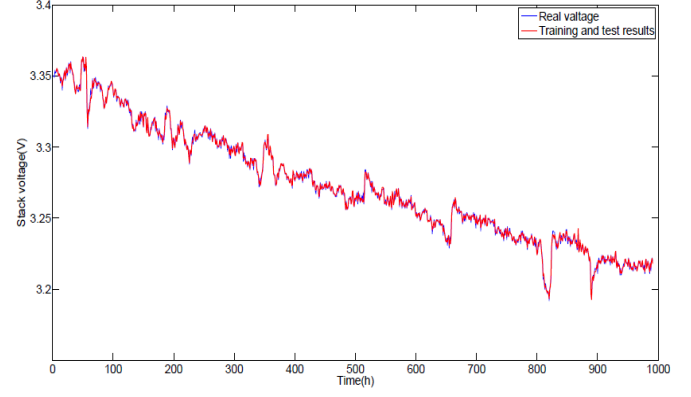


Figure 14 - Overall W-GMDH results on Stack 1 [6]

1.3.6 Model-based approach for PEMFC prognostics

Lechartier et al. [14] developed a model-based approach for PEMFC prognostics, able to give an accurate description of internal parameters and their behaviour. It is a combination of a static and a dynamic model, the first aiming at modelling the behaviour at constant currents and the latter aiming at giving a behaviour description under variable load.

The only input of this approach is the current. It is normalized in current density and then decomposed in direct and alternating components. These current densities are then used as inputs of the two models, which give as outputs the direct and alternating cell voltages. These are recomposed in total cell voltage and then de-normalized in voltage [14]. A scheme of the process is shown in Figure 15.

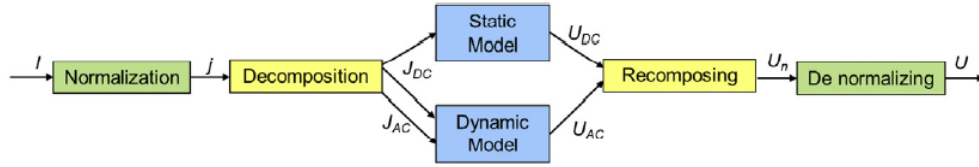


Figure 15 - Scheme of the model-based approach [14]

The static model is based on the Butler–Volmer law that evaluates the cell voltage taking into account all the overvoltage terms:

$$U_{DC} = E_n - R_{mem} \cdot j_{DC} - \frac{1}{b_a} \cdot \operatorname{asinh} \left(\frac{j_{DC}}{2j_{0a}} \right) - \frac{1}{b_c} \cdot \operatorname{asinh} \left(\frac{j_{DC}}{2j_{0c} \left(1 - \frac{j_{DC}}{j_{LC}} \right)} \right) \quad (12)$$

The overvoltage terms that lower the OCV, or Nernst potential (E_n), are three. The activation overvoltage, occurring both at the anode and at the cathode, can be defined as the loss of voltage linked to the kinetics of the chemical reactions at the electrodes. It depends on the static current density j_{DC} , on the anode and cathode exchange current densities j_{0a} and j_{0c} , and on the Tafel parameters b_a and b_c . The ohmic overvoltage is linked to the resistance that ions encounter when moving through the electrolyte and it depends on the internal resistance, R_{mem} . The diffusion (or concentration) overvoltage is linked to the mass transport limitations due to the resistance that the reactants encounter to reach the electrode and feed

the reaction. This term depends on the cathode limit current density j_{Lc} , while the hydrogen diffusion limitations at the anode side are neglected [14].

In the dynamic model, the phenomena are represented thanks to an electrical equivalent circuit, as shown in Figure 16, in the following way [14]:

- the diffusion of the gases at the cathode is modelled by a Warburg impedance W_{Oc} (which is an equivalent electrical circuit component that specifically models the diffusion processes), expressed as a network of several RC filters in series, as shown in Figure 17;
- the double layer capacities at the interface electrode-electrolyte on the anode and cathode are modelled by capacitors C_{dca} and C_{dcc} ;
- two resistances R_{ta} and R_{tc} represent the electrons transfer at the electrodes;
- the ionic conductance of the membrane is modelled by an equivalent resistance R_m ;
- the inductive behaviour due to the connectors is taken into account by an inductance L_{con} .

Finally, the global model is given by a recomposing block that sums up the AC and DC components of the current density [14].

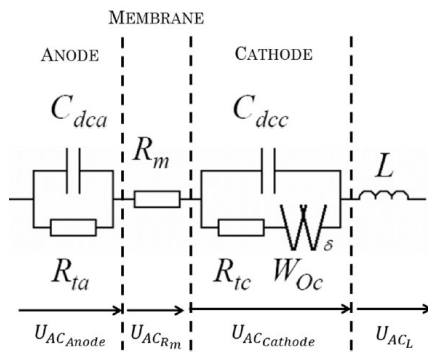


Figure 16 - Dynamic model electrical equivalency [14]

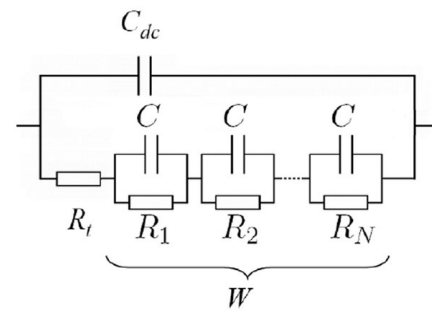


Figure 17 - Equivalent circuit for Warburg impedance [14]

Before performing prognostics, the parameters of the model should be adjusted in order to take into account their evolution with ageing. A polarization curve is used to adapt the parameters of the static part and some EIS characterizations, realized at different currents, are used for the dynamic part [14].

1.3.6.1 Example: application of the model for PEMFC prognostics

Lechartier et al. [14] applied the model on two PEMFC stacks: one was operated at constant current and the other was operated at dynamic current. The duration of the test was 1000 h. Polarization curves and EIS characterizations were taken every 160 h. The model was tuned by fitting the polarization curve, for the static part, and the EIS characterization, for the dynamic part.

The global model worked well, as it showed the same trend of the actual fuel cell voltage, as shown in Figure 18. However, there was a small difference of a constant value between the two curves when the current was evolving. This was because during the polarization

curve measurement the operating conditions were different from those during the ageing test [14].

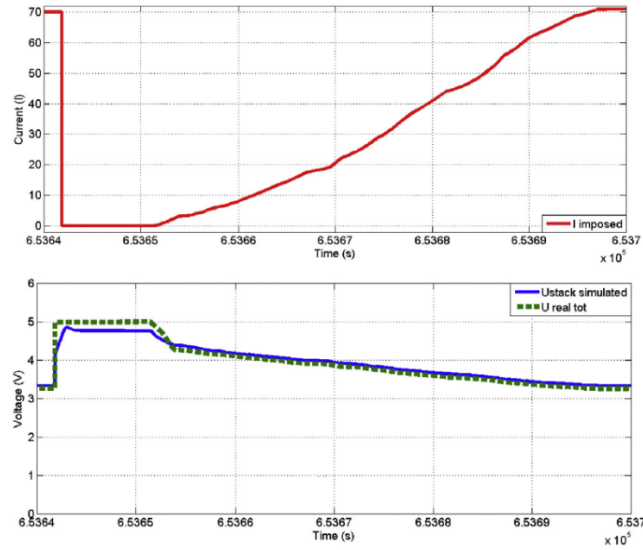


Figure 18 - Current profile and prediction results of the model-based method [14]

1.3.7 Particle Filtering approach for model-based prognostics

1.3.7.1 Bayesian problem and Particle Filtering

Particle Filtering (PF) approach is an effective tool to find an approximate solution for the Bayesian problem of a non-linear system. The Bayesian problem is a probabilistic approach, which aims at recursively estimating the Probability Density Function (pdf) of the state of a system, using incoming measurements and a mathematical system model. The initial pdf of the state must be known.

The problem can be defined with the following equations:

$$x_k = f(x_{k-1}, \theta_k, v_k) \quad (13)$$

$$y_k = g(x_k, \mu_k) \quad (14)$$

Eq. (13) is the system state model equation, which contains the information about the state of the system and allows to predict its evolution. Here, f is the transition function that specifies how the system evolves from the previous state variable x_{k-1} to the current one x_k ; θ_k is the vector of unknown parameters and v_k is a noise that takes into account the uncertainties in the data measurements. Eq. (14) is the observation model, which provides the real observations y_k from the system; g is the observation function that links the observations to the system state, and μ_k is a noise. As in most cases the Bayesian problem cannot be solved analytically, an approximate solution can be found using particle filtering [13].

Particle Filter is a Monte Carlo-based tool, made of different steps repeated to perform the estimation of the pdf of the system state until the end of the process [13]. These steps are shown in Figure 19.

- *First stage.* At state $k=1$, a certain number of random samples (called particles) is generated based on the initial probability distribution.
- *Prediction.* Particles propagate from state $k-1$ to k using the state model. A new pdf is obtained.
- *Update.* A new measurement y_k allows to assign weights at particles, according to the matching between the predicted pdf and the measurements. Particles with higher weights represent the most probable states.
- *Re-sampling.* Particles with the lower weights (compared to a chosen limit) are eliminated, whereas those with higher weights are duplicated. This is done because otherwise, after several iterations, the particles with low weights would become too numerous, altering the prediction.

This filter is used for the learning and prediction phases of the prognostics process. During the learning phase, it works as described above. The behaviour of the system is learned and the unknown parameters in the state model are adjusted consequently. Instead, during the prediction phase, no more measurement is available and the state x_k is propagated without performing the re-sampling [13].

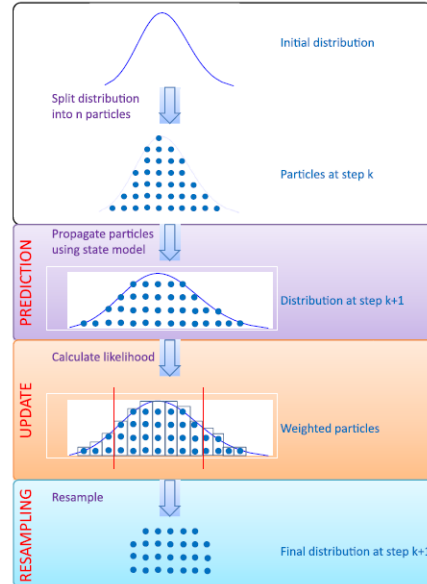


Figure 19 - Principle of particle filtering [13]

1.3.7.2 Example: Particle Filtering applied to a PEMFC model

Mao et al. [19] used the following equation to describe the stack behaviour during its lifetime:

$$U = E_n - \frac{RT}{2\alpha F} \ln\left(\frac{j}{j_{oc}}\right) - \frac{RT}{2\alpha F} \ln\left(\frac{j_n}{j_{oc}}\right) - m_{trans} e^{n_{trans} \cdot j} - j \cdot R_{mem} \quad (15)$$

Here, U is the cell voltage, E_n is the OCV, R is the universal gas constant, T is the cell temperature, α is the charge transfer coefficient, F is the Faraday constant, j_{oc} is the exchange current density at cathode, j_n is the internal current density, m_{trans} and n_{trans} are the mass transport loss coefficients, R_{mem} is the membrane resistance.

The model was applied on two PEMFC stacks: Stack 1 was operated at static current and Stack 2 at dynamic current. Polarization curve characterizations were taken every 160 h.

A first tuning of the parameters of Eq. (15) was performed using a polarization curve characterization. Then, the particle filtering approach was used to predict their future values: a state equation was defined for each parameter to reflect its evolution; then, a particle filter process was performed on each state equation. The observation model was given by the experimental voltage measurements [19].

So, multiple particle filters were used in parallel to estimate the model parameters. The results in both steady state and dynamic conditions are shown in Figure 20. The predicted voltage was close to the actual fuel cell performance [19].

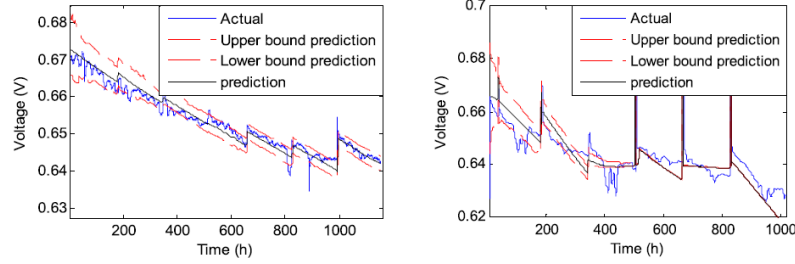


Figure 20 - Prediction results from particle filtering on Stack 1 (left) and Stack 2 (right) [20]

1.3.7.3 Example: application to three empirical models

Jouin et al. [13] applied the particle filtering approach on two PEMFC stacks: Stack 1 was operated at static current and Stack 2 at dynamic current. The voltage was chosen as health indicator, so that the state model represented the voltage evolution in time. Three state models were tested:

$$x_{k+1} = \exp(-\beta \cdot (t_{k+1} - t_k)) \cdot x_k \quad (16)$$

$$x_{k+1} = -\alpha \cdot \ln\left(\frac{t_{k+1}}{t_k}\right) - \beta \cdot (t_{k+1} - t_k) + x_k \quad (17)$$

$$x_{k+1} = -\beta \cdot (t_{k+1} - t_k) + x_k \quad (18)$$

The linear model (Eq. (18)) is commonly used to represent the voltage drop or the degradation under constant current, but it does not take into account what happens at the beginning and at the end of life. This can be modelled either by an exponential (Eq. (16)) or a logarithmic function (Eq. (17)), where a linear part is added. Here, the observation function was represented by the real voltage measurements available. The accuracy of the predicted RUL was evaluated by setting a tolerance interval around the actual RUL. The estimated RUL is the final particles distribution obtained when the failure threshold is reached [13].

The results on the two stacks are shown in Figure 21 and Figure 22, respectively. For Stack 1, the exponential model underestimated the RUL. The linear model showed predictions always in the interval, but they were often higher than the real RUL values, indicating late predictions. The logarithmic model, instead, was able to estimate values close to the real RUL, except for those in the first part of the graph, because the model had a too short training phase. During the experiment, some unexpected stops occurred (around 300 h

and 450 h), which affected the prediction results of all models. For Stack 2, the best results were given by the logarithmic model, as shown in Figure 22 [13].

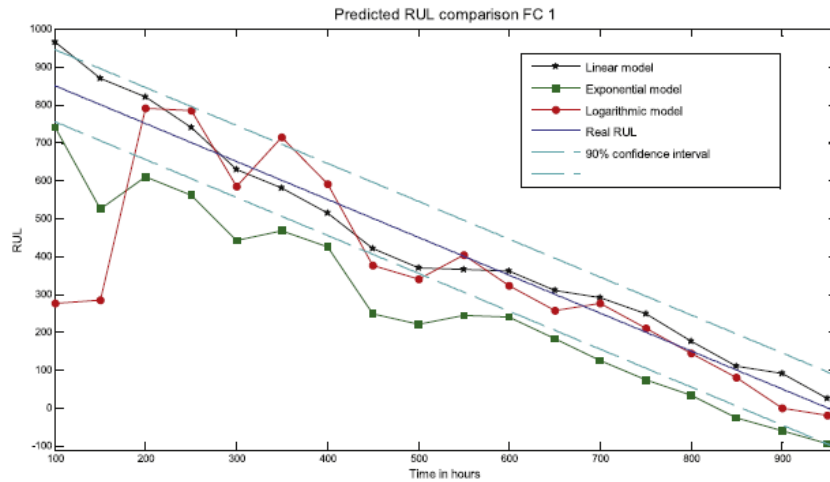


Figure 21 - RUL prediction results of the three models for Stack 1 [13]

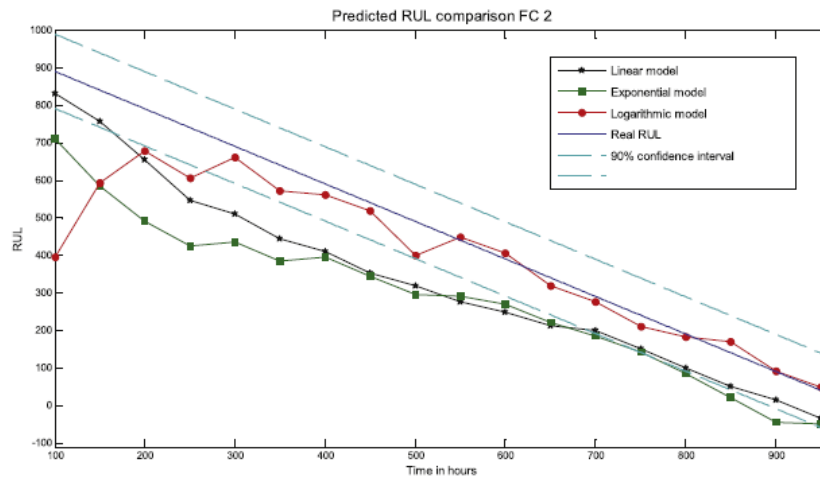


Figure 22 - RUL prediction results of the three models for Stack 2 [13]

1.3.8 Hybrid approach and moving window method

Zhou et al. [5] developed a fusion (or hybrid) prognostic method. It is composed by a voltage degradation model, associated with a particle filter, and by an ANN model.

As model-based method, the system state is expressed through a Bayesian problem, as described in Section 1.3.7.1, and a particle filter is applied to recursively estimate the state of the system. In the training phase, the particle filter estimates recursively the state variable, based on the initialization model and the experimental data. Then, in order to take into account all the state variables tuned during the training phase, their average value is evaluated and used during the prediction phase [5].

As data-driven method, a Nonlinear Auto Regressive Neural Network (NARNN) can be used, whose general structure is shown in Figure 23. First, the model must be initialized, setting the number of neurons, the transfer functions and the weights in each hidden layer. The aging data of training phase are, then, divided into training part and evaluation (or validation) part: the training data are used to recursively estimate the NARNN parameters,

while the validation data are used to evaluate its fitting ability, that is its prediction accuracy [5].

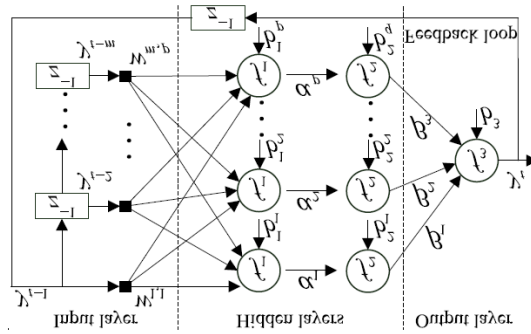


Figure 23 - Structure of a NARNN model [5]

To improve the accuracy of both the model-based and the data-driven approaches, the moving window method is adopted. Its aim is to iteratively update the training data as soon as new data become available [5]. A schematic representation of the moving window method is in Figure 24.

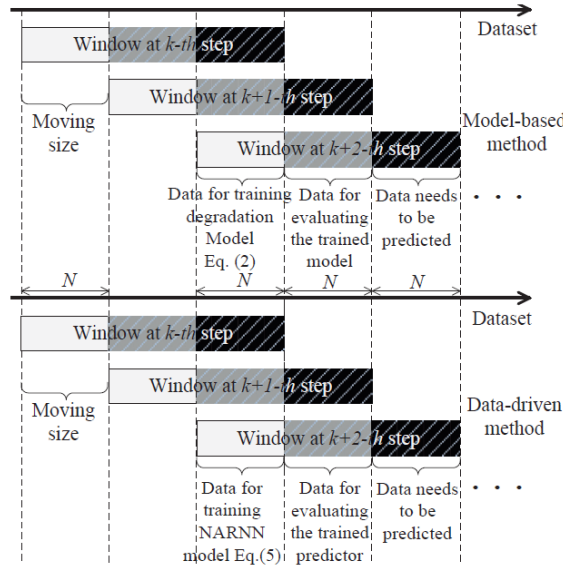


Figure 24 - Moving window method applied on both approaches [5]

Each window includes three parts: training part (white region, data measured in the past), evaluation part (grey region, data measured in the past) and prediction part (black region, prediction data for the future). The moving size, N , indicates the number of data used in each region. At each prediction step, the data in the white region (from 1 to N) are used to train the model. The data in the grey region (from $N+1$ to $2N$) are used to evaluate the fitting ability of the updated model, and the data in the black region (from $2N+1$ to $3N$) are the future data points that need to be predicted. At the following iteration, the data for each region are shifted forward for a length N [5].

In addition, by iteratively evaluating the fitting ability at each prediction step, a weight factor is assigned to both the model-based and the data-driven method. Indeed, during the evaluation process (grey region), the measured fuel cell voltage is compared with both model outputs to generate residuals, which are then used to calculate the weight factor for each

method. Finally, at each prediction step the overall result is the weighted average of the two models predictions [5]. The flow-diagram of the overall process is shown in Figure 25.

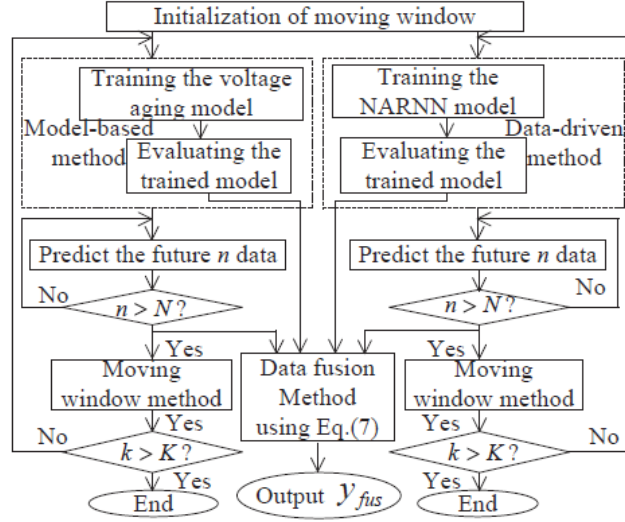


Figure 25 - Flowchart of the overall hybrid method [5]

Zhou et al. [5] used an exponential equation in order to describe the evolution of the PEMFC voltage:

$$V(t) = a(t) \cdot \exp(b(t) \cdot t) + c(t) \cdot \exp(d(t) \cdot t) \quad (19)$$

The system state equation and the observation equation (described in Section 5.7.1.) can be written as:

$$x_k = x_{k-1} + v_{k-1} \quad (20)$$

$$y_k = a_k \cdot \exp(b_k \cdot k) + c_k \cdot \exp(d_k \cdot k) \quad (21)$$

Here, the state variable x_k contains the unknown parameters needed to evaluate the voltage:

$$x_k = [a_k, b_k, c_k, d_k]^T \quad (22)$$

The hybrid method was applied on a PEMFC stack made of 47 cells, operating at a constant current for 400 h. The prediction results of Figure 26 show that the fusion method could well catch the fluctuations of the measured data, with a lower error with respect to the data-driven approach.

Indeed, comparing the RMSE of the three approaches, the hybrid prognostic method was characterized by the lowest error. The error increased with the forecasting time; this was because of the increasing error trend of the data-driven approach, while the accuracy of the model-based method was not affected by the prediction horizon, as shown in Figure 27. [5]

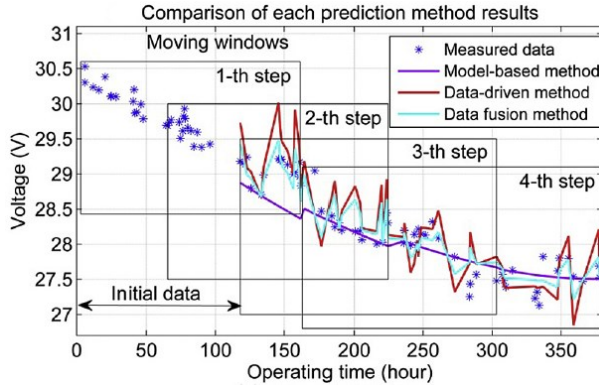


Figure 26 - Prediction results of the hybrid method [5]

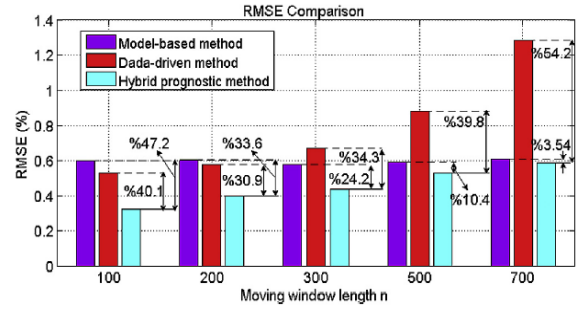


Figure 27 - Error comparison at different moving window lengths [5]

1.4 Prognostics models for Batteries

Battery health monitoring allows to evaluate the battery state-of-charge (SOC) and state-of-health (SOH). While SOC describes the percentage of remaining energy (capacity) before the battery needs to be recharged, SOH describes its general health condition and its ability to deliver the specified capacity compared with a new one. Due to the physical and chemical changes during battery operation, its performance tends to deteriorate. The health indicator used for batteries is the capacity Q , calculated as $Q = \int I dt$, where I is the current flow and t is the discharging time from fully charged to empty. The battery is considered as failed when its capacity drops below a given percentage of its nominal value. Generally, 80% of the nominal value is considered as the failure threshold [10].

1.4.1 Space state model and Unscented Particle Filter

1.4.1.1 UPF: Unscented Particle Filter

One of the methods that can be used in the RUL estimation of lithium-ion batteries is the Unscented Particle Filter (UPF). In this method, the battery state is described like a Bayesian problem (as in Section 1.3.7.1.), with a state equation and an observation equation. Then, to find an approximate solution of the Bayesian problem a combination of a Particle Filter (PF), (Section 1.3.7.1.), and an Unscented Kalman Filter (UKF) is used, called Unscented Particle Filter (UPF) [10].

To apply UKF, first an Unscented Transformation (UT) must be performed. Consider a vector of random variables x , with a given mean and covariance; this vector is linked to a second vector of random variables y by a known non-linear function $g: y=g(x)$. The aim of UT is to evaluate the mean and covariance of y , approximating x with a distribution of points, which has the same mean and covariance. Then, the UT can be used in the design of the UKF. The first step is the initialization of the first state vector (with mean and covariance) at time 0. Then, at successive time steps, the current state is updated to the new measurements according to the UT equations [20].

So, the UPF algorithm is divided into two steps: first, it uses the UKF to generate a proposal distribution, then it uses the PF algorithm to get the final results [10].

1.4.1.2 Example: application for Li-ion battery prognostics

Miao et al. [10] tested the UPF approach on the experimental data taken from four different batteries. The empirical model adopted to describe the capacity degradation was an exponential equation.

The results of PF and UPF methods were compared, choosing an arbitrary number of cycles (32, in this case) as a starting point for prediction. As shown in Figure 28 and Figure 29, the estimation accuracy with UPF was improved, with respect to the simple PF. Indeed, the RUL pdf is narrower, which indicates a higher accuracy. Moreover, UPF algorithm could predict the failure time with a RMSE less than 5%, better than the PF algorithm whose error was around 7% [10].

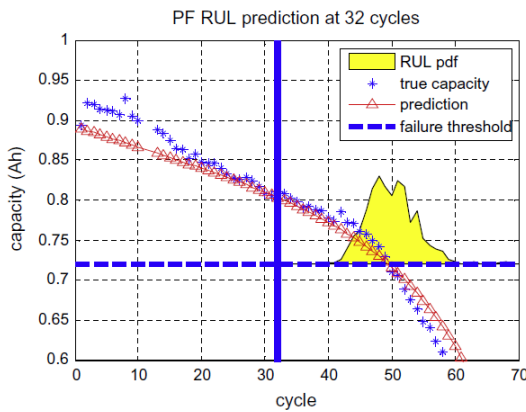


Figure 28 - PF prediction results at 32 cycles [10]

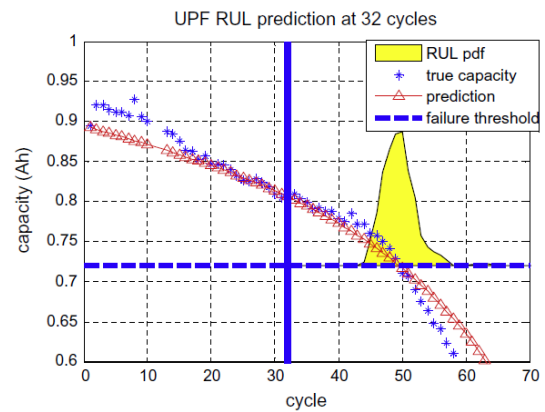


Figure 29 - UPF prediction results at 32 cycles [10]

In literature, several kinds of empirical models are also available, in order to take into account the different aging trends linked to the characteristics of the specific battery material. An example is given by Yang et al. [9], which used a two-terms logarithmic model to represent the degradation of a NMC (Nickel Manganese Cobalt) battery.

1.4.2 Discharge-rate-dependent prognostic method

The discharge rate of a battery is one of the most significant factors that influence its capacity degradation. Indeed, the higher is a discharge rate, the faster is the capacity degradation. In order to take into account this effect, a discharge-rate-dependent prognostic method can be used [21].

1.4.2.1 Discharge-rate-dependent method structure

To build a prognostic model suitable at different discharge rates (DDRs), three steps must be followed [21].

- Firstly, a failure threshold dependent from the discharge rate is defined. It can be set at the 80% of the initial battery capacity.
- Secondly, it is necessary to find an empirical battery degradation model, which depends on the different discharge rates applied to the battery.
- Thirdly, the discharge-rate-dependent empirical model, found in the preceding step, is expressed in the form of a Bayesian problem, in order to estimate its evolution with a Particle Filter approach (Section 1.3.7.1).

1.4.2.2 Example: application of DDR-dependent method for battery prognostics

In order to build the discharge-rate-dependent degradation model, Wang et al. [22] used an exponential equation, whose parameters were dependent on the DDRs. This model was tested on four lithium-ion batteries with the same specifications. The batteries could operate at different discharge rates (0.5C, 1C, 3C, and 5C). The C-rate is defined as the current that is used to charge or discharge a rated capacity in 1 h. The chosen prediction step was an interval made of four charge-discharge cycles. A random sequence of different discharge rates was applied to the battery [21], as shown in Figure 30.

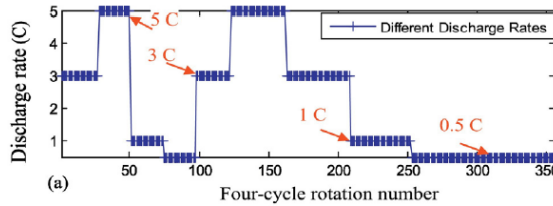


Figure 30 - Discharge rate profile applied to the battery [22]

As observed in Figure 31, the discharge-rate-dependent prognostic method shows a good prediction ability for the capacity profile and a great accuracy on RUL estimation. This method was compared with a model built with the same kind of exponential equation, but whose parameters were not dependent on the DDRs. Figure 32 shows that, with this model, the capacity prediction is inaccurate as the predicted curve does not represent in a good way the real measurements, so the RUL prediction is affected by a higher error [21].

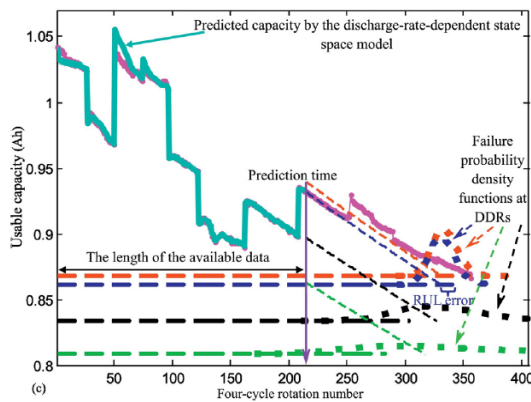


Figure 31 - DDR-dependent method RUL results [22]

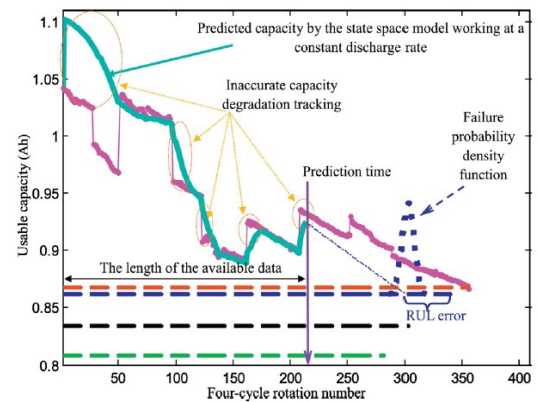


Figure 32 - Not DDR-dependent method RUL results [22]

1.4.3 Iterative Nonlinear Degradation Auto-Regressive model

To perform a Li-ion battery RUL prediction, a hybrid approach can be used, named as “Iterative Nonlinear Degradation Auto-Regressive” (IND-AR) model. It combines an improved auto-regression model with a particle filter algorithm. The battery capacity is used as health indicator [22].

1.4.3.1 IND-AR model structure

The battery capacity can be predicted with an Auto-Regressive (AR) model. It is a model in which the output variable at a certain time linearly depends on its preceding values. So, with the AR model, the capacity at each time-step is calculated as a linear combination of its historical values. However, as the capacity degradation in batteries generally does not follow a linear trend, the AR model should be modified with a so-called “accelerated degradation factor” that takes into account the non-linear trend of the capacity degradation. As the prediction of the battery capacity is performed through iteration, this method is finally called as “Iterative Nonlinear Degradation Auto-Regressive” (IND-AR) model [22].

1.4.3.2 Hybrid method with IND-AR model and PF algorithm

The hybrid method is obtained by combining a particle filter algorithm with the IND-AR model. For the particle filter, it is necessary to find an equation that describes the state of the system and its evolution.

In order to perform the battery capacity prediction, some steps should be performed. A first estimation is given by applying the IND-AR approach on the available capacity data. Then, the PF algorithm is applied, using the output from the IND-AR as an observation value. This prediction is used as a new input for the IND-AR model. Then, the whole process, shown in Figure 33, is iteratively repeated until the failure threshold is reached [22].

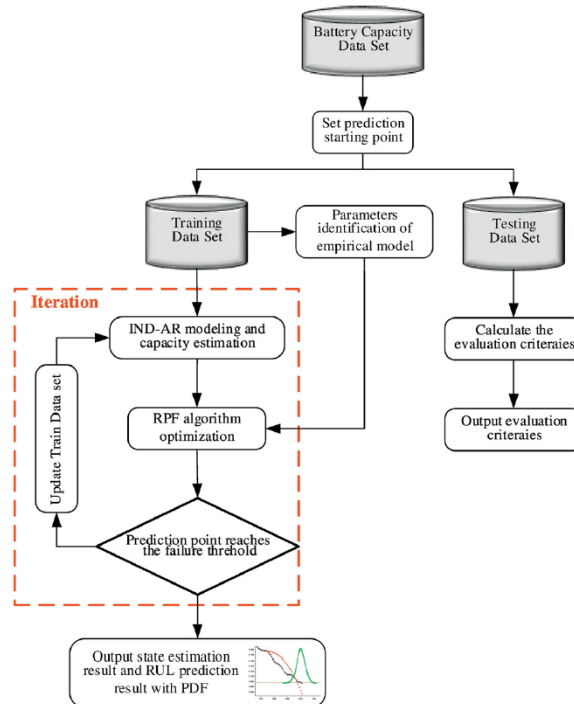


Figure 33 - Flowchart of the hybrid method [23]

1.4.3.3 Example: application for battery prognostics

Song et al. [22] applied the hybrid method on a lithium-ion battery with a nominal capacity of 1.3 Ah. The capacity failure threshold was set at the 80% of this nominal capacity. In order to apply the PF algorithm an exponential equation was chosen as state

equation to describe the evolution of the capacity, while the observation values were the output from the IND-AR model.

Figure 34 shows the prediction results. The RUL error and the RMSE were both small, 2.1% and 0.0264 respectively, so the method had a good prediction accuracy. Furthermore, it has great compatibility on different kinds of lithium-ion batteries under different operating conditions [22].

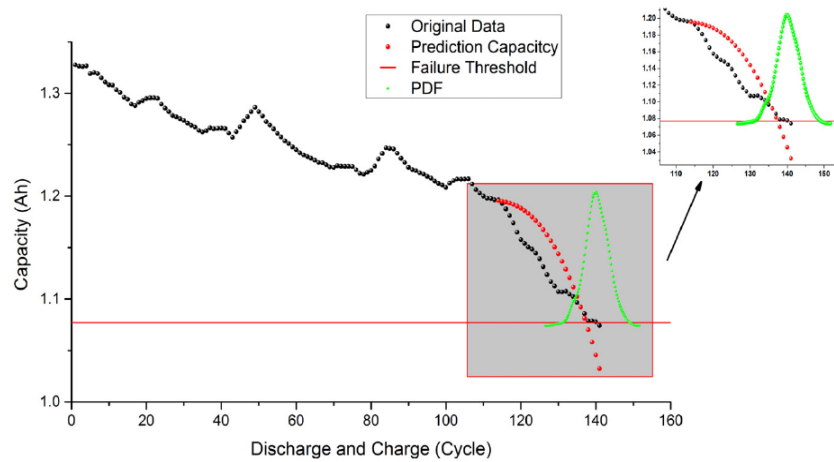


Figure 34 - Capacity prediction results of the IND-AR model [23]

1.5 Conclusions

The PHM of a system is useful in real applications as it allows to evaluate the current state of health of the system as well as its future degradation, in order to predict its failure before it occurs. In this chapter, different kinds of prognostics methods for fuel cells and batteries were described. Each of them has its own specifications, so it is needed to choose on the basis of the specific needs of the application.

Generally, the data-driven methods are suitable for every kind of system, because they learn directly from historical or observed data, and can be used for on-line predictions. Among these, the ANFIS is the most used one, as it achieves a good accuracy if enough data are available for its training and it can be also implemented with specific tools in software like Matlab. The ESN might be more tricky to implement, because the configuration of its parameters must be done by the user and, moreover, it requires the longest training time with respect to the other methods. On the contrary, the SW-ELM ensemble model needs only few parameters to be set by the user and can achieve acceptable results also with a lower amount of training data. Finally, the W-GMDH model could be suitable for systems operating in dynamic conditions but it might be complex to implement, due to the use of the wavelet analysis.

Considering the model-based approaches, they should be built according to the specific features of the system on which they are applied. Indeed, if the model does not describe well the system behaviour, the results will be poor and inaccurate. For this reason, they are less “general” than the data-driven methods but, if a suitable model equation is chosen, they can give more accurate results on long term predictions. One of the most common methods used in model-based approaches is the Particle Filter, which is able to give a good estimation of the system evolution and can be used on every kind of model equation.

Finally, the hybrid methods, which combine different models, can be more accurate but they are also more complex to implement and require a higher computational time, so they might not be suitable for on-line predictions.

For the application developed in this work, among all the proposed prognostics algorithms, the ANFIS method was chosen to be applied on the available experimental data, in order to compare its results with the ones given by the specific developed procedure, which will be described in Chapter 3.

The choice to apply the ANFIS algorithm in this work, was due to several reasons:

- Like most data-driven methods, it is not linked to a specific type of device (differently from model-based methods), but it is adaptable and applicable to every kind of system.
- It is a consolidated method, which has been widely reported in the scientific literature and used for many applications. Therefore, being the documentation and the applications examples more consistent compared to the other approaches, this allowed to study and understand the method in a good way, in order to be able to implement it.
- It was possible to implement it with the software used throughout all the work, which is MATLAB.

The ANFIS prognostic method will be described in details, together with some application examples, in Chapter 2.

Chapter 2: ANFIS. Method description and applications

In order to predict the performance evolution of a system and give an estimation of its Remaining Useful Lifetime, different prognostics methods can be used. Among those presented in the literature analysis of Chapter 1, one of the most used and adaptable to any kind of system is the Adaptive Neuro-Fuzzy Inference System (ANFIS). It uses a set of historical or directly measured data from the system in order to learn its behaviour and perform prognostics. For this reason, as it does not require a system model or prior knowledge, it is defined as a data-driven prognostics method.

In this Chapter, after an overview about Artificial Neural Networks and Fuzzy Logic systems (Section 2.1), the Adaptive Neuro-Fuzzy Inference System (ANFIS) is described, focusing on its structure and its learning algorithm (Section 2.2). Section 2.3 presents some examples of ANFIS applications, focused on the prediction and prognosis of PEMFC systems. In Section 2.4, some final considerations about the method are presented.

2.1 Artificial Neural Network and Fuzzy Logic systems

“Soft computing” is an approach to computing, aiming at emulating the ability of the human brain to learn and adapt to uncertain and changing environments [23]. Soft computing techniques include Artificial Neural Networks (ANN) and Fuzzy Logic (FL) systems. The combination of these two approaches defines the Neuro-Fuzzy techniques, such as the Adaptive Neuro-Fuzzy Inference System (ANFIS) [24].

2.1.1 Artificial Neural Networks

An Artificial Neural Network (ANN) is a system developed for information processing, designed to resemble the human brain and its capability to receive and process information in a fast and adaptive way. Indeed, according to the biological model, the basic computational units of these networks are called as ‘neurons’ or ‘nodes’, which are connected to each other to form a layer pattern, called ‘net architecture’ [25].

Generally, a basic ANN architecture consists of three different parts. The first one is an ‘input layer’, which receives the data or inputs from the external environment and sends them to the next layer. This layer is composed by one or more ‘hidden layers’, which receive the data from the input layer and process them using specific functions. Each hidden layer can contain one or more neurons, depending on the complexity of the operations to be performed. The results of these layers are then sent to the ‘output layer’, which further processes the received data and gives the final result of the network [25]. The simplest ANN

architecture is represented by a Single Layer Network, in which the input neurons are directly linked to the output ones, without any hidden layer between them [27, 3].

All or part of the neurons can be adaptive, which means that they depend on modifiable parameters that can be updated in order to obtain better results. Each adaptive neuron has a local parameter set; the union of all the local parameters is the network's overall parameter set. In conventional graphic representations, adaptive nodes are denoted with squares, while fixed nodes are represented with circles [24]. An example of an ANN architecture is shown in Figure 35.

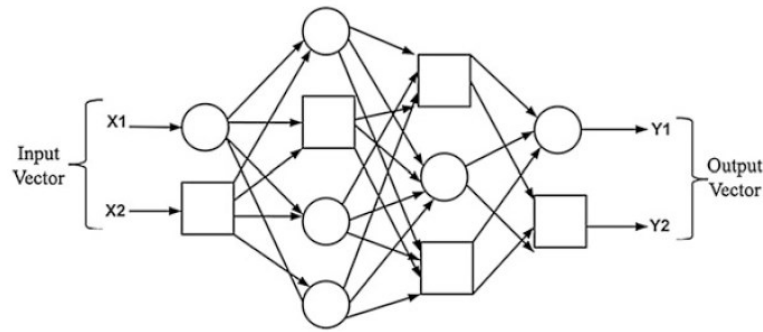


Figure 35 - Example of a generic ANN architecture [2]

Based on the pattern of connections between neurons, ANN architectures can be classified into two types: Feedforward Neural Networks and Feedback (or Recurrent) Neural Networks. In Feedforward Neural Networks, the connections between neurons are only in the forward direction; this means that the output of each layer does not have any effect on the previous layers. In Feedback (or Recurrent) Neural Networks, instead, there are some feedback links between neurons; data can propagate both in the forward and backward direction and the output of a layer can also be the input of the previous ones [26].

2.1.1.1 Learning process

In Artificial Neural Networks, a learning algorithm is needed in order to improve the network performance in giving reasonable outputs. It allows to modify the network's parameters so that it is able to give outputs that are consistent with the expected targets.

The learning processes can be divided into two main types: supervised learning and unsupervised learning.

- *Supervised learning* is based on the knowledge of a data set, called 'training data set', consisting of several inputs and the corresponding target outputs. The network parameters are adjusted in order to obtain the right mapping between the inputs and the outputs. This is done by using an error, defined as the difference between the target response and the actual response of the network. Generally, the learning process is stopped when the error goes under a specific threshold, defined by the user [26, 27].
- *Unsupervised learning*, on the contrary, does not use guidelines or target outputs in the learning process. The network only receives input samples and groups those with similar characteristics into some classes or categories. In this way, similar inputs will generate similar network responses [26, 27].

2.1.2 Fuzzy Inference Systems

A Fuzzy Inference System (FIS) is a computing technique based on the concepts of fuzzy reasoning and fuzzy rules. Fuzzy reasoning is an inference procedure in which knowledge and information are represented linguistically, in the form of fuzzy if-then rules [24]. A fuzzy if-then rule, also known as ‘fuzzy conditional statement’, is an expression that can be generally written as:

$$\text{If } X \text{ is } A \text{ then } Y \text{ is } B \quad (23)$$

The first part of the statement ($X \text{ is } A$) is called ‘antecedent’ or ‘premise’, while the second part ($Y \text{ is } B$) is called ‘consequent’ or ‘conclusion’ [24]. In Eq. (23), X and Y are the linguistic variables, while A and B are the linguistic labels, represented by specific Membership Functions (MF). The Membership Functions can be of different types, such as triangular, trapezoidal, monotonic, gaussian or bell-shaped [26].

The basic structure of a FIS consists of five functional blocks [26], as shown in Figure 36:

- a *Rule Base*, which contains the fuzzy if-then rules;
- a *Data Base*, which defines the membership functions associated with the fuzzy rules;
- a *Decision Making unit*, which performs the inference operations on the rules, deriving a reasonable output or conclusion;
- a *Fuzzification Interface*, which transforms the numerical inputs into linguistic variables;
- a *Defuzzification Interface*, which transforms the results of the fuzzy reasoning into numerical outputs.

Usually, the ensemble of Data Base and Rule Base is known as the Knowledge Base [25].

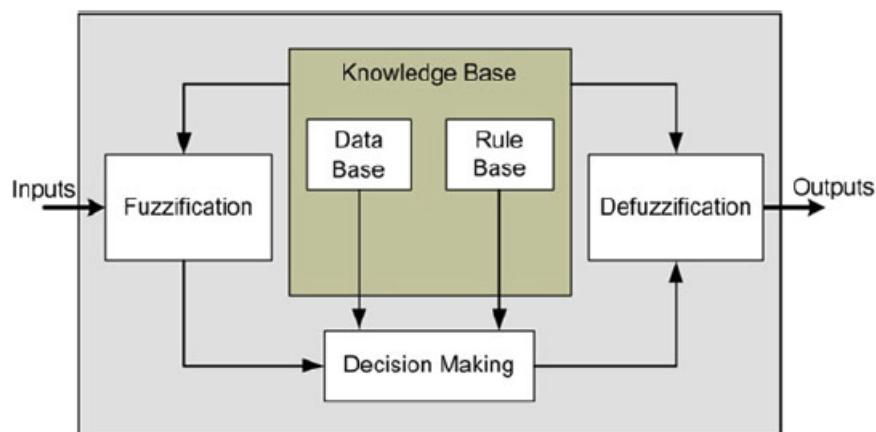


Figure 36 - Basic structure of a FIS [26]

The steps of the fuzzy reasoning performed by the Fuzzy Inference System are the following [26]:

- *Fuzzification*: the inputs are transformed in linguistic variables; then, they are compared with the membership functions indicated by the premise part of the fuzzy rule and the corresponding membership values are evaluated.
- *Aggregation*: the membership values are combined (usually with multiplication operators) to get the ‘firing strength’ or ‘weight’ of each fuzzy rule.
- *Activation*: the firing strength is used to generate the consequent part of each fuzzy rule.
- *Accumulation*: the outputs of each rule are aggregated to generate the overall output of the fuzzy system.
- *Defuzzification*: the fuzzy output is transformed into a numerical output.

Depending on the kind of fuzzy reasoning and fuzzy if-then rules employed, the fuzzy inference systems can be classified into three types [28, 24]:

- *Type 1 or Tsukamoto* fuzzy models: they use monotonic membership functions and calculate the overall output as the weighted average of each rule’s output, according to the firing strength of each rule.
- *Type 2 or Mamdani* fuzzy models: the firing strength of each rule is evaluated as the minimum of the membership values and the overall system output is calculated as the maximum of the outputs of each rule.
- *Type 3 or Takagi-Sugeno* fuzzy models: the firing strength of each rule is evaluated as the product of the input membership values; the output of each rule is expressed as a linear combination of the input variables and then the overall system output is calculated as the weighted average of each rule’s output.

Among these three types, the Takagi-Sugeno model is one of the most used to build the Adaptive Neuro-Fuzzy Inference System (ANFIS) [26], described in Section 2.2.

2.2 ANFIS: Adaptive Neuro-Fuzzy Inference System

The Adaptive Neuro-Fuzzy Inference System (ANFIS) is a Neuro-Fuzzy system, made by the combination of the Artificial Neural Network and the Fuzzy Inference System techniques. In this way, it combines the linguistic representation of fuzzy systems with the learning and adaptation capability of neural networks [24].

2.2.1 ANFIS architecture

In order to describe the structure of the ANFIS model, a system with two inputs (x and y) and one output (f) is considered here. The fuzzy if-then rules will be defined according to a Takagi-Sugeno (or type 3) FIS. Supposing that two rules are defined for the specified system, they can be written, for example, as [28]:

$$\text{Rule 1: If } x \text{ is } A_1 \text{ and } y \text{ is } B_1, \text{ then } f_1 = p_1 x + q_1 y + r_1 \quad (24)$$

$$\text{Rule 2: If } x \text{ is } A_2 \text{ and } y \text{ is } B_2, \text{ then } f_2 = p_2 x + q_2 y + r_2 \quad (25)$$

In these equations, A_1 and A_2 are the linguistic labels of the input x ; B_1 and B_2 are the linguistic labels of the input y ; p_1 , q_1 , r_1 , p_2 , q_2 and r_2 are the parameters of the consequent part [28].

The structure corresponding to the above fuzzy rules set is shown in Figure 37, which represents the basic architecture of an ANFIS.

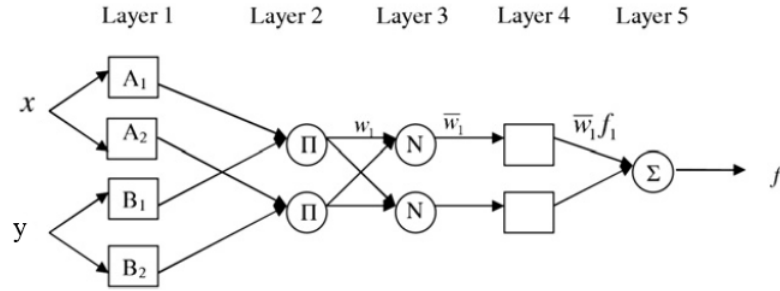


Figure 37 - Basic structure of an ANFIS [27]

The structure of an ANFIS is generally composed by five layers [28]:

- *Layer 1:* it is made by adaptive nodes, each one characterized by a Membership Function (MF). For example, for the input x :

$$O_i^1 = \mu_{A_i}(x) \quad , \quad i = 1,2 \quad (26)$$

Here, O_i^1 is the output of the layer 1 for the node i , it represents the value that the membership function μ_{A_i} assumes for the specific input. The membership functions can be of different types; one of the most used is the bell-shaped function (with minimum value 0 and maximum value 1), expressed as [28]:

$$\mu_{A_i}(x) = \frac{1}{1 + \left[\frac{(x-c_i)^2}{a_i^2} \right]^{b_i}} \quad (27)$$

Here, a_i , b_i and c_i are the parameters of the membership function, called as 'premise parameters'. As shown in Figure 38, c_i represents the centre of the bell-shaped function, a_i is its half width and b_i defines its slope.

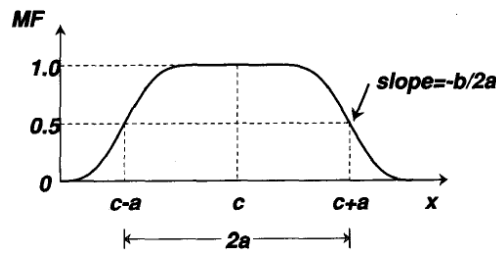


Figure 38 - Bell-shaped function [28]

The number of MFs for each input can be chosen by an expert, who is familiar with the system to be modelled, or by trial and error. Generally, the initial values of the premise parameters are set such that the MFs are equally spaced on the range of values of the input variables.

- *Layer 2:* it is made by fixed nodes, labelled as π . Each node performs the product of the incoming data from Layer 1 and sends the result to the next layer:

$$O_i^2 = w_i = \mu_{A_i}(x) * \mu_{B_i}(y) \quad , \quad i = 1,2 \quad (28)$$

The output O_i^2 of layer 2 for each node i is defined as the ‘firing strength’ w_i of the corresponding fuzzy rule, and represents its weight in the overall system output.

- *Layer 3*: it is made by fixed nodes labelled as N . Each node calculates the ‘normalized firing strength’ \bar{w}_i of the corresponding fuzzy rule, by performing the ratio of the firing strength of each rule to the sum of the firing strengths of all rules.

$$O_i^3 = \bar{w}_i = \frac{w_i}{\sum_i w_i} \quad , \quad i = 1,2 \quad (29)$$

- *Layer 4*: it is made by adaptive nodes, each one characterized by a specific node function. The nodes output O_i^4 is the product between the node function and the normalized firing strength of the corresponding fuzzy rule. For example, according to the fuzzy rules in Eq. (24) and Eq. (25):

$$O_i^4 = \bar{w}_i \cdot f_i = \bar{w}_i \cdot (p_i \cdot x + q_i \cdot y + r_i) \quad , \quad i = 1,2 \quad (30)$$

Here, p_i , q_i and r_i are the parameters of the node function, called as ‘consequent parameters’.

- *Layer 5*: it is made by a single fixed node labelled as Σ , which computes the overall system output f by summing up all the incoming inputs from layer 4:

$$O_1^5 = f = \sum_i \bar{w}_i \cdot f_i \quad (31)$$

To make sure that the network is able to correctly model the behaviour of a specified system, it is necessary to adapt the premise and consequent parameters of the adaptive nodes (in Layer 1 and Layer 4). For this reason, a learning algorithm must be used, as described in Section 2.2.2.

2.2.2 Hybrid Learning Algorithm

The training phase of the network allows adapting the parameters of the layers 1 and 4 that contain adaptive nodes. The network’s overall parameter set, in the case of a Takagi-Sugeno model, can be divided into two parts: the Layer 1 contains the premise parameters, while the Layer 4 contains the consequent parameters. For this reason, a hybrid learning algorithm can be used to adapt the two groups of parameters in different ways [26].

The hybrid algorithm is made by two parts [28]:

- a *backward path*, in which, once the consequent parameters are fixed, the premise parameters are adapted through a Gradient Descent (GD) method. This method is described in Section 2.2.2.1.
- a *forward path*, in which, once the premise parameters are fixed, the consequent parameters are adapted through a Recursive Least Square Estimator (RLSE). This method is described in Section 2.2.2.2.

This hybrid algorithm belongs to the class of supervised learning algorithms, as a training dataset is used to adjust the adaptive parameters [28].

2.2.2.1 Gradient Descent method

The Gradient Descent is an iterative optimization method, which is used to find the minimum of a function. It is used in the hybrid learning algorithm of an ANFIS, in order to adapt the premise parameters of the non-linear function in the first layer, assuming that the consequent ones are fixed. It requires a training data set, composed by pairs of inputs and targets, so it is a form of supervised learning [28].

Assuming that the training dataset is made by P pairs, the error E_p for each p^{th} sample of the set is defined as [28]:

$$E_p = \sum_{i=1}^M (T_{i,p} - O_{i,p})^2 \quad (32)$$

Here, T is the target output and O is the network output, evaluated for each node i of the layer (where M is the total number of nodes in the first layer). The error on each training pair E_p is used to calculate the overall error E :

$$E = \sum_{p=1}^P E_p \quad (33)$$

Then, an update formula is used to evaluate the variation $\Delta\alpha$ of each adaptive parameter:

$$\Delta\alpha = -\eta \frac{\delta E}{\delta \alpha} \quad (34)$$

Here, α is the specific parameter to be adapted; in the case of the bell-shaped function, α stands for the parameters a , b or c , described in Figure 38 and Eq. (26). Instead, η is a learning rate, which defines the speed of convergence of the algorithm. If the learning rate is too small, the method will be accurate but the convergence will be slow, as the parameters are adjusted with small variations at each iteration and the gradient has to be evaluated many times; on the contrary, if it is too large, the convergence will be fast, but the method will oscillate around the optimum [28].

2.2.2.2 Recursive Least Square Method

The Recursive Least Square Estimator (RLSE) is applied in the hybrid learning algorithm in order to adapt the consequent parameters of the fourth layer, assuming that the premise ones are fixed [28].

In the Takagi-Sugeno model, according to the functions specified in the fuzzy rules, the overall output of the ANFIS can be expressed through a linear combination of the inputs and the consequent parameters. By feeding the training data in this equation, it can be expressed in a matrix form as [28]:

$$IC = T \quad (35)$$

Here, T is the vector of target outputs from the training dataset (corresponding to the vector f of Figure 37), C is the vector of unknown consequent parameters, I is the matrix that contains the inputs from the training dataset (corresponding to the vectors x and y of Figure 37). Then, the RLSE method is used to adapt the consequent parameters in such a way that the squared error $\|IC - T\|^2$ is minimized [28].

The Recursive Least Square Estimator is more computationally complex than the Gradient Descent method. However, the hybrid learning approach, that includes both, has a faster convergence with respect to the Gradient Descent method applied on both premise and consequent parameters, and it can avoid its drawback of being trapped in local minima [28].

2.3 PEMFC voltage prediction using ANFIS

Among the most common applications, an Adaptive Neuro-Fuzzy Inference System (ANFIS) can be used to approximate non-linear functions or to model non-linear systems, which can allow the forecasting of their future behaviour for prognostic purposes [24]. In this Section, some ANFIS application examples are described, all of them focused on the ability of the method to predict the behaviour of an electrochemical system, in order to apply it for prognostics.

2.3.1 PEMFC voltage prediction at different operational conditions

Vural et al. [18] applied the ANFIS method in order to predict the performance of a Proton Exchange Membrane Fuel Cell (PEMFC). The aim was to evaluate the stack voltage under different operating conditions. Therefore, the voltage was set as output parameter, while the input parameters were the current density, the fuel cell temperature, the operating pressure and the temperatures of the inlet streams at the anode and cathode.

The number and type of membership functions were chosen by trial and error, running the model with different parameters for 400 iterations. The best results were obtained by assigning at each input two membership functions of the Gaussian type. The number of fuzzy rules was fixed at 32. A set of 333 experimental data samples (made by the ensemble of the five inputs and the corresponding voltage output) was used to train and test the ANFIS model: 200 samples were used for the training phase and 133 for the testing phase. The training phase was stopped when the Root Mean Square Error (RMSE) reached the minimum value (in this case, at 137 iterations) [18].

The results of the voltage prediction during the training and the testing phases are shown, respectively, in the diagrams of Figure 39(a) and Figure 39(b).

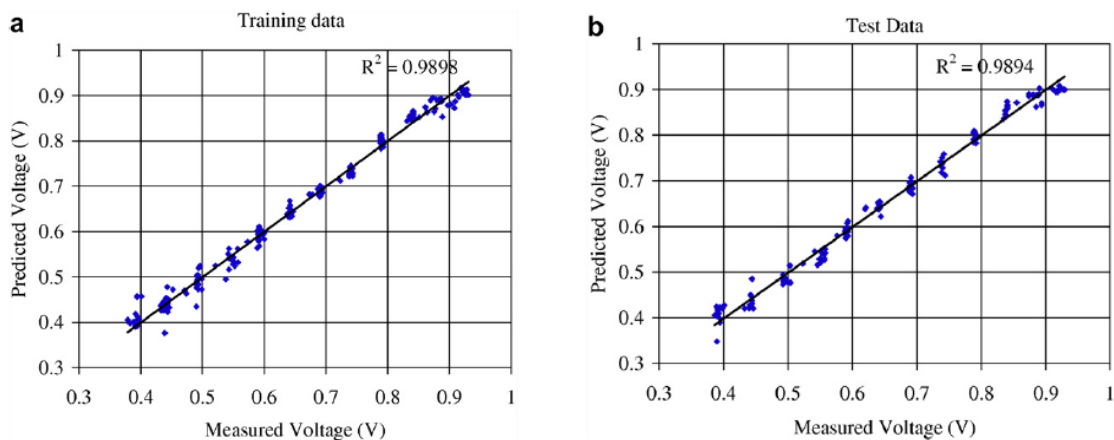


Figure 39 - PEMFC voltage prediction in training and testing phase [18]

In these plots, the voltage predicted by the model was compared with the measured stack voltage; the ANFIS results were close to the experimental data and the RMSE of the test phase was low (0.015) [18].

2.3.2 PEMFC voltage degradation prediction

Silva et al. [16] applied the ANFIS algorithm in order to predict the voltage degradation in Proton Exchange Membrane Fuel Cells, for prognostics purposes. In this study, two fuel cell stacks made of five cells were tested; the first stack (Stack 1) was operated at constant current, while the second one (Stack 2) was operated in ripple mode. Polarization curves and impedance spectra measurements were periodically performed.

In order to predict the future stack voltage, the ANFIS model was run with four inputs, chosen as the values of the voltage itself at four previous time instants. Three Gaussian type membership functions were associated to each input. The rule set was composed by 81 fuzzy rules [16].

For the two stacks, the experimental datasets used to train and test the ANFIS were made by the voltage values measured during 1000 hours of continuous operation. In order to choose the duration of the training phase, the value of the RMSE was analysed in three different cases, when a different number of training data was used (100, 250 and 500 hours). As shown by Figure 40 and Figure 41, the quality of the prediction was poor when few data were used to train the system (as the RMSE was highly increasing), whereas good predictions were obtained with a high number of training data (as the RMSE reached lower values) [16].

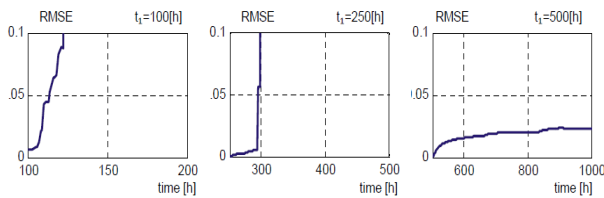


Figure 40 - Stack 1: RMSE vs training time [16]

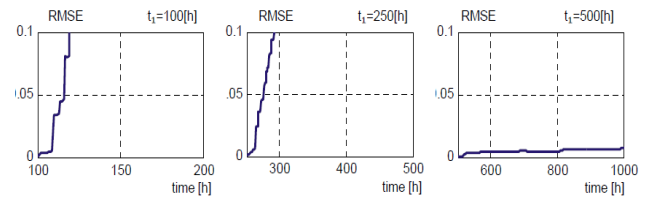


Figure 41 - Stack 2: RMSE vs training time [16]

So, in order to obtain the best prediction results with the lowest values of the RMSE, the measurements of the first 500 hours were used to train the model and the remaining ones were used to validate it [16].

The results for Stack 1 and Stack 2 are shown in Figure 42 and Figure 43, respectively.

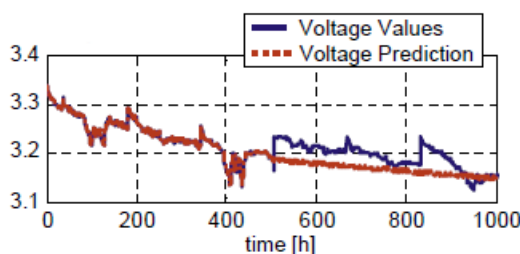


Figure 42 - Voltage prediction for Stack 1 [16]

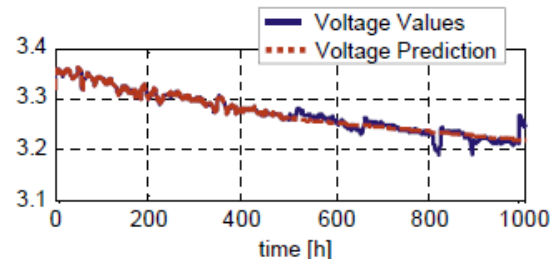


Figure 43 - Voltage prediction for Stack 2 [16]

The voltage values predicted by the algorithm were close to the real voltage measurements; however, abrupt and unexpected voltage changes could not be predicted by the ANFIS. The RMSE were 0.032 for the Stack 1 and 0.014 for the Stack 2 [16].

2.3.3 PEMFC performance prediction

Mao et al. [28] applied the ANFIS method for prognostics purposes, to forecast the voltage degradation in a PEMFC. The experimental dataset was provided by measurements made on a fuel cell stack, operating for about 1200 hours under the current profile shown in Figure 44.

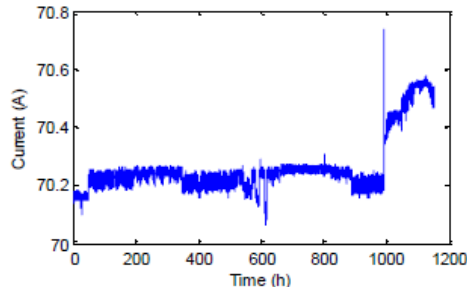


Figure 44 - Current profile applied to the PEMFC [28]

The 2/3 of the dataset were used to train the model, while the remaining was used to validate it. The ANFIS model was run with three inputs: the current, the cathode outlet temperature and the flow rate at the cathode. The stack voltage was the only output [28]. The prediction results are shown in Figure 45.

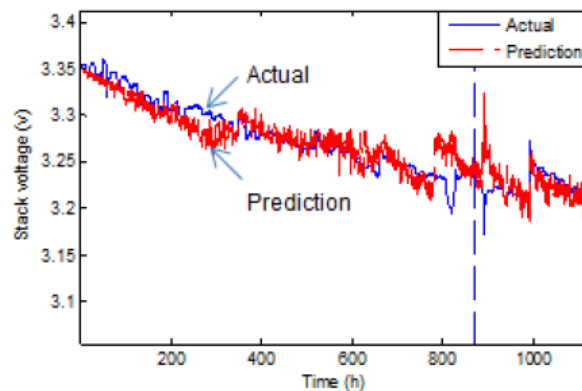


Figure 45 - Voltage prediction results using ANFIS [28]

The results predicted by the ANFIS were close to the experimental voltage measurements. However, as in the previous case, the model was not able to predict the voltage when the system conditions changed in a fast and unpredictable way, as shown in Figure 45 at about 800 h and 900 h [28].

2.4 Conclusions

In the field of systems prognostics and health management, different kinds of prognostics approaches are available. In this Chapter, the Adaptive Neuro-Fuzzy Inference System (ANFIS) method was presented. First, its general structure was described, together with its learning algorithm; then, some examples of application to PEMFC performance prediction were shown.

The ANFIS method is a computing technique that can be used for a wide range of applications. Indeed, one of its main advantages is that it does not need specific and deep knowledge about the system to be modelled, but it works only using historical or

experimental data, which allow the network to learn (and then predict) the behaviour of the system. Moreover, if the method is well trained by choosing suitable datasets for the training and testing phases, it can give results that represent the real system behaviour with a quite good accuracy.

However, the ANFIS approach is also characterized by several drawbacks. First, the choice of the datasets for the training and testing phases is a crucial point. These datasets should be both representative of the kind of data that the system is supposed to receive as inputs but they should be different enough, in order to prevent the so-called overfitting. Indeed, if the data used for the two phases are too similar, the network will learn “by heart” and it will not be able to give acceptable results for any other data different from the training ones. Moreover, the amount of training data should be large enough to find a good approximation of the adaptive parameters, but the higher is the number of data the higher will be the computational cost. In addition, the quality of the training data is important, as datasets that are too irregular or not representative of the system behaviour will result in a poor training and lead to bad and inaccurate predictions.

Another drawback is that the results of the network depend on the choice of the number and type of membership functions. Generally, the prediction accuracy increases when increasing the number of membership functions assigned to each input; this will, however, affect the amount of computational time needed for the system’s training. Regarding the choice of the type of membership functions, there is not a specific rule, and they should be chosen or according to an expert knowledge of the system or by trial and error.

In this work, the ANFIS algorithm was used with one of the available experimental datasets, for the approximation of the daily profiles of some relevant system variables, with the aim to analyse and predict their future behaviour. The results are shown in Chapter 3, compared with the ones given by the averaging approximation procedure, described in Chapter 3, too.

Chapter 3: Profiling algorithm for “event-based” prognosis

In this chapter, an analytic prognostic methodology, which was applied on the available experimental datasets, is described. The work was developed as a part of the research made by EIFER to propose a new prognostic algorithm to be applied for the RUL forecasting of electrochemical devices, like fuel cells, electrolysers and batteries.

The degradation of a system due to its aging can occur in different ways, depending on its operating conditions. Indeed, a device that is operated at heavy load conditions will probably exhibit a faster degradation, with a higher aging rate. Therefore, the proposed algorithm is based on the identification of all the possible operating configurations in which the device can work, called as operational points. A different aging rate will be associated to each operational point and, in order to evaluate it, the behaviour of the system in each condition should be known. Moreover, in order to evaluate the system’s RUL, it is important to know at which operational points the device is working in the future and for how much time, that is its future operational profile.

In this work, a profiling algorithm was, therefore, developed for these two purposes: identify the features of the device behaviour at each operational point and build the operational profile expected in the future. For these specific features, this algorithm represents an approach which can be used in the context of a particular kind of prognosis, different from the traditional one based on aging, which can be called as “event-based” prognosis.

The different features of the aging-based and event-based prognosis are presented in Section 3.1. In Section 3.2, the profiling algorithm developed in this work is described. In Section 3.3, the quality indicators used to evaluate the accuracy of the algorithm are presented.

3.1 “Event-based” prognosis

The profiling algorithm, which has been developed in this work, is not a method that can be used to perform the traditional prognosis, describing the aging of a system. Its aim is, instead, to perform a preliminary analysis of the behaviour of a device, which is needed as an input for the “aging-based” prognosis. This process has been, here, defined as “event-based” prognosis.

The main feature of the aging-based prognosis is that the behaviour of the system can be described and analysed through the monitoring of a physical quantity, specific for each

device. Usually, as emerged from the literature analysis of Chapter 1, the behaviour of a fuel cell is described by its voltage, while for a battery the evaluated quantity is its capacity. Through the monitoring of these physical parameters on a long time horizon, it is possible to observe the progressive degradation of the system, as its aging is identified by a decreasing trend of these physical quantities.

On the contrary, the aim of the event-based prognosis is to analyse the experimental data on short time windows, in order to identify all the different operating conditions of the device. In this way, it is possible to describe how the system works and predict how it will work in the future. This operational profile is an important information needed to perform the aging-based prognosis, as a specific degradation rate is, then, assigned to each operating condition of the device, in order to evaluate its overall aging behaviour. Therefore, the event-based prognosis is needed as input to perform the traditional aging-based prognosis.

In this prognostic approach, the different operating modes are identified by analysing the random events that can occur on the system. In this work, they are represented by the daily profiles of the power produced or consumed by each device of the system (fuel cell, electrolyser and battery). The profiling of these events allows to determine the past and current operating conditions of the system, which is then used to predict the future operational profile. Indeed, the main assumption of this approach is the repeatability of the system behaviour in the time, so the future operational profile is assumed to be equal or similar to the one recorded in the past. This is, however, also the main limitation of the approach because, if the system exhibits a behaviour that is different from the profiled one, the forecast will be inaccurate.

3.2 Profiling algorithm

The proposed prognostic algorithms is based on the profiling of the random events that can occur on the system. In this work, the events are represented by the daily profiles of power produced or consumed by the fuel cell, the electrolyser and the batteries of each plant. Moreover, the daily power consumption of the end user and the solar irradiance were also analysed and treated with the profiling algorithm (when these data were available).

The algorithm works according to the following steps, which are schematically represented in Figure 46:

- First, the daily profiles of each variable were extracted from the raw data;
- They were divided into several classes, or categories, using as main classification criterion the daily energy associated to the profile. In some cases, besides the daily energy, additional classification criteria were used, in order to take into account the specific features of the profiles. For each device, the number of classes and the energy thresholds of each class were chosen after a preliminary analysis of the data, in such a way to group in the same class profiles with similar features and to have approximately the same number of profiles in each class.
- For each of the generated classes, an average profile was built, which should be representative of all the experimental profiles contained in the class.

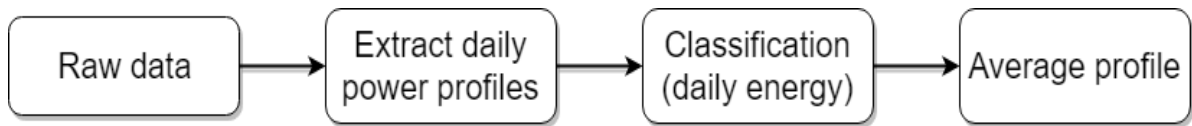


Figure 46 - Flowchart of the profiling algorithm

The general procedure that was applied in order to build the average profile for each class, is described by the steps listed below:

- The experimental profiles were shifted along the time axis, in order to make their starting point (the first point with a power higher than zero) coincide. This was possible because, for the prognostics purposes, it is not relevant to know when the power is generated during the day, but it is important to know how many days are characterized by those specific load conditions. Indeed, what affects the degradation of the device is not the time at which it works, but the amount of energy produced, the power and the amplitude of its changes.
- The average profile was built by taking at each time the mean of the non-zero values of the power, among all the experimental profiles of the class. This allowed to preserve the real shape of the experimental profiles, avoiding the presence of steps that would have been created by averaging the power with the null values.
- The generated profile was, finally, scaled in order to make its energy coincide with the mean cumulated energy of the experimental profiles. To do this, the average profile was modified by reducing its duration. In this way, the profile is able to represent the highest power values and its duration will not be the maximum but a mean of the durations of the experimental profiles. In those cases in which the duration of the power profile covers the whole day, the energy scaling was made by multiplying each point of the profile by a scaling factor, evaluated as the ratio between the energy of the average profile and the mean of the energies associated to the experimental profiles of the class.

The scheme of Figure 47 summarizes all the steps of the applied algorithm, clarifying them with a graphic example.

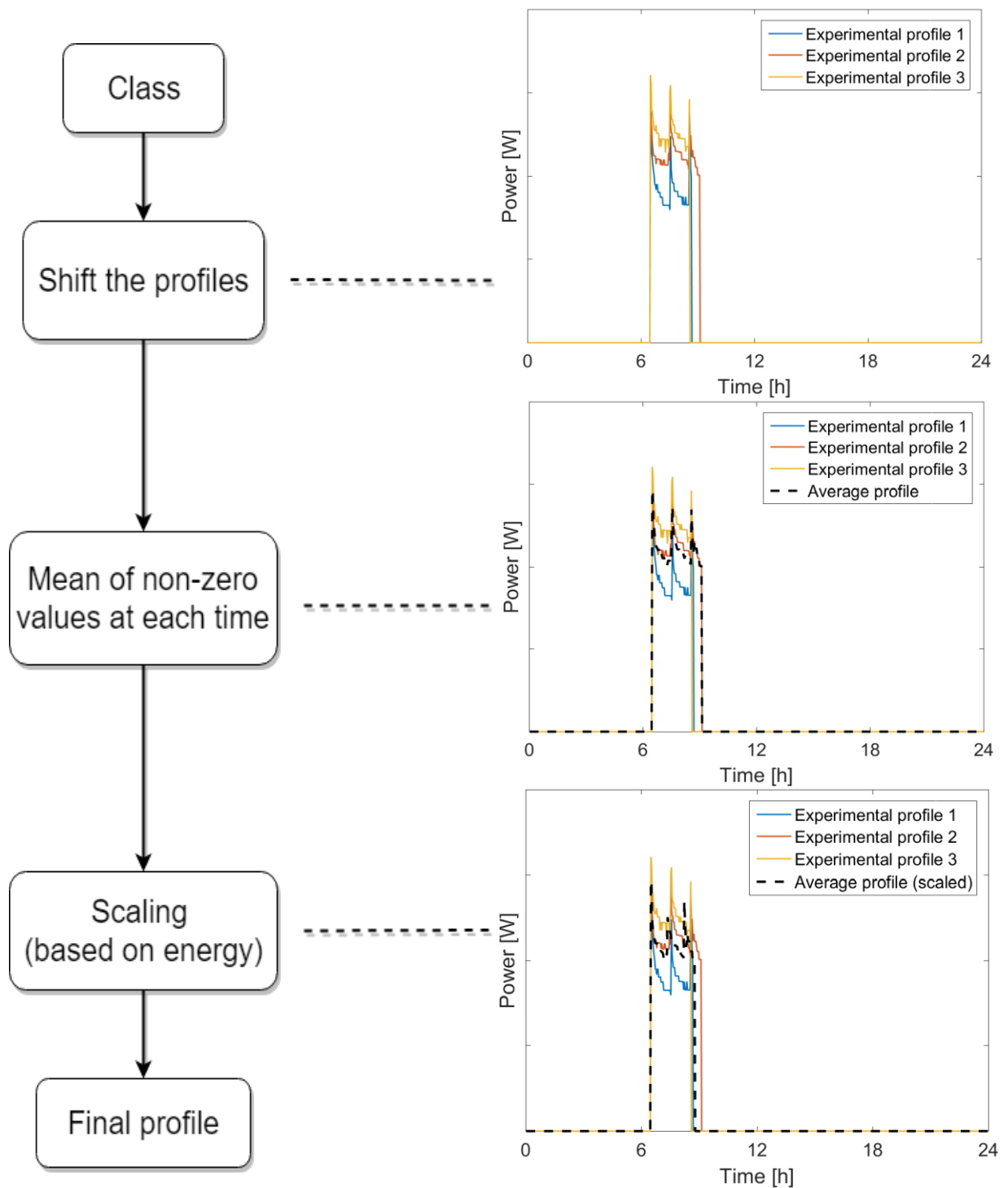


Figure 47 - Flowchart of the averaging procedure

3.3 Quality evaluation of the average profiles

In order to evaluate whether the average profiles represent a good approximation of the real data, the errors between the average and the experimental profiles were evaluated in different ways.

It is important to highlight that, for all the indicators, in order to perform the error evaluation, the profiles to be compared were sorted in descending order, from the highest to the lowest value of the power. This was done because otherwise, even if the shape of the

profiles is similar, it is possible that the time positions are not always coinciding; this can heavily affect the evaluation of the error, even if it is not so relevant for the prognosis.

The first and simplest way was to evaluate, for each point of the profiles (at each time-step t), the relative difference between the average and the experimental profiles, expressed as a percentage (Eq. (36)).

$$\text{Relative Error } (t) [\%] = \frac{\|Power_i(t) - PowerAP(t)\|}{PowerAP(t)} * 100 \quad (36)$$

Here, $PowerAP(t)$ is the power of the average profile at time t and $Power_i(t)$ is the power of the i -th experimental profile at time t . Then, the error on the whole profile was evaluated as the mean of the values at all the times, corresponding to the Mean Average Percentage Error (MAPE), expressed in Eq. (2).

The second quality indicator used for the error estimation was the Standard Deviation σ or Absolute Error, evaluated at each time t , as shown in Eq. (37) with the same symbols of Eq. (36).

$$\sigma(t) = \sqrt{\frac{\sum_{i=1}^N (Power_i(t) - PowerAP(t))^2}{N}} \quad (37)$$

This kind of error is expressed in the same unit of measure of the evaluated quantity, which is here always a power unit (Watts or Watts per square meter). The evaluation of this quantity allows to calculate a quality indicator, named as Difference of Energy, as shown in Eq. (38).

$$\text{Difference of Energy } [\%] = \frac{\int_0^{\infty} \sigma(t) dt}{\int_0^{\infty} PowerAP(t) dt} * 100 \quad (38)$$

This indicator compares the energy associated to the absolute error and the energy associated to the average power profile, expressing it as a percentage. It was used in order to evaluate the quality of the profiles classification, as in this work it is always based on the daily energy. High values of this error indicate that the profiles classification should be improved, for instance by increasing the number of classes or choosing some additional classification criteria.

Another indicator used for the quality estimation was the Percentage Relative Standard Deviation (PRSD), evaluated for each point of the profile (at each time t). This was done by normalizing the value of the standard deviation, dividing it by the value of the average profile $PowerAP(t)$ and expressing it as a percentage (Eq. (39)).

$$PRSD(t) = \frac{\sigma(t)}{PowerAP(t)} * 100 \quad (39)$$

Here, N is the number of profiles of each category, $PowerAP(t)$ is the value of the average profile at each time t (each point of the profile) and $Power_i(t)$ is the value of the i -

t th experimental profile at the time t . The overall error on the entire profile was, then, evaluated as the average of the values obtained for each time. In addition, for the devices that are not working continuously during the whole day (such as the fuel cell and the electrolyser), an average value of the PRSD was evaluated only on the running hours, in order to have an estimation of the approximation accuracy of the method.

As it is evaluated at each time-step, this quantity indicates whether the average profile is able to properly represent the dynamics of the experimental profiles, that is their maximum power and their shape.

3.4 Conclusions

The profiling algorithm developed in this work was used in the context of the “event-based” prognosis, needed as input of the traditional “aging-based” prognosis, which is used to forecast the Remaining Useful Life (RUL) of a system. It was performed on two sets of experimental data, one presented in the Chapter 4, the other described in Chapter 5. The monitored variables were analysed on a daily time window and their daily profiles were divided in different classes, according to their specific features. Then, for each of these classes, an average profile was evaluated, in order to approximate and represent the specific characteristics of all the profiles of the class.

These average profiles could, then, be used for prognostic purposes, as explained above. The analysis and the profiling of variables like the solar irradiance or the load required by the end user could be useful to build the future operational profile of the system. Indeed, if the future user power request or solar irradiance are not known, a way to overcome the problem would be to suppose that these quantities will have a future profile similar to the one observed in the past. Instead, the average profiles built with the power data of the single devices (fuel cell, electrolyser, batteries) could be used to define the features, and consequently the aging rate, of the operational points for each device.

Chapter 4: Mafate energy system. Profiling of experimental data for prognostics

In this chapter, the profiling prognostic methodology described in Chapter 3, was applied on the first of the two available experimental datasets, containing the data monitored on a power installation located in the Cirque de Mafate, in the Reunion Island (in the Indian Ocean, east of Madagascar).

This chapter is organized in the following way. Section 4.1 presents the description of the power system, its operating modes and the experimental dataset available from the direct measurements performed on it. Section 4.2 shows an overview about the energy produced and consumed in the system and its different sources. In Section 4.3, Section 4.4 and Section 4.5, the profiling analysis and averaging process performed, respectively, on the power data of the fuel cell, the electrolyser and the battery are presented. Section 4.6 shows the profiling of the solar irradiance data. Section 4.7 presents the analysis performed on the end user load data, comparing the application of the profiling and averaging procedure (Section 4.7.1) with the implementation of the ANFIS algorithm (Section 4.7.2). Section 4.8, finally, presents some final considerations and comments.

For confidentiality reasons, in all the plots, the axis of the ordinates has been omitted.

4.1 System description

The first power production system, whose experimental data were analysed in this work, is a stand-alone installation, used to produce power for three buildings (a school, a small clinic and a workshop) in a small village located in the Cirque de Mafate, in the Reunion Island.

The main components of the power system are:

- four strings of photovoltaic panels (PV), with nominal power of 7.8 kW;
- a proton exchange membrane fuel cell (PEMFC), with nominal power of 2.5 kW;
- two electrolysers, with nominal production of 500 l/h of hydrogen;
- a hydrogen storage, with capacity of 1100 l and pressure of 30 bars;
- four Li-ion batteries, with nominal capacity of 16 kWh.

In order to satisfy the user power demand, first, the power produced by the PV is used; if this is not enough, it is taken from the batteries. When the state of charge of the batteries goes below 30% of their nominal capacity, the needed power is produced by the fuel cell, using the stored hydrogen. A simple scheme is shown in Figure 48.

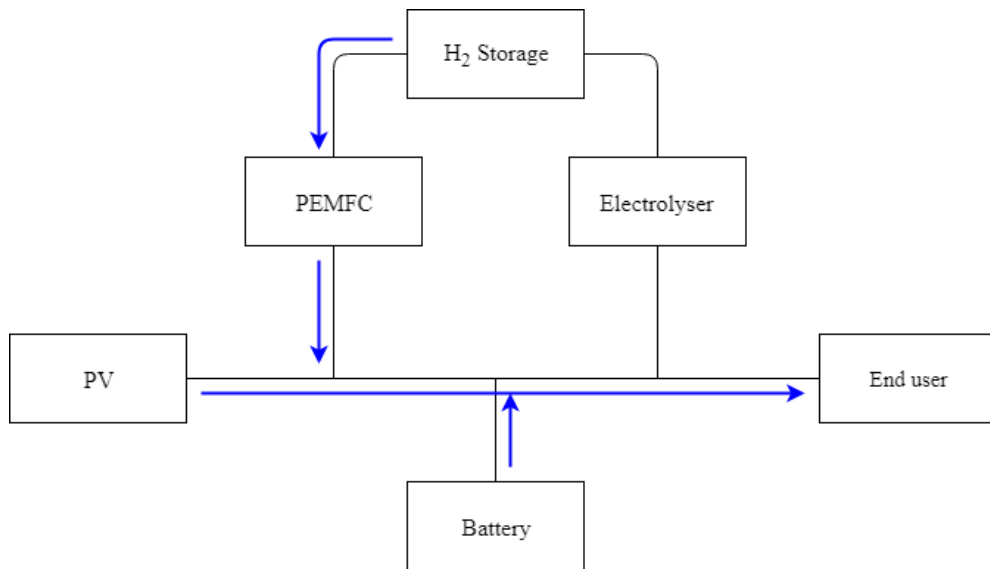


Figure 48 - System scheme in case of lack of PV power

On the contrary, if the PV produces an excess of power, this is used to charge the batteries (if they are not fully charged) or it is used to produce hydrogen for the storage through the electrolyzers. A simple scheme is shown in Figure 49.

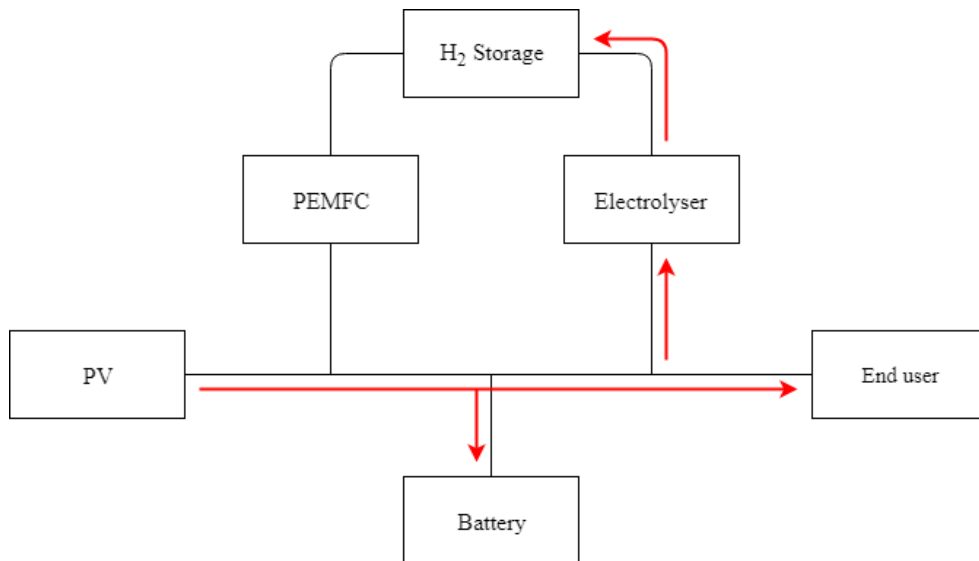


Figure 49 - System scheme in case of excess PV power produced

The direct measurements on the system cover a period of nine months, from May 2017 to January 2018, but the data related to some days are missing. The total number of days analysed was 238.

4.2 Energy balance and power consumption

This section presents an overview about the energy and power data collected from May 2017 to January 2018, in order to understand how much energy is produced and consumed by the system and which are the different sources of power production.

Figure 50 shows, for each month, the energy balance of the system, highlighting the different sources of energy production and consumption, respectively denoted by positive and negative values. The month of June is not reported, because few data are available.

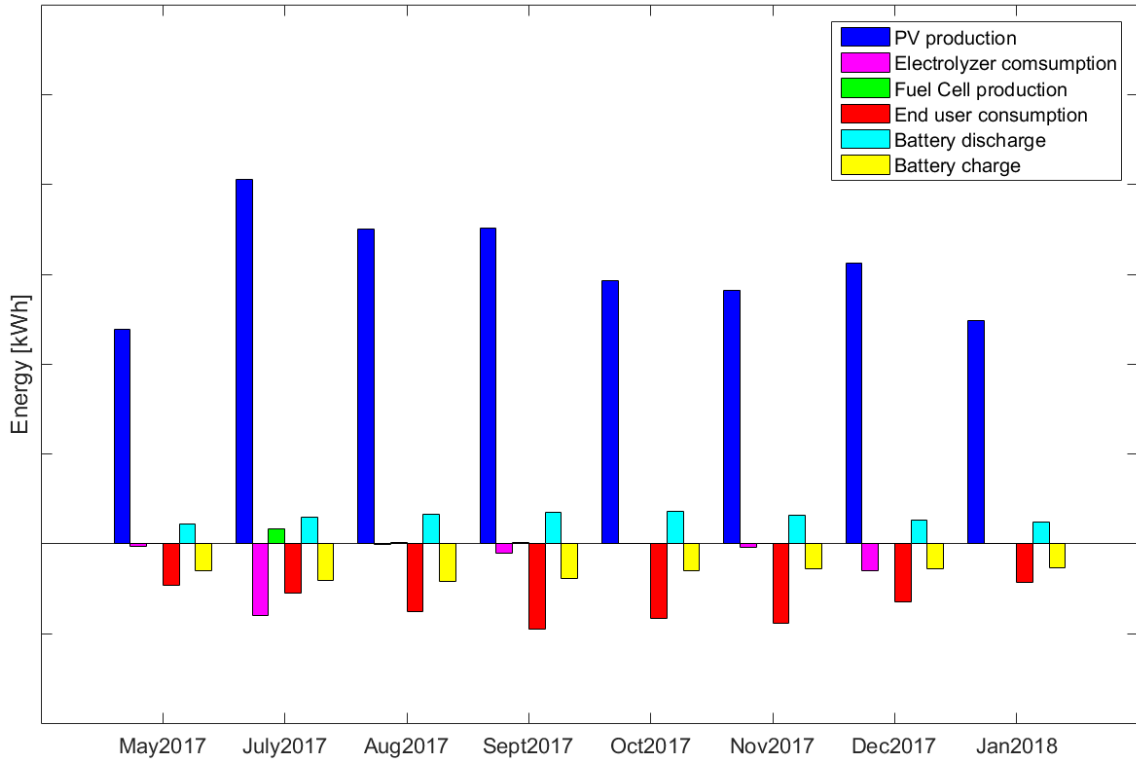


Figure 50 - System energy balance

As shown in Figure 50, the energy produced by the photovoltaic panels is significantly higher than the consumed energy. This huge difference is justified by the producer as the energy needed for the system auto-consumption. When the solar energy is not available, the power required by the end user is supplied by the batteries, whose state of charge (SOC) is shown, for each month, in Figure 51.

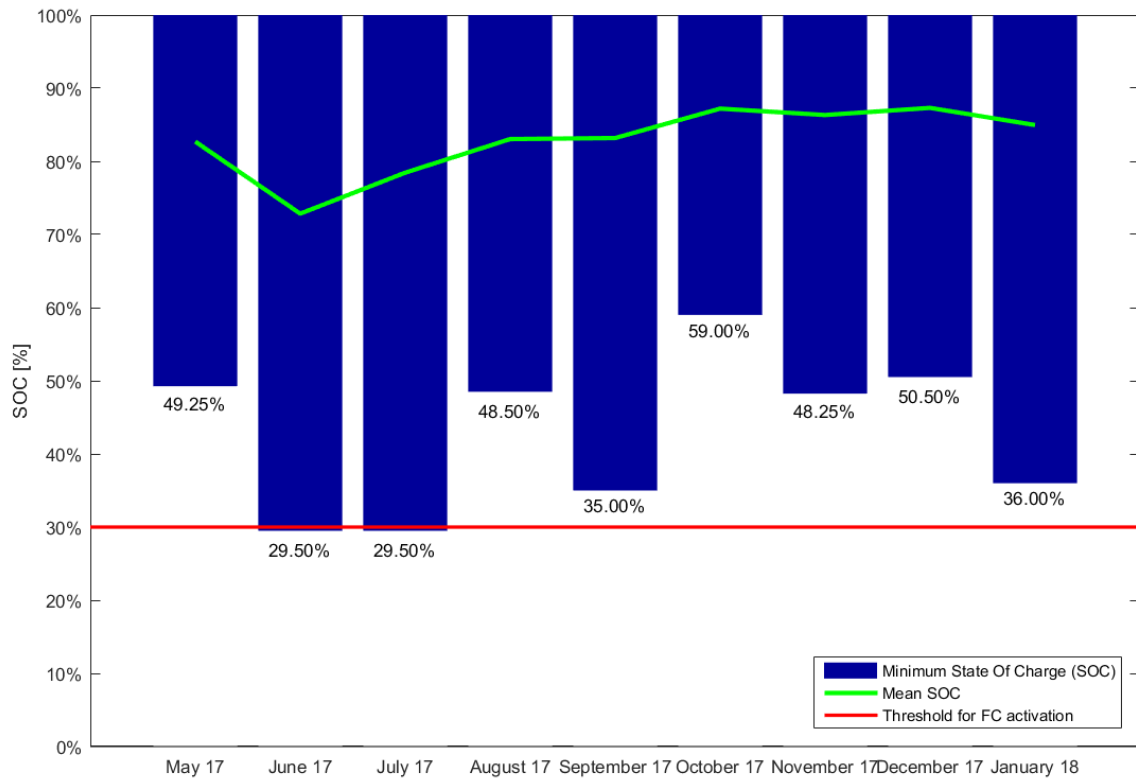


Figure 51 - Batteries state of charge (SOC)

The fuel cell starts to produce power when the battery SOC goes below the threshold of 30%. This happens only in the months of June and July, when the fuel cell is characterized by the highest values of power production, as shown in Figure 52. During the other months, instead, the battery is always able to supply the needed power and the fuel cell is only started to perform periodical tests. As a consequence, the running time of the electrolyzers is small, as shown in Figure 53.

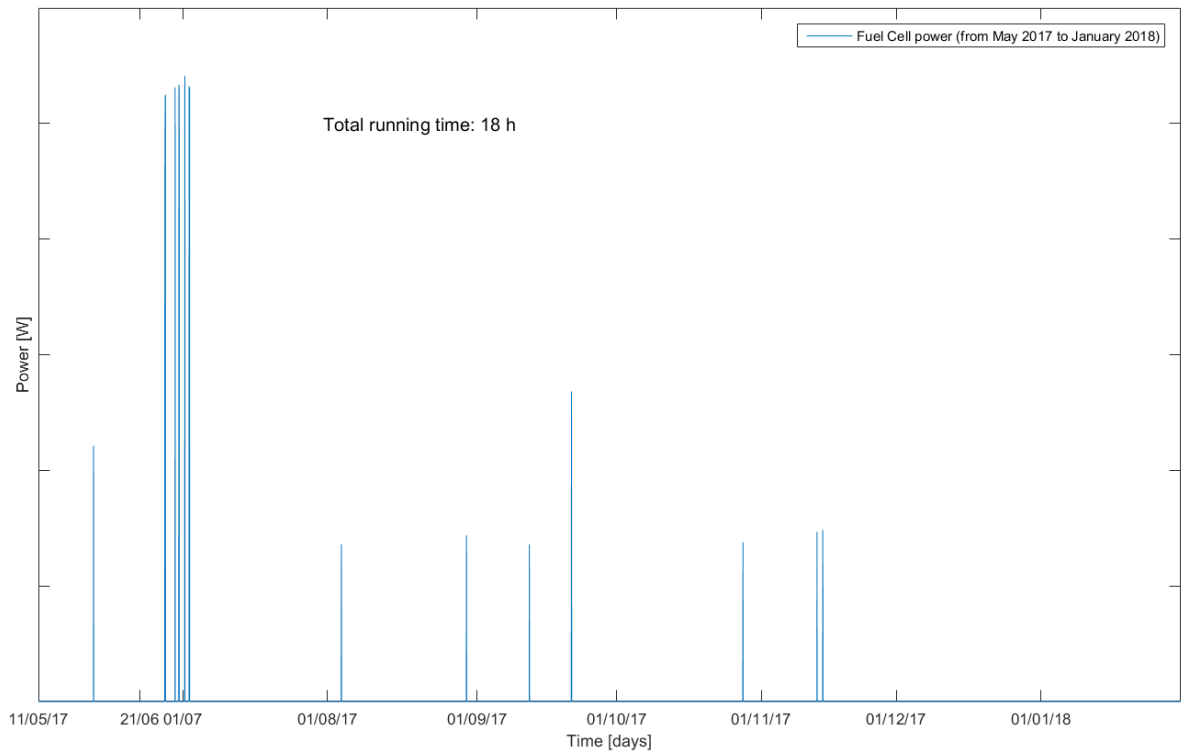


Figure 52 - Fuel cell power production

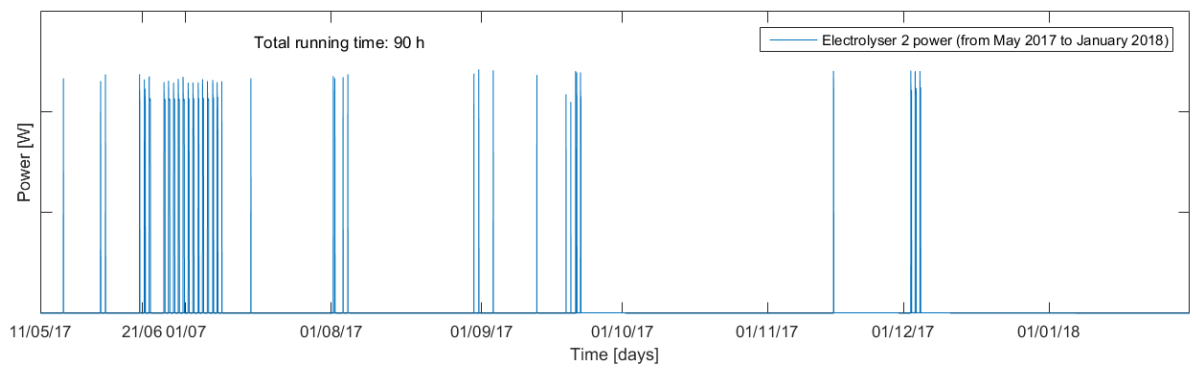
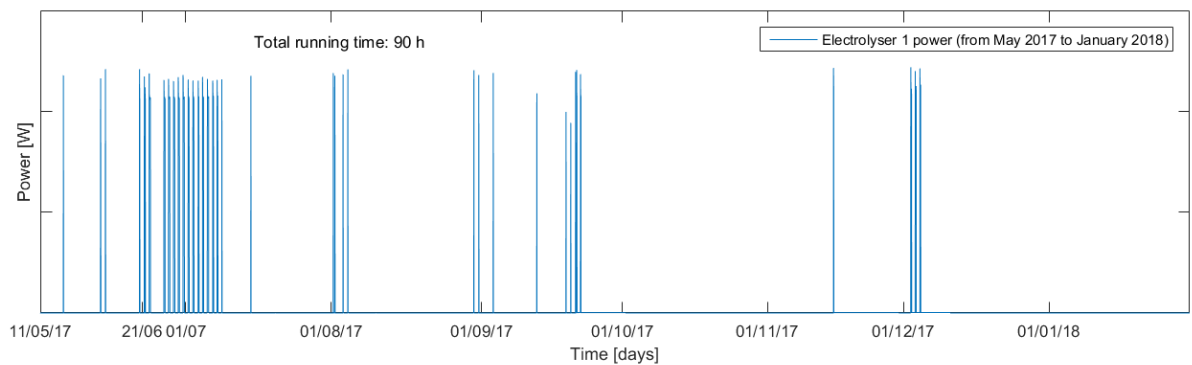


Figure 53 - Electrolysers power consumption

Finally, the different sources of power production were analysed. The plots in Figure 54 and Figure 55 allow understanding how the different devices are used to supply power to the user; they represent two different cases, corresponding to a sunny day and a cloudy day, respectively. In both plots, the positive area (corresponding to the power produced) is higher

than the negative area (which represents the power consumed). As already shown in Figure 50, this means that only a small part of the power produced by the PV is used to cover the end user demand, while the remaining part is used by the system as auto-consumption or wasted.

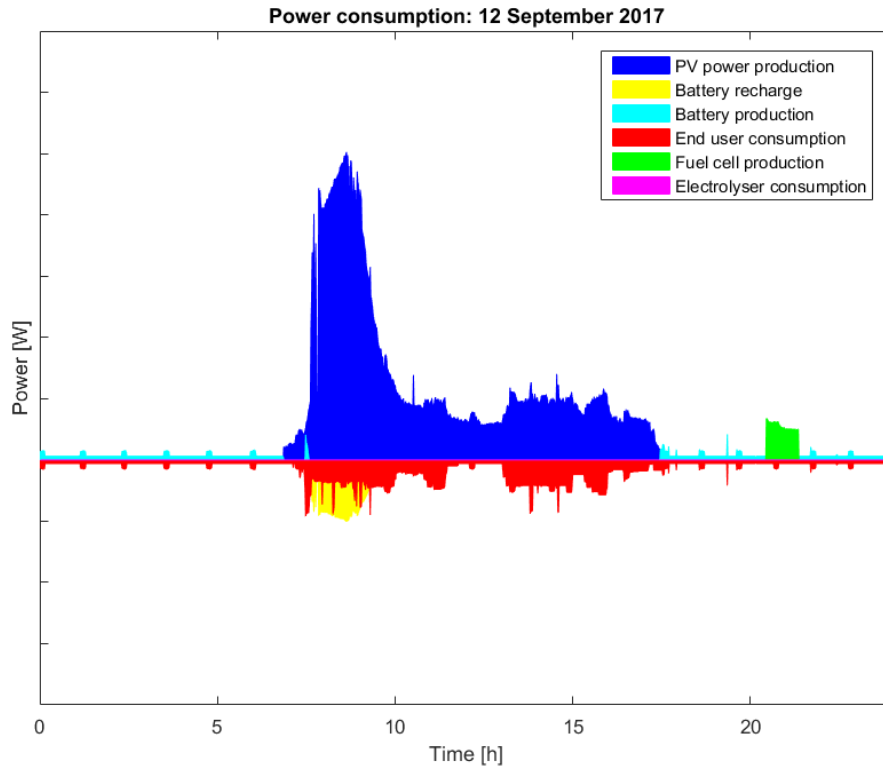


Figure 54 - Sources of power consumption (sunny day)

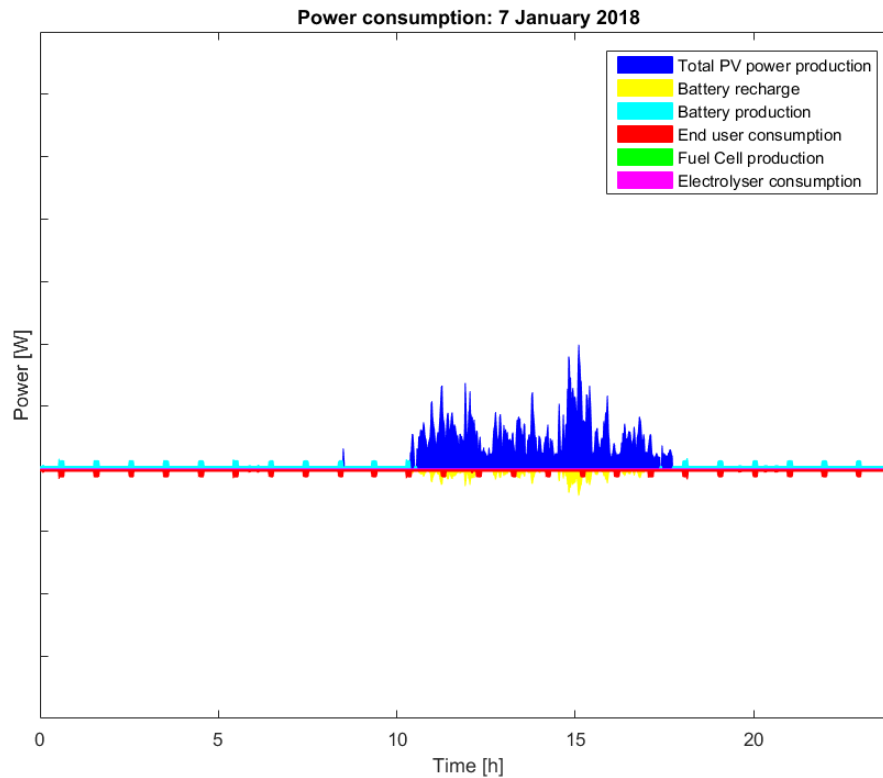


Figure 55 - Sources of power consumption (cloudy day)

4.3 Fuel Cell power profiles

In this Section, the data about the power produced by the fuel cell were analysed. In order to identify the behaviour of the device in each of its operational points and to forecast its future performance, some daily average profiles were built to describe and approximate the different operating conditions of the PEMFC, observed through the experimental data. In order to build the average power profiles, first, the data were analysed and the profiles of each day were assigned to some classes or categories; then, an averaging procedure, described in this Section, was applied.

As seen from Figure 52, during the whole period of monitoring, the fuel cell was running for less than 20 hours. Indeed, the device ran only during 13 days, which were divided in 4 classes according to the daily produced energy, which was chosen as classification criteria. The number of classes and the energy thresholds of each class were chosen after a preliminary analysis of the data, in such a way to group in the same class profiles with similar features and to have approximately the same number of profiles in each class. The features of each class are shown in Table 1, where the percentage of occurrence of each class over the whole period is also shown. In this case, the low values indicate again the short running time of the fuel cell during the nine months analysed.

Table 1: Fuel cell power profiles classes

Class	Daily Energy (DE) [kWh]	Percentage on total days [%]
FC1	$DE < 0.6$	2.5 %
FC2	$0.6 < DE < 2$	0.8 %
FC3	$2 < DE < 5$	0.8 %
FC4	$DE > 5$	1.3 %

For each of the categories shown in Table 1, an average profile was built according to the steps described in Section 3.2 and Figure 47. The plots from Figure 56 to Figure 59 show the average profile obtained for each class, compared with all the corresponding experimental profiles. In these figures, the experimental profiles were not represented in their shifted positions, but in the real ones.

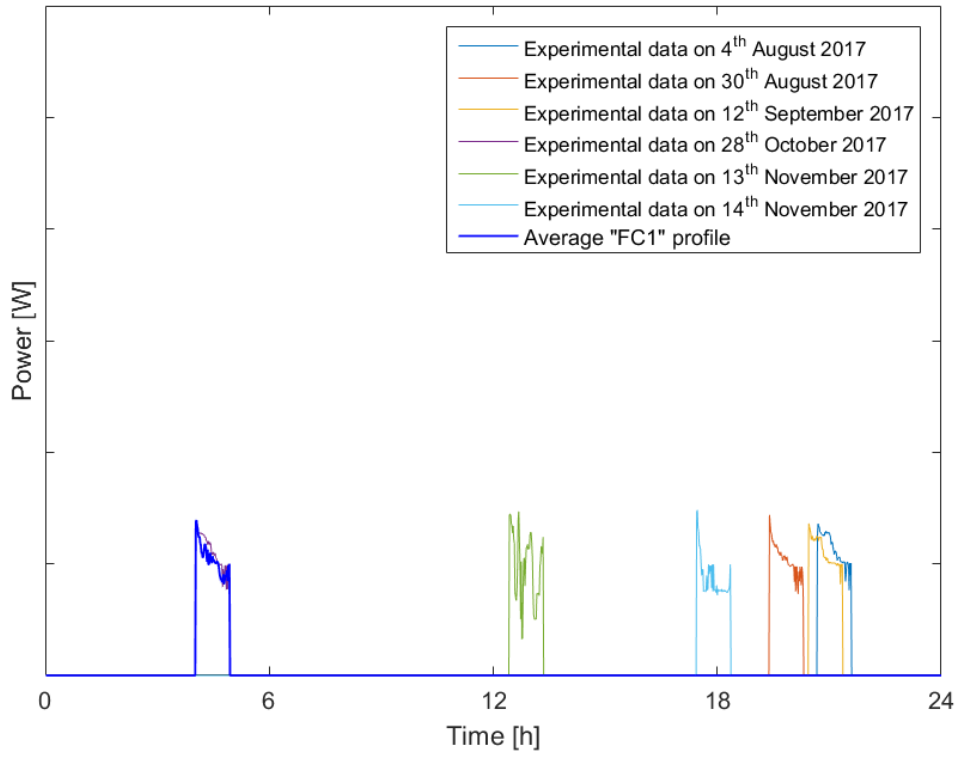


Figure 56 - Average fuel cell power profile "FC1"

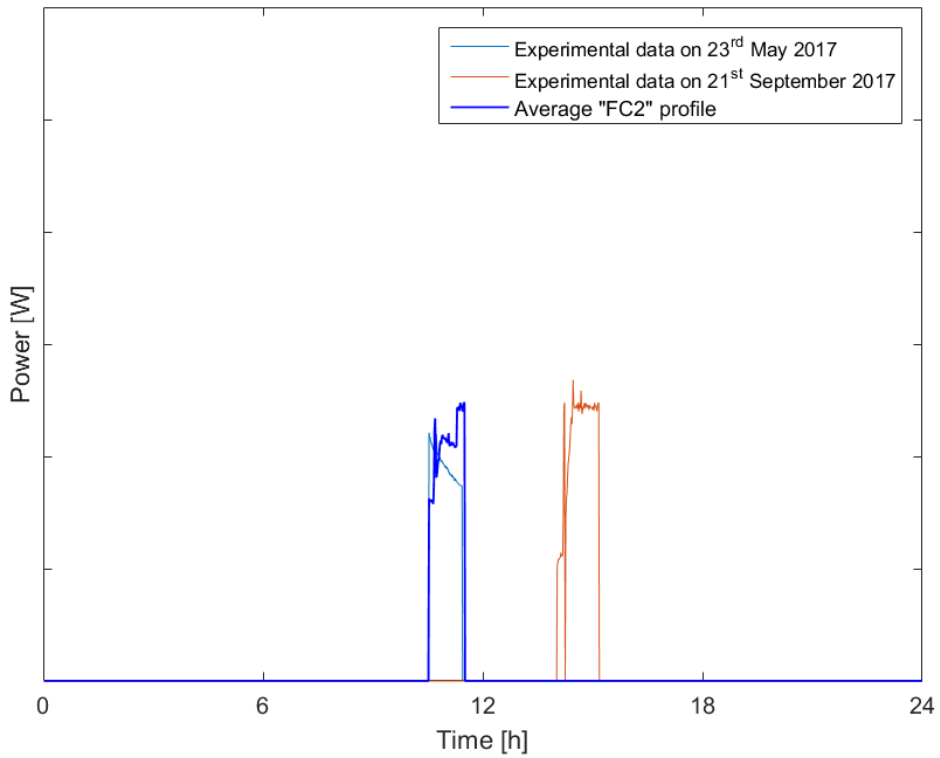


Figure 57 - Average fuel cell power profile "FC2"

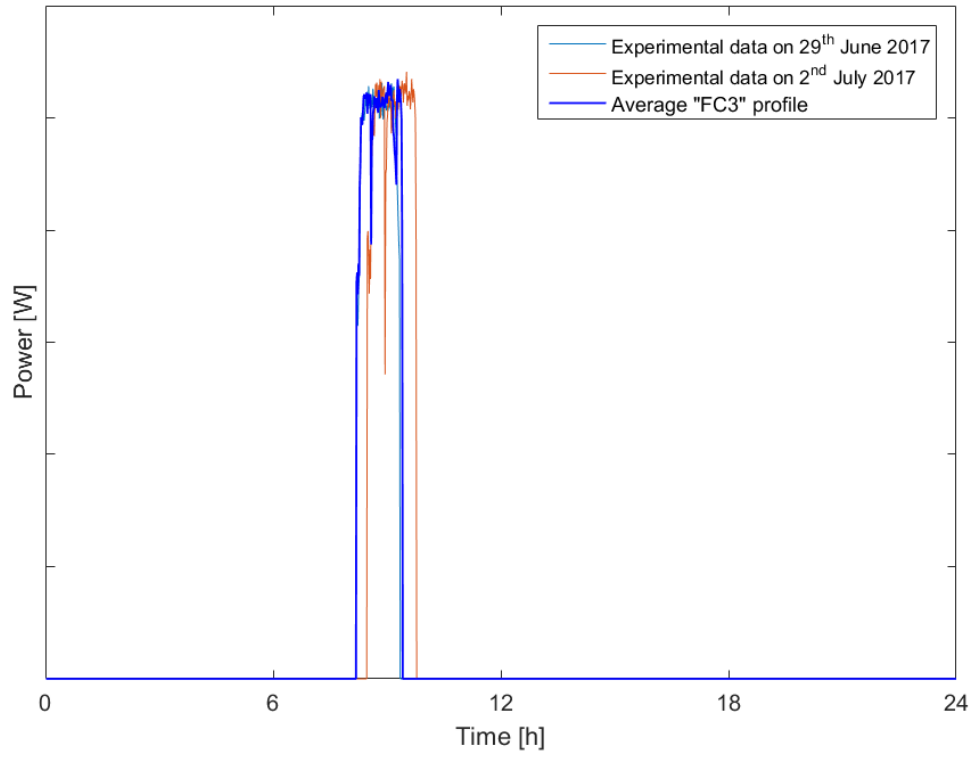


Figure 58 - Average fuel cell power profile "FC3"

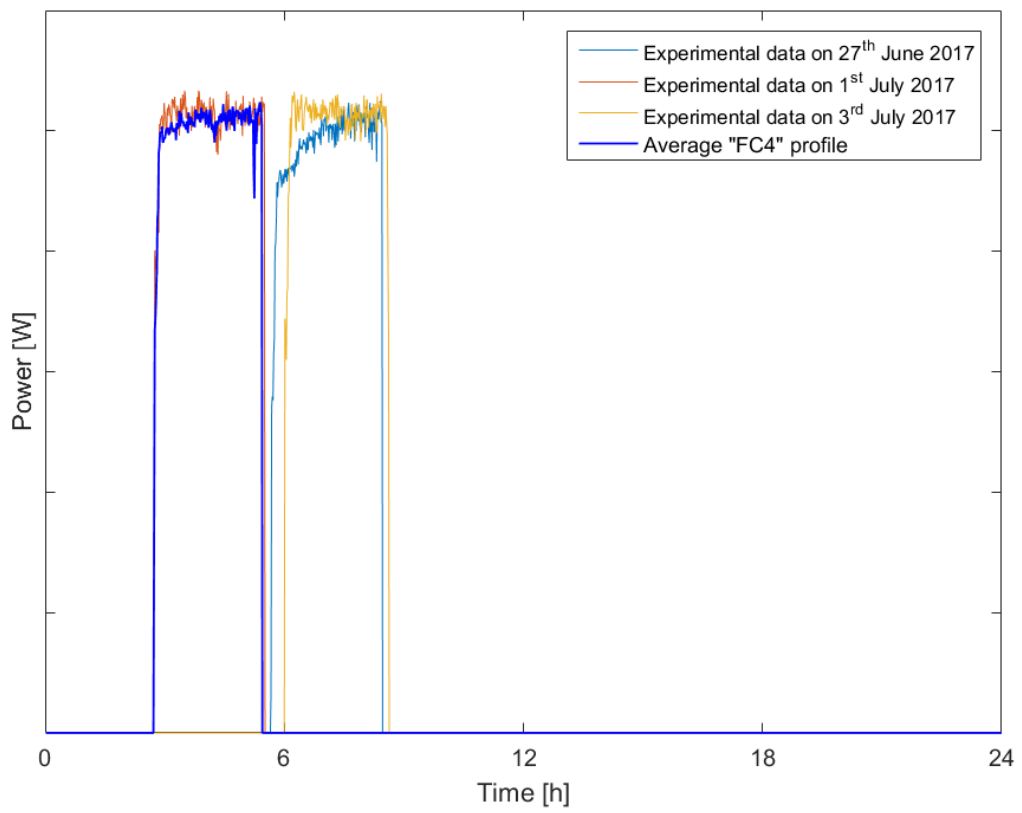


Figure 59 - Average fuel cell power profile "FC4"

4.3.1 Quality evaluation

As explained in Section 3.3, in order to evaluate the quality indicators for each class, the profiles were first sorted, representing the power from the highest to the lowest value, as shown in Figure 60 for the fuel cell power profiles of the class “FC4”. Then, the quality indicators were evaluated at each time, so that an error profile could be built as in Figure 61, where the PRSD profile of the class “FC4” is shown. In both figures the time scale is cut, because the durations of the profiles are not covering the whole day. The PRSD profile is quite good, as most values are below or around 10%. However, the high values reached at the end of the profile are caused by the huge power difference that occurs because of the different durations. Here, indeed, the high difference between the experimental profile of the 1st or the 3rd July 2017 and the average one just before 3 hours, generates the huge peak of the error profile.

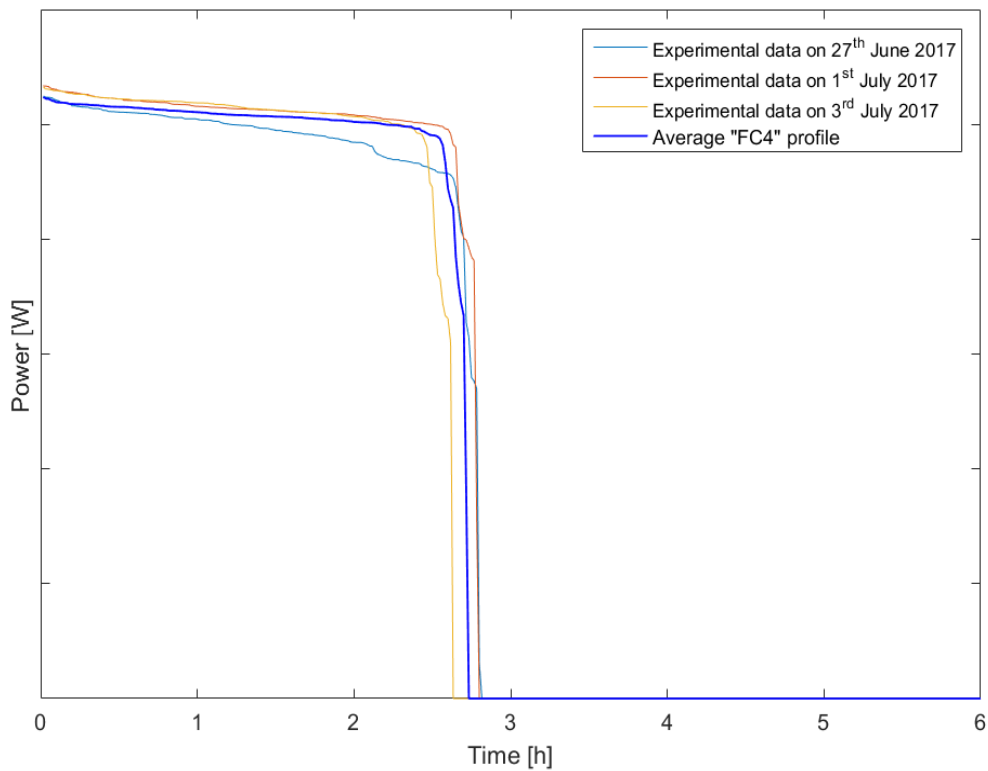


Figure 60 – Sorted profiles of the class “FC4”

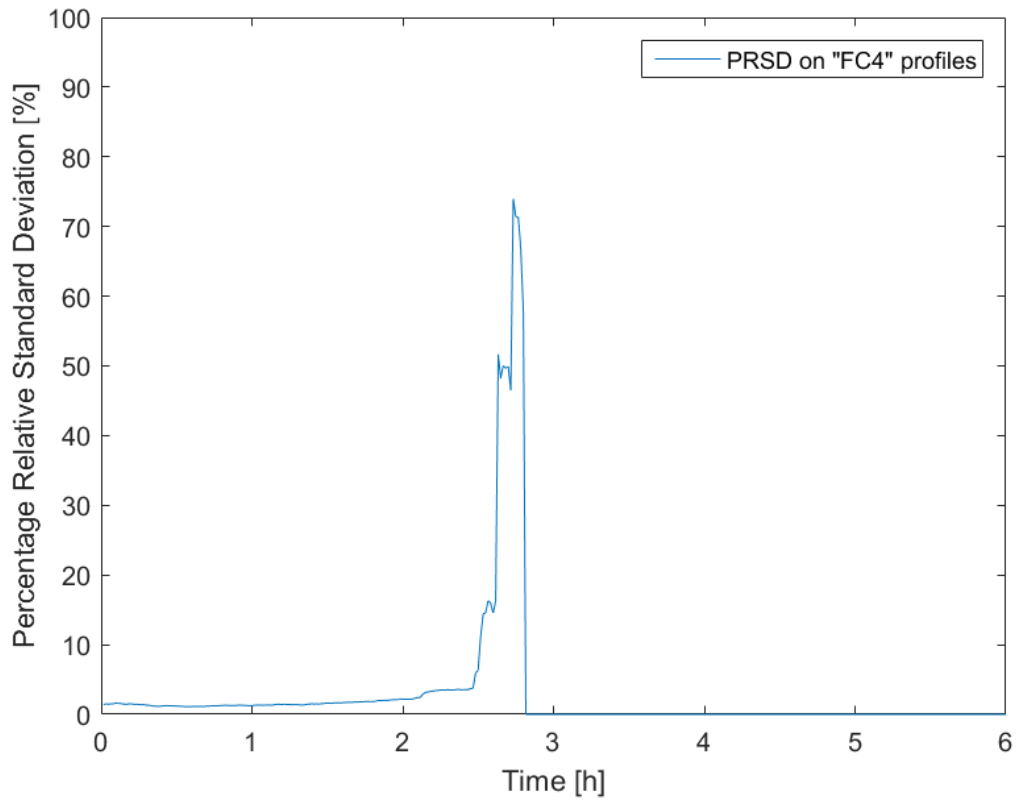


Figure 61 – PRSD on fuel cell power profiles of the class “FC4”

The same comments apply for all the other classes, whose PRSD profiles are shown in Figure 62.

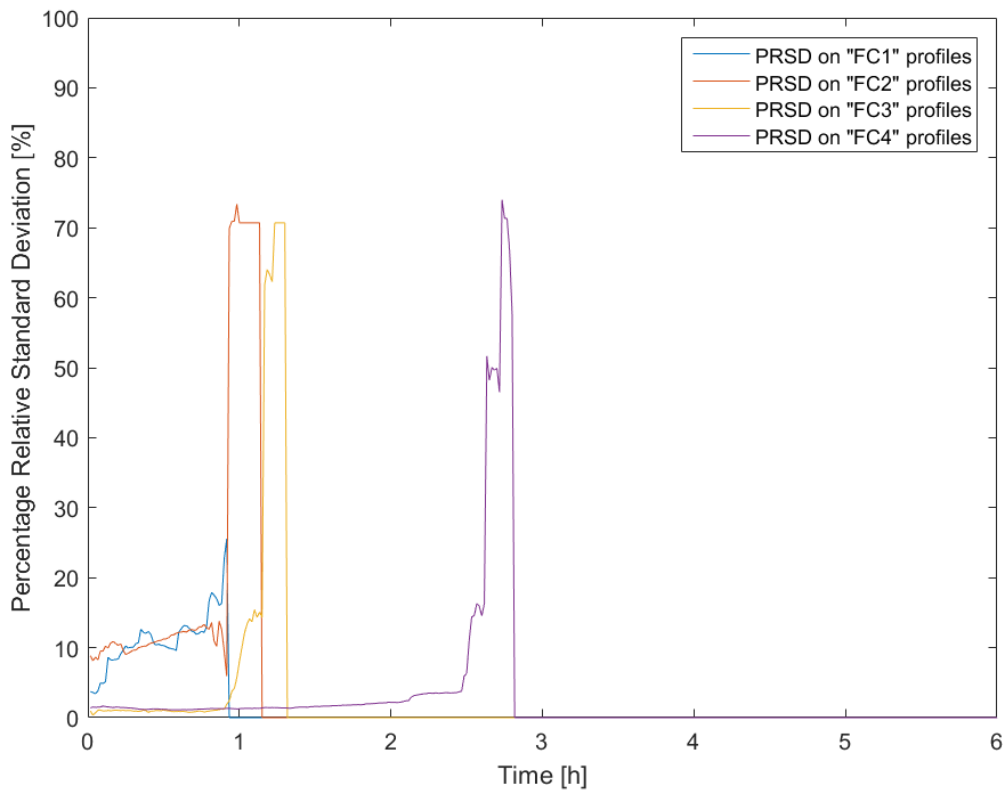


Figure 62 - PRSD on fuel cell power profiles

For each category, the values of the relative error (or MAPE) and the PRSD, averaged on the whole profiles, are shown in Table 2, together with the values of the PRSD evaluated only on the running hours of the device.

Table 2: PRSD and MAPE on average fuel cell power profiles

Class	MAPE [%]	PRSD [%]	PRSD on running time [%]
FC1	0.4 %	0.4 %	12.4 %
FC2	0.9 %	1.1 %	16.2 %
FC3	0.5 %	0.6 %	6.8 %
FC4	0.6 %	0.7 %	4.9 %

Figure 63 shows the absolute standard deviation evaluated between the average and the experimental profiles; its behaviour is similar to the PRSD, for the same reasons. Table 3 shows, finally, the values of the Difference on Energy for each class. The class “FC2” shows the highest value of the error, due to the difference between the two profiles of the class, both in the energy and in the shape.

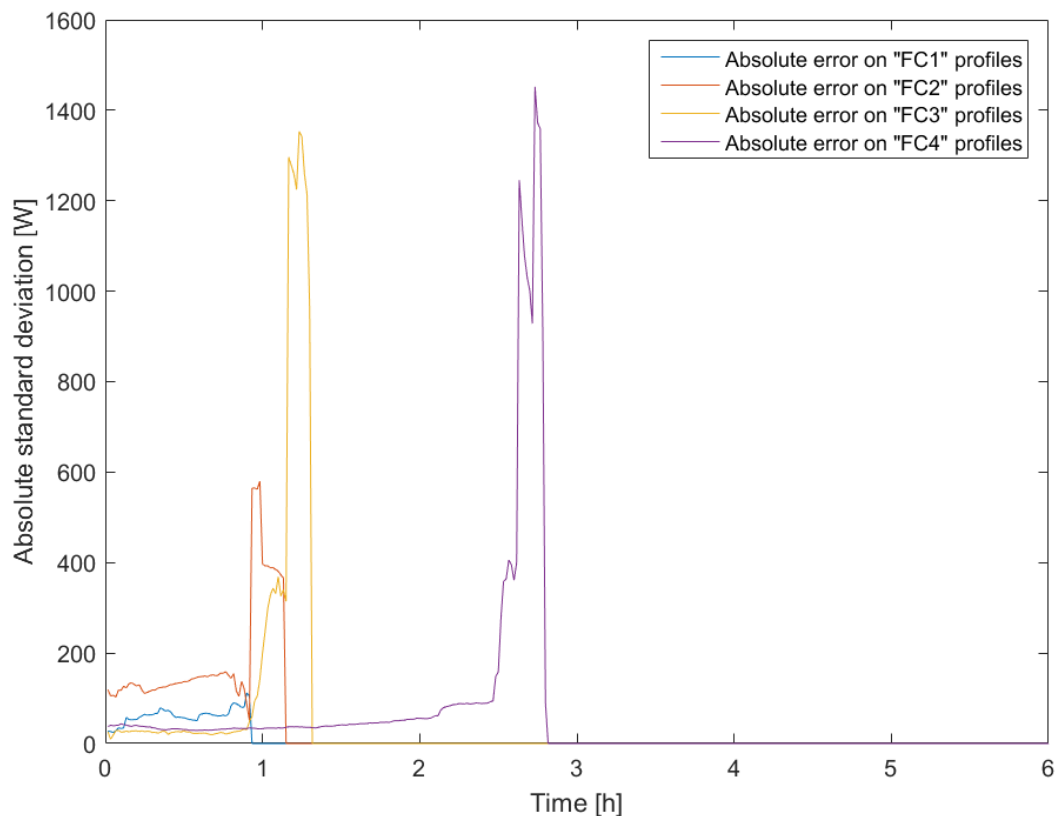


Figure 63 - Absolute error on fuel cell power profiles

Table 3: Difference of energy for fuel cell profiles

Class	Difference of Energy [%]
FC1	11.8 %
FC2	20.4 %
FC3	8.9 %
FC4	5.2 %

4.4 Electrolyser power profiles

In this Section, the data about the power consumed by the electrolysers were analysed. As it was done for the power produced by the fuel cell, the daily power data were profiled and averaged.

During the nine months observed, the electrolysers had a total running time of around 90 hours (see Figure 53), corresponding to 27 daily profiles. The behaviour of the two electrolysers was almost identical, therefore in this Section only the results obtained on the first one are presented. According to the daily consumed energy, the experimental profiles were divided in four classes, whose features are shown in Table 4, together with the percentage of occurrence of each class over the whole period. The low values indicate, again, the short running time over the nine months analysed.

Table 4: Electrolysers power profiles classes

Class	Daily Energy (DE) [kWh]	Percentage on total days [%]
EL1	DE < 1	2.1 %
EL2	1 < DE < 2	1.7 %
EL3	2 < DE < 5	3.4 %
EL4	DE > 5	4.2 %

An average profile was built to represent the experimental profiles of each category, with the same averaging process used for the fuel cell power profiles and described in Section 3.2.

Figure 64 to Figure 67 show the average profile obtained for each class, compared with all the corresponding experimental profiles.

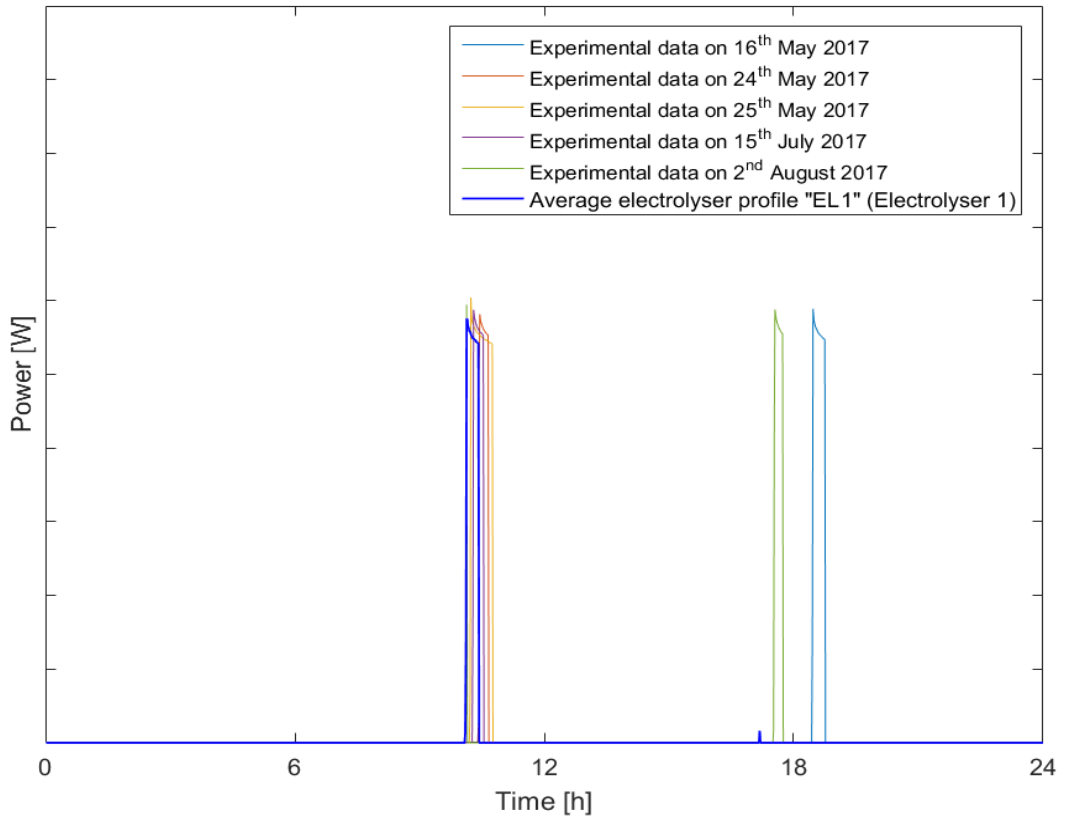


Figure 64 - Average electrolyser power profile "EL1"

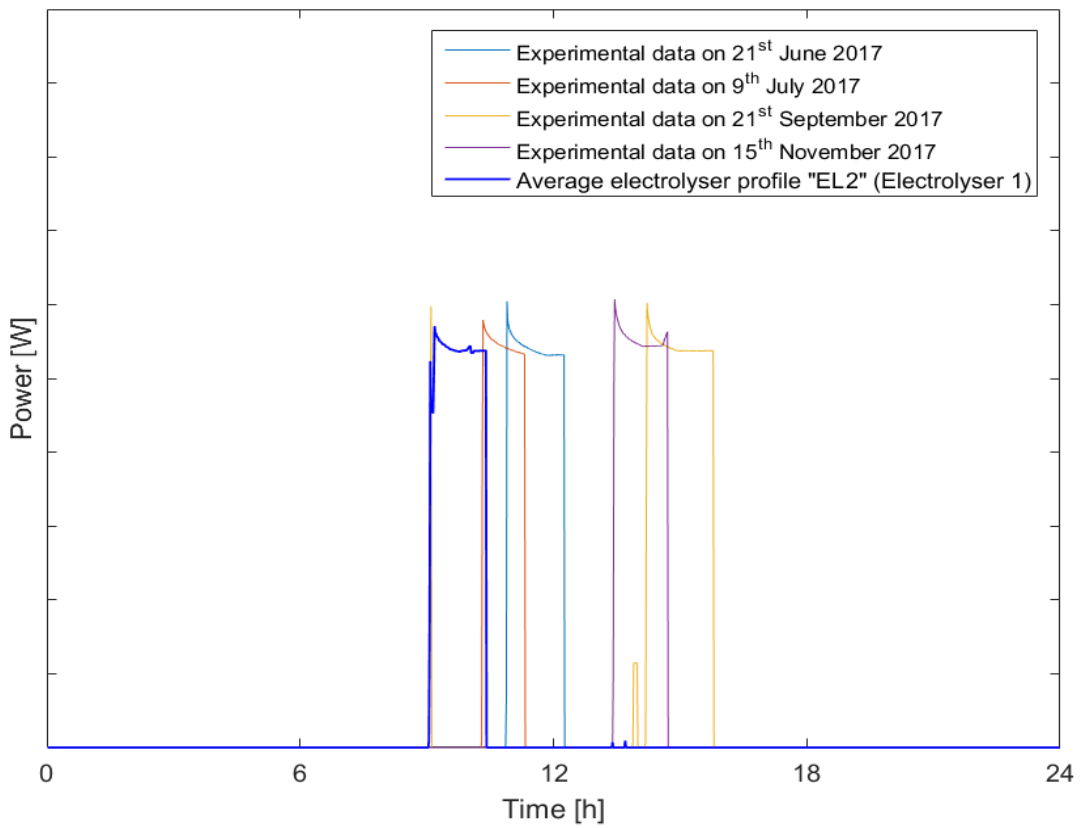


Figure 65 - Average electrolyser power profile "EL2"

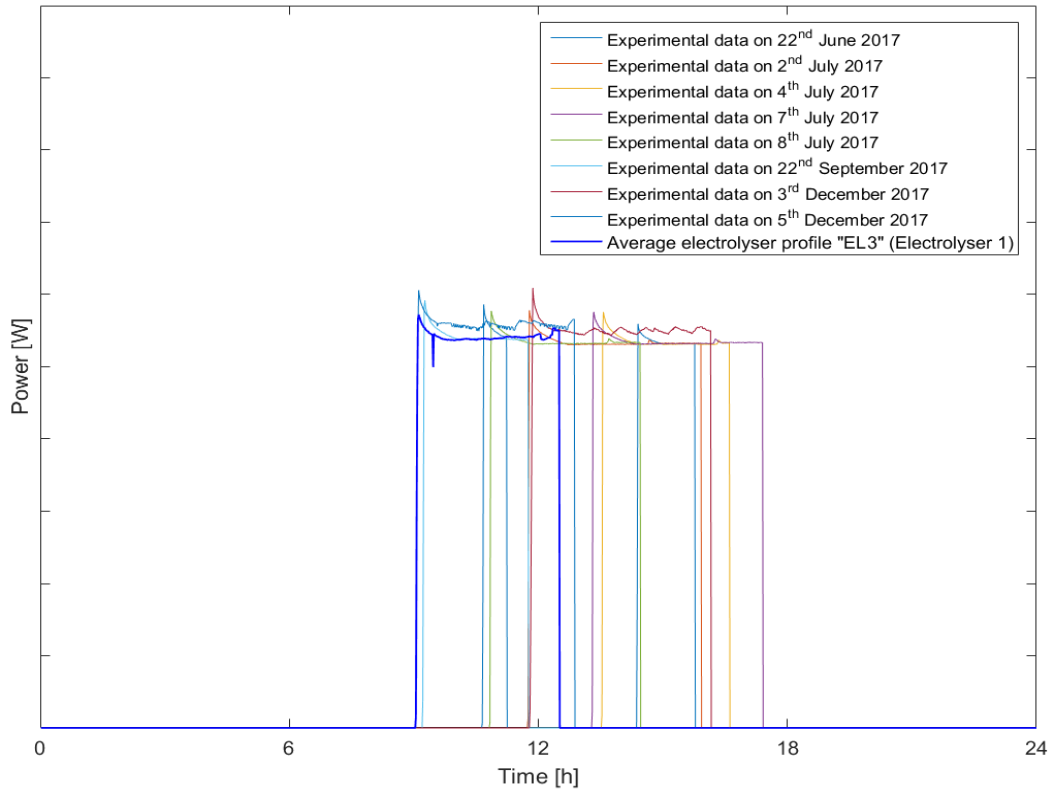


Figure 66 - Average electrolyser power profile "EL3"

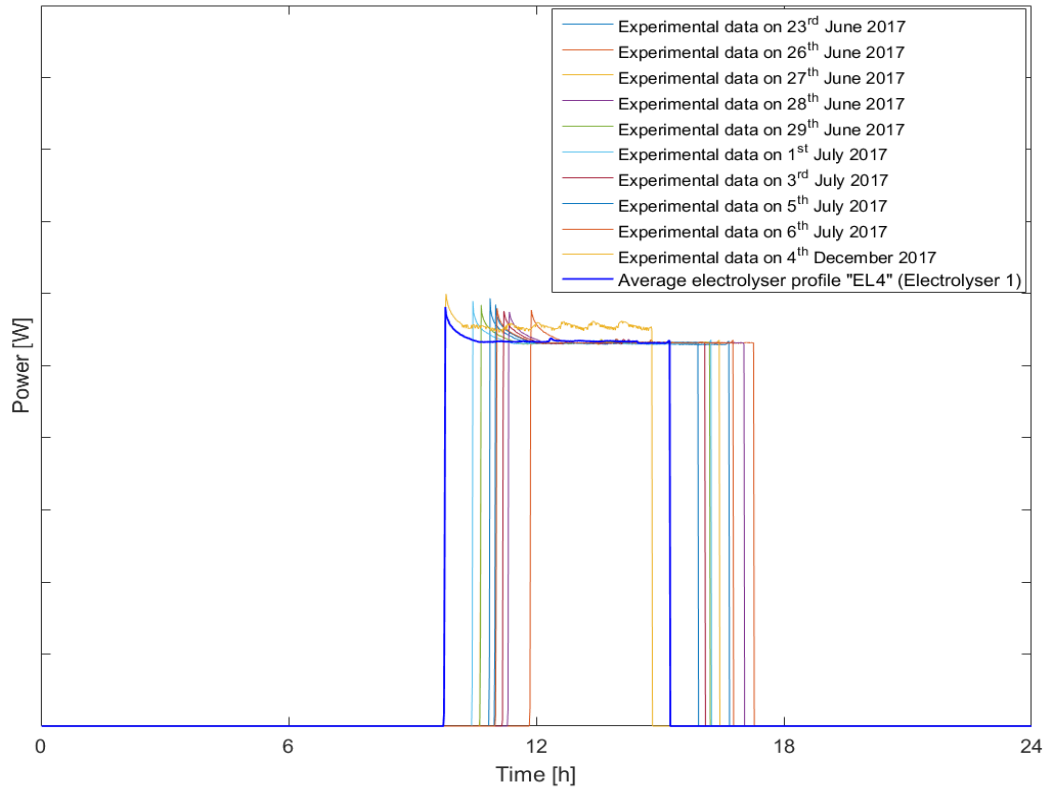


Figure 67 - Average electrolyser power profile "EL4"

4.4.1 Quality evaluation

For the quality evaluation of the average profiles of each class, the profiles were sorted, representing the power from the highest to the lowest value, as shown for instance in Figure 68 for the power profiles of the class “EL3”. The time scale is cut, because the durations of the profiles are not covering the whole day. The PRSD profiles for all the categories are shown in Figure 69.

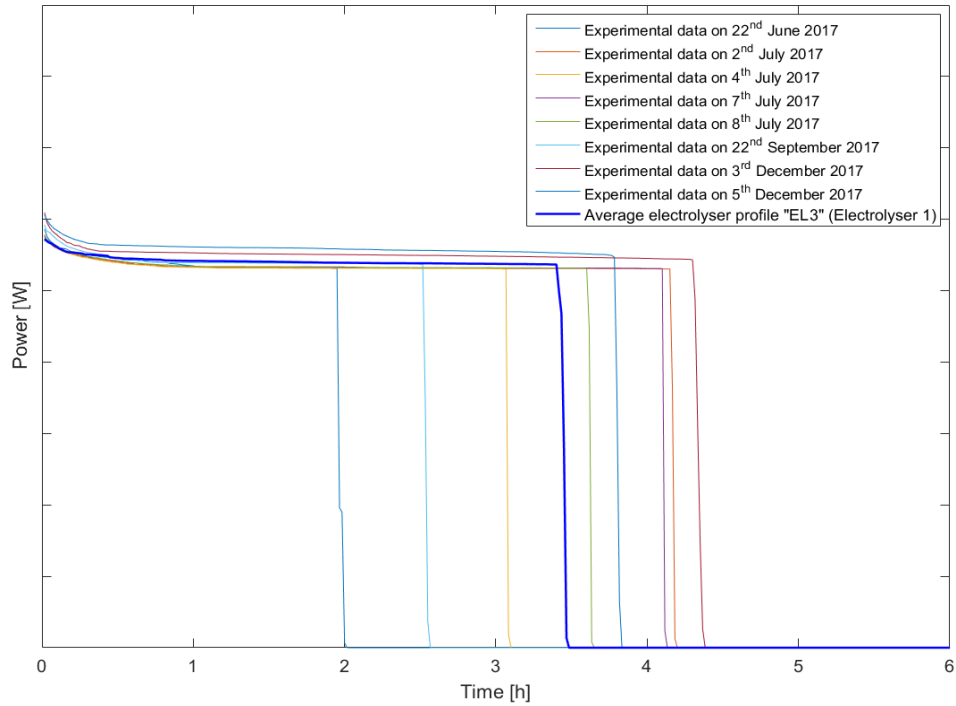


Figure 68 - Sorted profiles of the class "EL3"

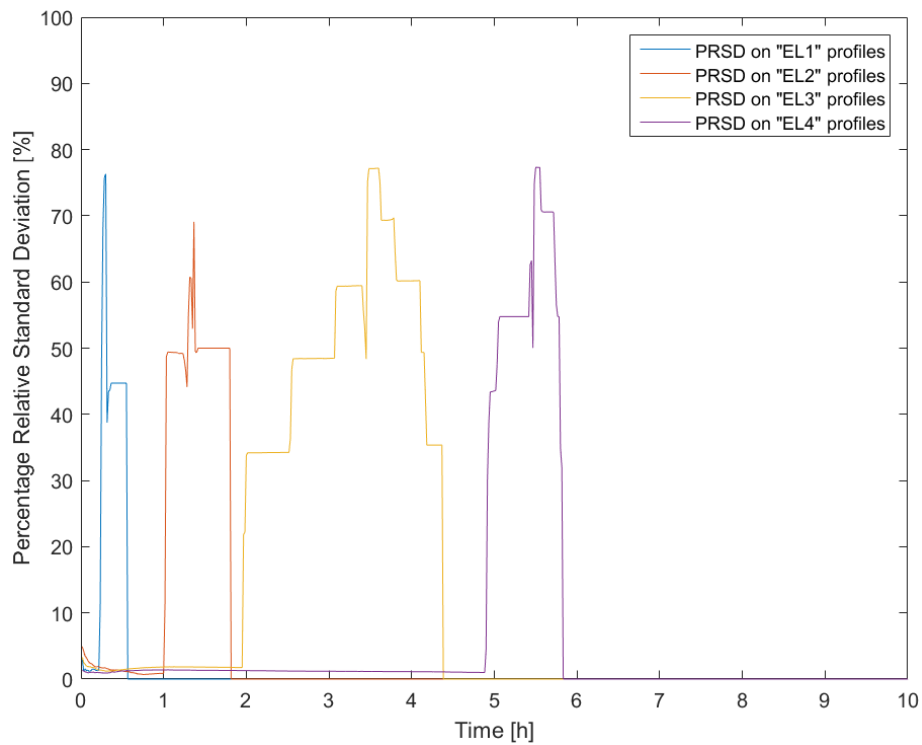


Figure 69 - PRSD of the electrolyser power profiles

Table 5: PSRD and MAPE on average electrolyser power profiles

Class	MAPE [%]	PRSD [%]	PRSD on running time [%]
EL1	0.3 %	0.7 %	29.1 %
EL2	0.3 %	1.7 %	22.9 %
EL3	2.0 %	5.2 %	28.6 %
EL4	2.6 %	2.4 %	10.1 %

The absolute standard deviation is shown in Figure 70.

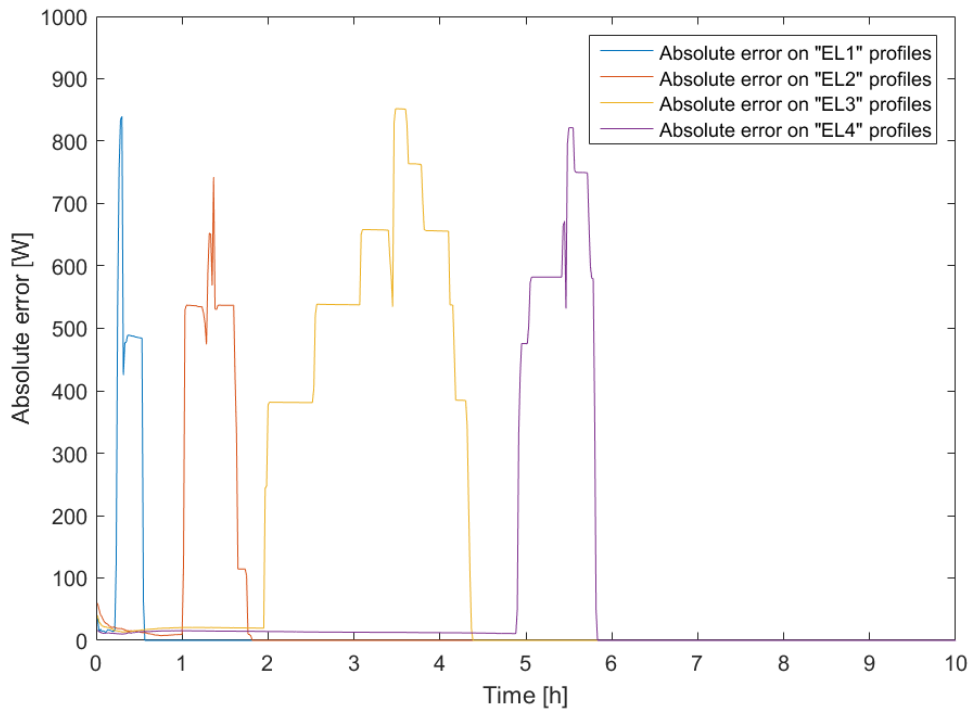


Figure 70 - Absolute standard deviation on the electrolyser power profiles

Also in this case, some points reach very high values because of the different power durations of the profiles. This differences are significant for the profiles of the class “EL1” and “EL3”, as shown in Figure 68; for this reason, the averaging algorithm is not able to approximate properly all the profiles of this classes and the corresponding absolute error is high, as shown in Table 6.

Table 6: Difference of energy on the electrolyser power profiles

Class	Difference of Energy [%]
EL1	48.1 %
EL2	25.1 %
EL3	36.5 %
EL4	10.6 %

4.5 Battery power profiles

Differently from the behaviour of the fuel cell and the electrolysers, the batteries are used every day to supply power to the end user when the PV power is not available and receive power to recharge when the power produced by the PV is in excess. In this Section, the 238 daily experimental power profiles were analysed and classified in some categories, in order to build the representative average profiles. The criteria used for the classification was, also in this case, the daily amount of energy charged or discharged by the batteries (calculated in absolute value). The experimental profiles were divided in 8 classes. The number of classes and the energy thresholds were chosen after a preliminary analysis of the data, in order to group in the same class profiles with similar features. The classes are shown in Table 7, together with the percentage of occurrence of each class over the nine months analysed.

Table 7: Batteries power profiles classes

Class	Daily Energy (DE) [kWh]	Percentage on total days [%]
P1	DE < 1.6	8.0 %
P2	1.6 < DE < 2.0	19.7 %
P3	2.0 < DE < 2.2	21.0%
P4	2.2 < DE < 2.4	18.1 %
P5	2.4 < DE < 2.7	13.9 %
P6	2.7 < DE < 3.0	5.9 %
P7	3.0 < DE < 4.0	9.7 %
P8	DE > 4.0	3.8 %

Figure 71 to Figure 78 show the generated average profiles, compared with two experimental profiles, one representing the best approximation case, one the worst.

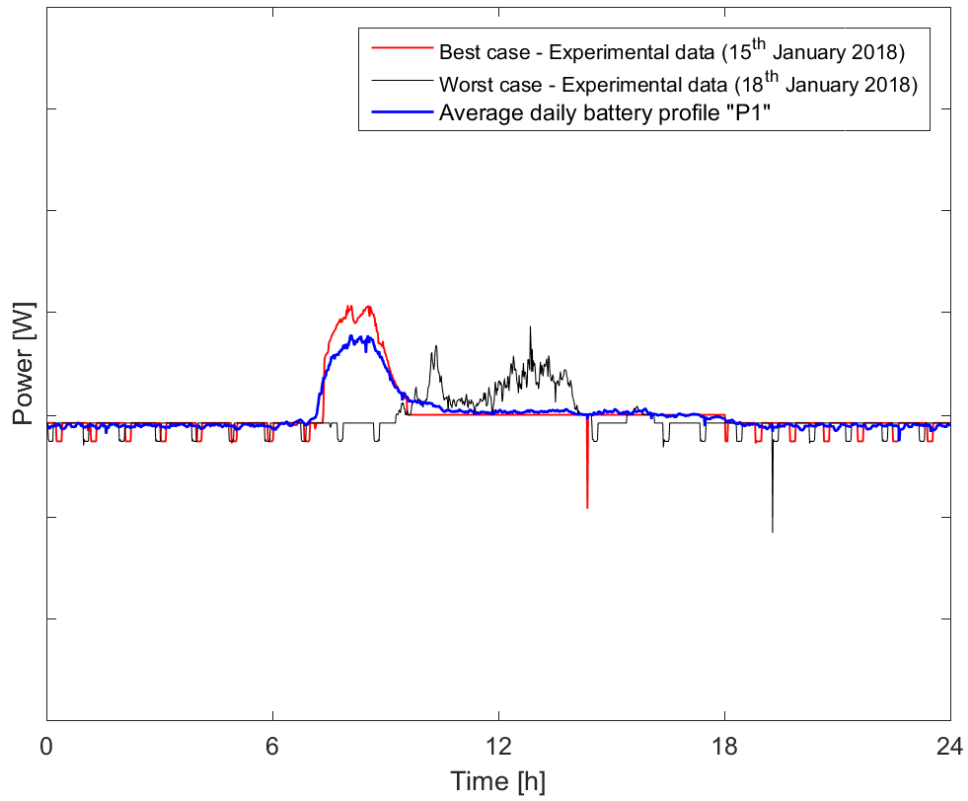


Figure 71 - Average battery power profile "P1"

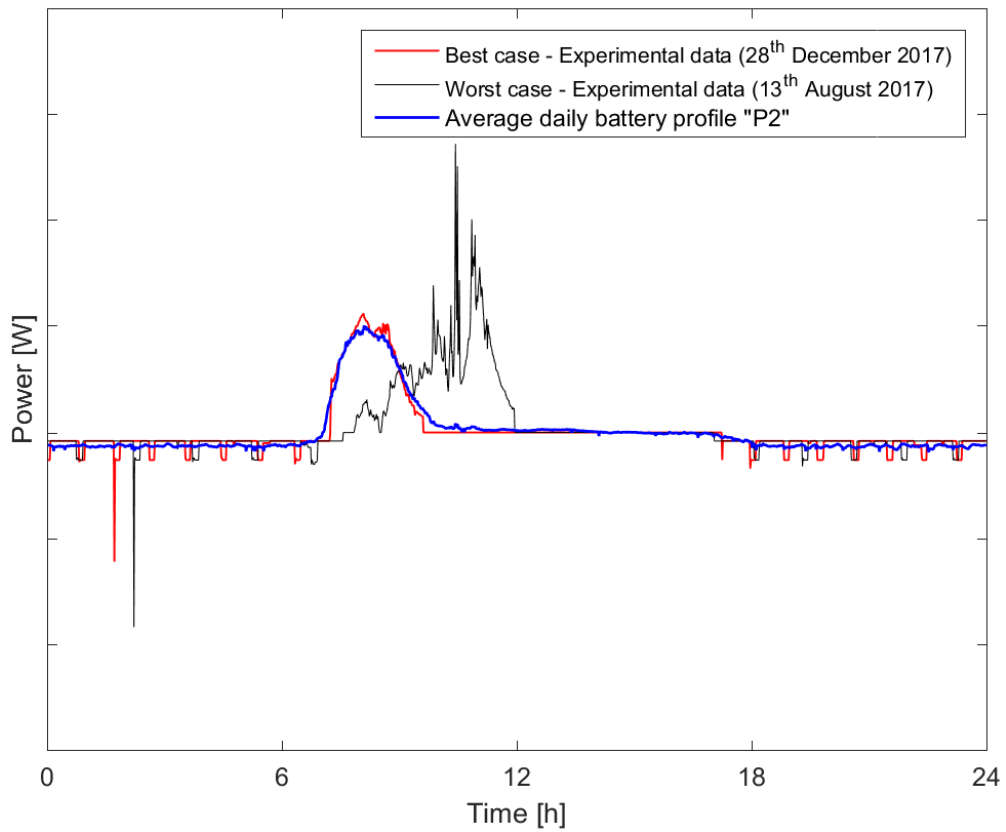


Figure 72 - Average battery power profile "P2"

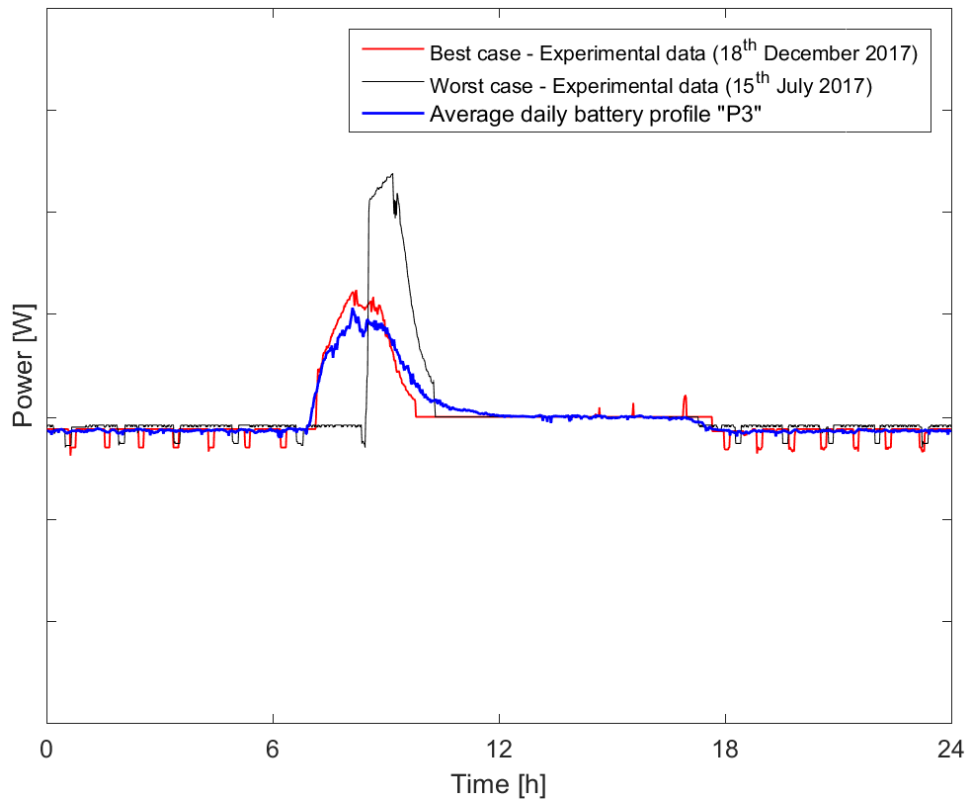


Figure 73 - Average battery power profile "P3"

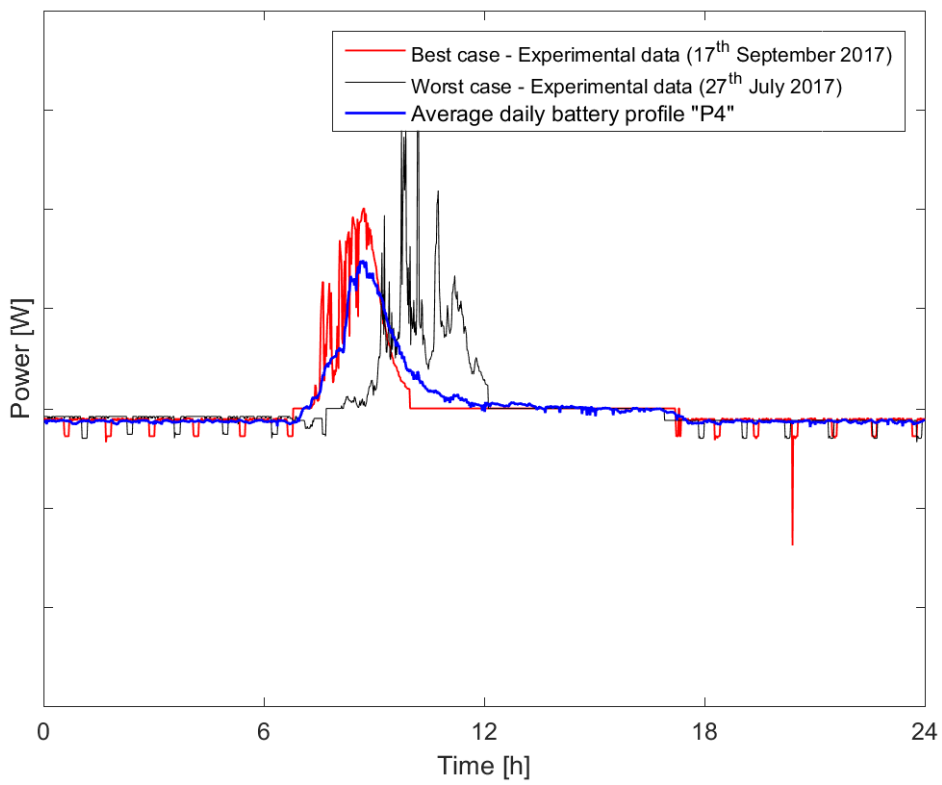


Figure 74 - Average battery power profile "P4"

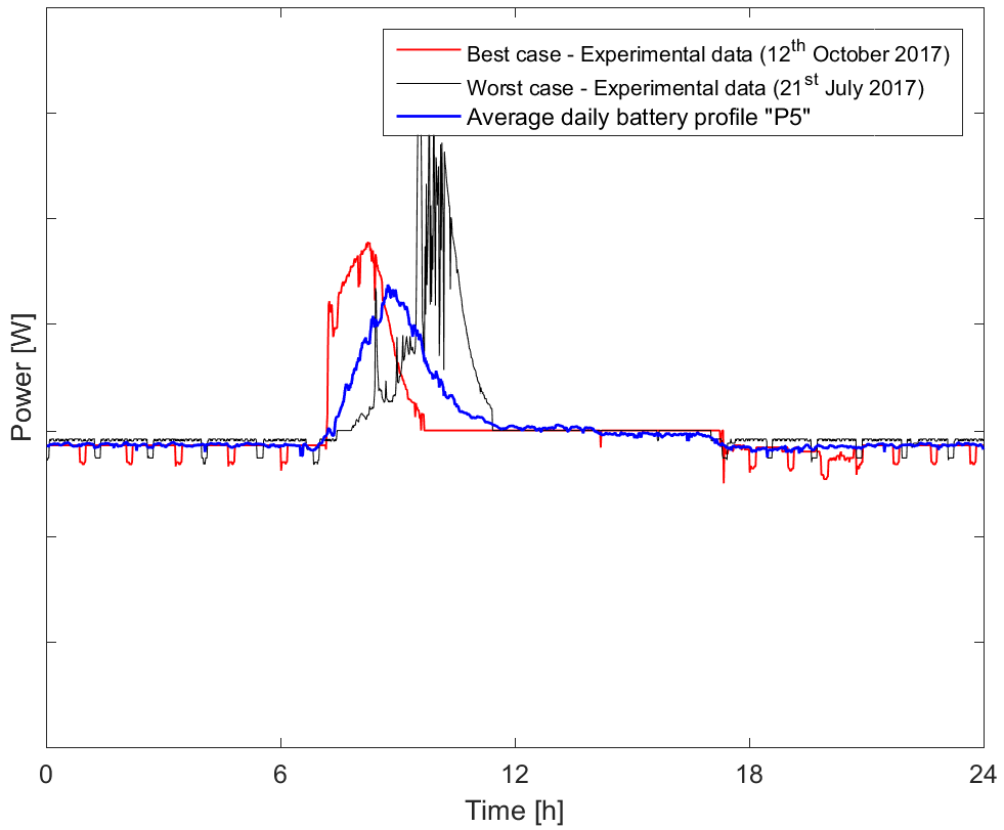


Figure 75 - Average battery power profile "P5"

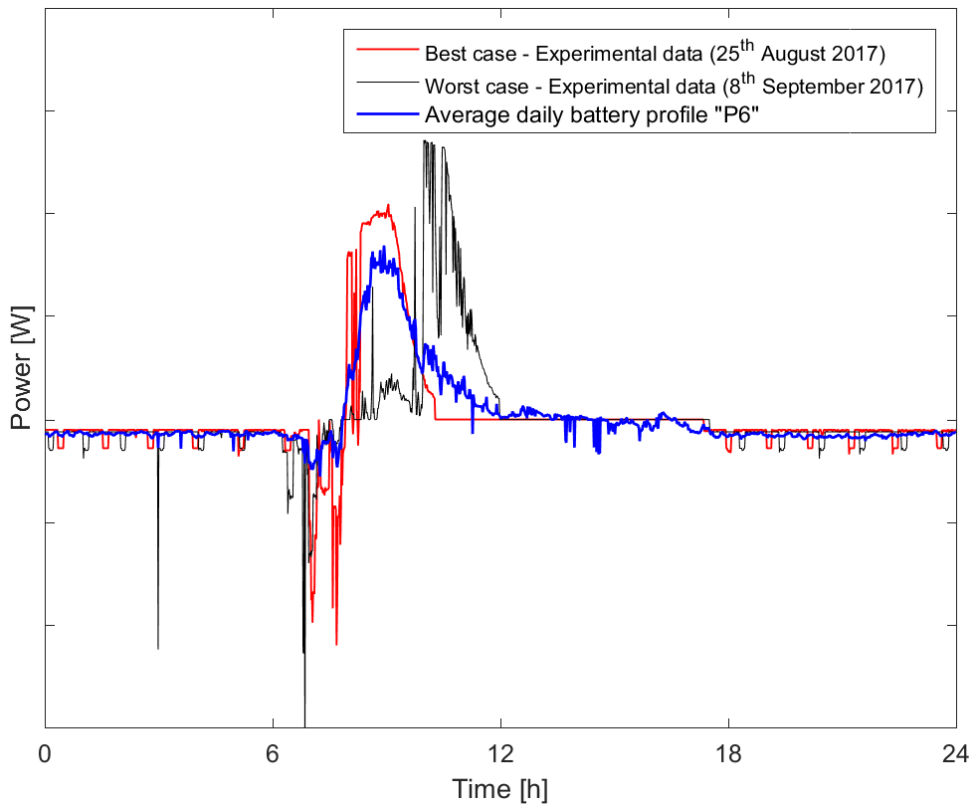


Figure 76 - Average battery power profile "P6"

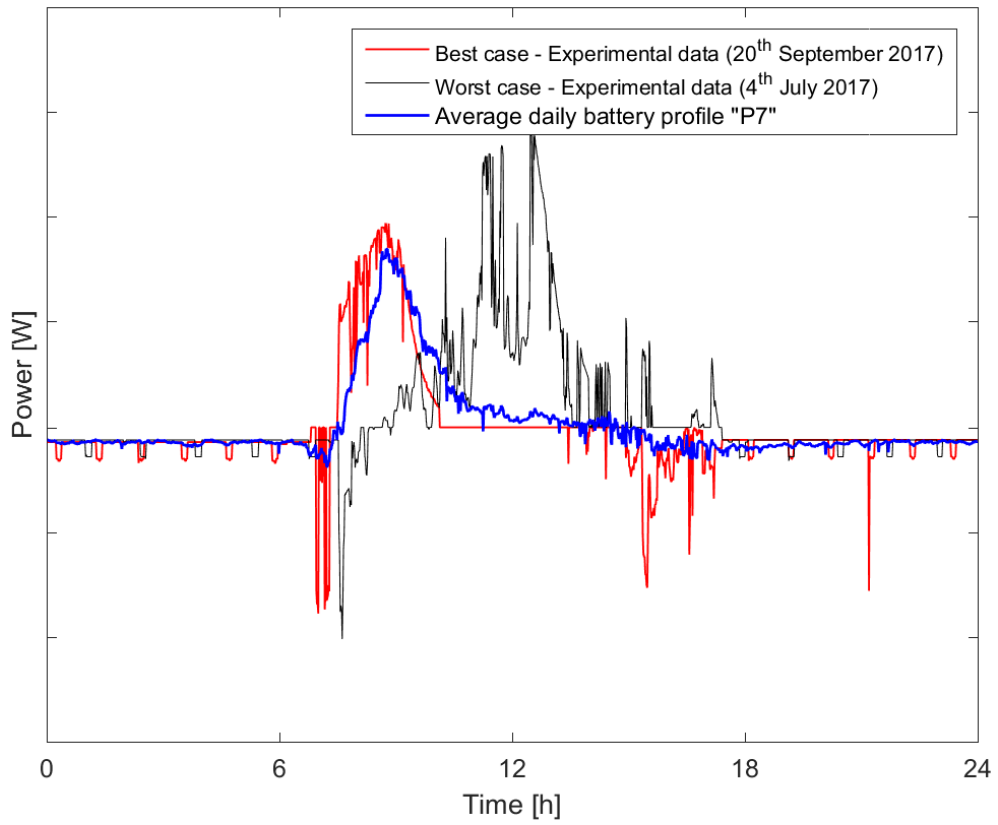


Figure 77 - Average battery power profile "P7"

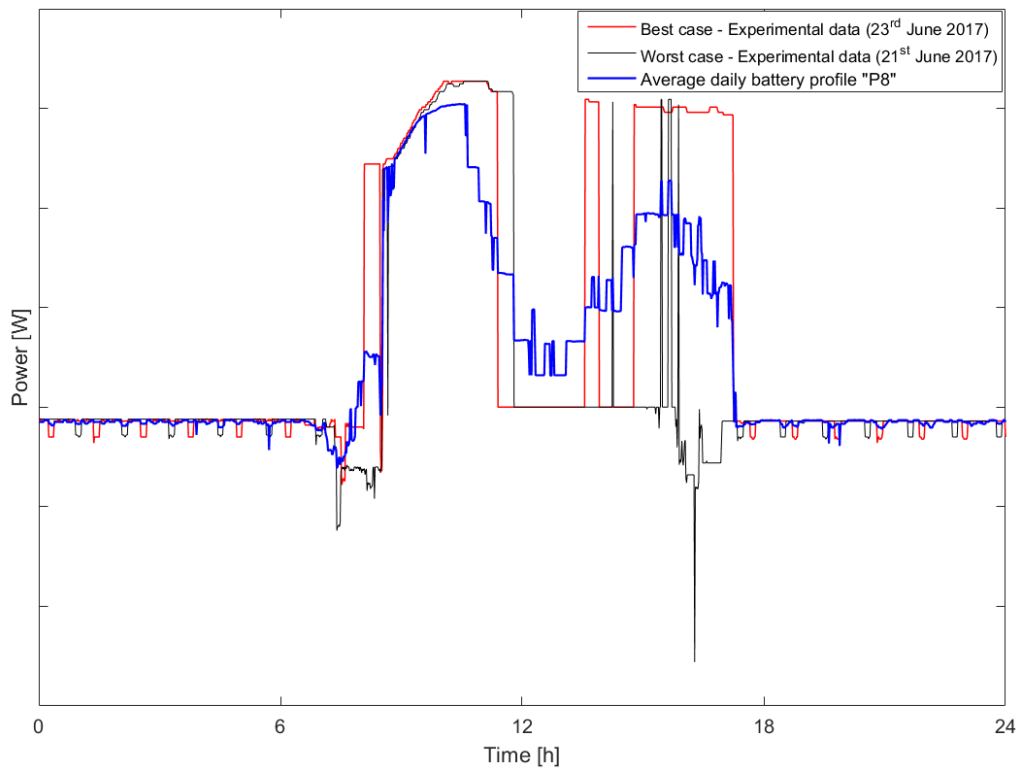


Figure 78 - Average battery power profile "P8"

4.5.1 Quality evaluation

In order to evaluate the error between the average and the real profiles, the percentage relative standard deviation (PRSD) and the absolute standard deviation were calculated. They are respectively shown in Figure 79 and Figure 80.

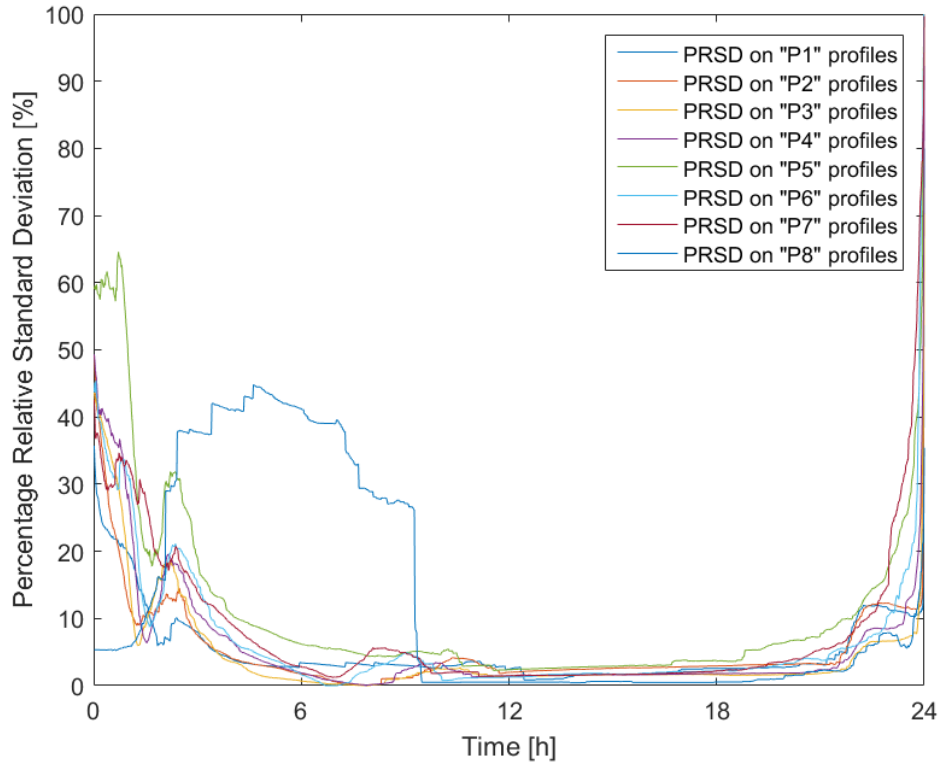


Figure 79 - PRSD on battery power profiles

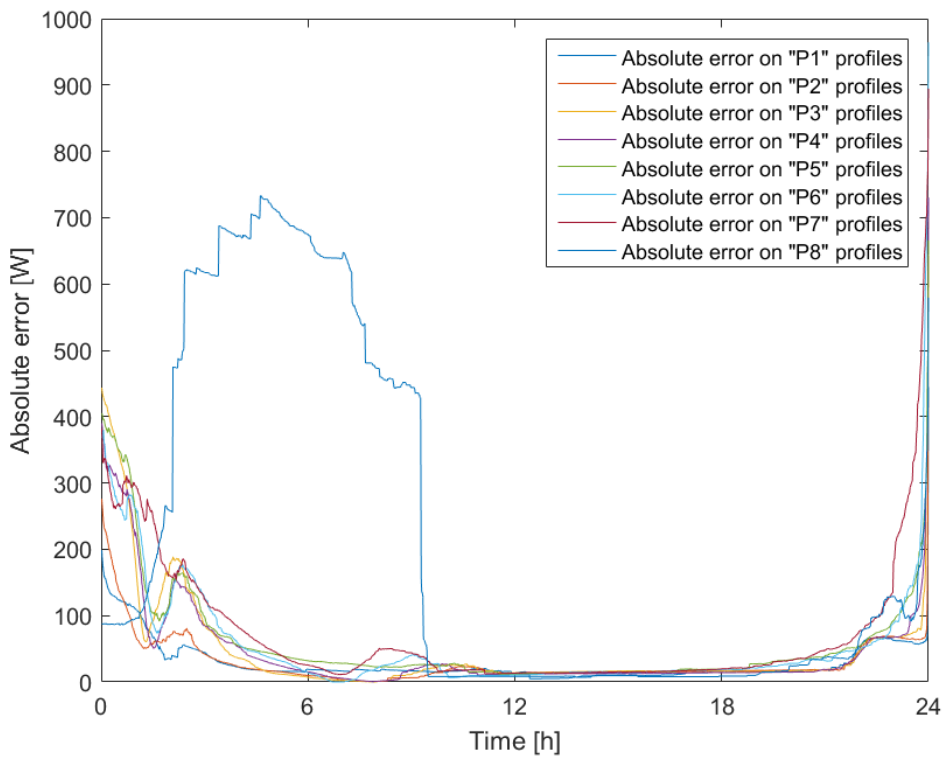


Figure 80 - Absolute standard deviation on battery power profiles

The increase of the error in the last part of the plots is due to the fact that the average profile is not always able to properly represent the negative peaks that, in the sorted vectors, are located in the final part of the profile. Moreover, both the error estimations reach high values for the classes of profiles “P8” because, even if their daily energy is similar, their shapes are strongly different. This can be clearly seen in Figure 81 and Figure 82, which show respectively the sorted profiles of the class “P8” and “P4”, highlighting that the profiles of the class “P8” are more irregular than those of the class “P4”.

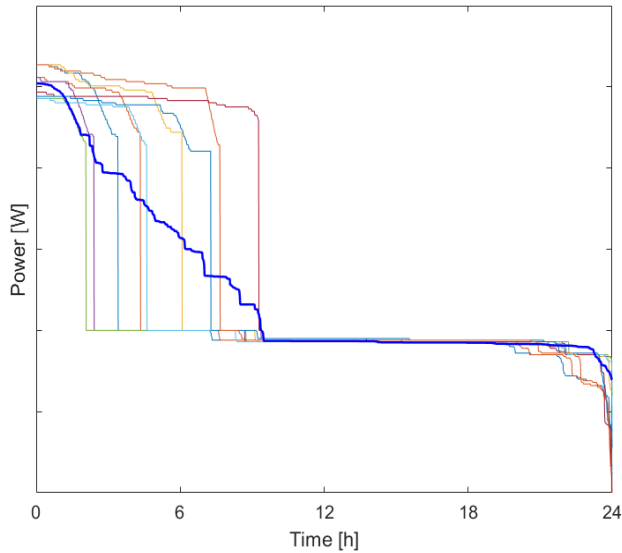


Figure 81 - Sorted profiles of the class "P8"

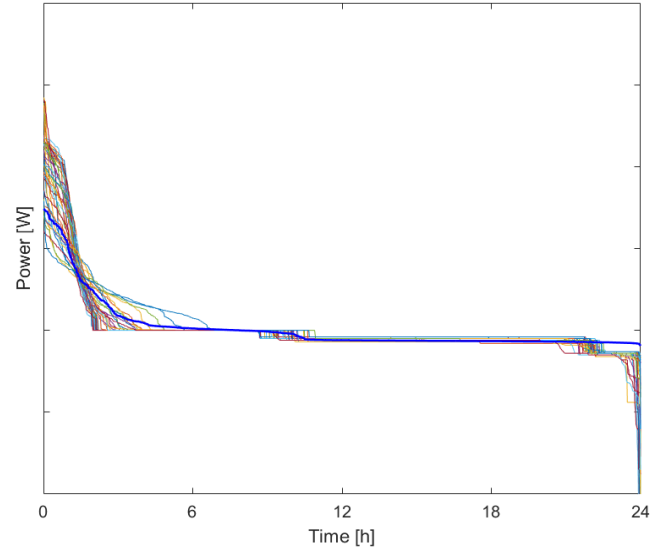


Figure 82 - Sorted profiles of the class "P4"

The values of the error estimations for each category are shown in Table 8.

Table 8: PSRD and energy error on average battery power profiles

Class	PSRD [%]	Difference of Energy [%]
P1	5.1 %	44.5 %
P2	5.3 %	39.1 %
P3	4.5 %	52.5 %
P4	5.6 %	46.1 %
P5	10.9 %	54.9 %
P6	6.6 %	47.0 %
P7	8.1 %	53.2 %
P8	12.9 %	52.2 %

The values of the energy-based quality indicator are high for all the classes. This indicates that the classification of the profiles should be improved, as the daily energy only is not a sufficient criterion to group the profiles according to their features. Indeed, the battery power profiles can have very different features, resulting in various and irregular shapes, as they are the first to be influenced by random factors like the variation of the user load or of the solar irradiance. Therefore, some additional criteria should be taken into account in the classification, in order to better categorize the profiles according to their specific features.

4.6 Solar irradiance profiles

A relevant indicator that could be helpful to predict the behaviour of the different components of the energy system is the daily solar irradiance. Indeed, the knowledge of the weather conditions could allow to predict the PV power production and, consequently, the behaviour of the electrochemical devices of the system. As it is difficult to have an accurate long term weather forecasting, it is possible to assume that the weather conditions observed through the available measured data will be repeated in a similar way in the future. For this reason, the solar irradiance data of the observed 238 days were classified in 10 classes according to their daily energy and, then, for each class an average representative profile was built. The number of classes and the energy thresholds of each class were chosen after a preliminary analysis of the data, in order to group in the same class profiles with similar features and to have approximately the same number of profiles in each class. The features of each category are shown in Table 9, together with the corresponding percentage of occurrence over the whole nine-months-period.

Table 9: Solar irradiance profiles classes

Class	Daily Energy (DE) [Wh / m ²]	Percentage on total days [%]
S1	1000 < DE < 1700	2.5 %
S2	1700 < DE < 2400	2.9 %
S3	2400 < DE < 3100	5.9 %
S4	3100 < DE < 3800	10.9 %
S5	3800 < DE < 4500	15.1 %
S6	4500 < DE < 5200	12.2 %
S7	5200 < DE < 5900	14.3 %
S8	5900 < DE < 6600	18.9 %
S9	6600 < DE < 7300	14.7 %
S10	7300 < DE < 8000	2.5 %

The plots from Figure 83 to Figure 92 show the average profiles obtained for each class, compared with the best and the worst case of the experimental data.

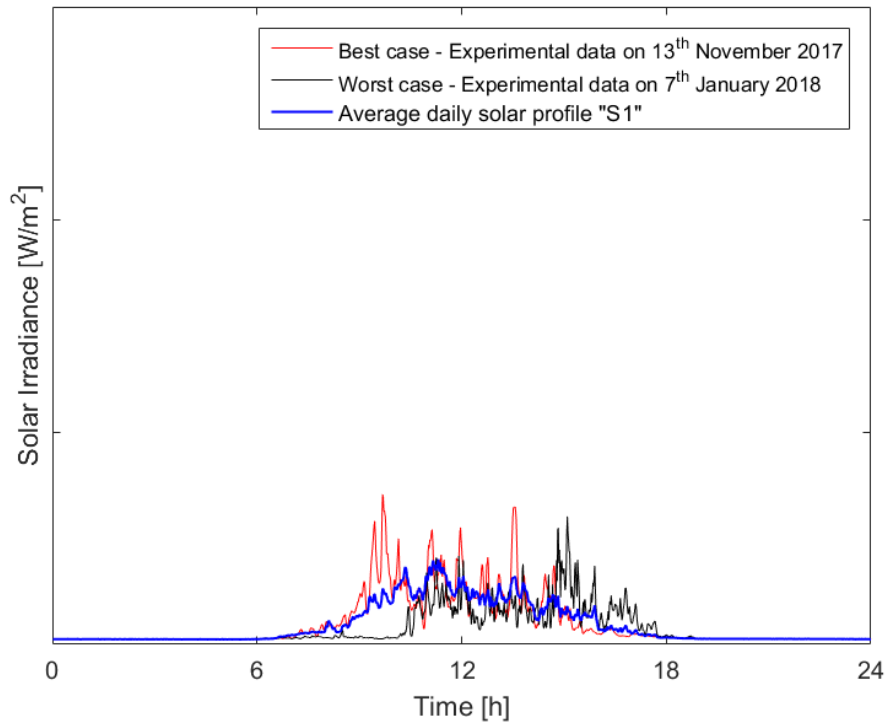


Figure 83 - Average solar irradiance profile "S1"

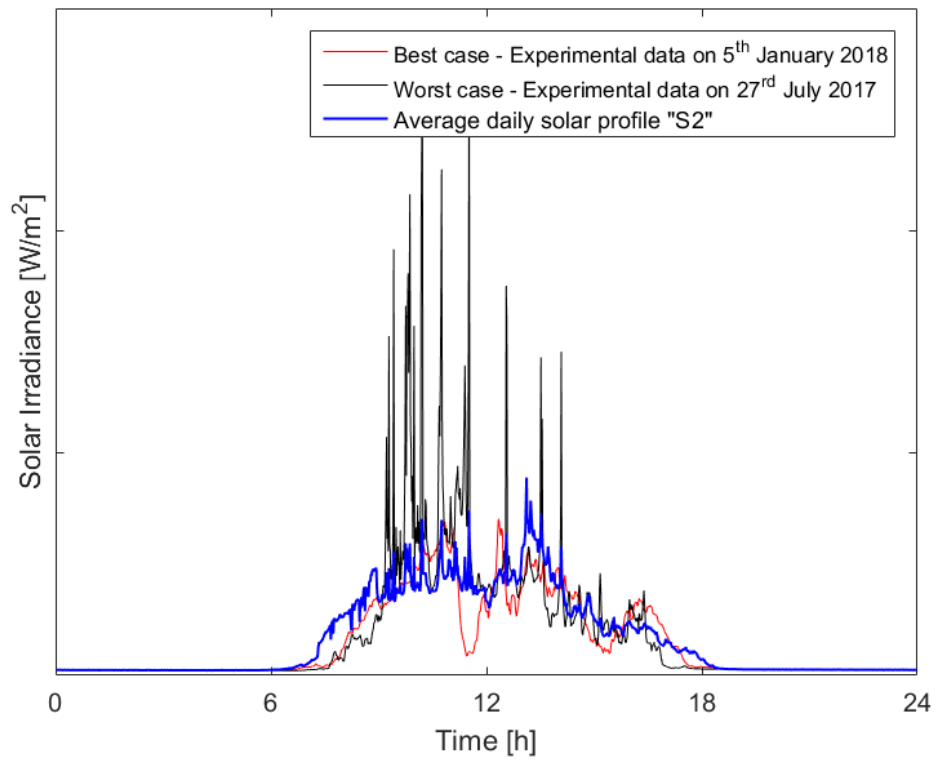


Figure 84 - Average solar irradiance profile "S2"

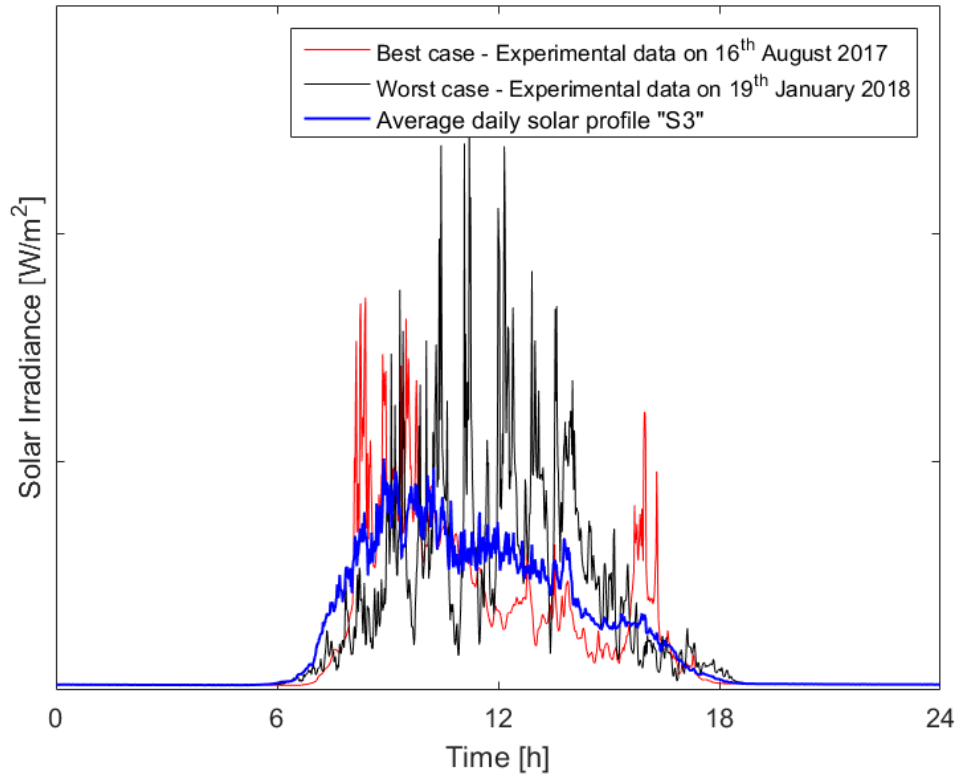


Figure 85 - Average solar irradiance profile "S3"

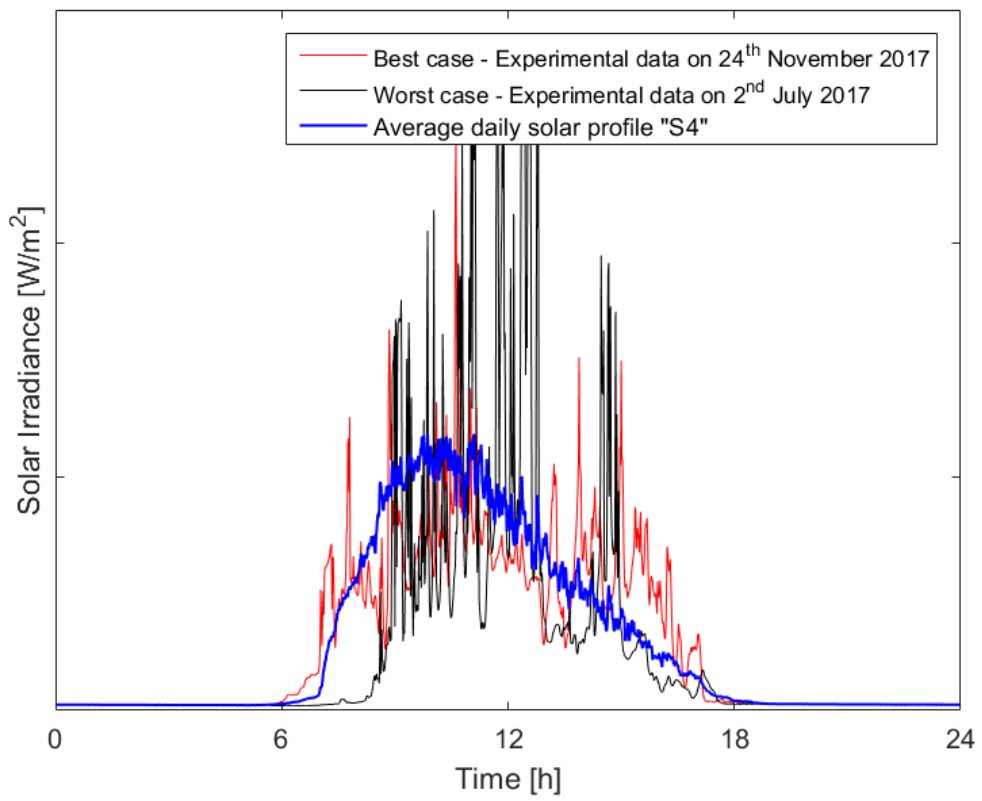


Figure 86 - Average solar irradiance profile "S4"

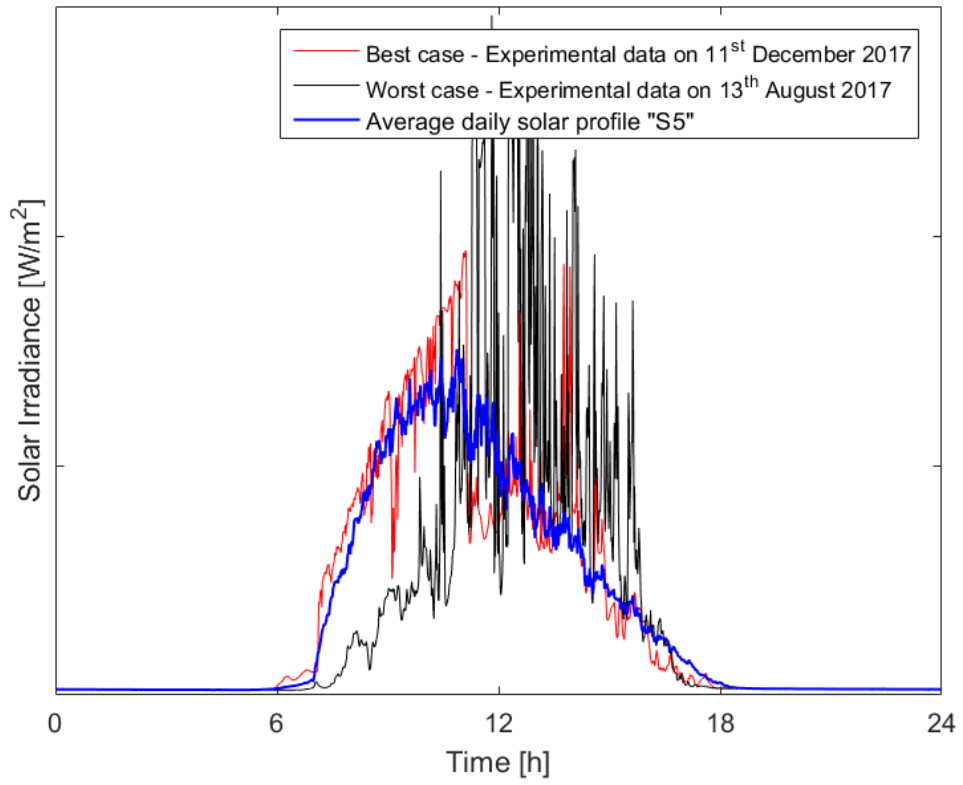


Figure 87 - Average solar irradiance profile "S5"

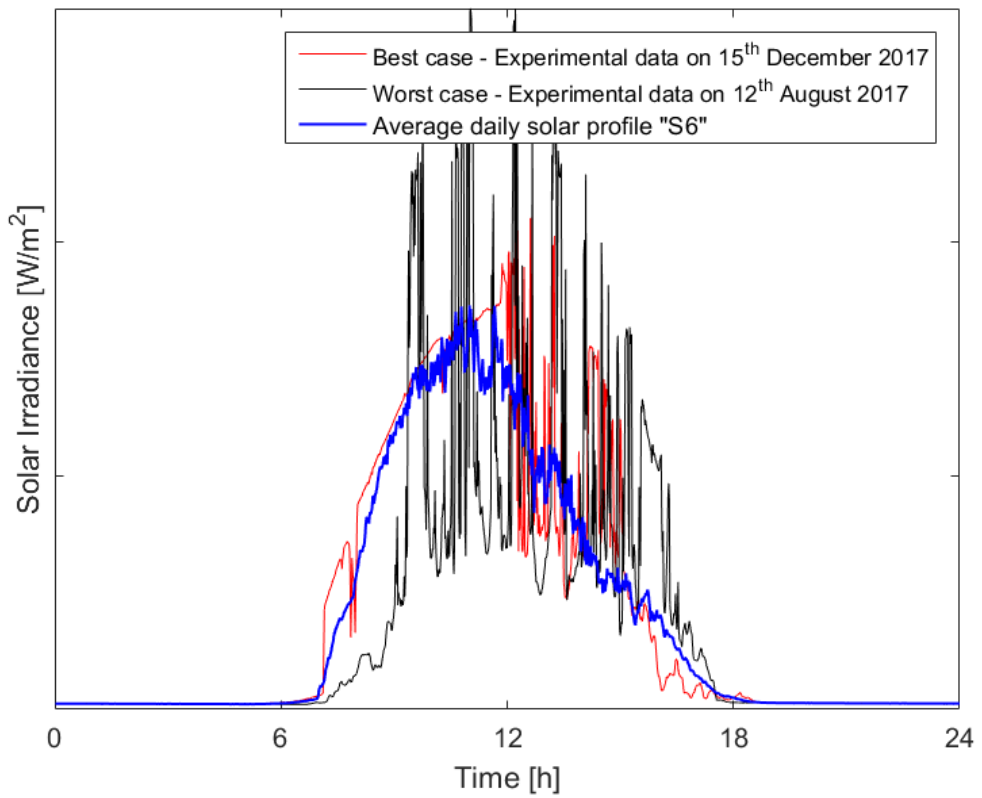


Figure 88 - Average solar irradiance profile "S6"

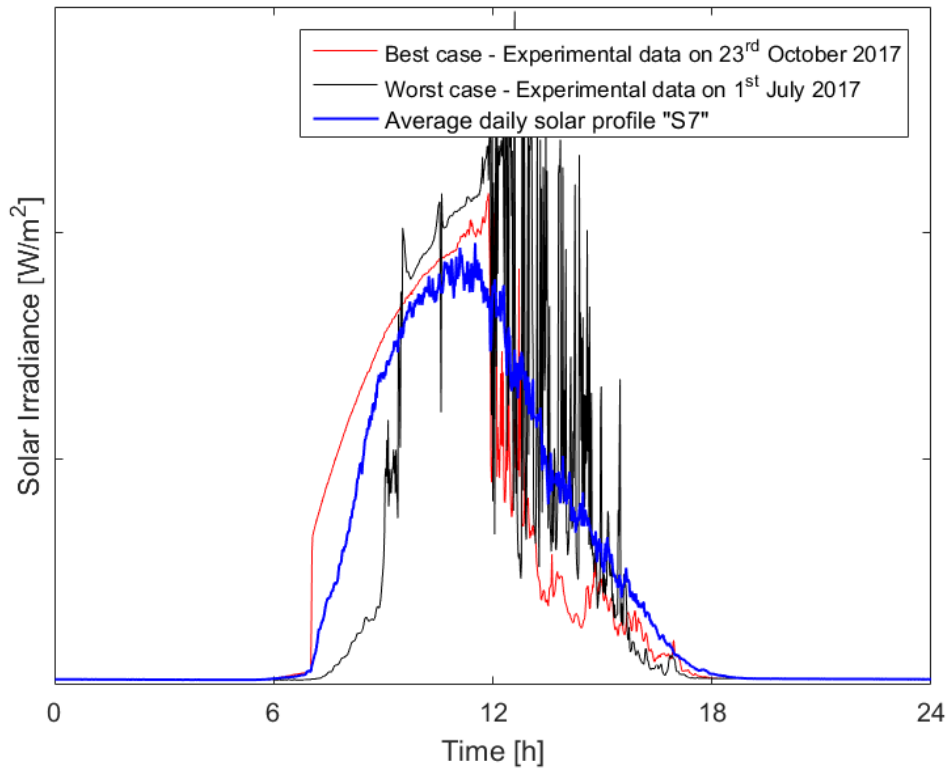


Figure 89 - Average solar irradiance profile "S7"

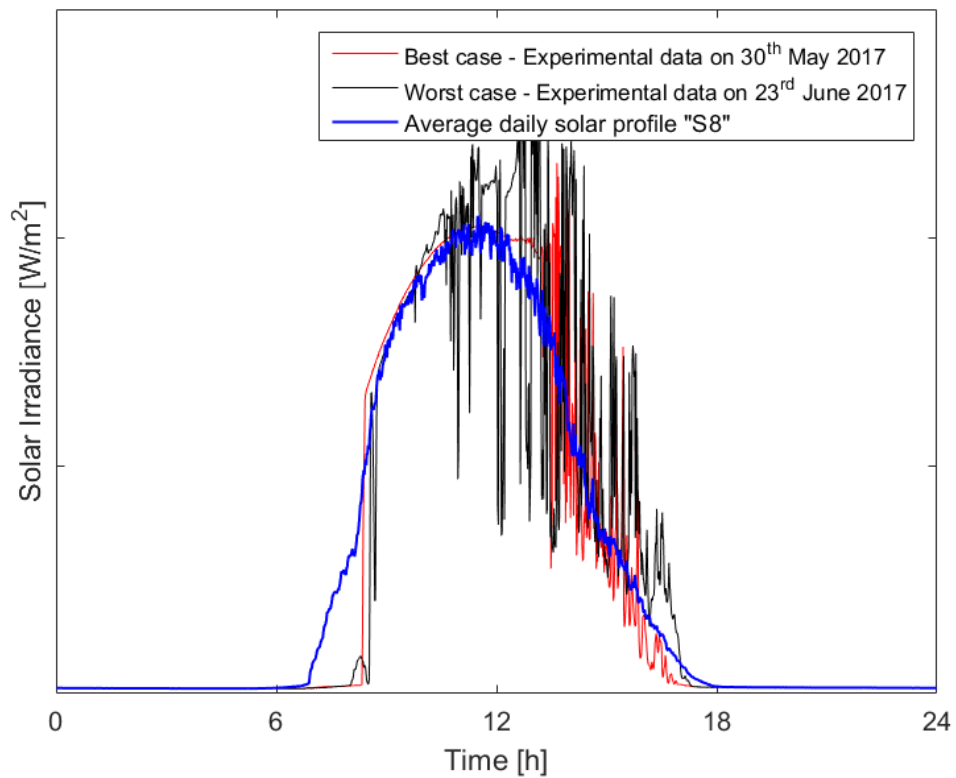


Figure 90 - Average solar irradiance profile "S8"

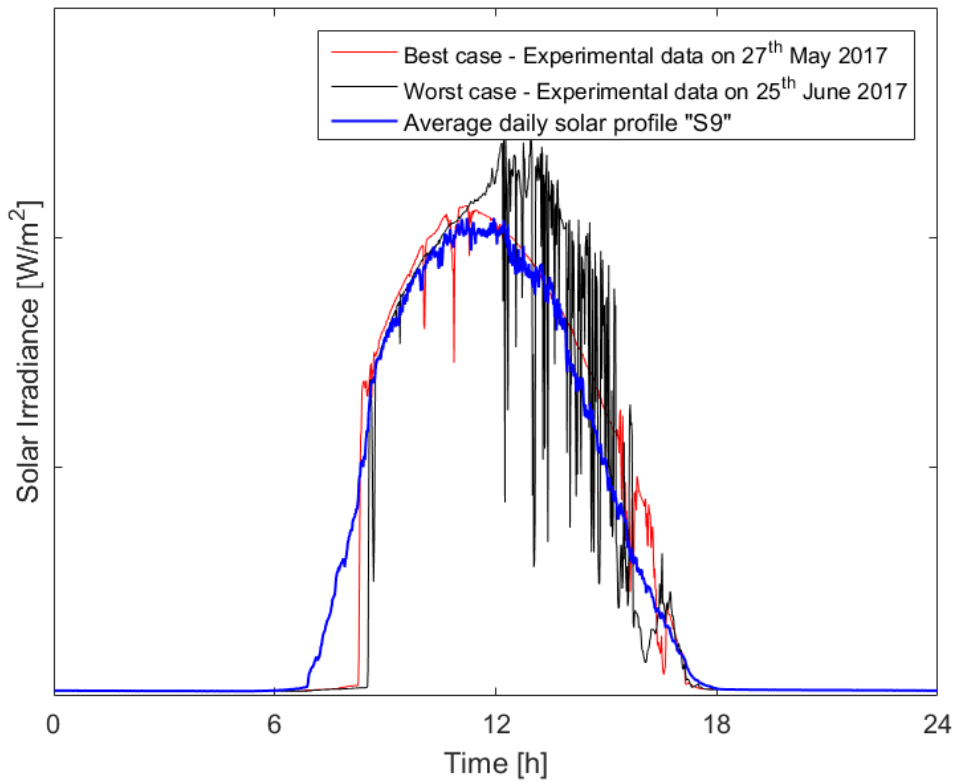


Figure 91 - Average solar irradiance profile "S9"

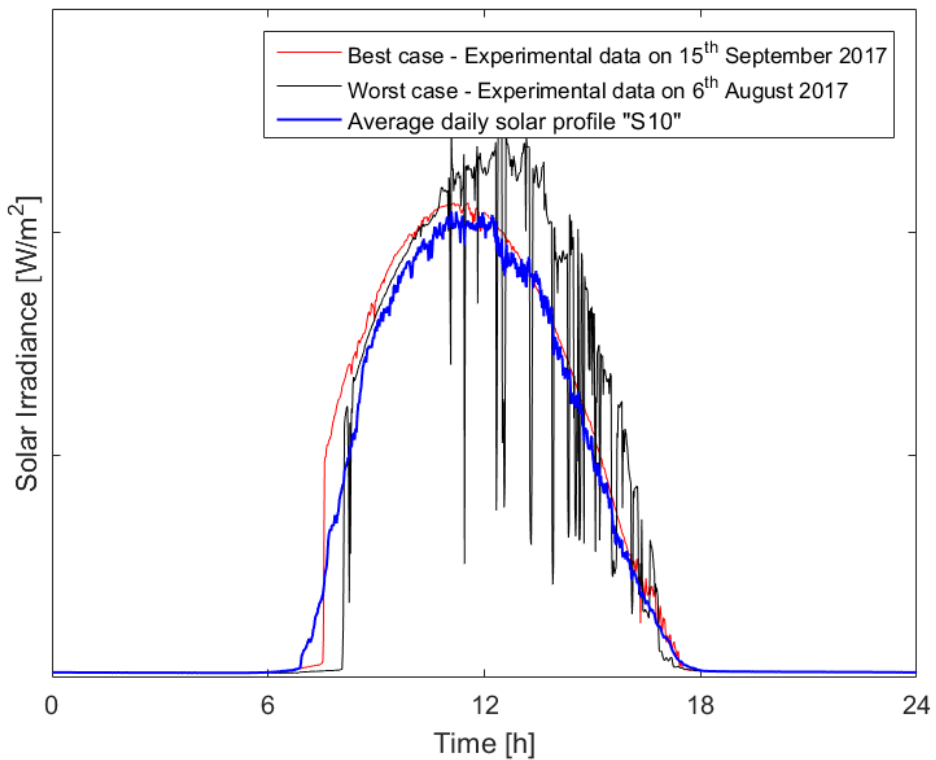


Figure 92 - Average solar irradiance profile "S10"

The errors between the profiles were evaluated with the PRSD, shown in Figure 93, the relative error and the absolute standard deviation, in Figure 94. The percentage values of the PRSD, the MAPE and the Difference of Energy, for each class, are shown in Table 10.

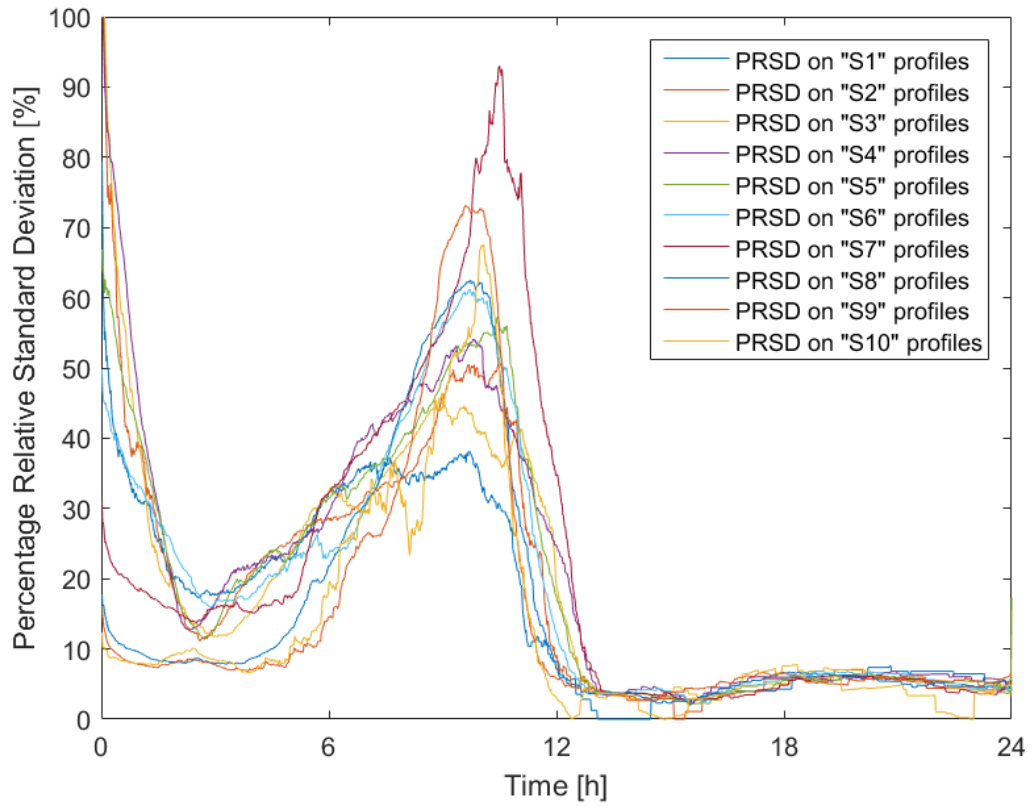


Figure 93 - PRSD on solar irradiance profiles

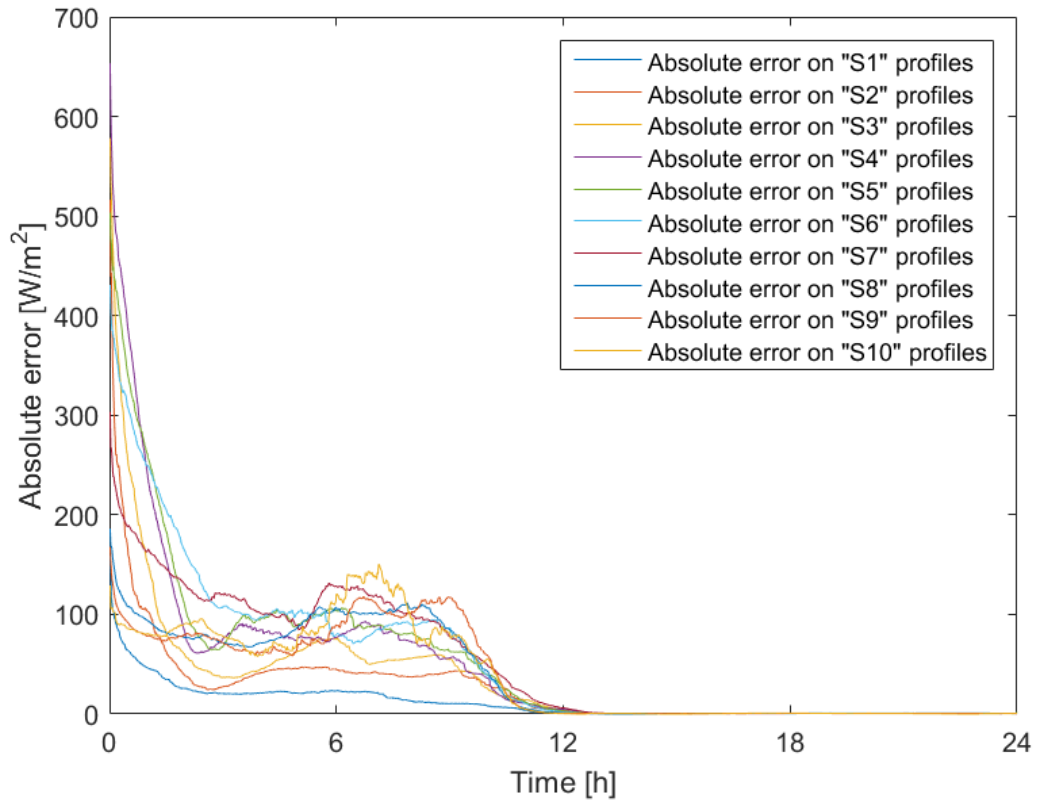


Figure 94 - Absolute error on solar irradiance profiles

Table 10: PSRD, MAPE and Difference of Energy on the average solar irradiance profiles

Class	MAPE [%]	PSRD [%]	Difference of Energy [%]
S1	14.1%	16.2%	24.8%
S2	15.6%	18.3%	30.2%
S3	15.9%	18.7%	30.1%
S4	18.6%	21.2%	33.4%
S5	16.7%	19.6%	29.8%
S6	15.5%	19.0%	27.3%
S7	16.5%	21.1%	22.5%
S8	12.8%	15.2%	14.7%
S9	12.0%	14.4%	13.2%
S10	11.6%	12.6%	13.3%

The PSRD profiles, shown in Figure 93, are characterized by high values in the middle part and even the percentage values, shown in Table 10, are higher than 10%, differently from the results obtained on the other variables analysed so far. This happens because often, as seen from Figure 83 to Figure 92, the average profile is not able to properly approximate the dynamic behaviour of the irradiance. Indeed, in most cases, the fast alternation of high and low values, occurring because of intermittent clouds, is not well followed by the average profile, which tends instead to give a smooth approximation. Moreover, considering the values obtained for the difference on energy indicator, also in this case the classification could be improved, by taking into account additional classification criteria to better group the profiles.

4.7 User load power profiles

In order to perform the prognosis of the electrochemical devices of the system (fuel cell, electrolyzers and batteries), it is important to analyse the daily power load required by the user. Indeed, this could be useful to understand the different operational conditions of the energy system, allowing to associate a different aging rate to each operational point. For this reason, it is useful to build some average load profiles, which approximate the data measured on the system and are assumed to represent its future behaviour.

The analysis and the prediction of the daily load profiles was performed in two ways. In Section 4.7.1, the daily profiles were built with the averaging procedure described in Chapter 3, as it was done with the other variables described in previous Sections. In Section 4.7.2, instead, the load analysis was performed by applying the ANFIS algorithm (described in Chapter 2) to the experimental data.

4.7.1 Average procedure for user power profiles

To describe the different operating conditions in which the system works, a profiling of the experimental data was made by analysing the daily power required by the end user. According to their specific features, the measured daily power profiles were classified in some categories (or classes), following two criteria: the cumulated daily energy, as for all the other variables analysed in the previous sections, and, in addition, the maximum power value reached during the day (in order to take into account the specific features of some profiles). Then, for each category, an average profile was built, that approximates the real data and that is assumed to represent the future load conditions of the system.

There are three main resulting profiles, named as “Low”, “Medium” and “High”, each one further divided in some sub-classes. First, the “High” profiles were separated from the others considering the maximum power value; then, the “Low” and “Medium” profiles were classified by taking into account the daily energy. The generated classes have the following features:

- “Low” profiles: are characterized by the regular presence of small peaks (always lower than 200 W) over a constant base load. This behaviour is also present in all the other profiles, especially during the night and the early morning hours, when no additional power is required by the end user.
- “Medium” profiles: are characterized by irregular shapes and medium peaks (always lower than 2000 W), and the main part of the load is concentrated in the central part of the day, especially between 8 am and 4 pm.
- “High” profiles: are characterized by the presence of high peaks (higher than 2000 W), on a basis of a regular “Low” profile.

The classification was made in an automatized way: each profile was automatically assigned to a specific class, once that the user had chosen the number of classes in which the profiles should be divided or the daily energy levels associated to each class.

Here, three sub-classes were chosen for the “Low” profiles, nine sub-classes for the “Medium” profiles, and two sub-classes for the “High” profiles. The number of sub-classes was chosen in such a way that the number of profiles assigned to each sub-class was approximately the same, and to have a good approximation of the real profiles. The features of the generated classes are shown in Table 11.

Table 11: End user power profiles classes

Class	Daily Energy (DE) [kWh]	Peak Load (PL) [W]
Low 1	1200 < DE < 1500	PL < 2000
Low 2	1500 < DE < 1800	PL < 2000
Low 3	1800 < DE < 2100	PL < 2000
Medium 1	2100 < DE < 2466	PL < 2000
Medium 2	2466 < DE < 2832	PL < 2000
Medium 3	2832 < DE < 3198	PL < 2000

Medium 4	3198 < DE < 3564	PL < 2000
Medium 5	3564 < DE < 3930	PL < 2000
Medium 6	3930 < DE < 4296	PL < 2000
Medium 7	4296 < DE < 4662	PL < 2000
Medium 8	4662 < DE < 5028	PL < 2000
Medium 9	5028 < DE < 5400	PL < 2000
High 1	1700 < DE < 6700	2300 < PL < 3000
High 2	1900 < DE < 3600	PL > 3000

Table 12 shows the percentage of occurrence on the nine-months-period, both for each sub-class and for the overall main classes “Low”, “Medium” and “High”. From these data, it can be seen that the most frequent classes are the “Low” and the “Medium” ones, while the “High” profiles can be considered just as a special case.

Table 12: Percentage of occurrence of the end user consumption profiles

Class	Percentage on total days [%]	
Low 1	26.1 %	55.9 %
Low 2	16.4 %	
Low 3	13.4 %	
Medium 1	4.6 %	40.3 %
Medium 2	3.4 %	
Medium 3	6.3 %	
Medium 4	4.6 %	
Medium 5	5.9 %	
Medium 6	3.4 %	
Medium 7	4.2 %	
Medium 8	6.7 %	
Medium 9	1.3 %	
High 1	2.1 %	3.8 %
High 2	1.7 %	

In this case, for each of the three main classes, some modifications were applied to the averaging procedure described in Chapter 3, in order to better approximate the experimental data.

4.7.1.1 “Low” profiles

In order to obtain an average profile that represents the “Low” load days, the process described below was applied:

- The highest values (load > 200 W) were removed in order to obtain only the base load present in all the days, made by a series of high values (referred in this paragraph as “peaks”) and low values (referred here as “valleys”), regularly alternated.
- For each day, some quantities were evaluated: the overall time (in minutes) corresponding to the presence of peaks or valleys, the sum of the energy (in W*min) corresponding to peaks and valleys, a vector containing the duration (in minutes) of peaks and valleys.
- The mean duration of peaks and valleys was calculated. The value of the load of peaks and valleys was evaluated by dividing their overall energy by the total duration during which they occur.
- The number of peaks/valleys was calculated dividing the total energy of peaks/valleys by the average energy of a single peak/valley.
- Finally, knowing the mean value and the mean duration of peaks and valleys, the average daily profile was built by alternating them (starting and ending with a valley).

The resulting profiles, for the three sub-classes, are shown in Figure 95, Figure 96 and Figure 97, each compared with two of the experimental profiles belonging to that class (the best and the worst case).

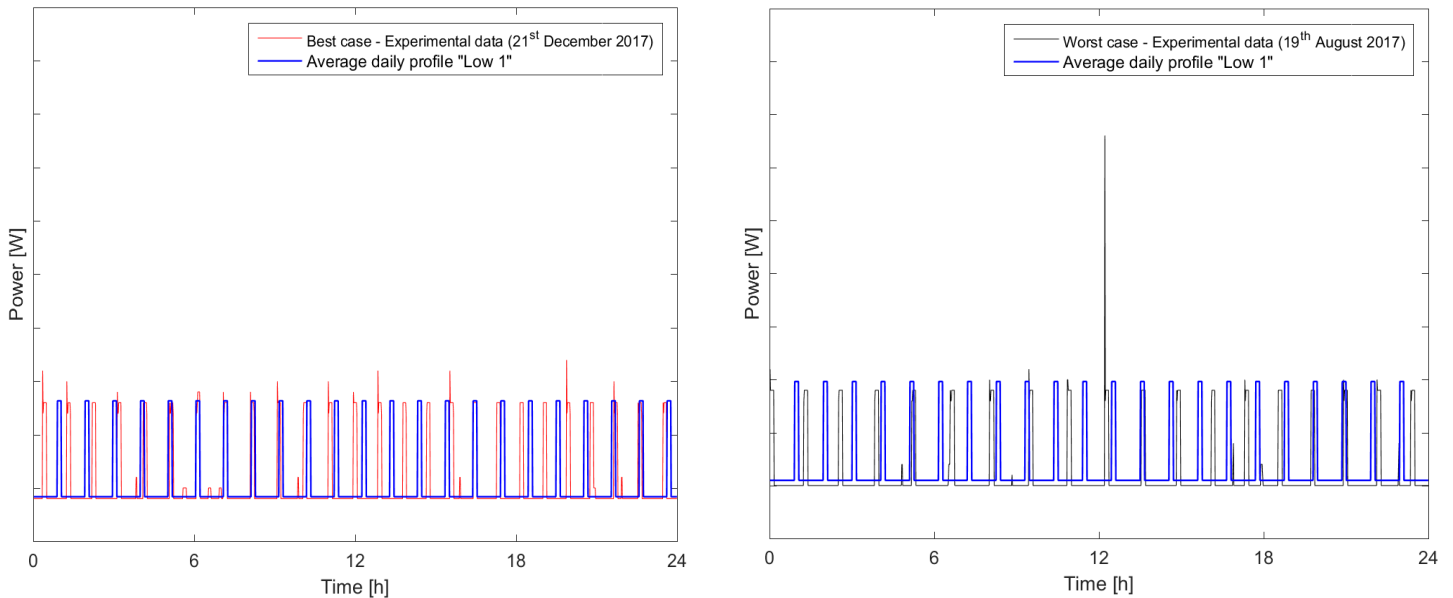


Figure 95 - Average load profile "Low 1"

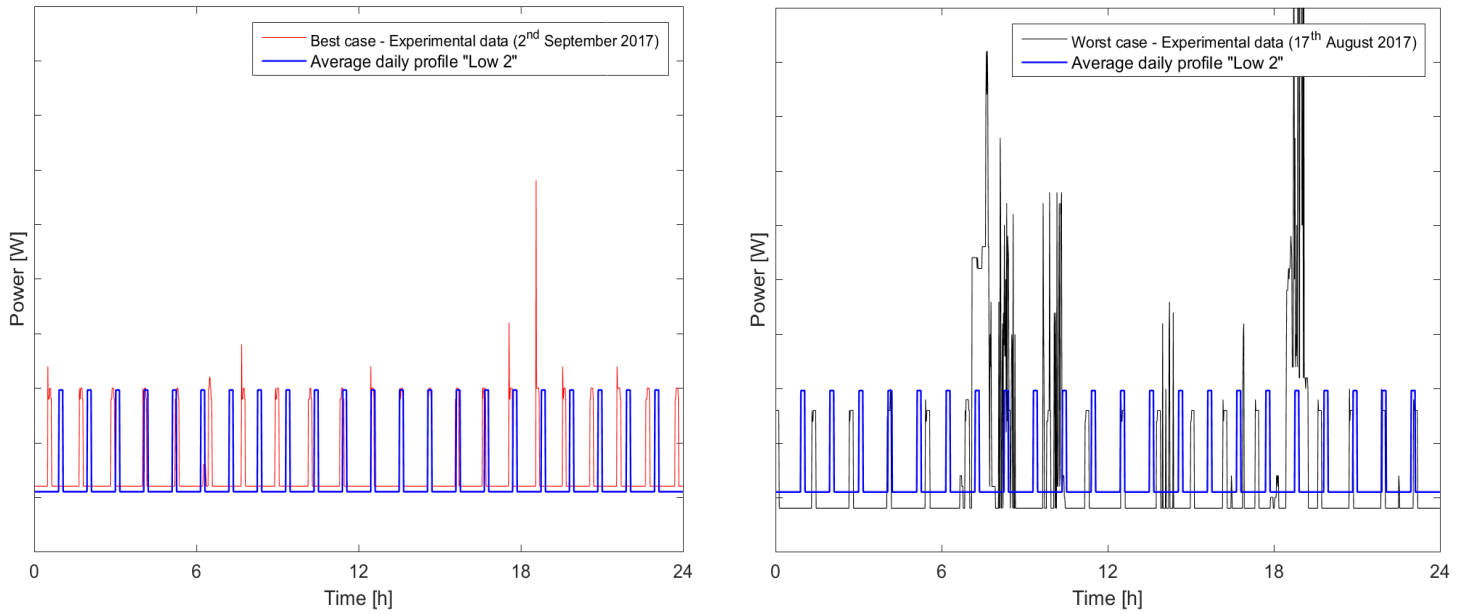


Figure 96 - Average load profile "Low 2"

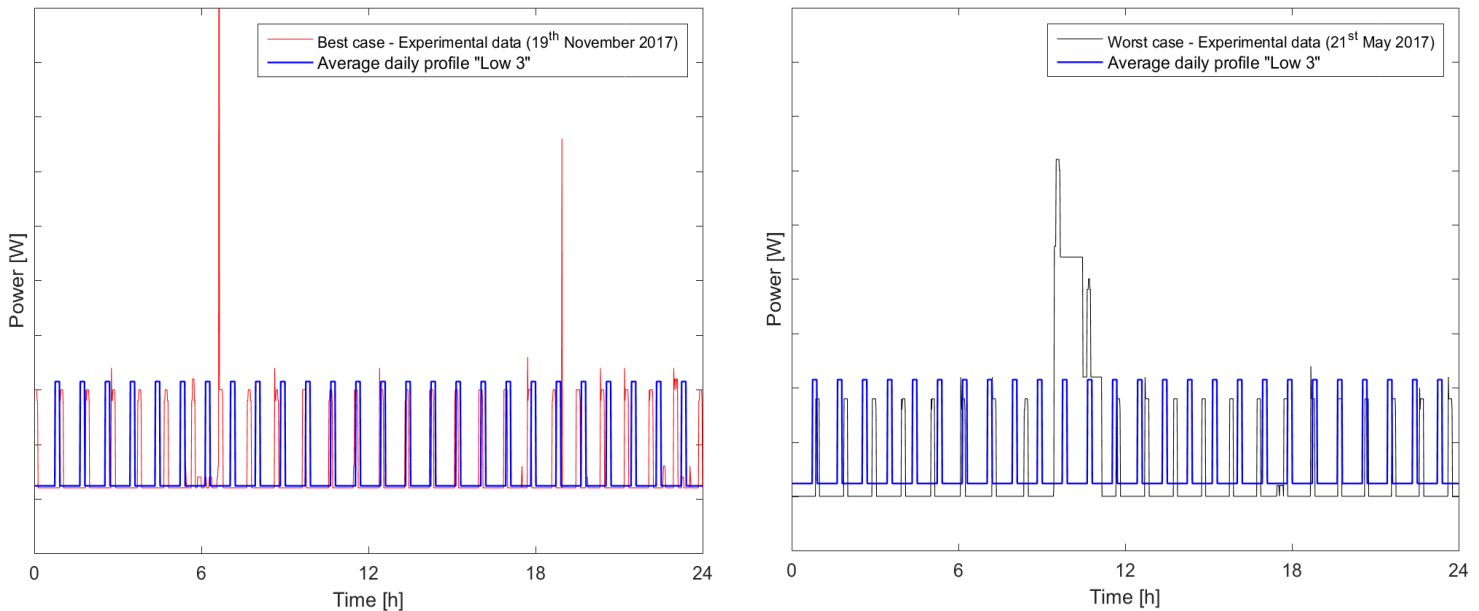


Figure 97 - Average load profile "Low 3"

4.7.1.2 “Medium” profiles

The load profiles belonging to the “Medium” classes were processed by dividing them into two parts: the edges of the profile, corresponding to the early morning and night hours, were the same as one of the “Low” profiles, while the central part of the day was averaged with the process described below:

- First, the starting and ending points of the central part were evaluated. For each day, the first point of the profile with a load higher than 200 W was recorded and then the mean of these positions was chosen as the starting point of the central average profile. The same was made for the ending point, by recording and then averaging the last minute of each day, with a load higher than 200 W.

- Once that the boundaries were set, the central profile was evaluated as the maximum load value at each time, in order to preserve the shape and the peaks of the real profiles. However, in this way, the daily energy of the average profile is higher with respect to the mean cumulated energy of the real profiles. Therefore, the profile was scaled to make sure that the energy of the average profile was equal to the mean daily energy of real profiles.
- Finally, the overall average profile was built by associating to the central part (before and after it) one of the “Low” profiles previously evaluated (here, the “Low 1” profile was chosen, as it is the most frequent).

Figure 98 to Figure 106 show the results obtained for each of the “Medium” categories, compared with the best and worst case of the experimental profiles of each class.

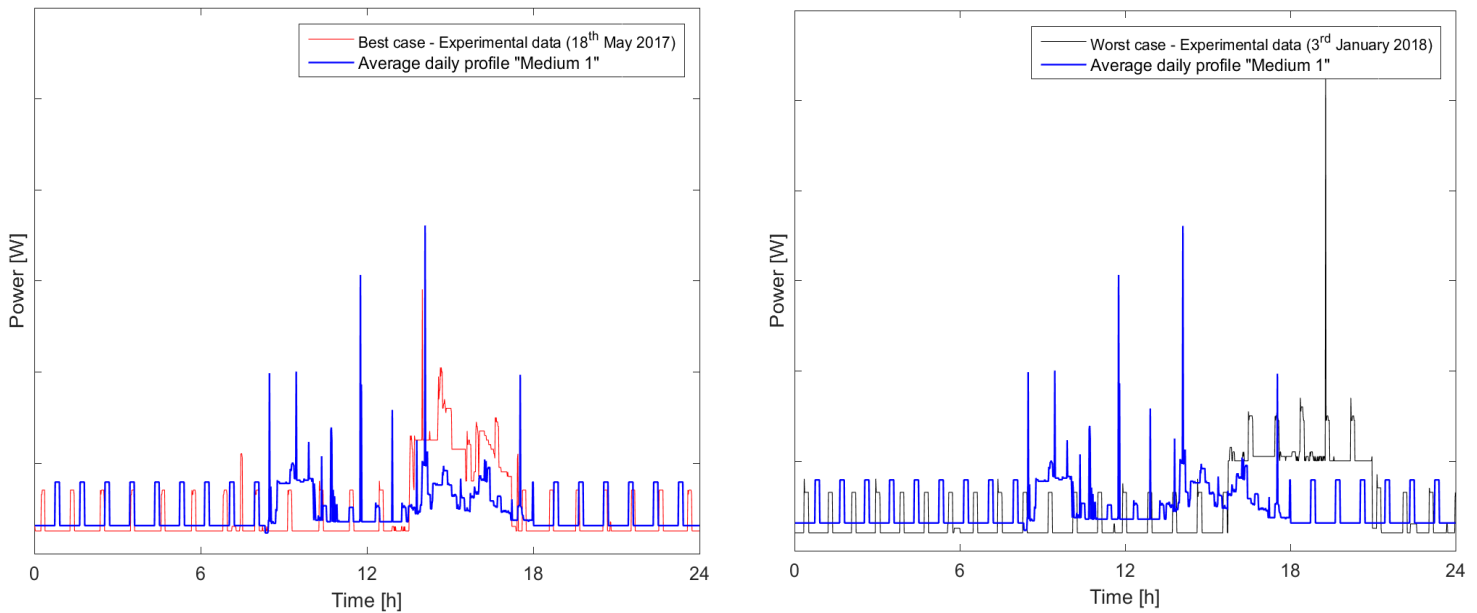


Figure 98 - Average load profile "Medium 1"

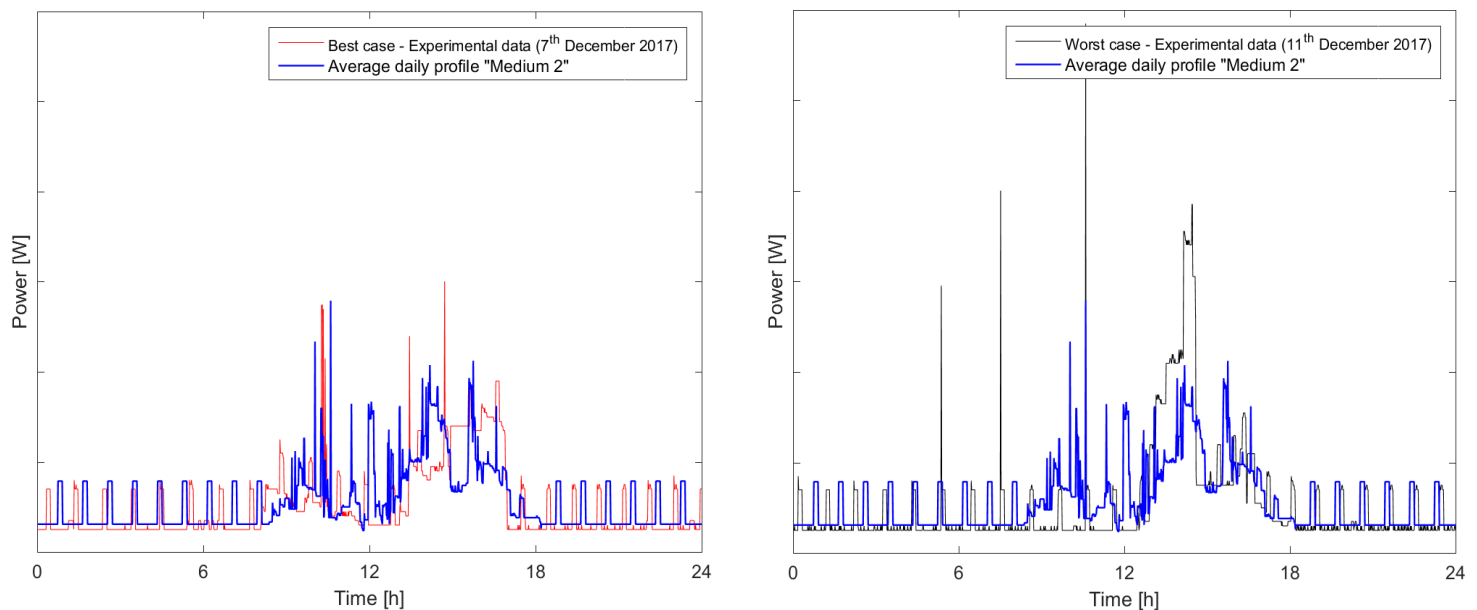


Figure 99 - Average load profile "Medium 2"

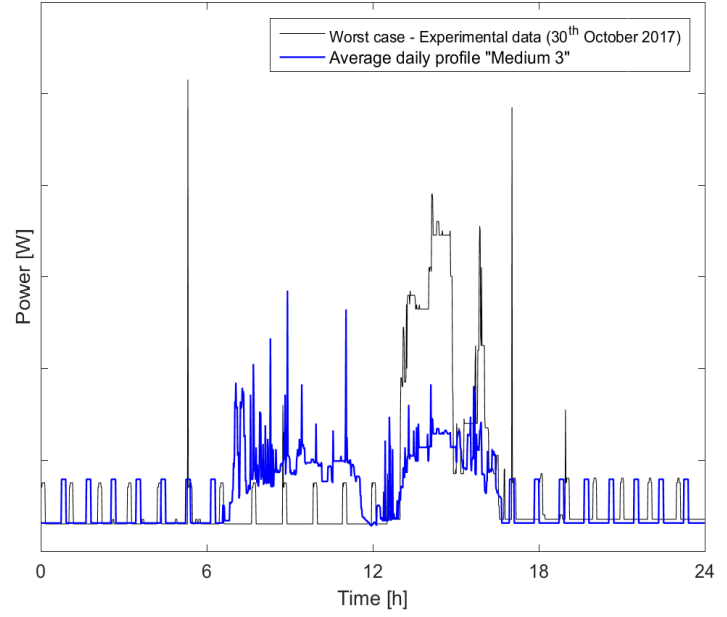
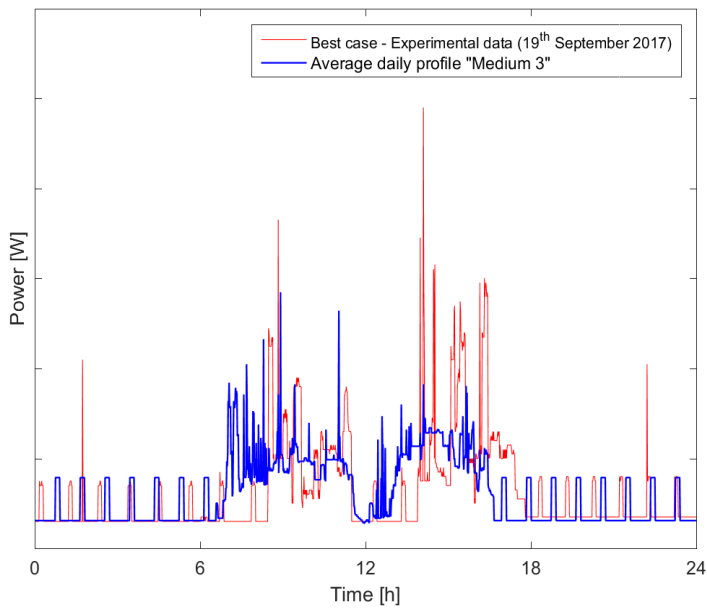


Figure 100 - Average load profile "Medium 3"

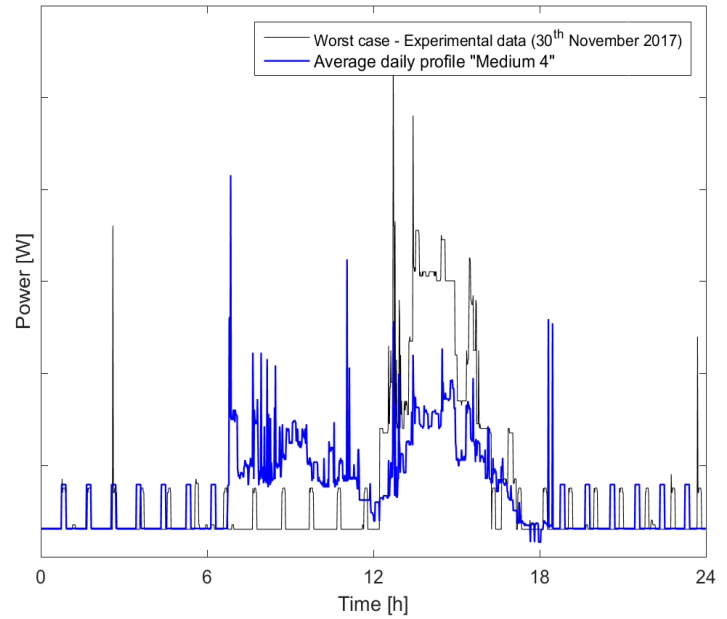
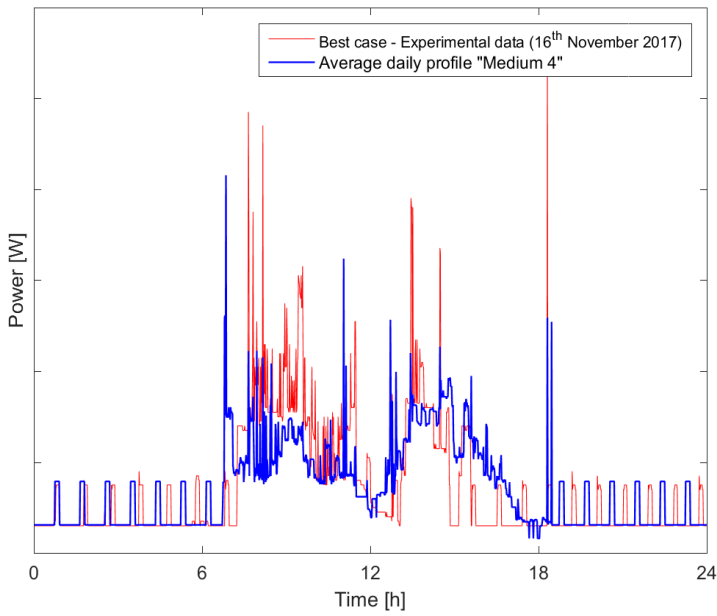


Figure 101 - Average load profile "Medium 4"

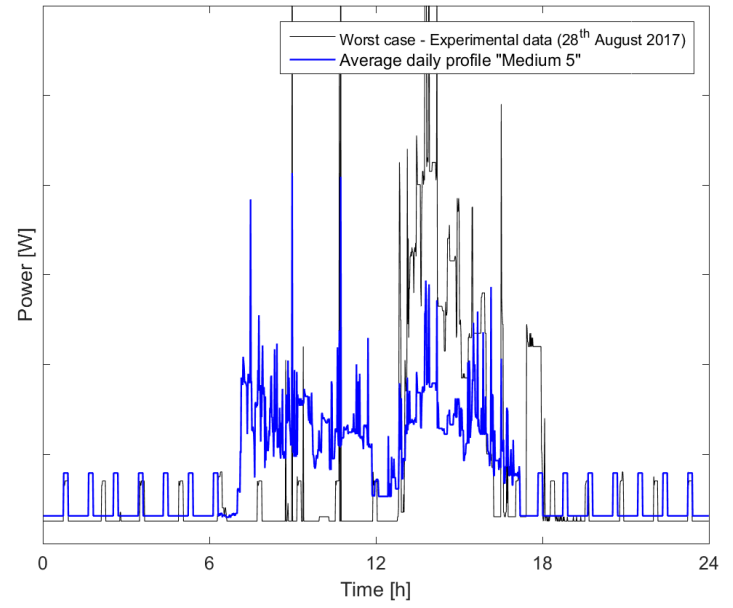
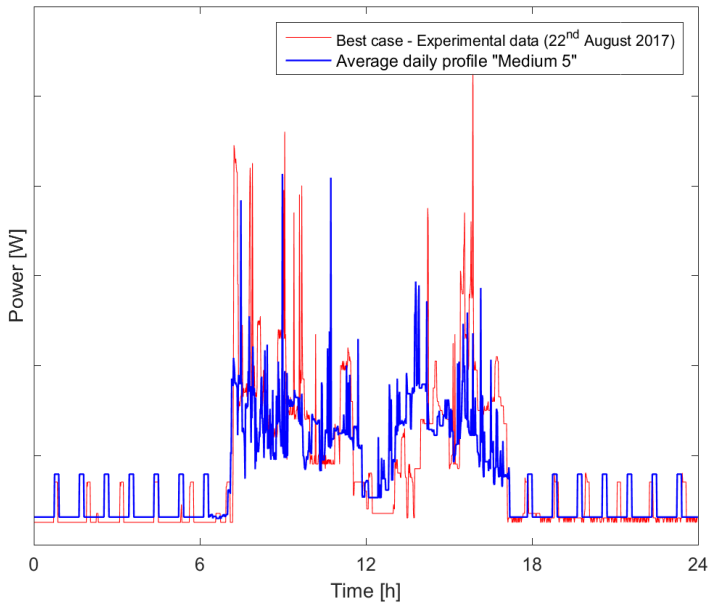


Figure 102 - Average load profile "Medium 5"

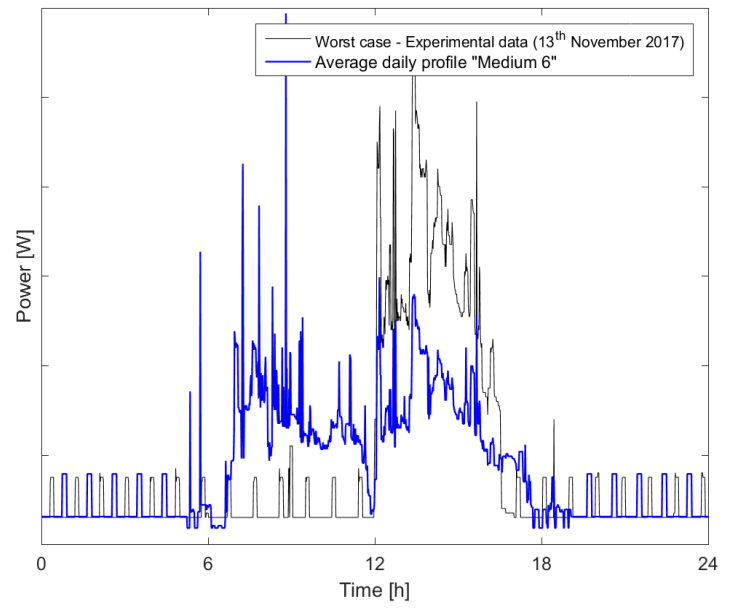
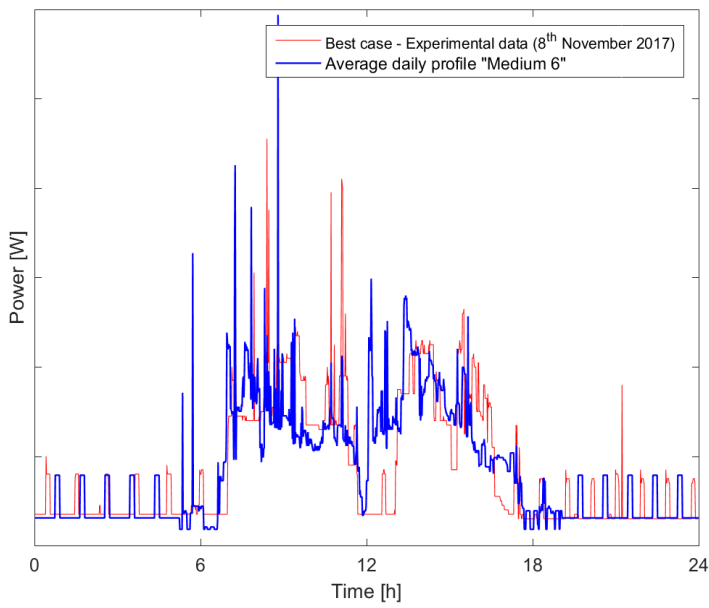


Figure 103 - Average load profile "Medium 6"

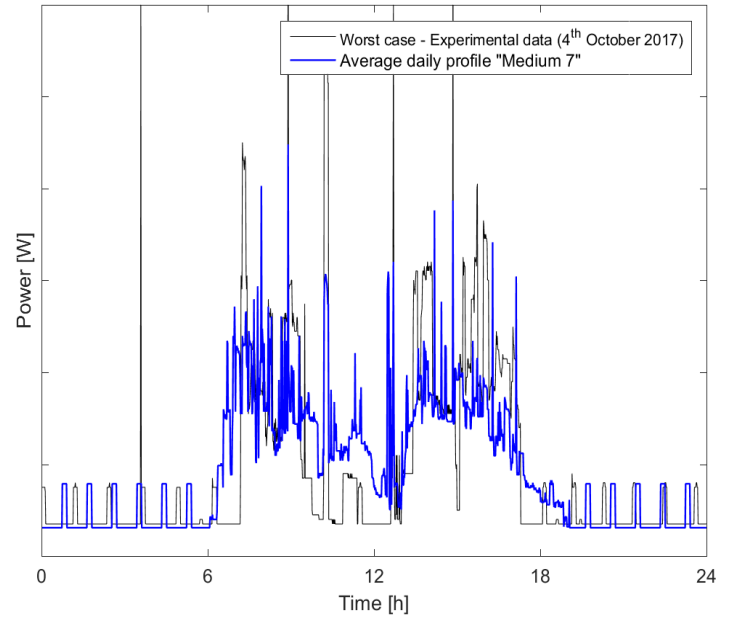
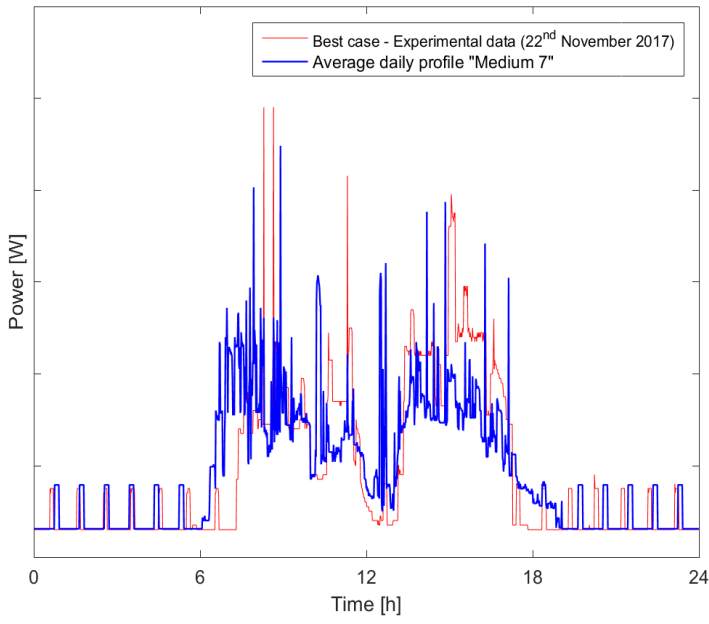


Figure 104 - Average load profile "Medium 7"

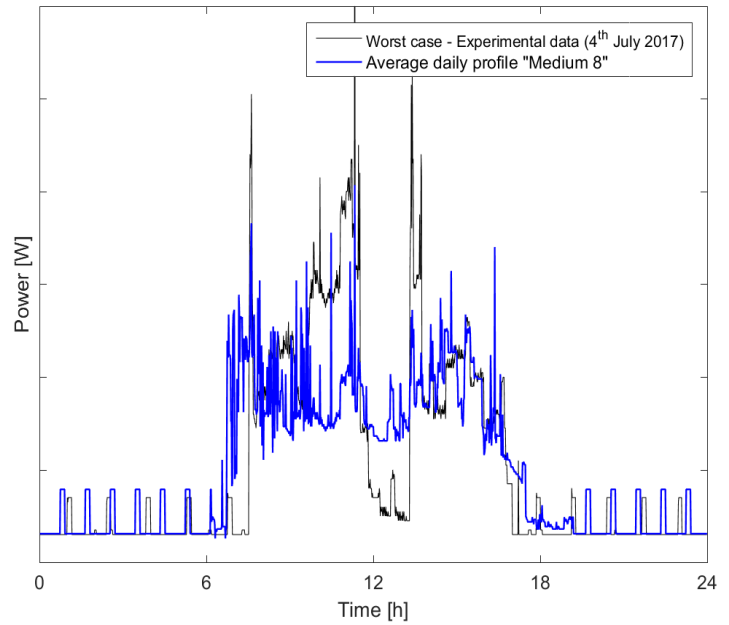
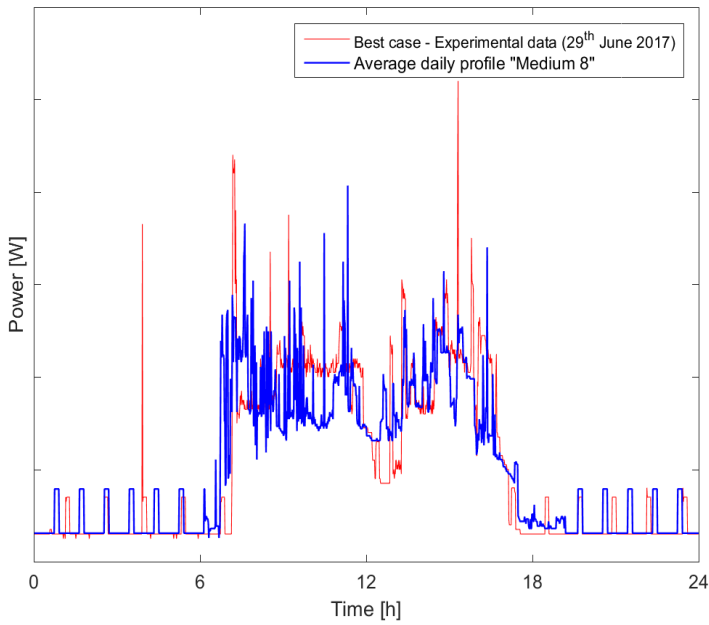


Figure 105 - Average load profile "Medium 8"

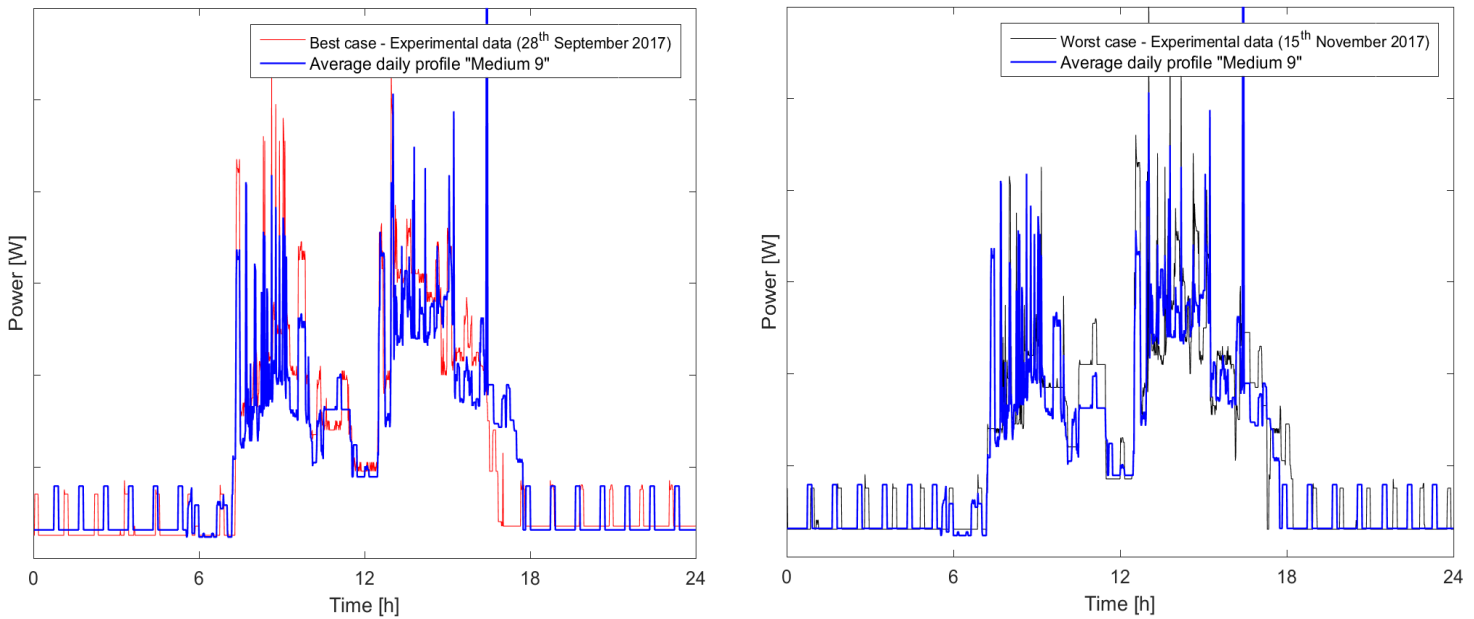


Figure 106 - Average load profile "Medium 9"

4.7.1.3 “High” profiles

As for the “Medium” profile classes, the “High” load profiles can also be divided into two parts. The early morning and night hours are represented by one of the “Low” profiles (here, the “Low 1” was chosen, as it is the most frequent) evaluated in Section 4.7.1.1, while a different average profile was built for the central remaining part.

- First, the boundaries of the central part were evaluated. For each day, the first point of the profile with a load higher than 1000 W was found; then, the mean of these times was set as the starting point of the central average profile. The same was made for the ending point, by recording and then averaging the last minute of each day, with a load higher than 1000 W.
- Once the boundaries were set, the values of the load for each day were sorted in descending order, ordering them from the highest to the lowest power.
- For each point of the sorted profile, the mean values of the power and of the corresponding time were evaluated.
- By sorting again the values in ascending order according to the value of the time (from the lowest to the highest time), an average load profile was obtained, as shown in Figure 107.

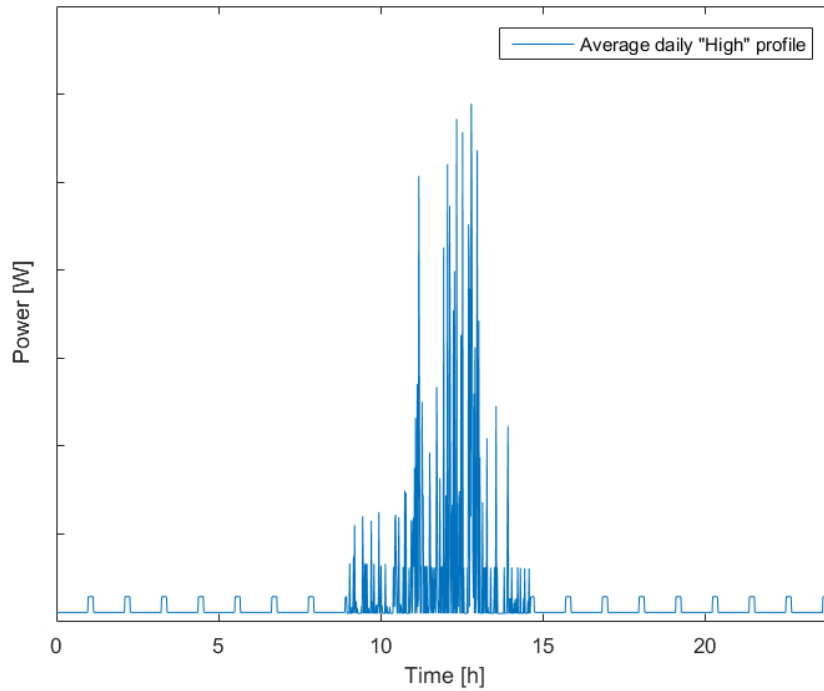


Figure 107 - Average daily "High" load profile

In this way, however, the resulting average profile does not have the same shape as real profiles, as all the peaks are concentrated in the central part of the day, while in real profiles they are always divided into two groups. To solve this problem, for each position of the sorted load profiles, the mean value of the time was calculated only considering the first or the second half of the day, choosing the one containing the highest number of load values. The final average profiles obtained are shown in Figure 108 and Figure 109, compared with two corresponding experimental daily profiles (best and worst case).

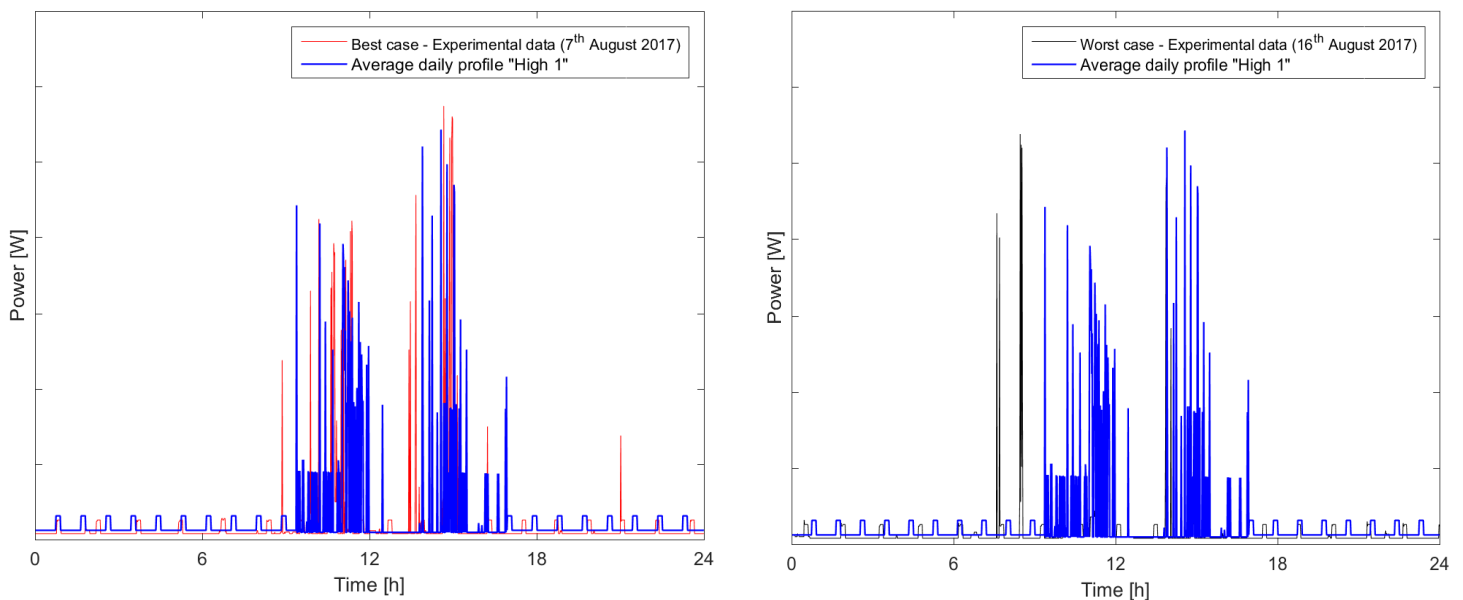


Figure 108 - Average load profile "High 1"

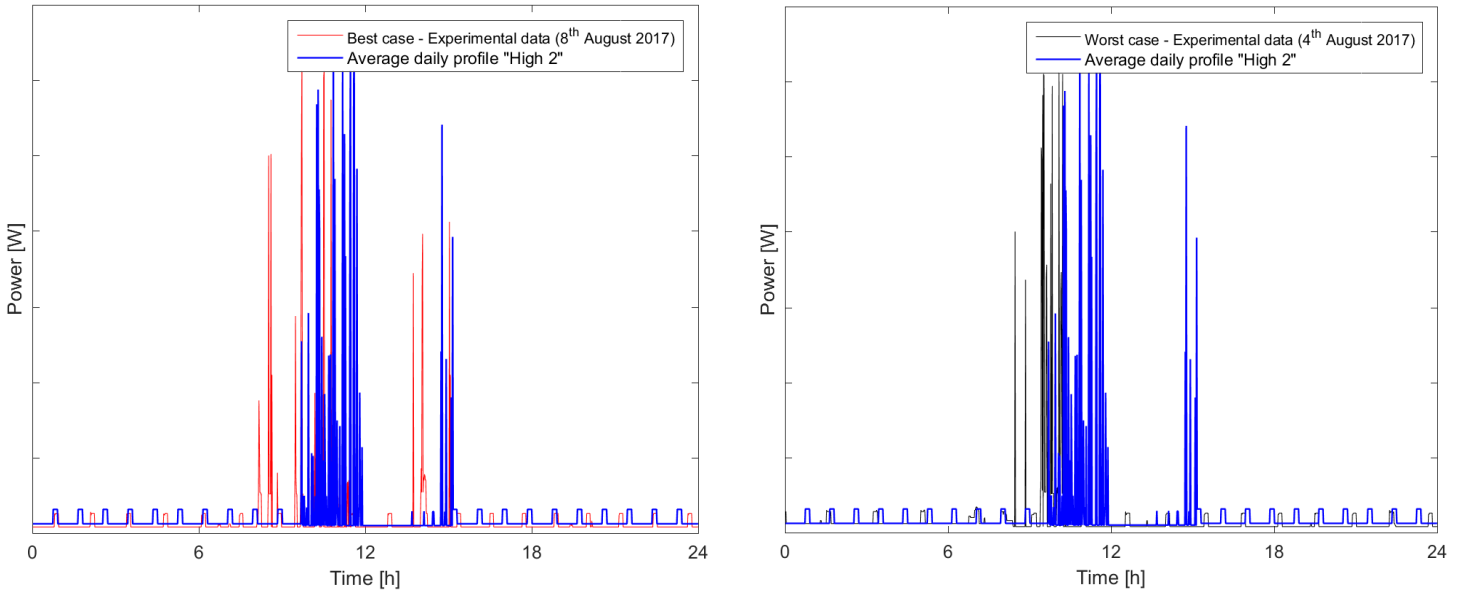


Figure 109 - Average load profile "High 2"

4.7.2 ANFIS implementation for load prediction

A method that can be used to predict the future load profile of a system is the ANFIS, whose structure and features were described in Chapter 2. It was used, in this Section, in order to forecast the future user load profile, by using as training and testing data the available direct measurements from the system. In particular, taking into account the classification and the average load profiles built in Section 4.7.1, for each category the ANFIS model was used in the following way: the mean profiles were used to train the model in the learning phase, while the real load profiles were used to test and validate it.

The ANFIS algorithm was implemented on MATLAB in two ways: by using the Neuro-Fuzzy Designer toolbox, as shown in Section 4.7.2.1, and by writing a script in the Editor mode, as shown in Section 4.7.2.2. In both cases, the computed ANFIS was based on the Takagi-Sugeno model, characterized by the following features:

- only one output;
- only constant or linear output membership functions;
- the weighted mean value is used as defuzzification method.

4.7.2.1 Implementation with Neuro-Fuzzy Toolbox

The first way to implement an ANFIS is by using the Neuro-Fuzzy Designer toolbox. This tool allows the user to build a FIS and then to adaptively optimize its parameters to obtain the best results.

First, it is needed to load the datasets for the training and the testing phase. These datasets are built as matrices with two columns: the first one contains the inputs and the second one the corresponding target outputs (represented by the experimental data), that the model should give as results in the best case.

Here, for instance, the training dataset was the average load profile of the class "Low 3" and the testing dataset was one of the real daily profiles belonging to that class (occurring on the 19th November). 250 samples, made by couples of inputs and the corresponding

outputs, were used for the training phase and the testing phase was performed on 500 samples. The training dataset was plotted in the upper part of the window, as shown in Figure 110.

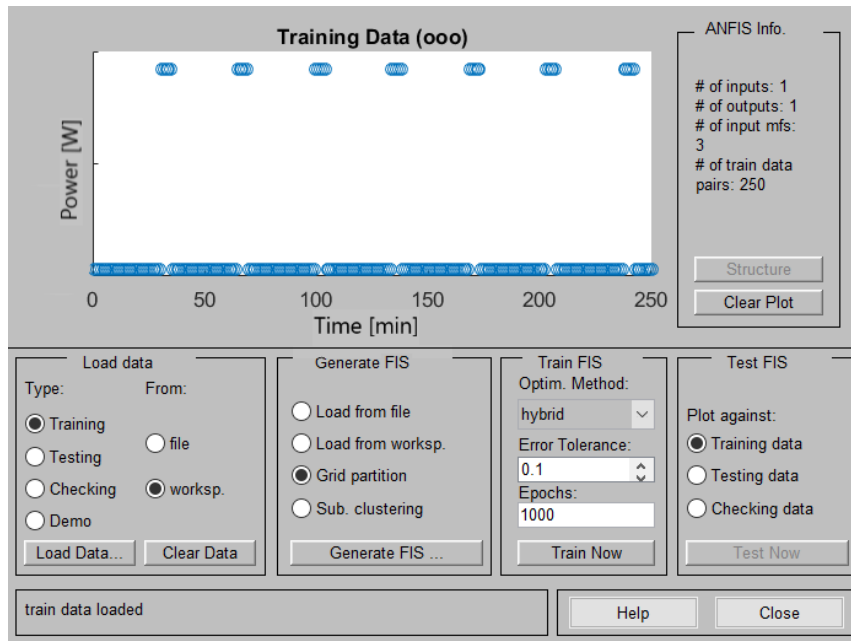


Figure 110 - Neuro-Fuzzy MATLAB toolbox with training data plotted

Then, the Fuzzy Inference System was generated by choosing the number and the type of both input and output membership functions. In this case, a FIS with 30 membership functions was built, whose layout is shown in Figure 111. The input membership functions were set as ‘gaussian’, while the output ones as ‘linear’. These parameters were chosen by trial and error, in order to obtain the best results from the simulation.

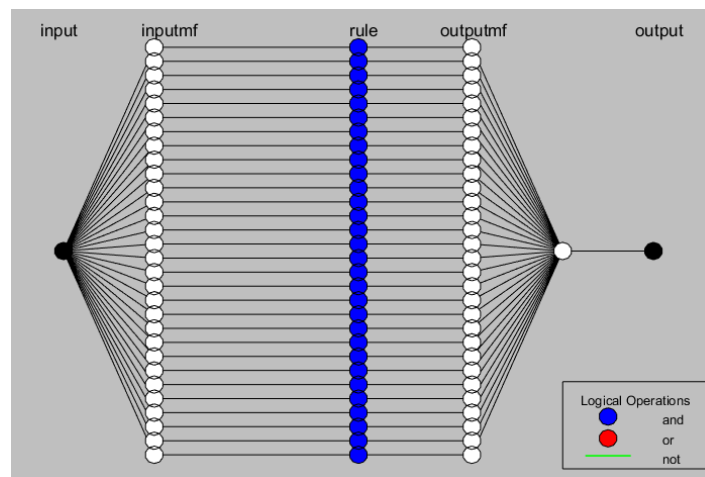


Figure 111 - Structure of the generated FIS

Then, for the training phase, some parameters must be set by the user:

- *optimization method*, choosing between the hybrid algorithm described in Section 2.2.2 or the Gradient Descent only (Section 2.2.2.1);
- *error tolerance*;
- *maximum number of iterations*.

The training phase ends either when the training error becomes lower than the error tolerance set by the user or when the maximum number of iterations is reached. The training error is evaluated by comparing, at each iteration, the target output and the result computed by the model.

Finally, the outputs obtained by the ANFIS model after 1000 iterations were plotted against the average profile used as training dataset, as shown in Figure 112, and against the experimental power load used as testing dataset, as shown in Figure 113.

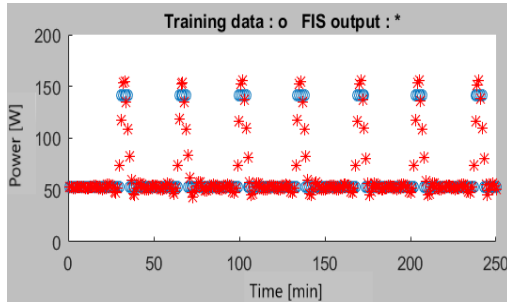


Figure 112 - Plot of ANFIS results vs training data

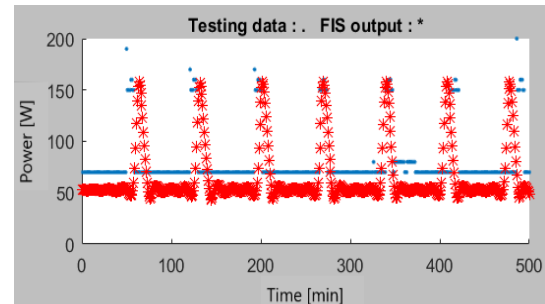


Figure 113 - Plot of ANFIS results vs testing data

The results of the model look quite close to the experimental data; however, if more samples are used for the training and testing phase (using, for example, the entire daily profiles) the computational time increases significantly while the resulting profiles are characterized by a higher error.

4.7.2.2 Implementation in Editor Mode

The ANFIS model was also implemented by writing a script within the MATLAB Editor. As a starting point, the training and testing datasets were loaded. These were built as matrices, in which the inputs were organized in columns and the last column was the output.

The Fuzzy Inference System was initialized with the command “*genfis1*”, which takes as inputs the training dataset, the number of membership functions assigned to each input and their type. In the following examples, 30 Gaussian membership functions were chosen. Then, the FIS parameters were optimized using the ANFIS, activated with the command “*anfis*”. It takes as inputs the training and testing datasets, the FIS previously generated and the stopping criteria chosen by the user, expressed as a vector containing the maximum number of iterations and the error tolerance. The prediction results given by the ANFIS network were, then, extracted as vectors with the command “*evalfis*”, so that they could be plotted in order to evaluate if they are close to the real measurements (or target outputs).

The first simulations were performed on the profiles of the “Low” classes: the training data were taken from the average load profile built each class and the testing data from one of the daily experimental power profiles. The limit training error was set at 0.1%, and the maximum number of iterations was chosen as 3000. The results obtained after the testing phase are shown in Figure 114, Figure 115 and Figure 116. In all simulations, the training phase stopped after 3000 iterations, as the limit error was never reached.

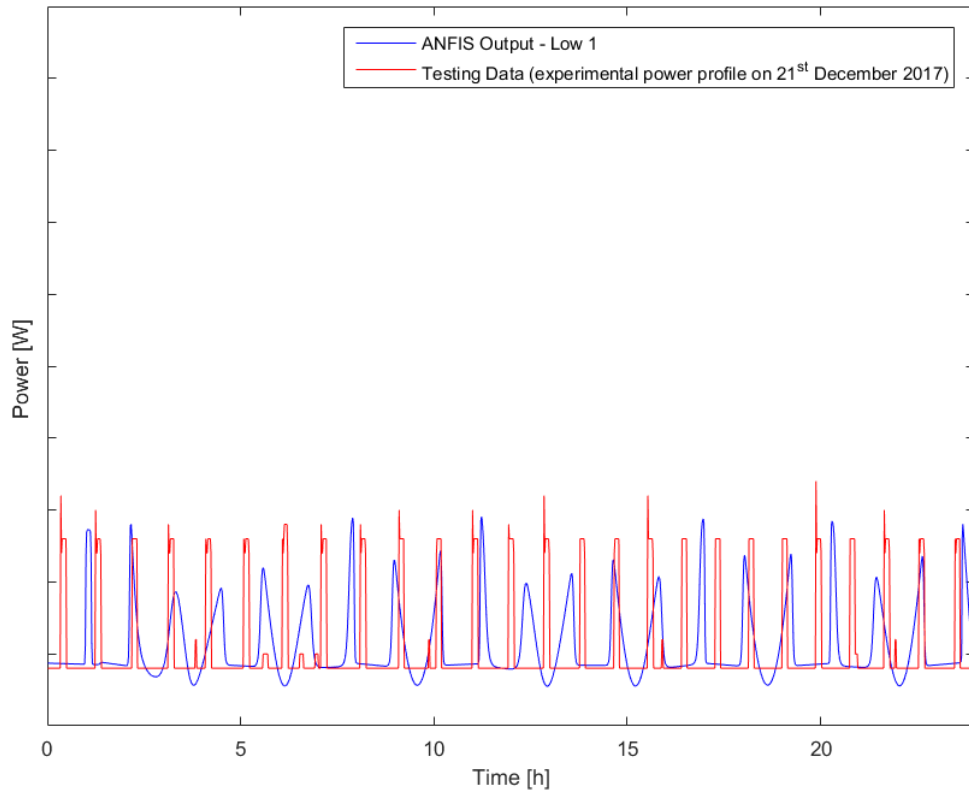


Figure 114 - ANFIS results vs test data for the “Low 1” profile

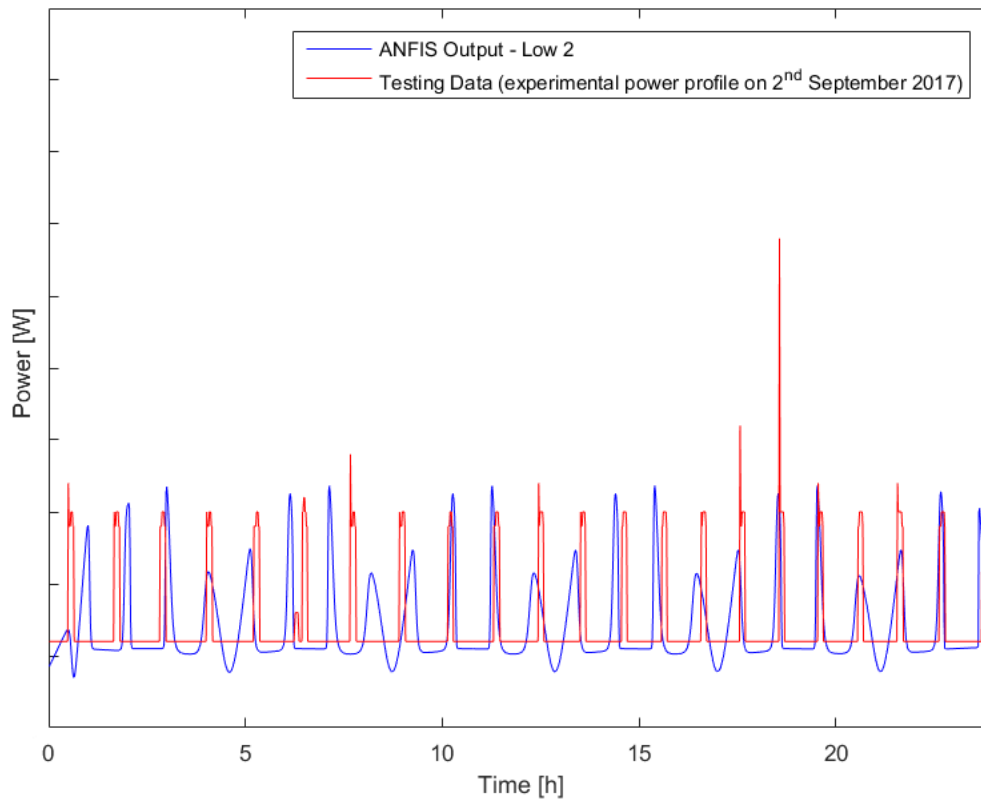


Figure 115 - ANFIS results vs test data for the “Low 2” profile

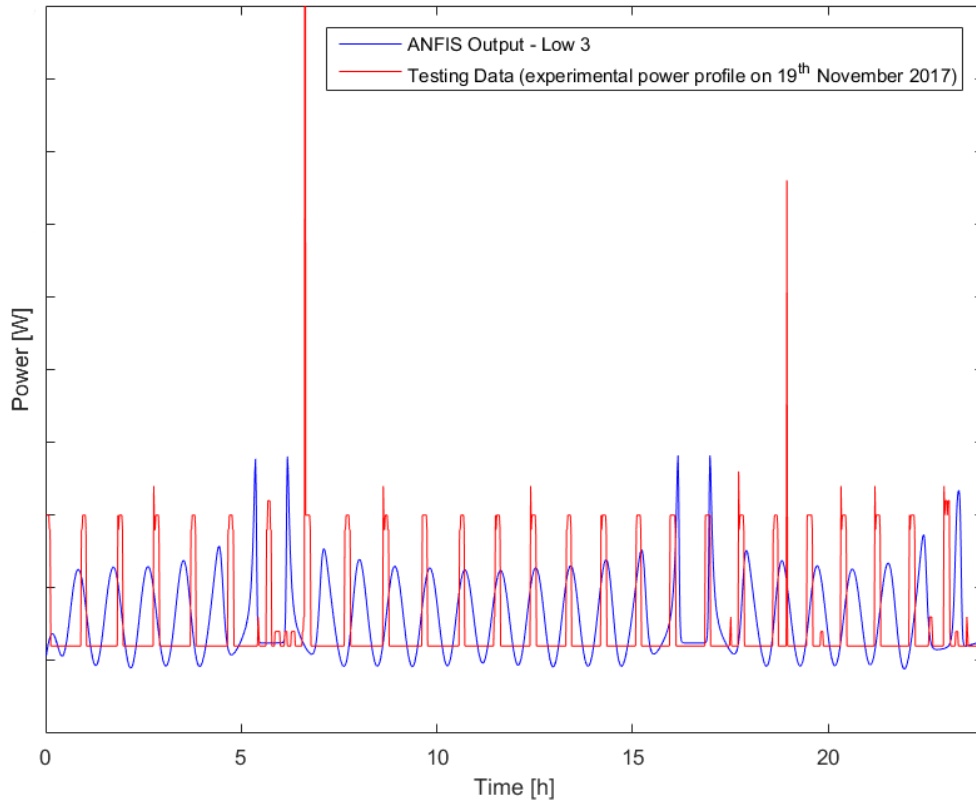


Figure 116 - ANFIS results vs test data for the “Low 3” profile

The algorithm was able to predict approximately the shape of the experimental profile, but the profiles do not look as similar as those obtained with the averaging procedure described in Section 4.7.1.1.

Other simulations were performed on the load profiles taken from the “Medium” categories, characterized by an irregular shape. The training was performed using the average profile built for each category, while the testing was done on a real daily profile belonging to that category. For all simulations, the limit error for the training phase was set at 0.1% and the maximum number of iterations at 3000; all of them were performed until the 3000 iterations, as the limit error was never reached. Figure 117 to Figure 125 show the prediction results obtained after the testing phase, for each of the “Medium” classes.

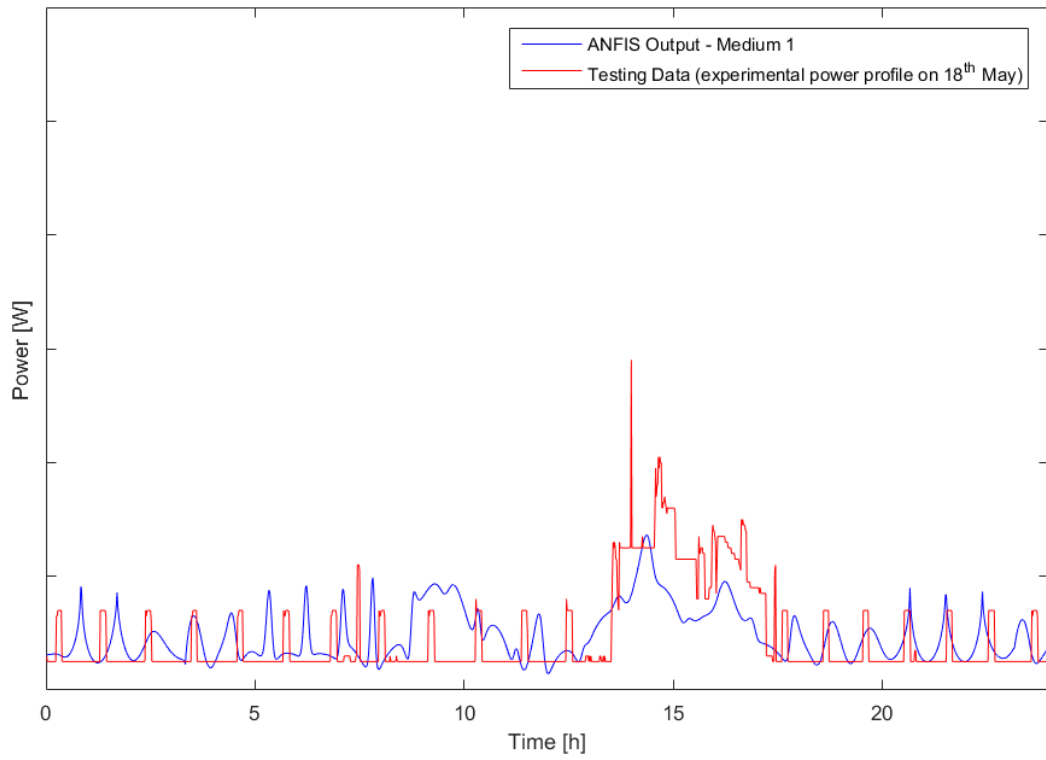


Figure 117 - ANFIS results vs test data for the “Medium 1” profile

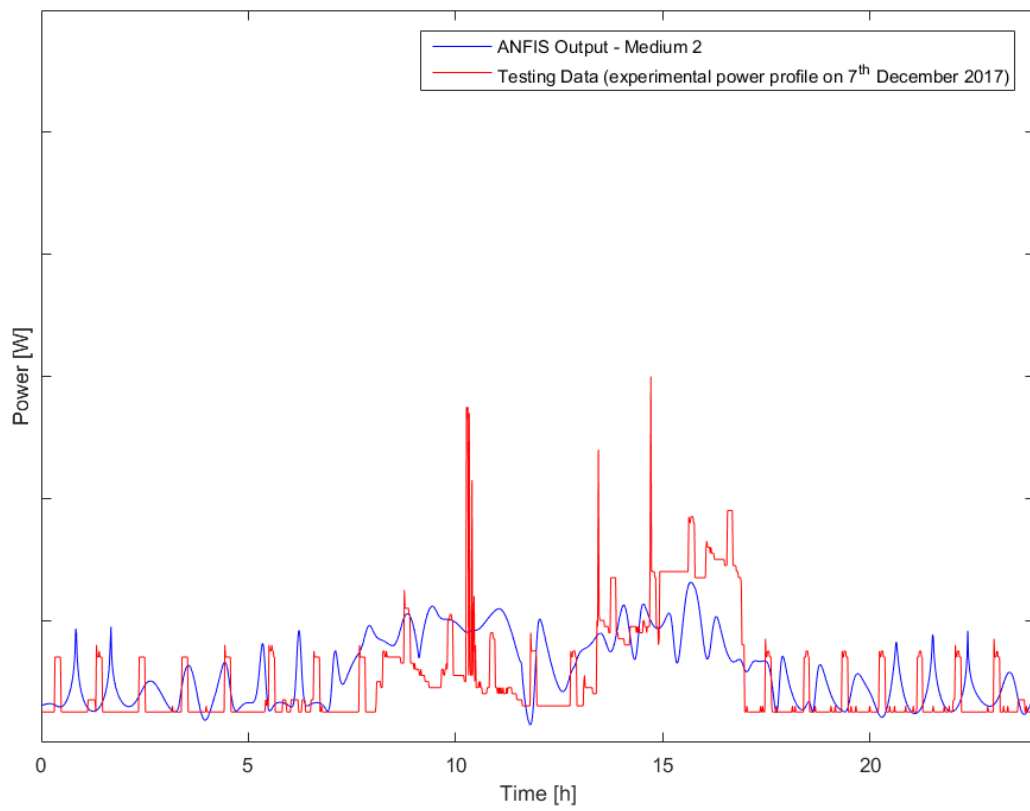


Figure 118 - ANFIS results vs test data for the “Medium 2” profile

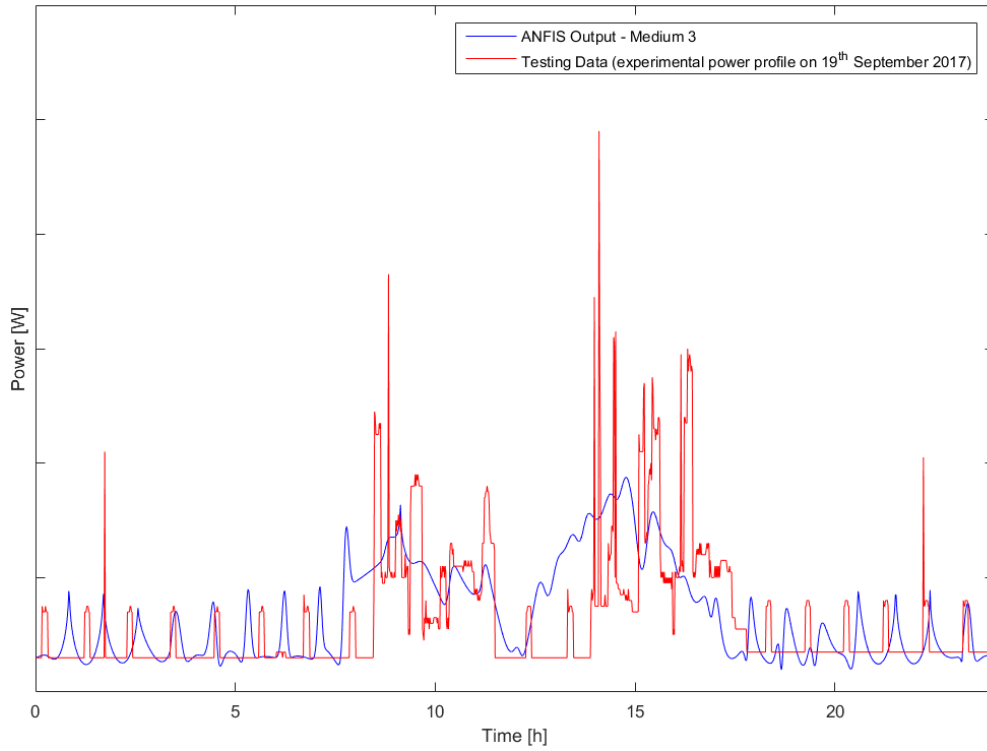


Figure 119 - ANFIS results vs test data for the “Medium 3” profile

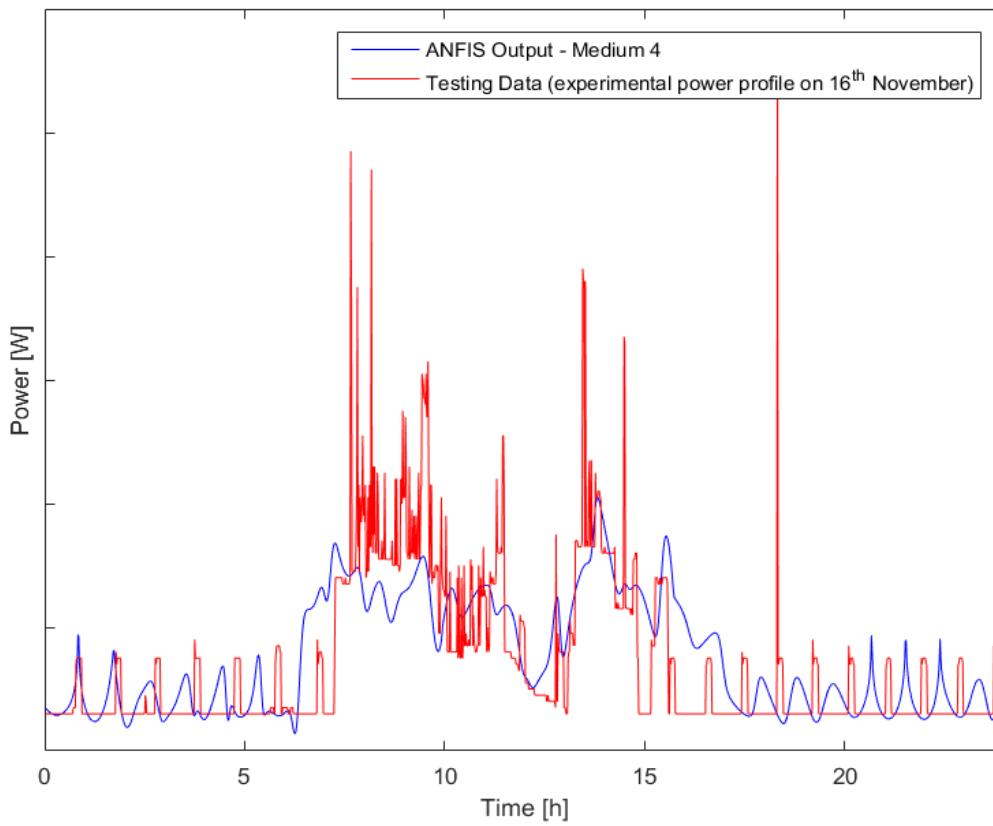


Figure 120 - ANFIS results vs test data for the “Medium 4” profile

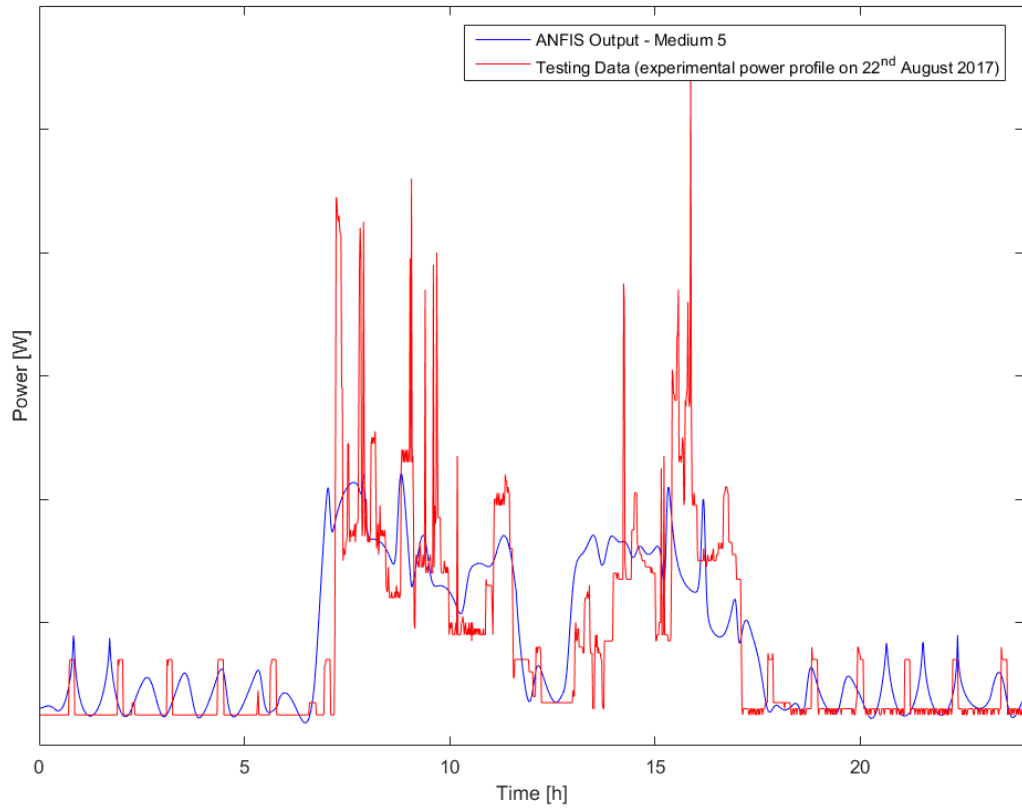


Figure 121 - ANFIS results vs test data for the “Medium 5” profile

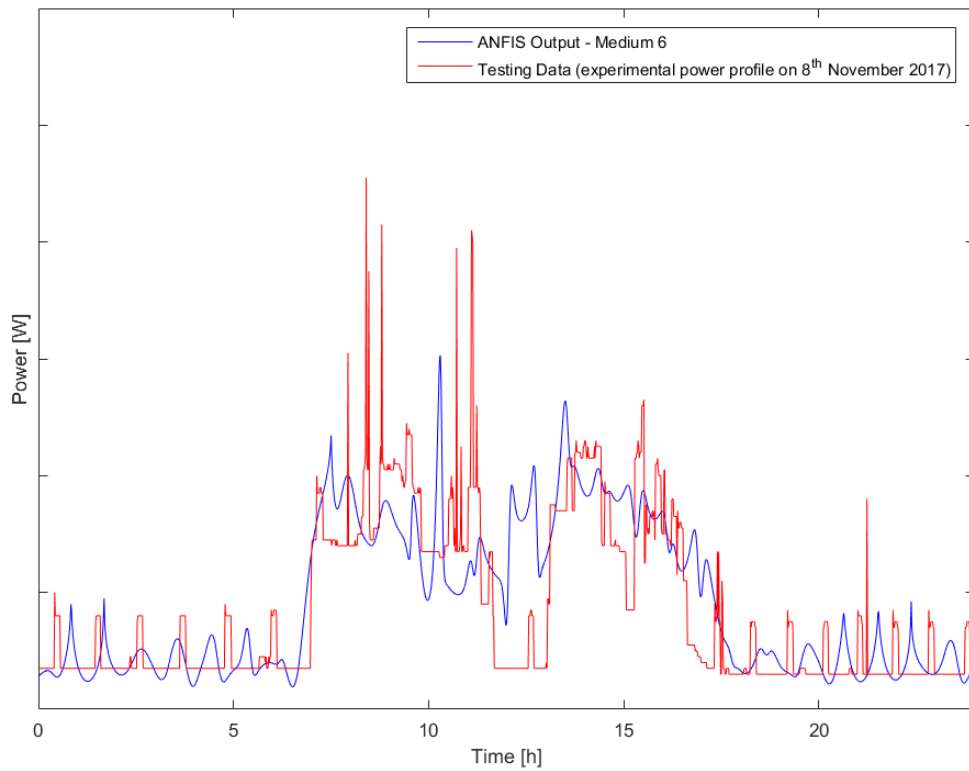


Figure 122 - ANFIS results vs test data for the “Medium 6” profile

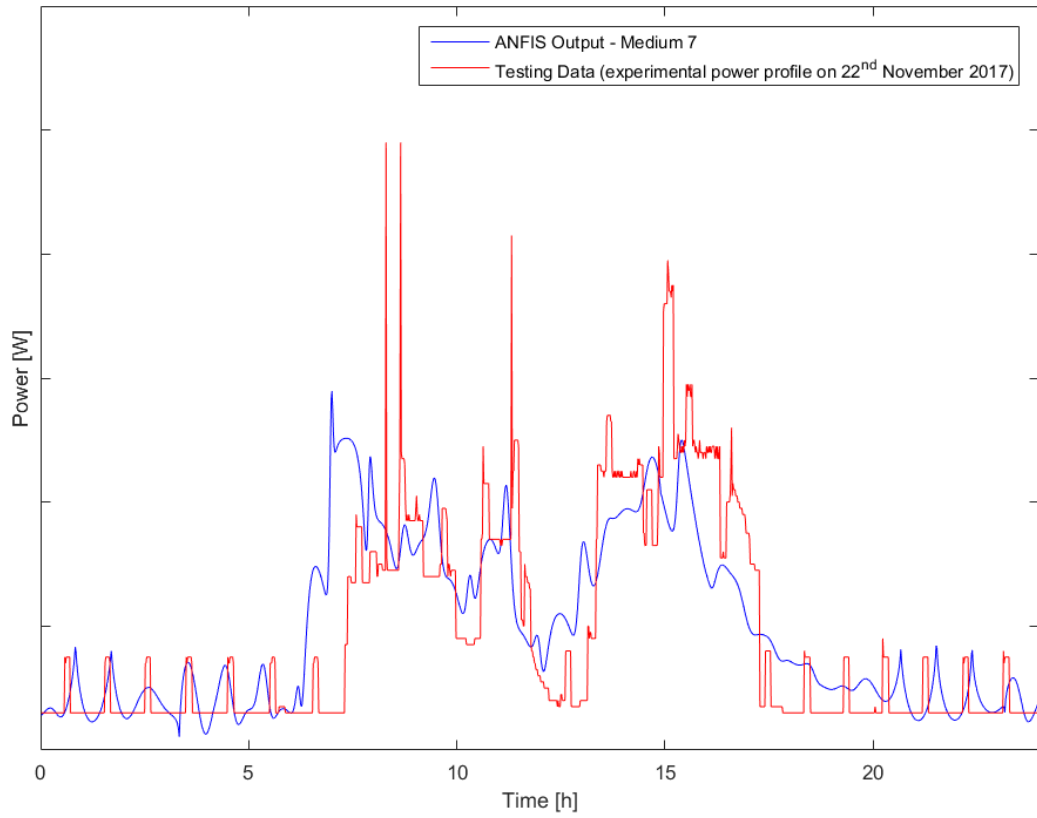


Figure 123 - ANFIS results vs test data for the “Medium 7” profile

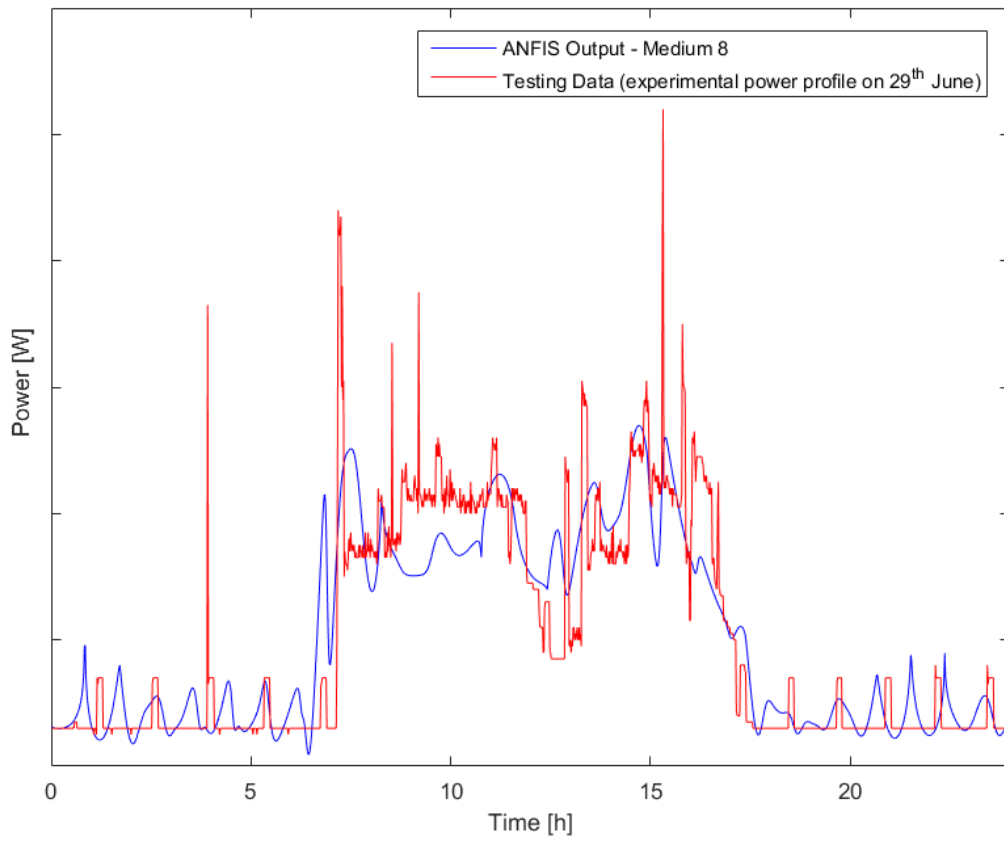


Figure 124 - ANFIS results vs test data for the “Medium 8” profile

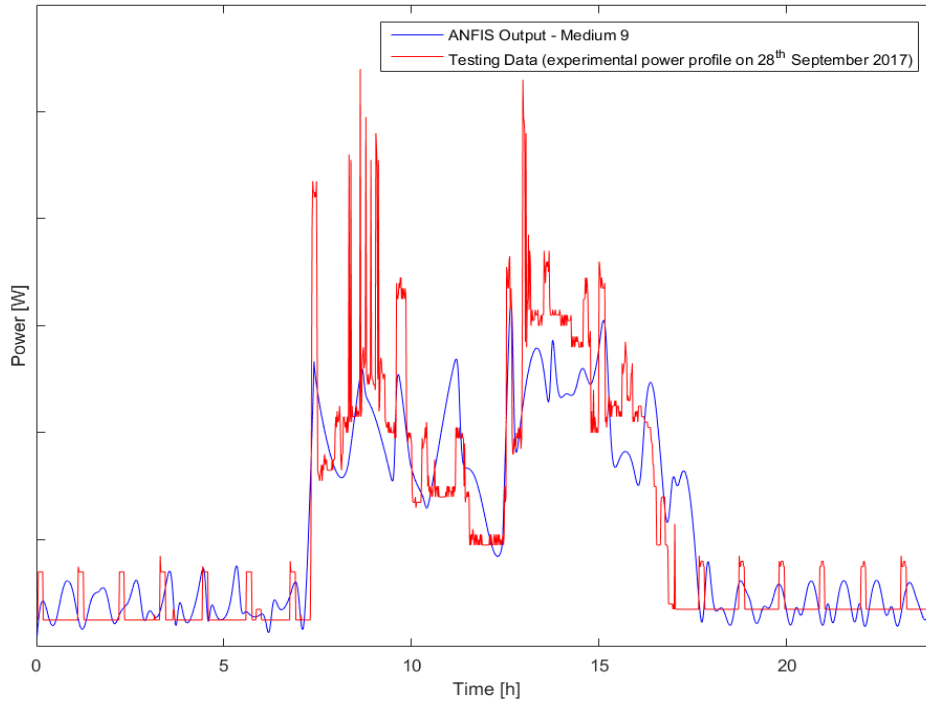


Figure 125 - ANFIS results vs test data for the “Medium 9” profile

For these “Medium” classes profiles, thanks to the training phase, the ANFIS was able to catch and represent the shape of the daily load, but it was not able to predict unexpected load changes, too high peaks or behaviours that are different from the one on which the algorithm was trained. For this reason, the application of ANFIS to the class of the “High” load profiles was harder than for the other ones, as they are characterized by high and fast variations of the power during the day. Indeed, the application of the ANFIS to the “High” profiles using only the time as input led to poor prediction results, as shown in Figure 126 and Figure 127.

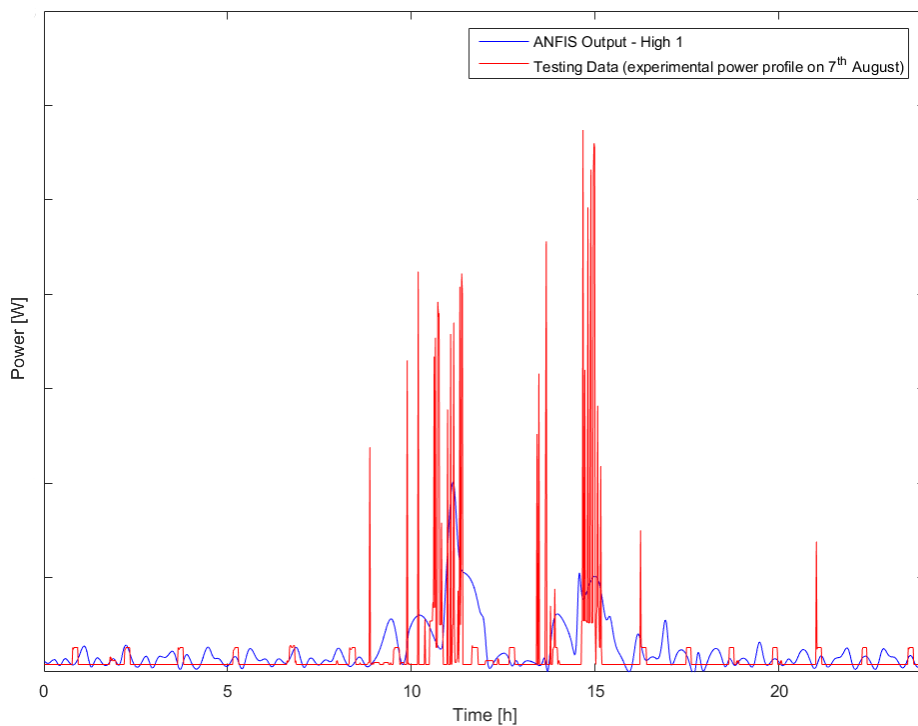


Figure 126 - ANFIS results (with one input) vs testing data for the “High 1” profile

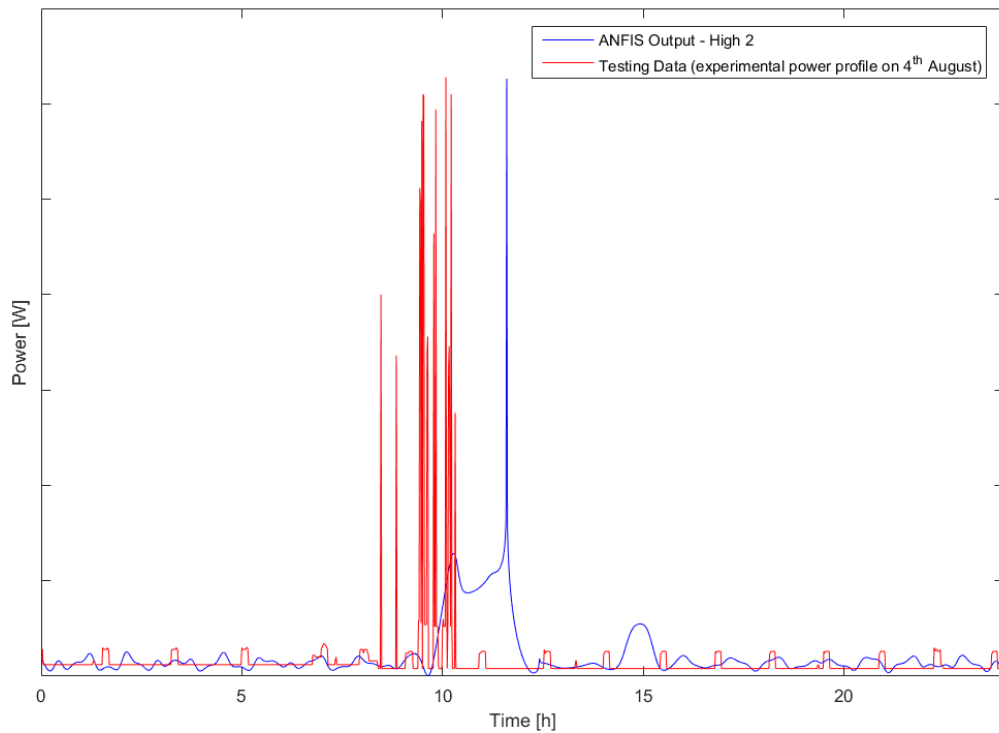


Figure 127 - ANFIS results (with one input) vs testing data for the "High 2" profile

4.7.3 Comparison between the average and ANFIS procedure

In Section 4.7.1 and Section 4.7.2, two different methods for the forecasting of the user load were described. Here, their results are compared by analysing the PRSD and the absolute Standard Deviation between the average profiles built with the two methods and the experimental ones.

The absolute errors evaluated on the profiles of the “Low” classes, obtained using the analytic and the ANFIS algorithms are shown in Figure 128(a) and Figure 128(b), respectively. The errors on the “Medium” classes profiles are in Figure 129(a) and Figure 129(b). The errors on the profiles of the “High” classes are shown in Figure 130(a) and Figure 130(b). The plots were cut on the x-axis before the 24 hours, because in the final part the errors are very close to zero.

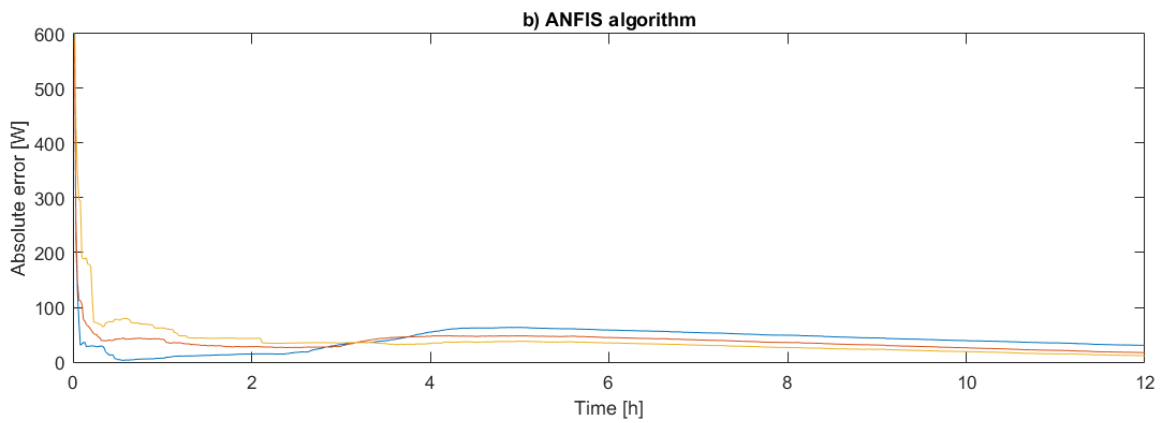
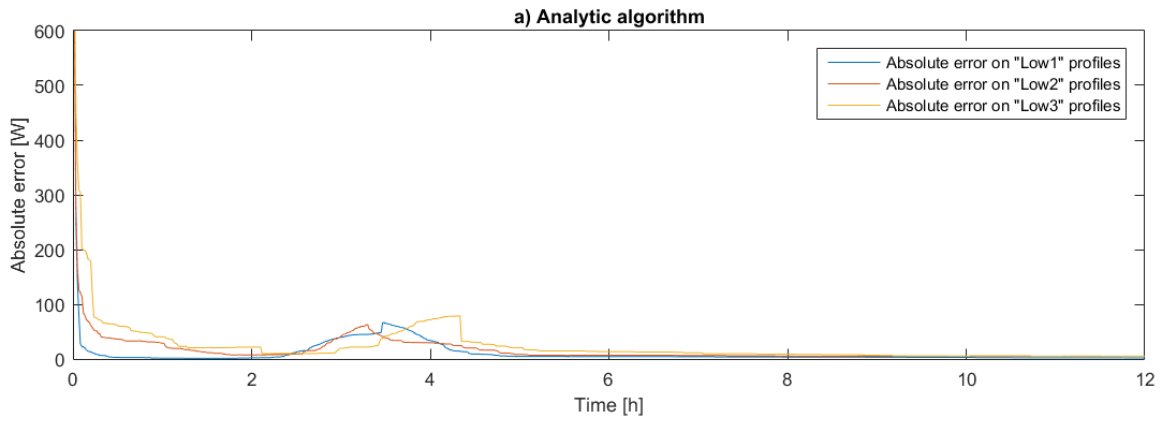


Figure 128 - Absolute error on "Low" load profiles obtained with analytic (a) and ANFIS (b) algorithm

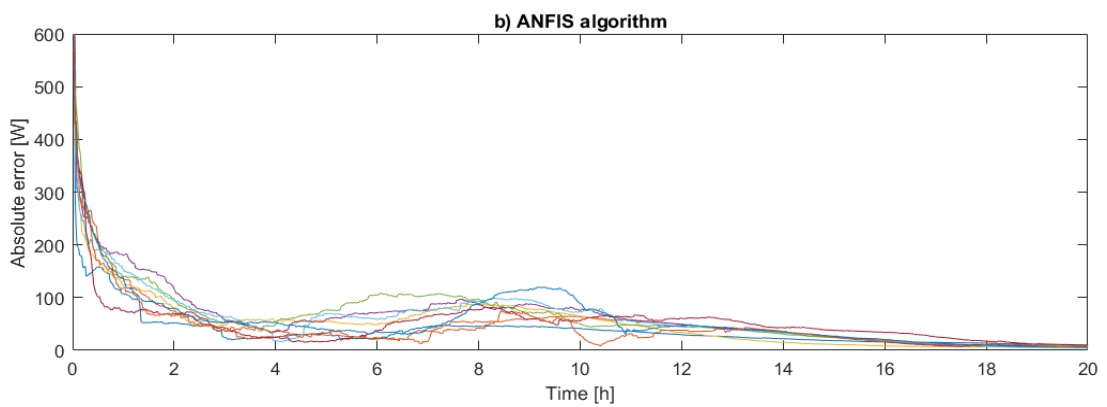
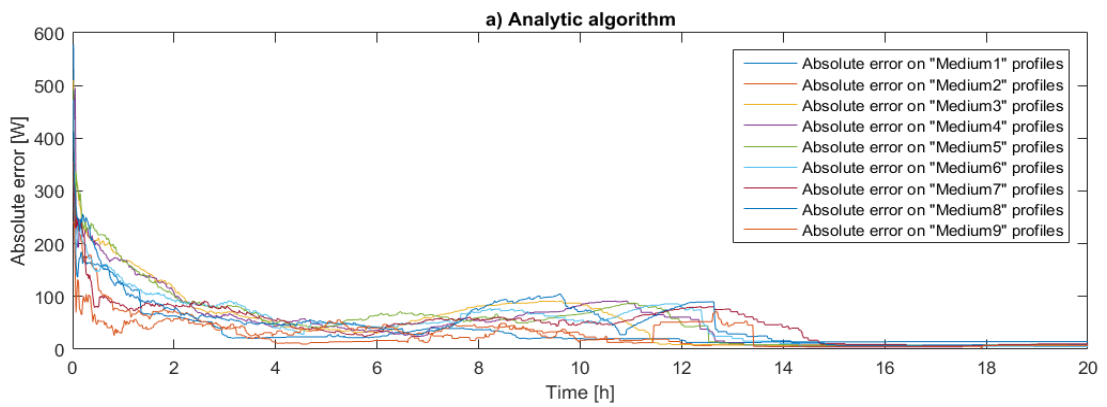


Figure 129 - Absolute error on "Medium" load profiles obtained with analytic (a) and ANFIS (b) algorithm

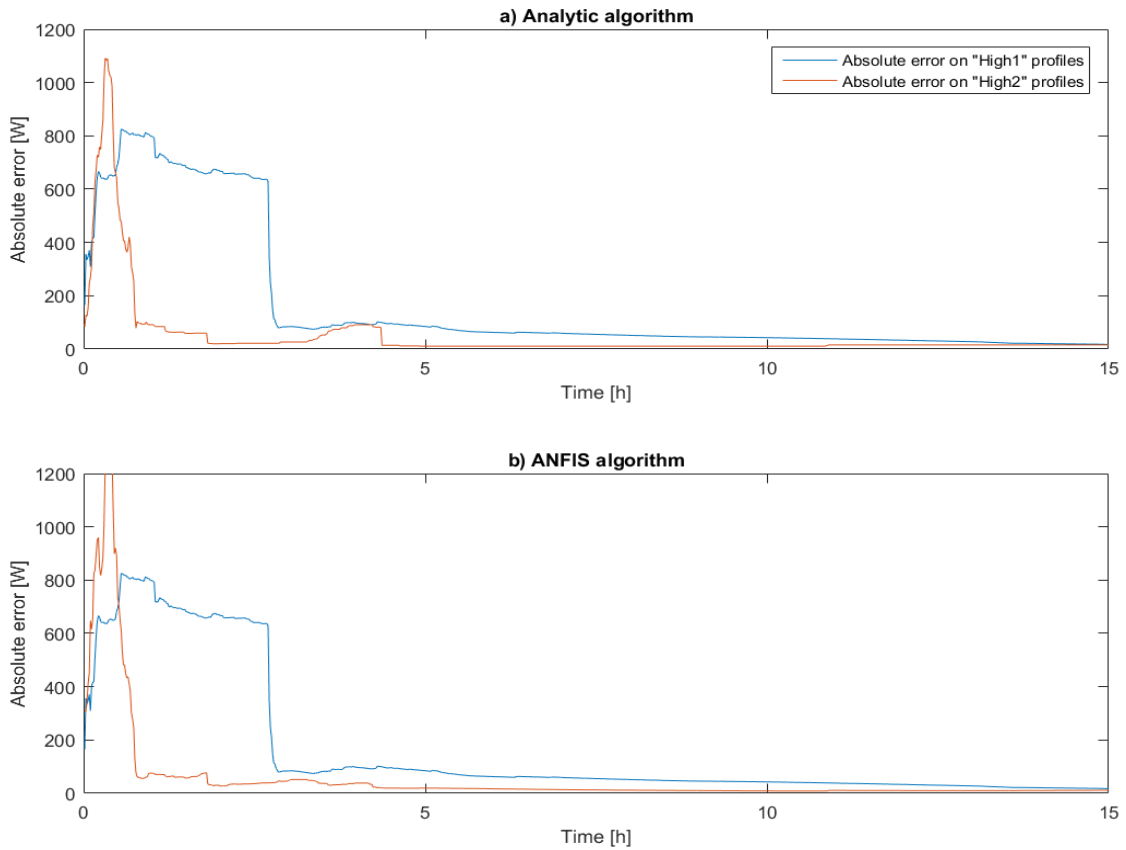


Figure 130 - Absolute error on "High" load profiles obtained with analytic (a) and ANFIS (b) algorithm

From the comparison shown in Figure 128, Figure 129 and Figure 130, the two methods seem to have the same errors; however, the profiles obtained with the averaging procedure are able to approximate the experimental data in a better way than those obtained by applying the ANFIS algorithm. Indeed, as shown in Table 13, for each load class, the overall absolute error of the average profiles, presented in Section 4.7.1, is always lower than the one of the ANFIS profiles (Section 4.7.2), especially concerning the forecasting of the “High” classes profiles.

Table 13: Comparison of the Absolute Error for the analytic and the ANFIS methods

Class	Difference of Energy on analytic profiles [%]	Difference of Energy on ANFIS profiles [%]
Low 1	12.7 %	29.2 %
Low 2	16.5 %	27.3 %
Low 3	19.4 %	20.8 %
Medium 1	30.3 %	34.5 %
Medium 2	21.8 %	36.6 %
Medium 3	34.8 %	35.4 %
Medium 4	30.6 %	38.2 %
Medium 5	30.3 %	35.0 %

Medium 6	25.1 %	29.6 %
Medium 7	22.4 %	24.1 %
Medium 8	21.5 %	24.0 %
Medium 9	11.1 %	16.9 %
High 1	69.5 %	90.9 %
High 2	33.1 %	70.1 %

The higher effectiveness of the averaging procedure is also shown by the comparison of the PRSD values, presented in Table 14.

Table 14: Comparison of the PRSD for the analytic and the ANFIS methods

Class	PRSD on analytic profiles [%]	PRSD on ANFIS profiles [%]
Low 1	13.6%	26.3 %
Low 2	15.3%	23.9 %
Low 3	16.4%	17.7 %
Medium 1	21.7%	26.1 %
Medium 2	18.3%	29.9 %
Medium 3	25.7%	27.8 %
Medium 4	24.2%	31.0 %
Medium 5	24.5%	28.9 %
Medium 6	22.4%	25.8 %
Medium 7	21.7%	26.2 %
Medium 8	19.8%	24.0 %
Medium 9	12.3%	19.6 %
High 1	54.2%	63.9 %
High 2	24.6%	43.0 %

In some cases, especially for the “Medium” classes, the difference between the errors obtained with the two methods is not so high, even if it is clear from a graphical point of view that the profiling algorithm is performing significantly better than the ANFIS one. Indeed, the averaging algorithm is able to represent in a better way the power peaks, while the profiles evaluated by ANFIS are always lower and smoother. However, the two quality indicators used to compare the methods are not able to give an estimation about this specific feature, while it is important that the average profile is able to correctly represent the maximum power reached.

Moreover, considering only the error values related to the profiling method, they are not small because, like the solar irradiance, the user power request is an unpredictable variable, which is often irregular and can vary from a day to another for different reasons. Therefore, to reduce the errors, the classification of the profile should be improved, both by increasing the number of classes and by introducing new classification criteria that could help to take into account other particular features of the power profiles.

4.8 Conclusions

In this Chapter, the analysis of the experimental data monitored on the power production system located in the Cirque de Mafate, in the Reunion Island, was presented. After a short description of the system and an overall analysis of the sources of power and energy production and consumption, the results obtained by applying the averaging procedure, described in Chapter 3, were described. This analytic method was applied for prognostic purposes to the most relevant monitored quantities, such as the fuel cell and electrolyser power, the battery power, the end user load and the solar irradiance. It works on a daily time window by classifying the daily profiles into some categories, according to specific classification criteria, and then evaluating an average profile for each of them.

The procedure was applied on the power data of the fuel cell, the electrolysers and the battery in order to identify the different operating conditions of each device and examine their features. It was, then, applied also on the solar irradiance and on the user load data, in order to examine the historical operating conditions of the system and to build, based on them, the operational profile expected in the future.

Besides the application of the analytic averaging procedure, a forecast based on the ANFIS algorithm was also performed on the user power load data, in order to approximate and predict the experimental daily profiles. The results of the two methods were, then, compared by using the criteria of the Percentage Relative Standard Deviation and the Difference of Energy between the average and the experimental profiles. The errors obtained with the analytic procedure were always lower than those obtained with the ANFIS method, showing the higher effectiveness of the first method. Indeed, the results of the ANFIS are highly dependent on the settings of the algorithm (number and type of membership functions, number of iterations), which are not easy to choose. Moreover, the algorithm is not able to forecast unexpected or abrupt changes in the profiles; therefore, as most profiles (especially those belonging to the “High” classes) are characterized by an irregular shape and unexpected peaks, the resulting ANFIS predictions are not accurate.

Chapter 5: Col du Palet energy system. Profiling of experimental data for prognostics

In this chapter, the proposed prognostic methodology for electrochemical devices was applied on the second available experimental dataset.

In order to perform the profiling and average analysis, the relevant monitored quantities were analysed on a daily time window, profiled in different classes and then, for each of them, an average profile was evaluated, to approximate and represent the features of all the profiles belonging to the class. In this case, the procedure was performed only on the power data of the single devices (fuel cell, electrolyser, battery), as no data about the solar irradiance or the end user load were available.

The chapter is organized in the following way. Section 5.1 presents the description of the system, its operating modes and the experimental dataset available. Section 5.2 shows an overview about the energy produced and consumed in the system and its different sources. In Section 5.3, Section 5.4 and Section 5.5, the profiling analysis and averaging process performed, respectively, on the power data of the fuel cell, the electrolyser and the battery are presented. Section 5.6 presents some final considerations and comments.

For confidentiality reasons, in all the plots, the axis of the ordinates has been omitted.

5.1 System description

The second power production system, whose experimental data were analysed in this work, is a stand-alone installation, located in Peisey-Nancroix, in France, used to supply power to the Col du Palet mountain refuge.

The main components of the power production system are:

- six photovoltaic panels (PV), with nominal power of 2 kW;
- a diesel generator, with nominal power of 4.8 kW;
- twenty-four batteries connected in series, with nominal capacity of 700 Ah;
- a proton exchange membrane fuel cell (PEMFC), with nominal power of 2.5 kW;
- an electrolyser, with nominal production of 500 l/h of hydrogen;
- two hydrogen tanks, with total capacity of 1700 l and pressure of 33 bars.

In order to supply energy to the end user in a continuous and uninterrupted way, the power produced by the PV is used at first; if this is not sufficient, the power stored in the battery starts to be used. When the state of charge of the battery is too low, the fuel cell is used both to produce the power requested by the user and to charge the battery. Then, in case of lack

of hydrogen or unavailability of some of the components, the diesel generator is turned on in order to provide the remaining power. A simplified scheme is shown in Figure 131.

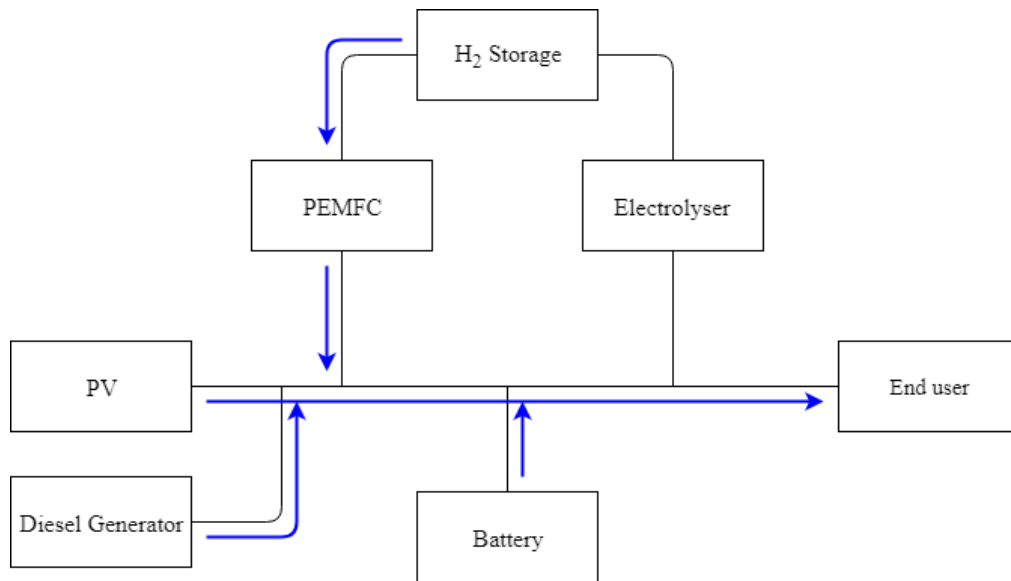


Figure 131 - System scheme in case of lack of PV power

When, instead, the PV production is higher than the end user demand, the excess power is stored in the batteries. If the batteries are completely charged, the power is used to produce and store hydrogen through the electrolyser. A simplified scheme is shown in Figure 132.

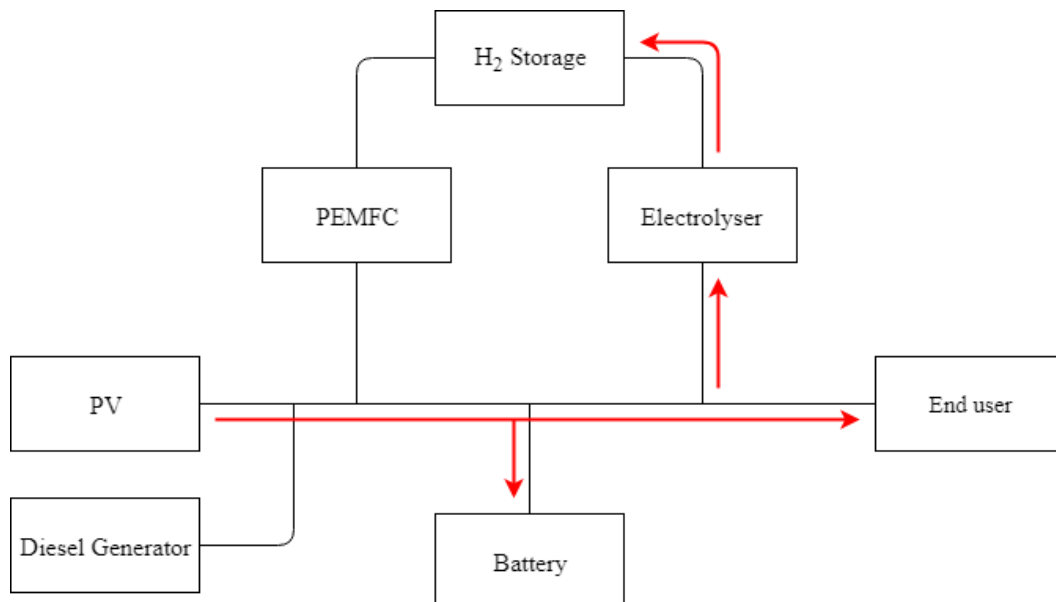


Figure 132 - System scheme in case of excess PV power produced

A monitoring system allows collecting data from the different components, with a sampling time of 2 minutes. The monitored quantities are:

- power consumed by the electrolyser;
- power produced by the fuel cell;
- battery current and voltage;
- external temperature;
- room temperatures of the batteries, the fuel cell and the hydrogen storage.

The available data, collected through the direct measurements on the system, are related to a period of almost two years, from January 2016 to October 2017, corresponding to 640 days. This allows analysing the system data on a seasonal basis, in order to compare the behaviour of its components in the same operational conditions and identify, in some cases, periodical features.

5.2 Energy balance and power consumption

In this Section, an analysis of the different sources of power production and consumption is presented. The monthly energy balance between the production terms (denoted with positive values) and the consumption terms (denoted with negative values) is shown in Figure 133 and Figure 134, for the data of the year 2016 and 2017, respectively. From the monitored data, no information about the power produced by the PV nor the power consumed by the end user is available.

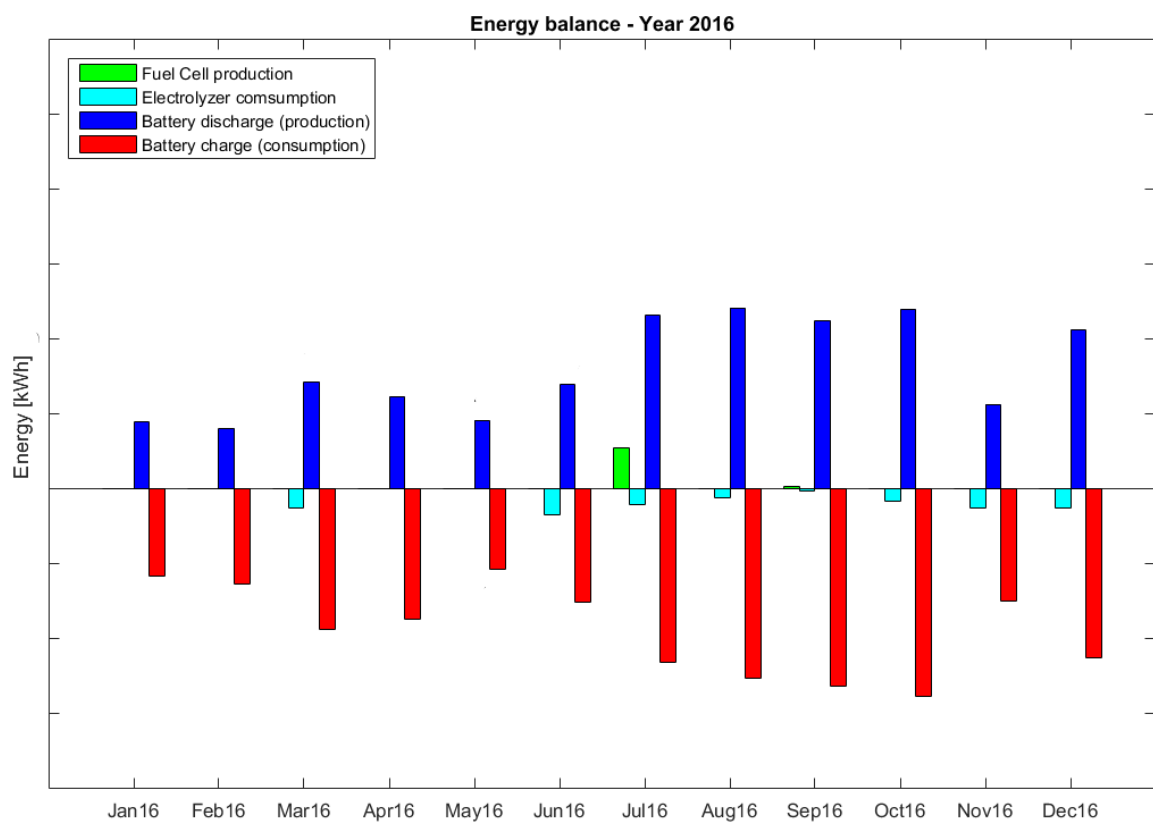


Figure 133 - System energy balance (year 2016)

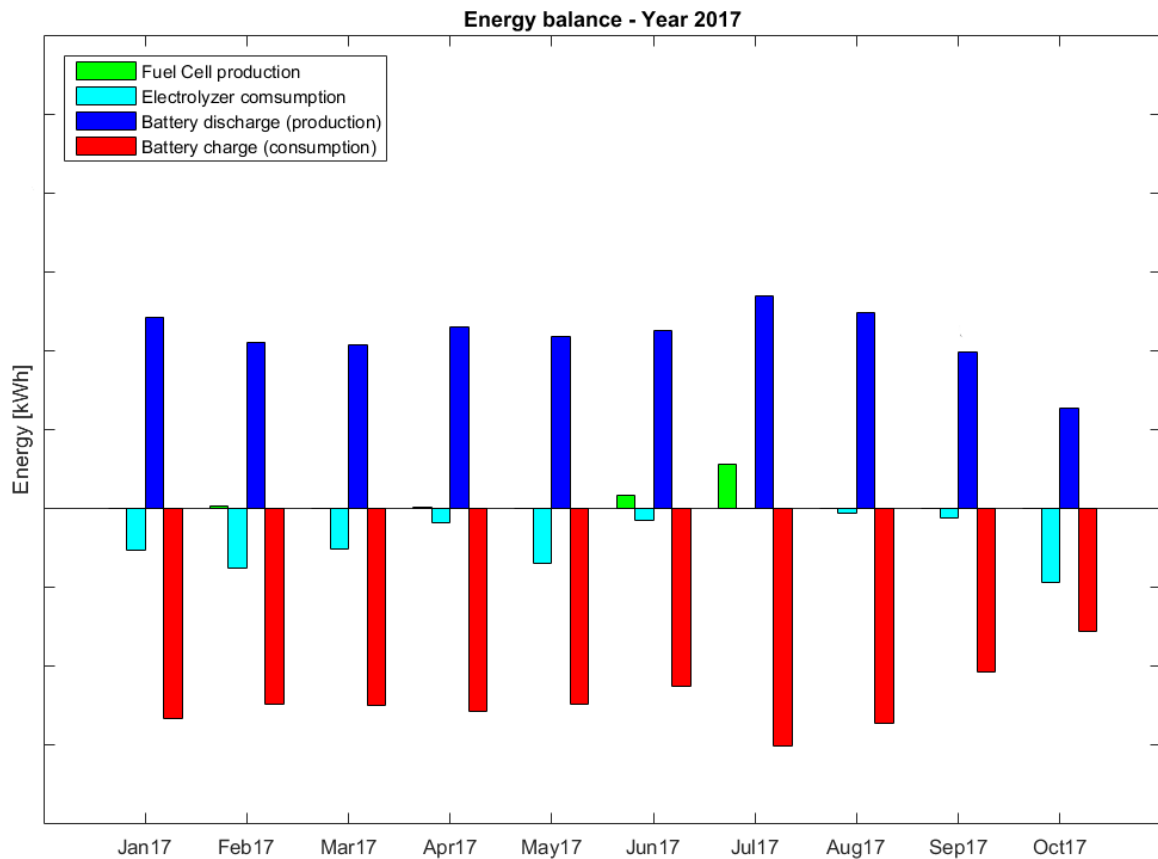


Figure 134 - System energy balance (year 2017)

The power produced or consumed by the batteries, the electrolyser and the fuel cell during the whole monitored period are respectively shown in Figure 135, Figure 136 and Figure 137. These plots give information about the utilization of the different devices during the year. The battery shows a continuous operation that is almost constant during the whole year. The electrolyser has, instead, an operation that is not continuous; however, it does not seem to be linked to specific seasons, as its behaviour is not similar in the comparison of the same periods between the two years. The only device that shows a seasonal behaviour is the fuel cell, which is running only during the summer, as it is the period in which the mountain retreat is used the most and when a higher amount of energy is needed.

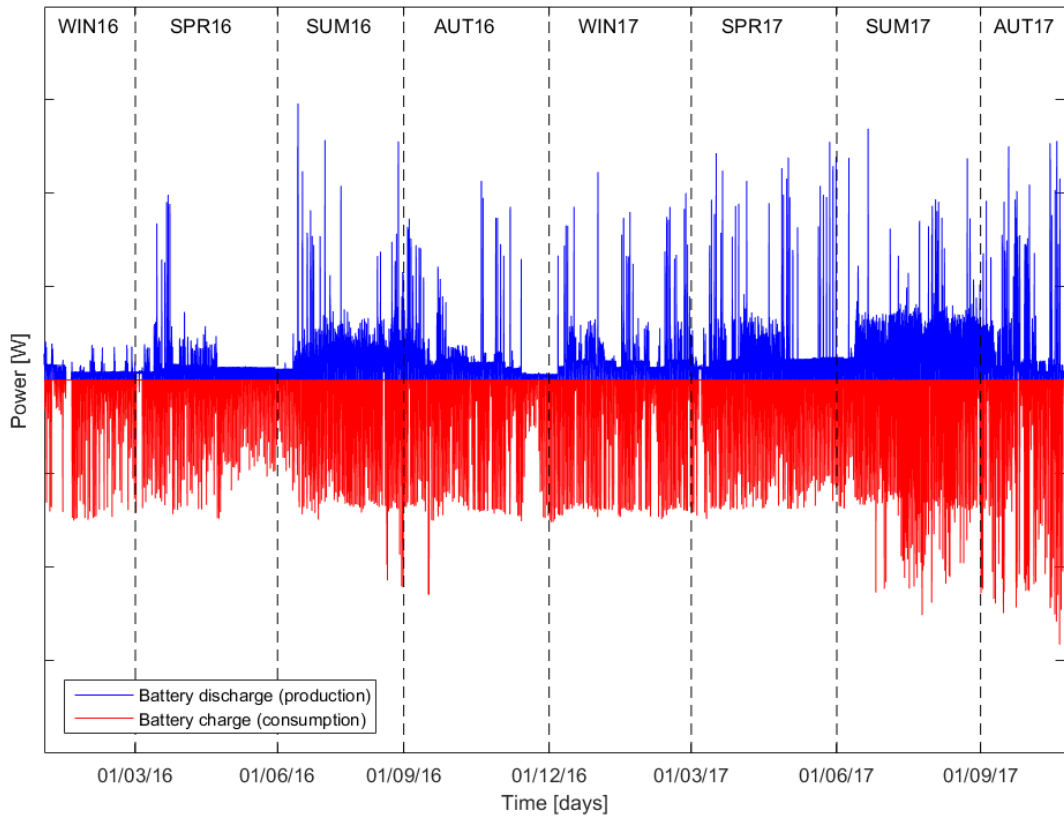


Figure 135 - Battery power production and consumption

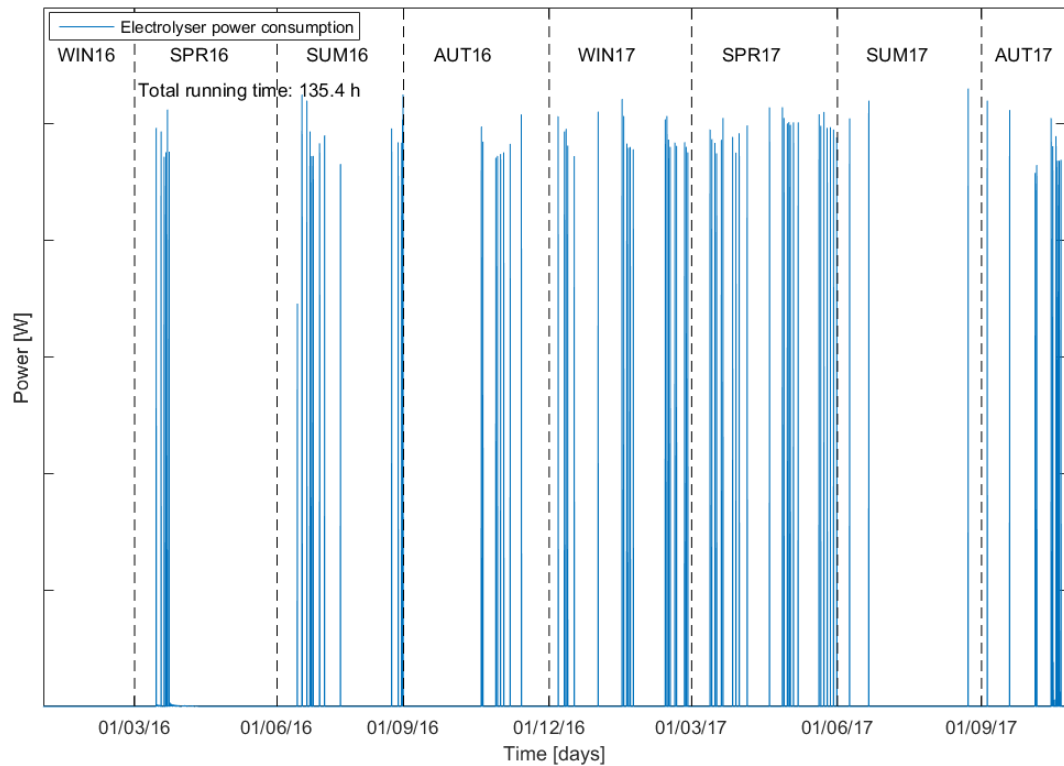


Figure 136 - Electrolyser power consumption

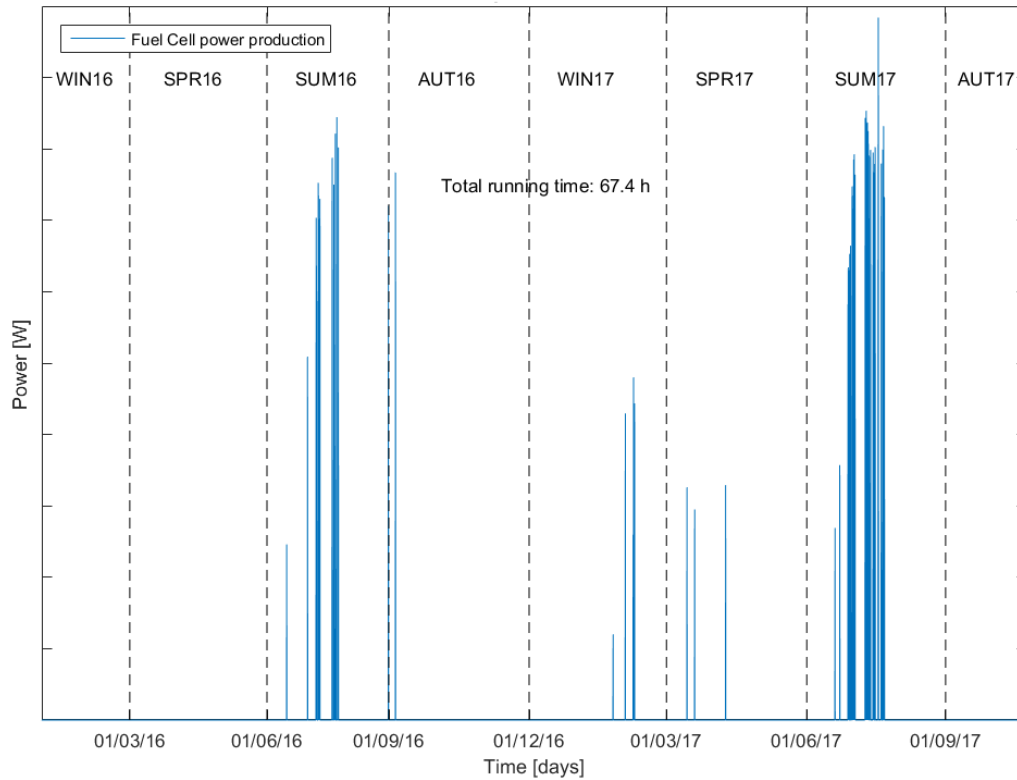


Figure 137 - Fuel cell power production

5.3 Fuel Cell power profiles

In this Section, the analysis of the experimental data about the power produced by the fuel cell is presented. The power data were analysed and the different kinds of daily profiles were defined, classified and averaged. In particular, the average profiles were built by using the data collected during the year 2016 and, then, they were compared with the data measured in the year 2017, to understand if they could represent a good approximation of the future behaviour of the device.

As seen in Section 5.2, the fuel cell is running each year only during the summer, which is the season with the highest energy request. As shown in Figure 138, the running time during each year is approximately 30 hours, corresponding to 13 days in 2016 and 20 days in 2017. However, even if the running time of the device in the two years is similar, the amount of power produced and its profile are very different. This is one of the biggest problems associated to prognostics and highlights the limits of this procedure. Indeed, even if it is reasonable to assume that the power profile of a device, measured during a year, will be repeated in a similar way in the following one, this is not always true as the yearly profiles can vary in a significant way. This difficulty can explain the high errors that were found, in some cases, during the prognostics attempt presented in Section 5.3.2.

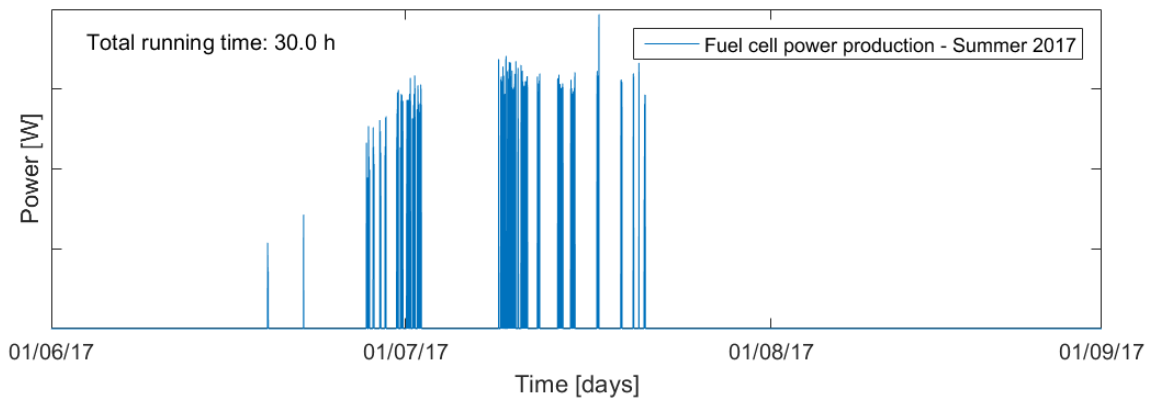
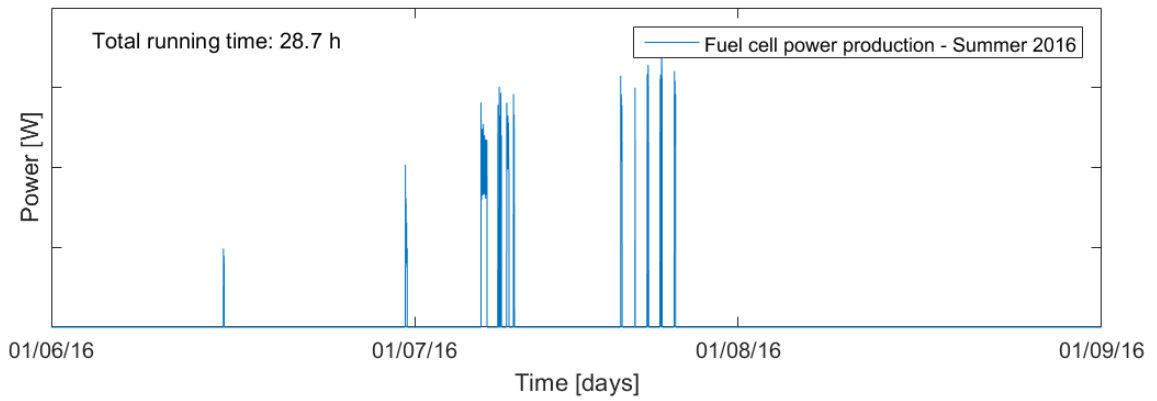


Figure 138 - Fuel cell power production in summer 2016 and 2017

The two yearly profiles were, first, ordered from the highest to lowest value of the power; their difference and the absolute standard deviation between them are shown in Figure 139 and Figure 140. The time scale was cut because, for most of the time, the power is zero. The overall absolute error between the two profiles was 31.4 %.

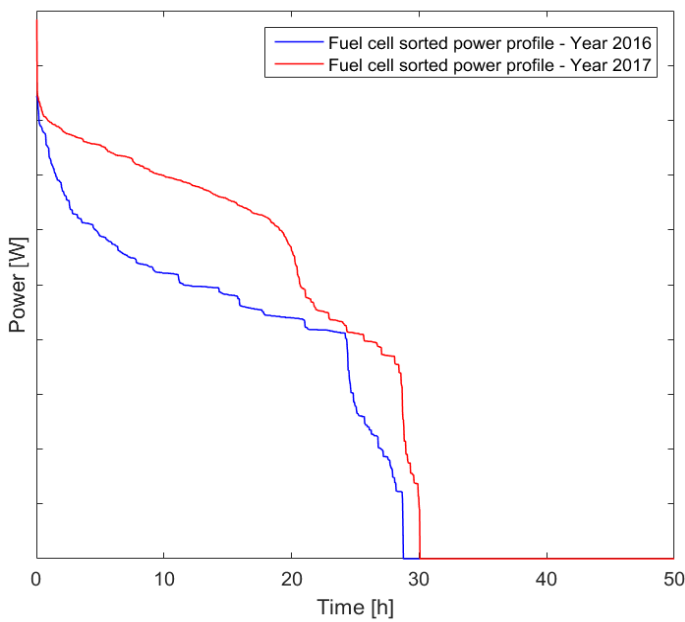


Figure 139 – Comparison between the fuel cell profiles of 2016 and 2017

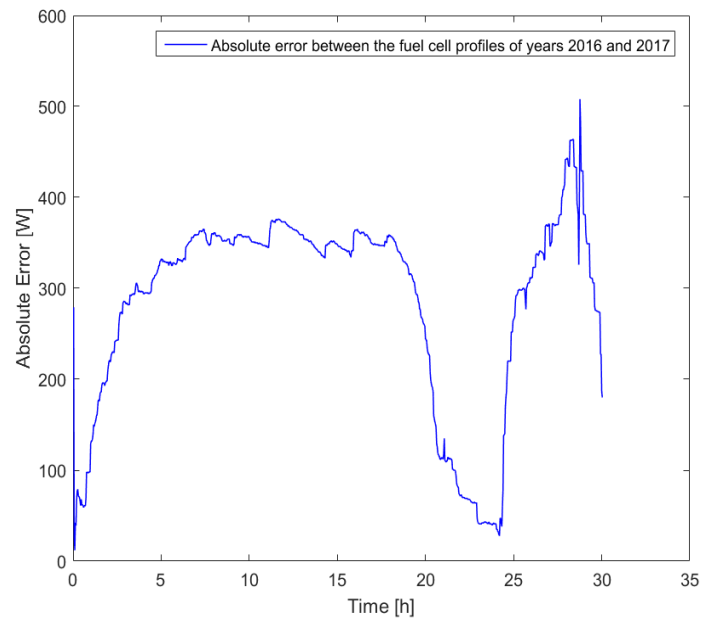


Figure 140 - Absolute standard deviation between the fuel cell profiles of 2016 and 2017

The classification of the daily profiles was based on two criteria. The first one was the running mode, divided in “*continuous*”, if the device worked continuously for more than 20 minutes, and “*discontinuous*”, if the behaviour was characterized by intermittent runs, whose durations were lower than 20 minutes. Then, in each of these two categories, the profiles were further divided according to the daily produced energy. The features of the generated classes are shown in Table 15, together with the percentage of occurrence of each profile during the first year of operation.

Table 15: Fuel cell power profiles classes

Class	Running mode	Daily Energy (DE) [kWh]	Percentage on year 2016 [%]
C1	Continuous	$DE < 2$	1.2 %
C2	Continuous	$2 < DE < 4$	0.9 %
C3	Continuous	$DE > 4$	0.6 %
D1	Discontinuous	$DE < 0.6$	0.6 %
D2	Discontinuous	$DE > 0.6$	0.6 %

In order to average the “continuous” and “discontinuous” kinds of profile, two different procedures were used. For the C-class profiles, the general averaging procedure, described in Section 3.2, was applied. Instead, the averaging procedure used for the D-class profiles was the same as the one used for the averaging of the “High” user profiles classes (described in Section 4.7.1.3):

- First, the values of the power for each day were sorted in descending order (from the highest to the lowest value of the power), together with the corresponding time instants.
- For each point of the sorted profile, the mean values of the power and of the corresponding time were evaluated.
- By sorting again the values in ascending order according to the value of the time (from the lowest to the highest), the average power profile was obtained.

5.3.1 Year 2016 power data

The averaging procedure was applied to the 13 experimental profiles of the year 2016. The average profile of each class, compared with one of the corresponding experimental profiles, are shown in the plots from Figure 141 to Figure 145. In this plots, the experimental profiles were not represented in the shifted position, but in the real ones.

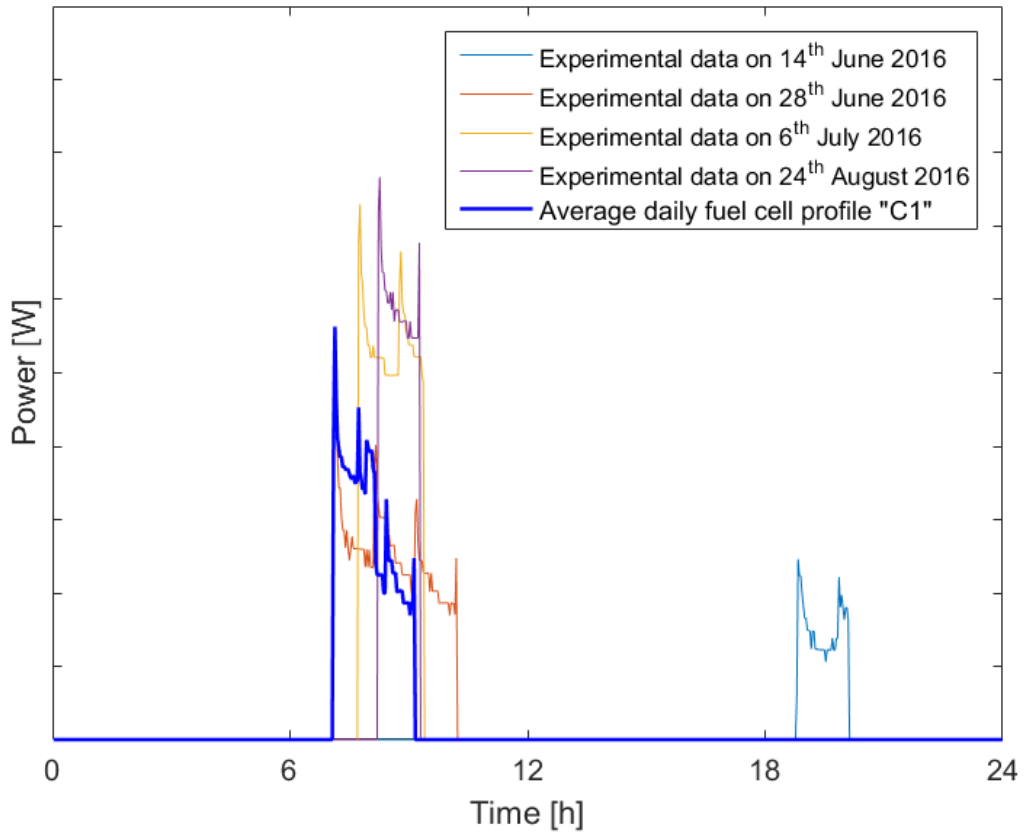


Figure 141 - Average fuel cell power profile "C1"

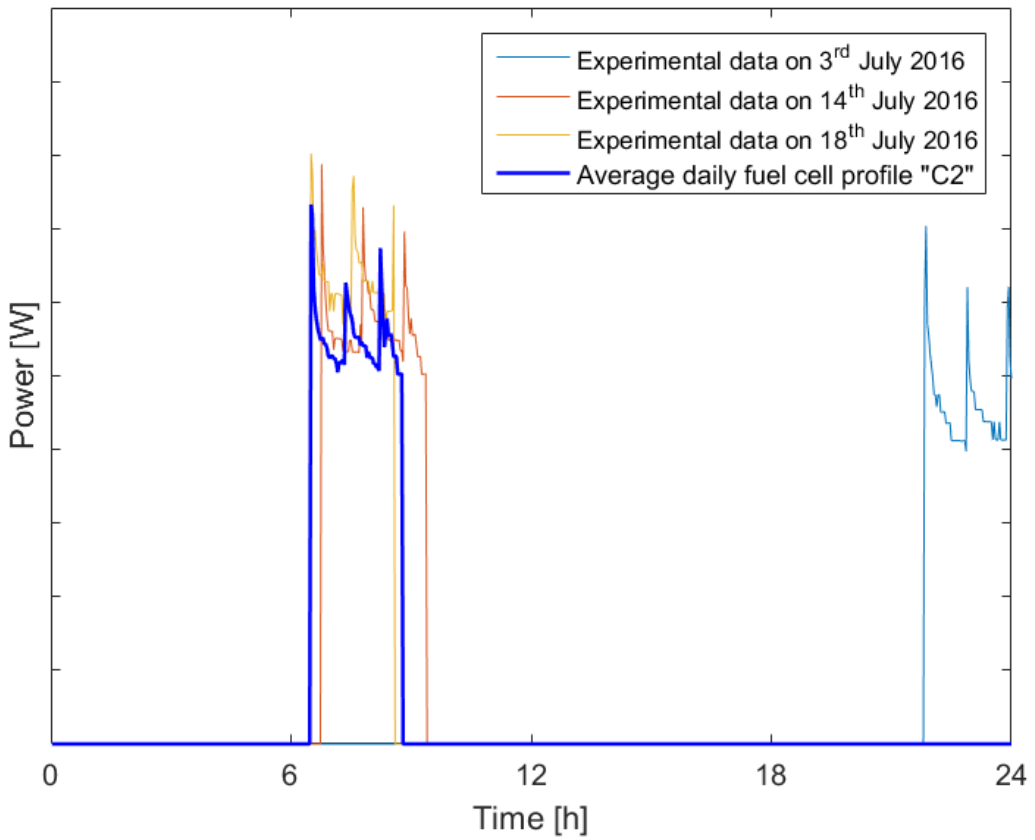


Figure 142 - Average fuel cell power profile "C2"

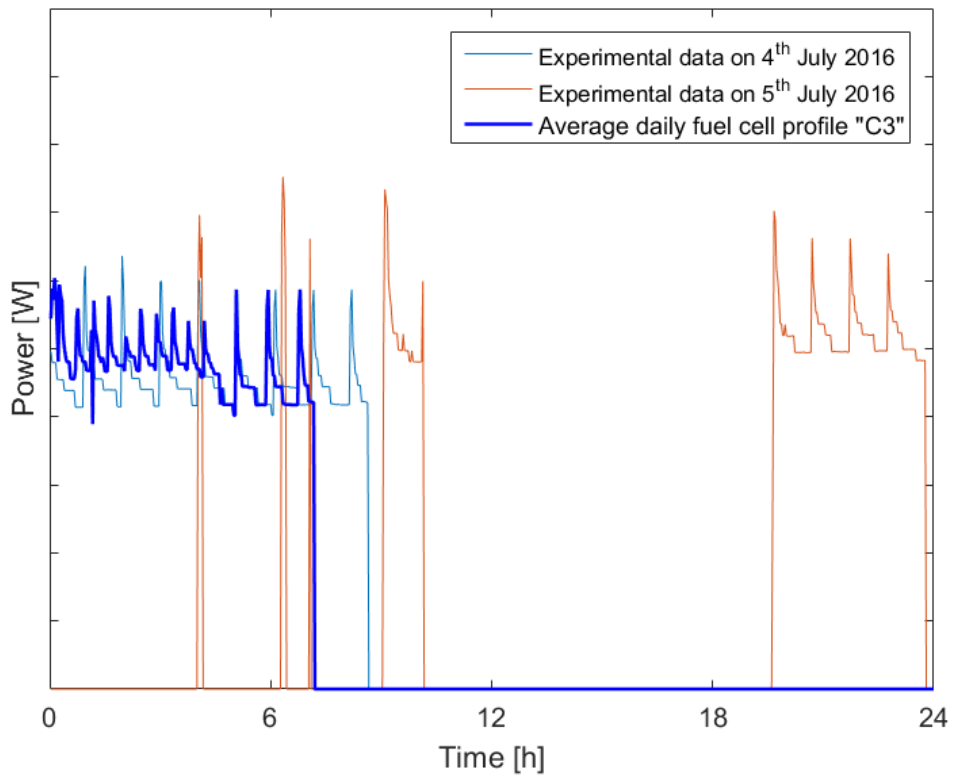


Figure 143 - Average fuel cell power profile "C3"

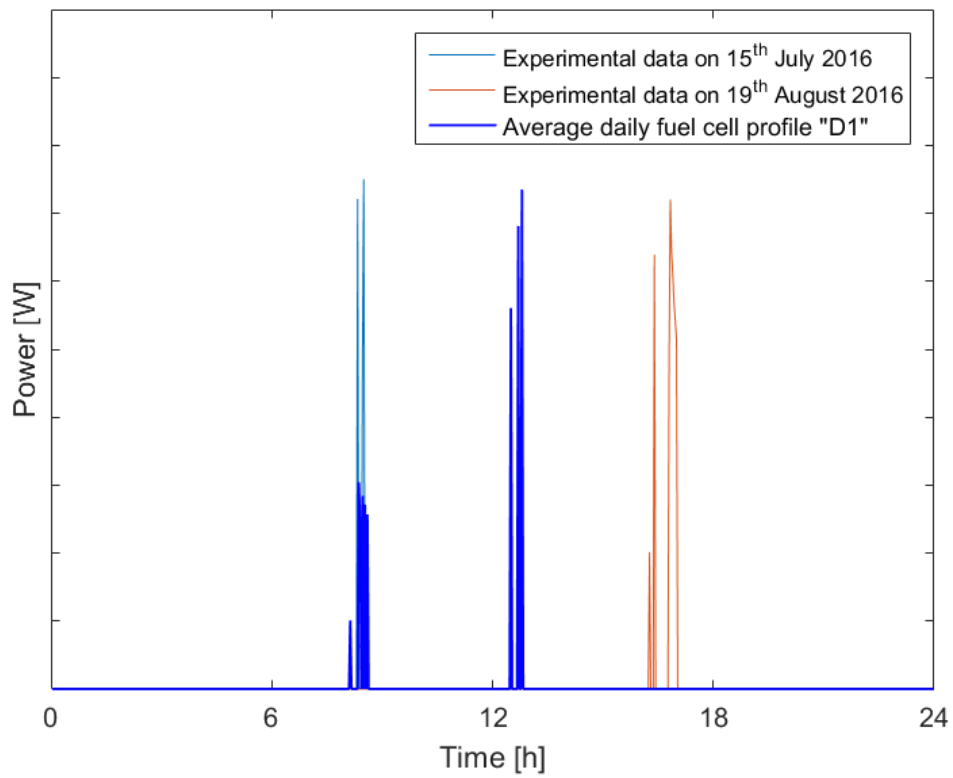


Figure 144 - Average fuel cell power profile "D1"

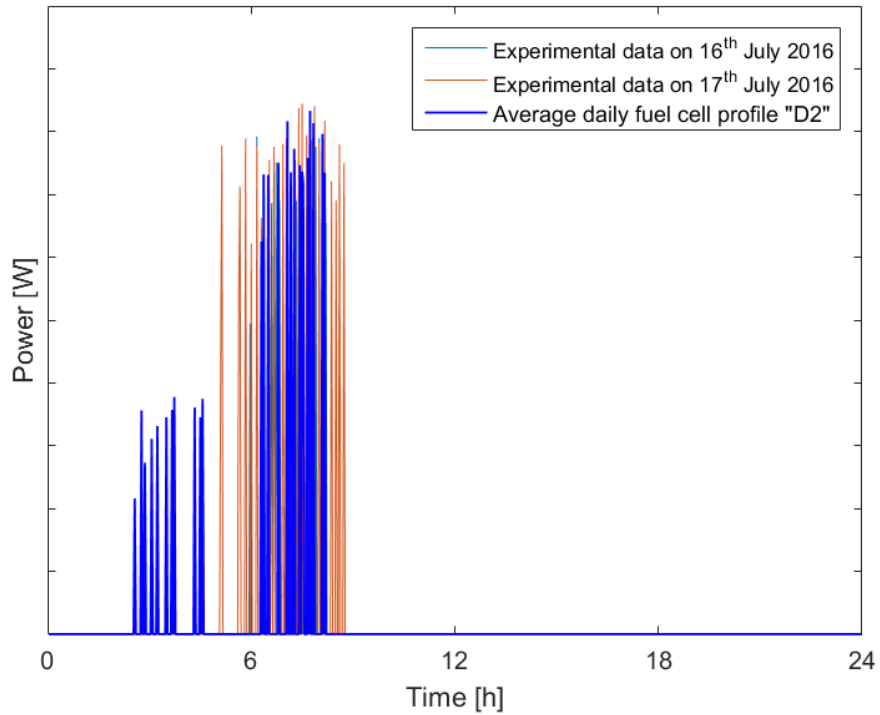


Figure 145 - Average fuel cell power profile "D2"

For the quality evaluation of the average profiles of each class, the profiles were sorted, representing the power from the highest to the lowest value, as shown for instance in Figure 146 for the power profiles of the class "C1". Then, the quality indicators were evaluated at each time, so that an error profile could be built as in Figure 147 for the PRSD profile of the class "C1". The time scale is cut, because the durations of the profiles are not covering the whole day.

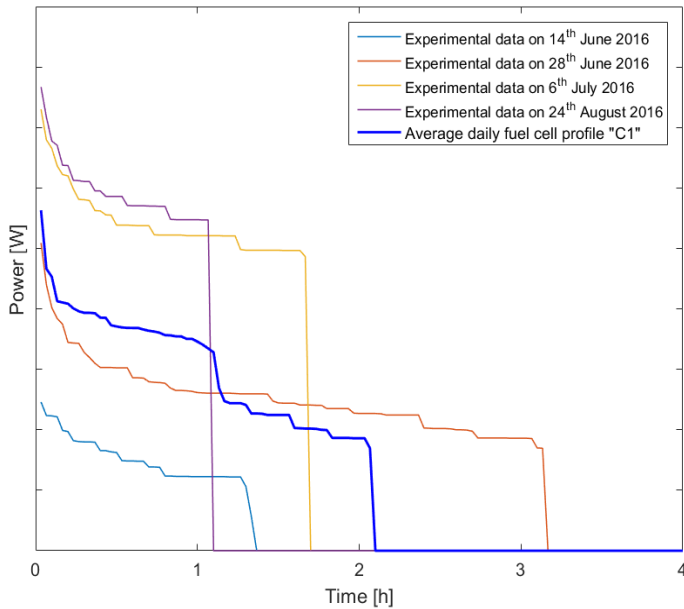


Figure 146 - Sorted profiles of the class "C1"

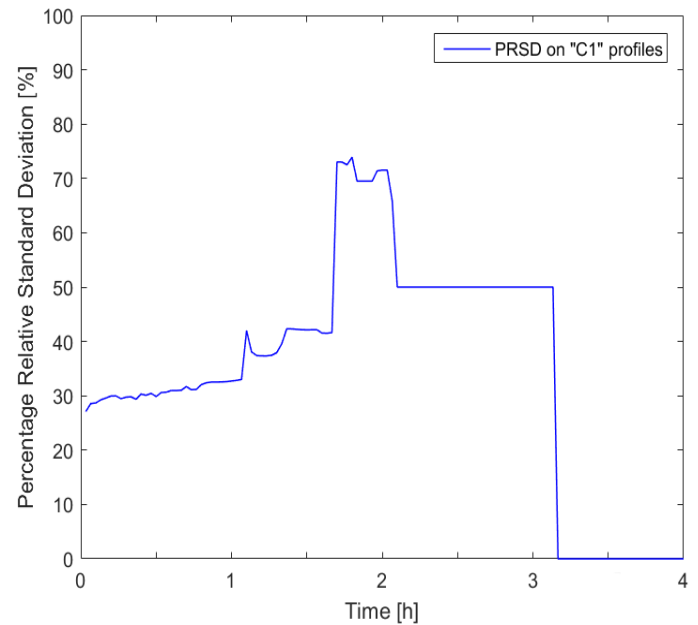


Figure 147 - PRSD on fuel cell power profiles of the class "C1"

The PRSD profiles for all the categories are shown in Figure 148. The high values reached at the end of the error profiles are caused by the huge power difference that occurs because of the different durations of the power profiles.

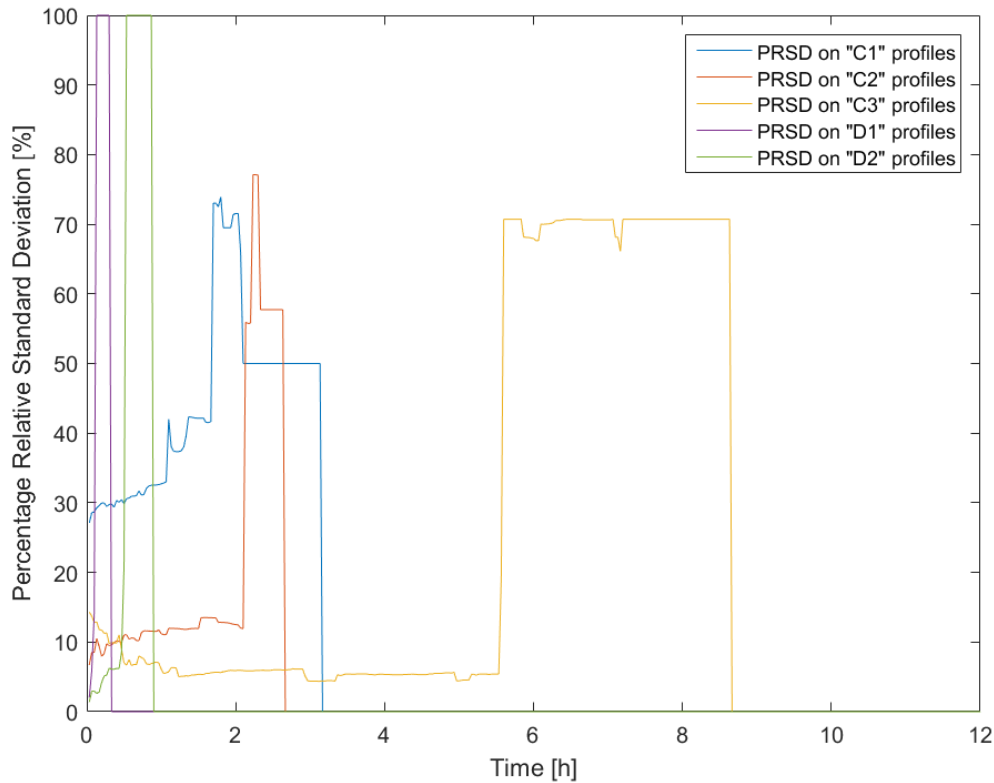


Figure 148 - PRSD of the fuel cell power profiles

The values of the MAPE and the PRSD, evaluated both on the whole profile and on the running time, are shown in Table 16.

Table 16: PRSD and MAPE on fuel cell average profiles

Class	MAPE [%]	PRSD [%]	PRSD on working hours [%]
C1	4.4 %	5.8 %	67.0 %
C2	1.8 %	2.3 %	18.0 %
C3	7.7 %	10.4 %	21.0 %
D1	0.9 %	0.9 %	69.1 %
D2	1.6 %	1.6 %	45.7 %

The PRSD evaluated only on the time when the fuel cell is running is high for all the classes. This is due, as shown for the class “C1” in Figure 146, to the different shapes and durations of the profiles; to solve the problem and improve the results, new classification criteria should be added in order to have a better grouping of the profiles, according to their features.

Figure 149 shows the absolute standard deviation profiles for all the classes. Then, the values of the difference on energy indicator are shown in Table 17.

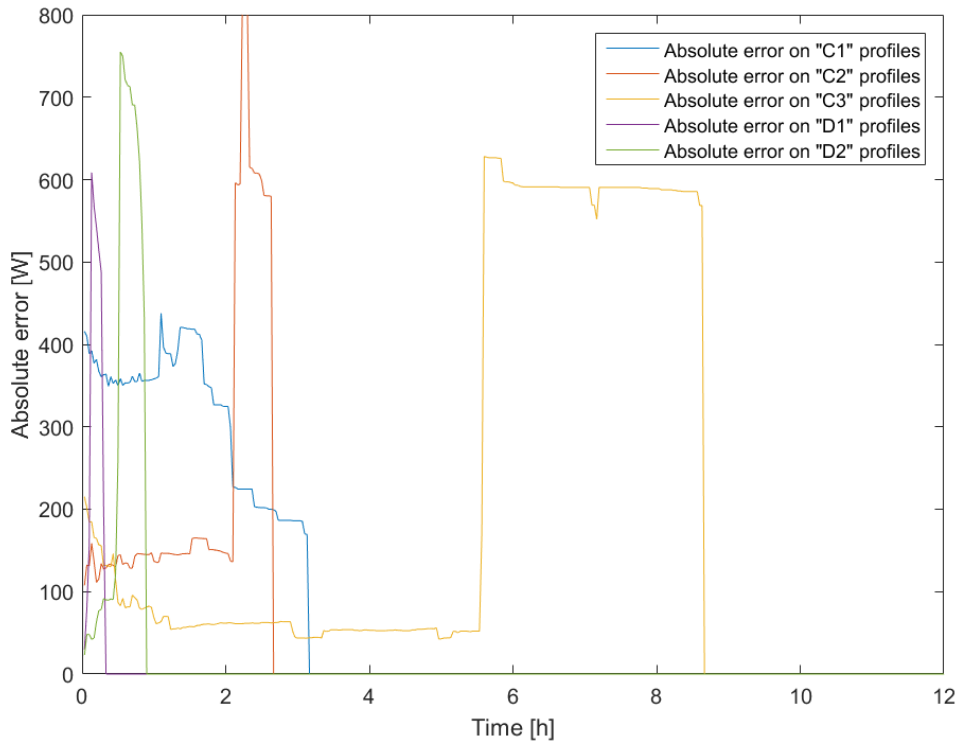


Figure 149 - Absolute error on fuel cell power profiles

Table 17: Difference of Energy on fuel cell average power profiles

Class	Difference on Energy [%]
C1	74.4 %
C2	25.0 %
C3	31.9 %
D1	46.4 %
D2	28.6 %

The values of the absolute error are quite high, especially for the “C1” class, as the average profile was not able to represent in an accurate way all the profiles of the category, due to the fact that more energy levels should be introduced and the number of the classes should be increased. However, this was not possible with this kind of dataset, because of the very short running time of the fuel cell over the year. Indeed, being the daily power profiles only 13, to increase the number of classes would mean that most of them would contain only one profile, allowing no more the calculation of an average.

5.3.2 Year 2017 power data

The classification shown in Table 15 was applied to the 20 experimental profiles collected in the year 2017. Most of them were included in the three “discontinuous” classes and just few were assigned to the “C1” and “C2” categories. No profiles were assigned to the class “C3”. For each class, a comparison was made between the experimental profiles of the year 2017 and the average profiles built with the data of 2016, in order to see if they approximate

the real profiles in an acceptable way. The results for some classes (“C1”, “C2” and “D1”) are shown in Figure 150, Figure 151 and Figure 152.

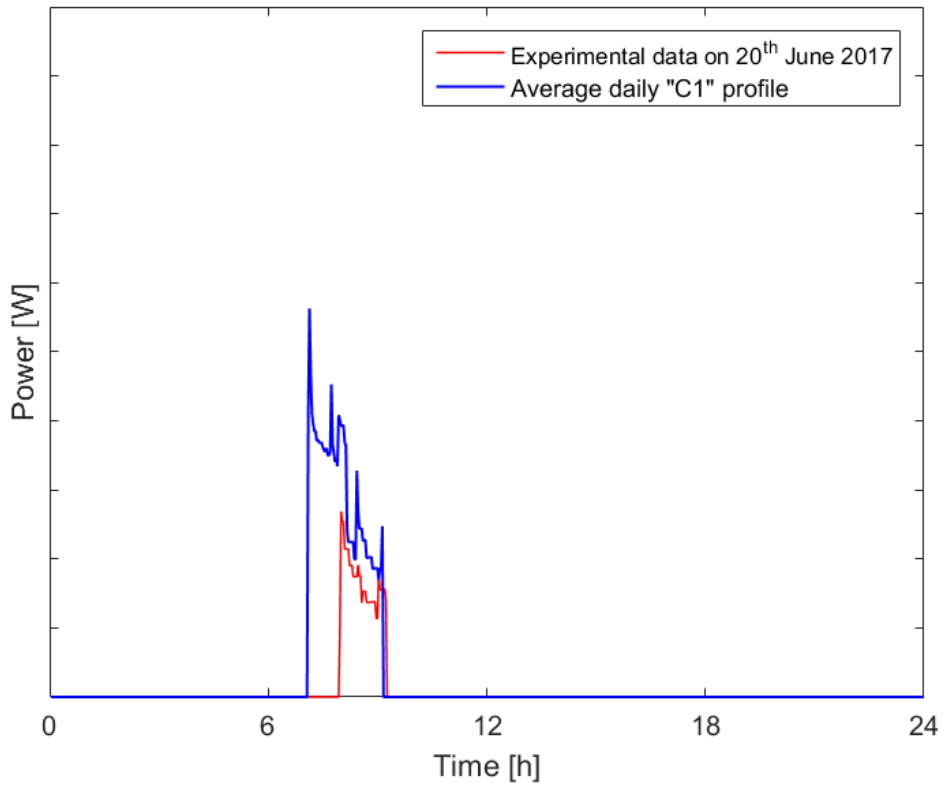


Figure 150 - Comparison between experimental fuel cell profile and average "C1"

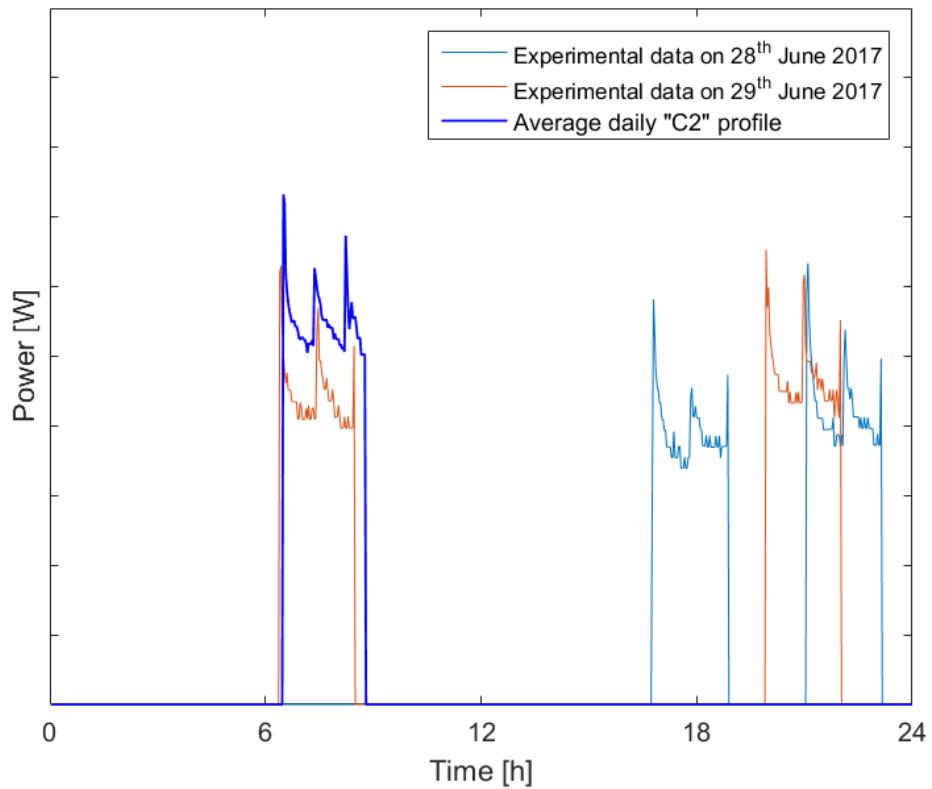


Figure 151 - Comparison between experimental fuel cell profile and average "C2"

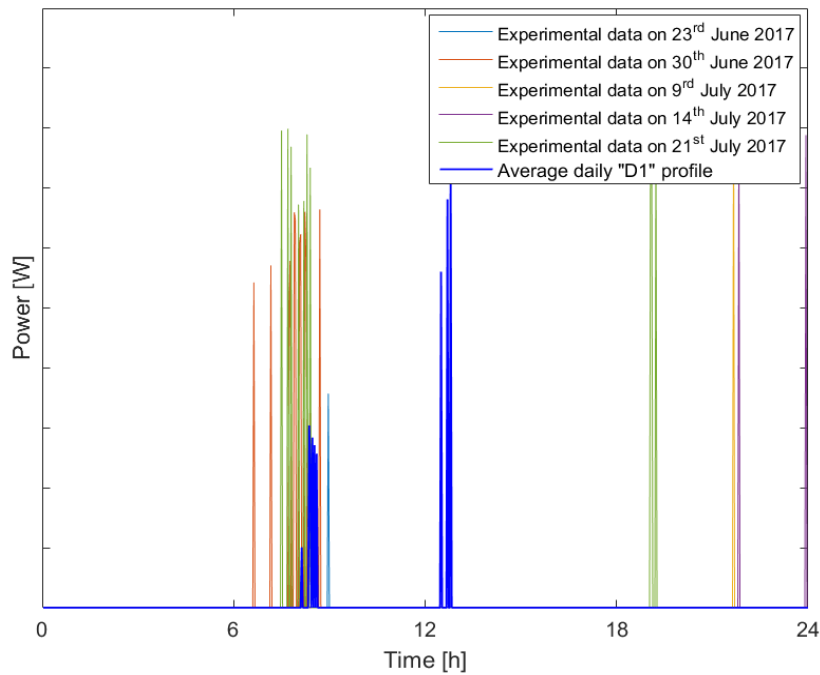


Figure 152 - Comparison between experimental fuel cell profile and average "D1"

The accuracy of the prognostics was evaluated with the standard deviation, in Figure 153, for all the classes compared. The errors are very high as shown also by the values of the Difference of energy, in Table 18. This is because, being the fuel cell behaviour completely different from the first year to the second one, as shown before in Figure 138, the average profiles built with the data of the year 2016 are not able to predict the experimental profiles of the year 2017. These results show that if its main assumption of repeatability of the events is not respected, the event-based prognosis does not give good results.

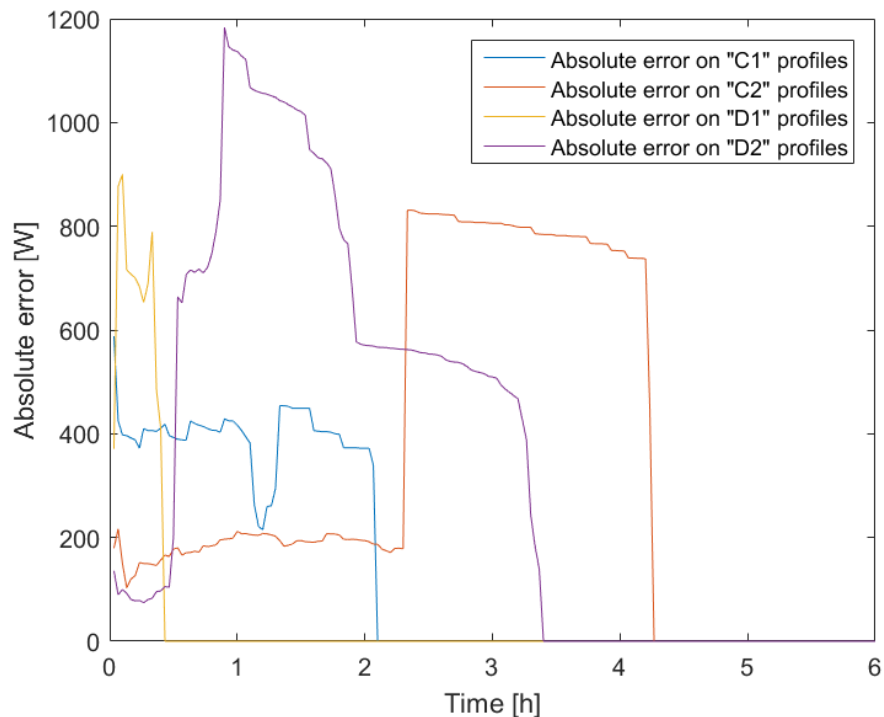


Figure 153 - Absolute error on the compared fuel cell power profiles

Table 18: Difference of energy on the compared fuel cell power profiles

Class	Absolute Error [%]
C1	186 %
C2	53.3 %
D1	112 %
D2	93.0 %

5.4 Electrolyser power profiles

In this Section, the experimental data about the power consumed by the electrolyser are analysed. The daily power profiles were analysed, classified in different categories and then averaged. Also in this case, as done for the fuel cell power profiles, the average profiles were built by using the data collected during the year 2016 and, then, they were compared with the data measured in the year 2017, to evaluate the goodness of the prediction.

However, in this case (as for the fuel cell power shown in Section 5.3), the yearly power profile of the electrolyser monitored during the year 2016 is also very different from the one of the year 2017 (as shown in Figure 154), making the prognosis procedure difficult and inaccurate.

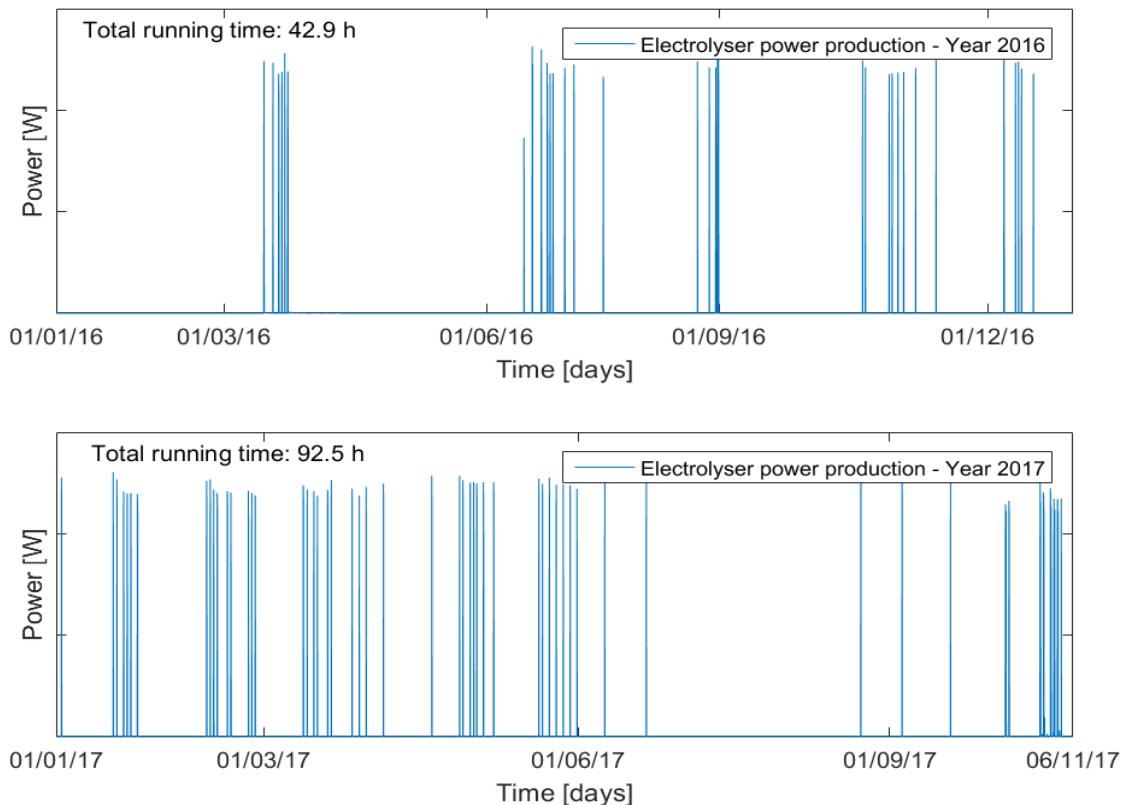


Figure 154 - Electrolyser power consumption in 2016 and 2017

The two yearly profiles were, first, ordered from the highest to lowest value of the power; their difference and the absolute standard deviation between them are shown in Figure 155 and Figure 156. The overall absolute error between the two profiles was 22.0 %.

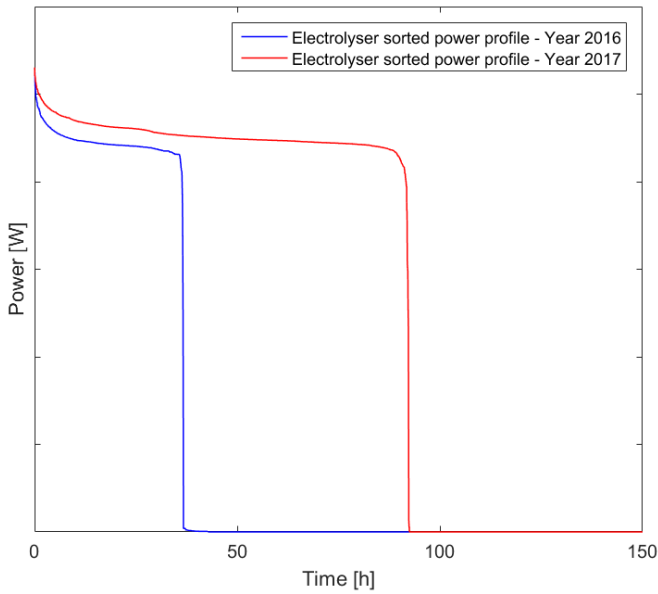


Figure 155 – Comparison between the electrolyser profiles of 2016 and 2017

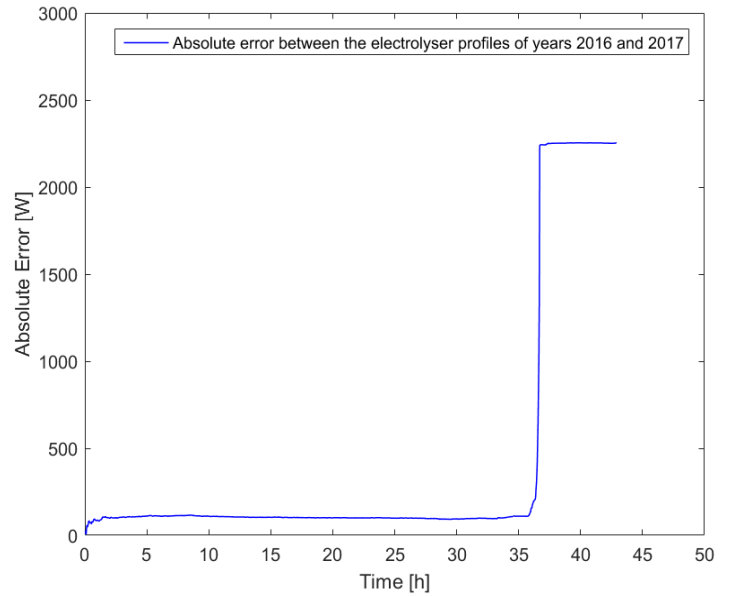


Figure 156 - Absolute standard deviation between the electrolyser profiles of 2016 and 2017

As seen in Figure 154, the electrolyser works in a not systematic way during the year and its behaviour is not linked to the specific season. Indeed, by comparing the power consumed during the same period of the two years, as shown in the plots from Figure 157 to Figure 159, it can be seen that the running time of the device is highly different, showing that there is no specific correlation between the electrolyser behaviour and the seasons.

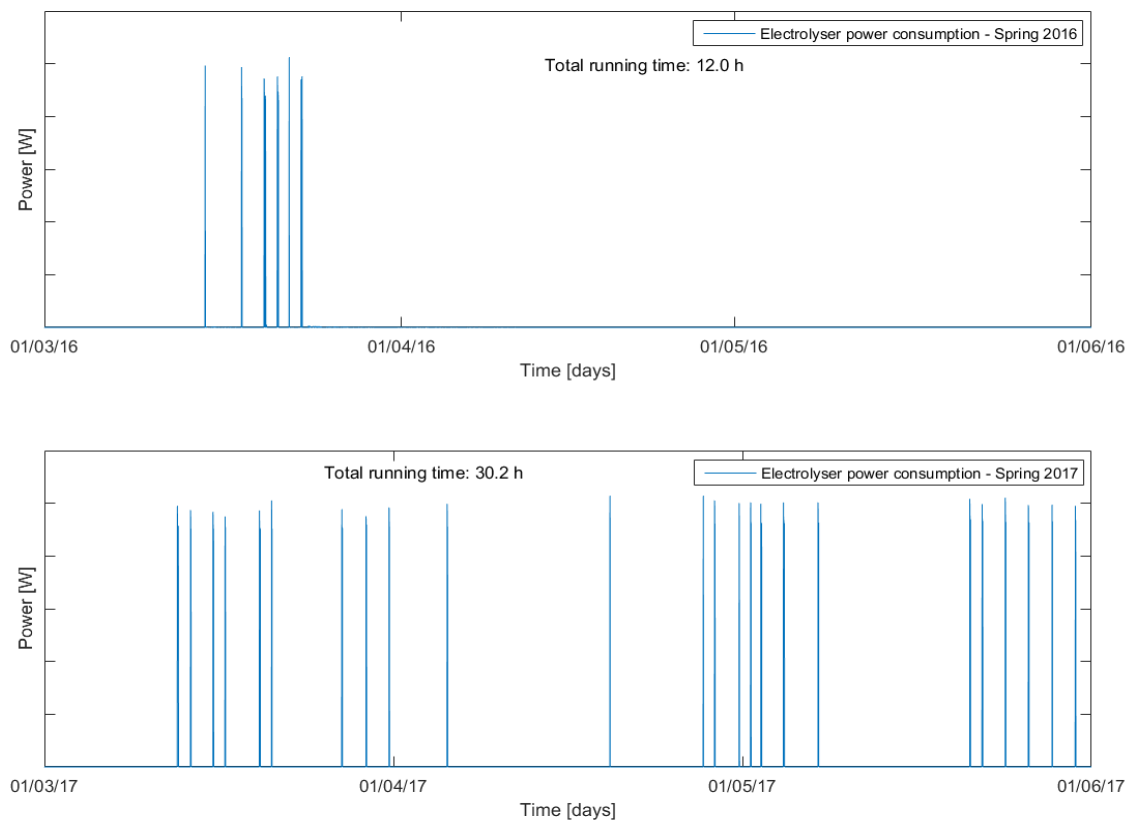


Figure 157 - Electrolyser power consumption in spring 2016 and 2017

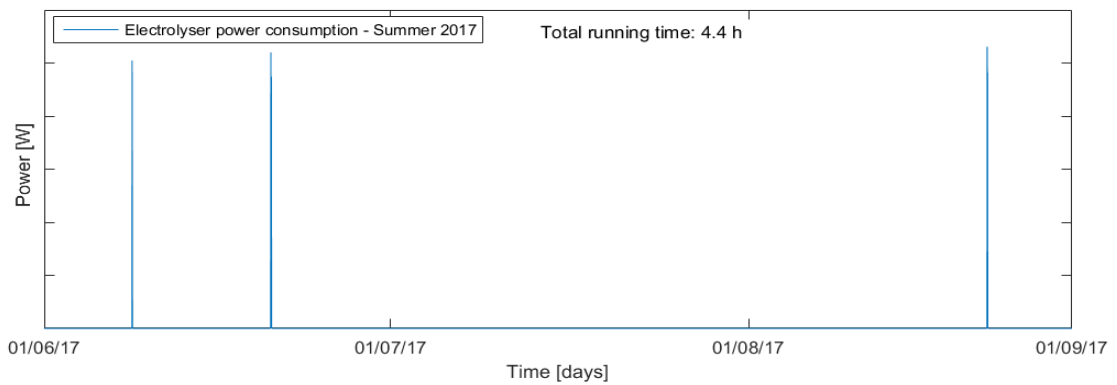
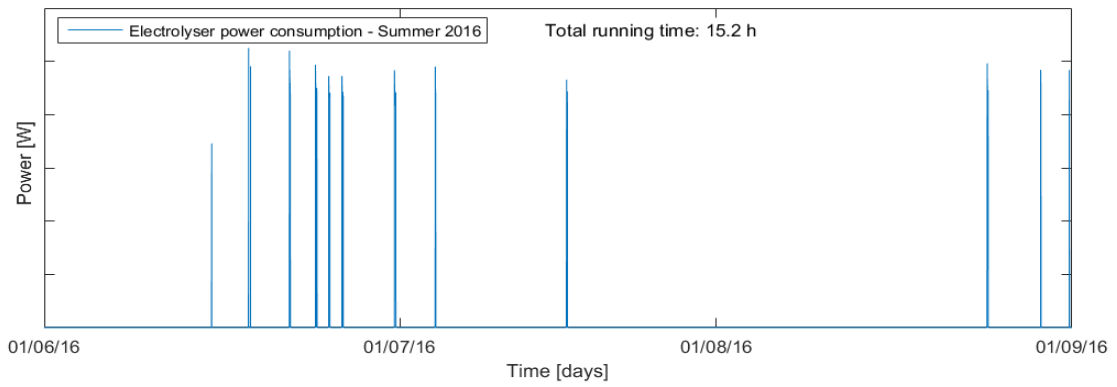


Figure 158 - Electrolyser power consumption in summer 2016 and 2017

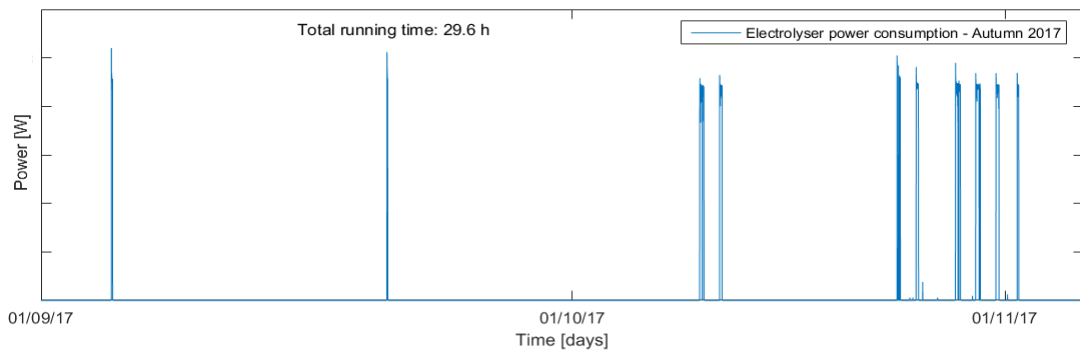
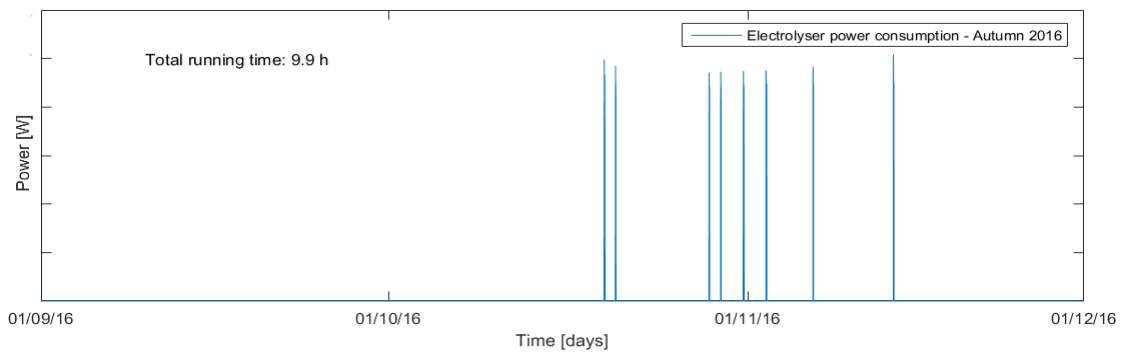


Figure 159 - Electrolyser power consumption in autumn 2016 and 2017

The days of operation of the electrolyser, and therefore the daily power profiles, were 27 for the year 2016 and 59 for 2017. The classification was based on the same two criteria shown in Section 5.3 (running mode and daily energy), and also the averaging process was

the same as the one used for the fuel cell profiles, explained in the same Section. The features of the resulting classes are shown in Table 19, together with the percentage of occurrence of each class in the year 2016.

Table 19: Electrolyser power profiles classes

Class	Running mode	Daily Energy (DE) [kWh]	Percentage on year 2016 [%]
C1	Continuous	DE < 2	1.2 %
C2	Continuous	2 < DE < 3	2.3 %
C3	Continuous	3 < DE < 4	1.7 %
C4	Continuous	4 < DE < 5	0.6 %
C5	Continuous	DE > 5	1.2 %
D1	Discontinuous	DE < 0.6	1.4 %
D2	Discontinuous	DE > 0.6	0.9 %

5.4.1 Year 2016 power data

The averaging procedure was applied to the 27 experimental profiles of the year 2016. Figure 160 to Figure 166 show the average profile of each class, compared with all the corresponding experimental profiles of the class.

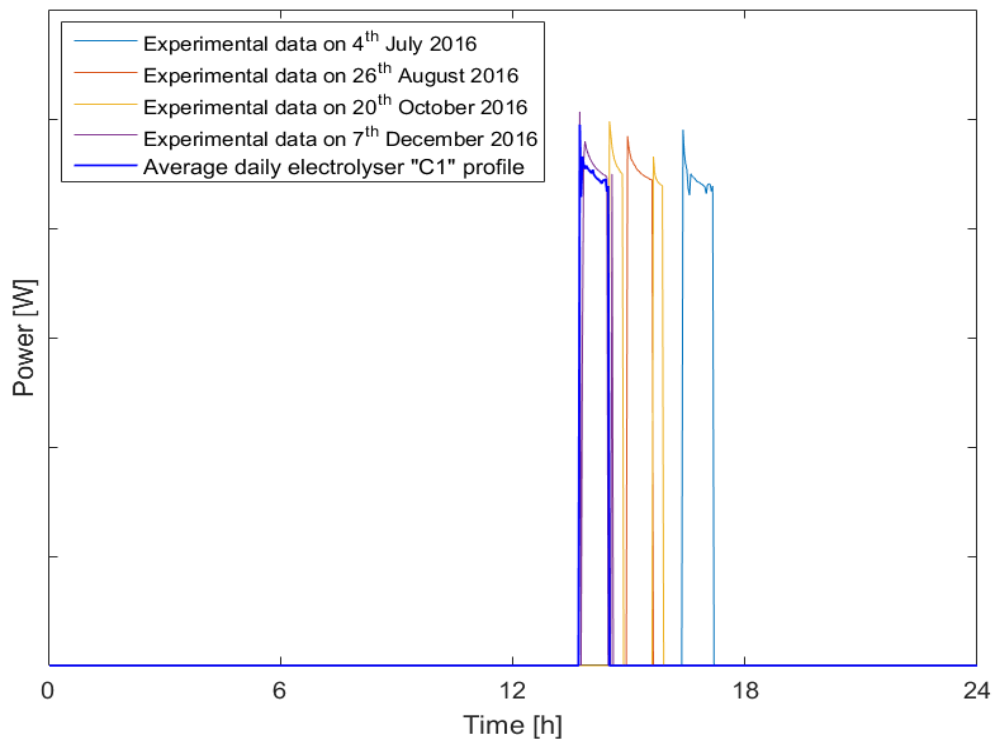


Figure 160 - Average electrolyser power profile "C1"

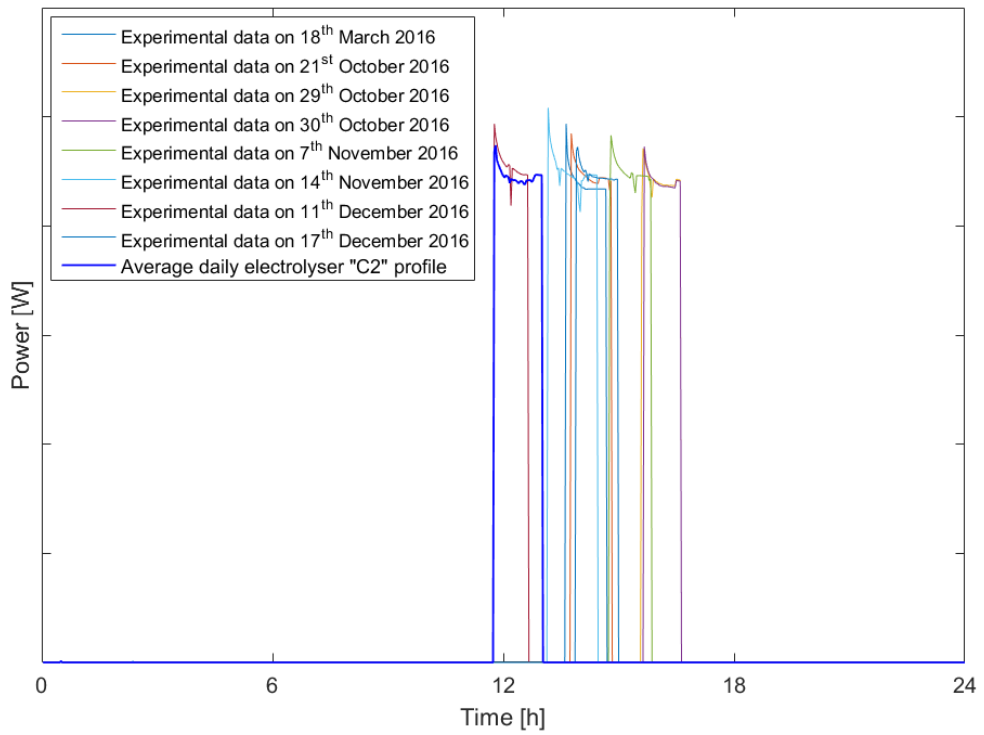


Figure 161 - Average electrolyser power profile "C2"

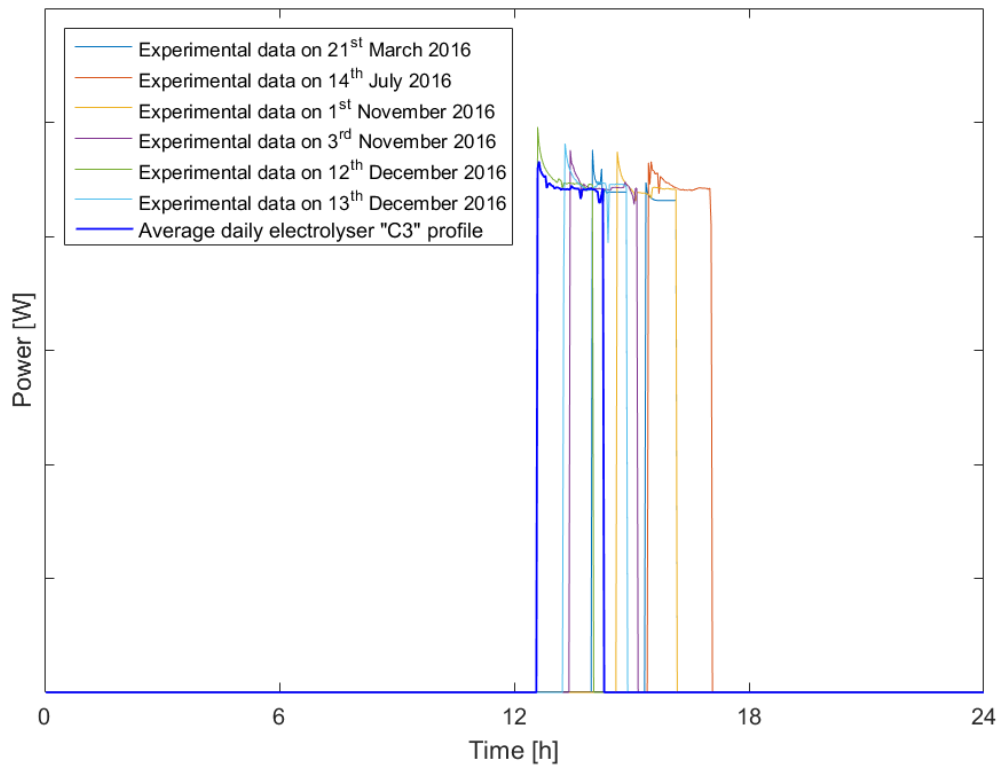


Figure 162 - Average electrolyser power profile "C3"

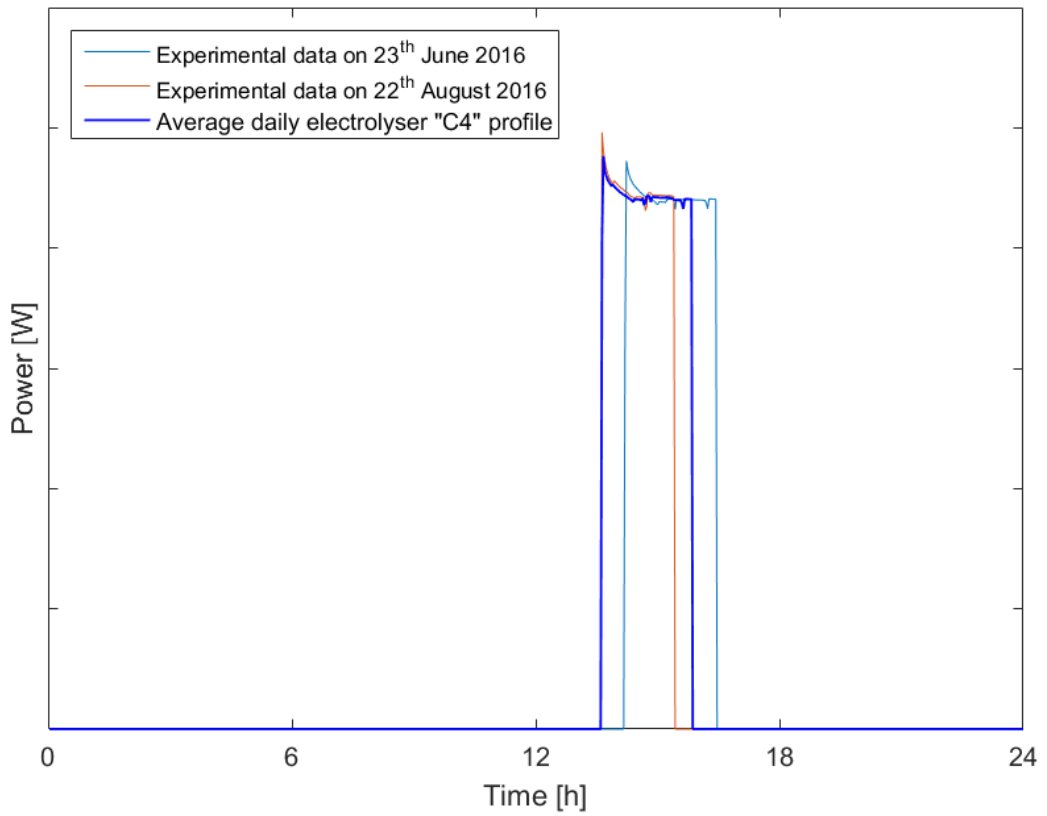


Figure 163 - Average electrolyser power profile "C4"

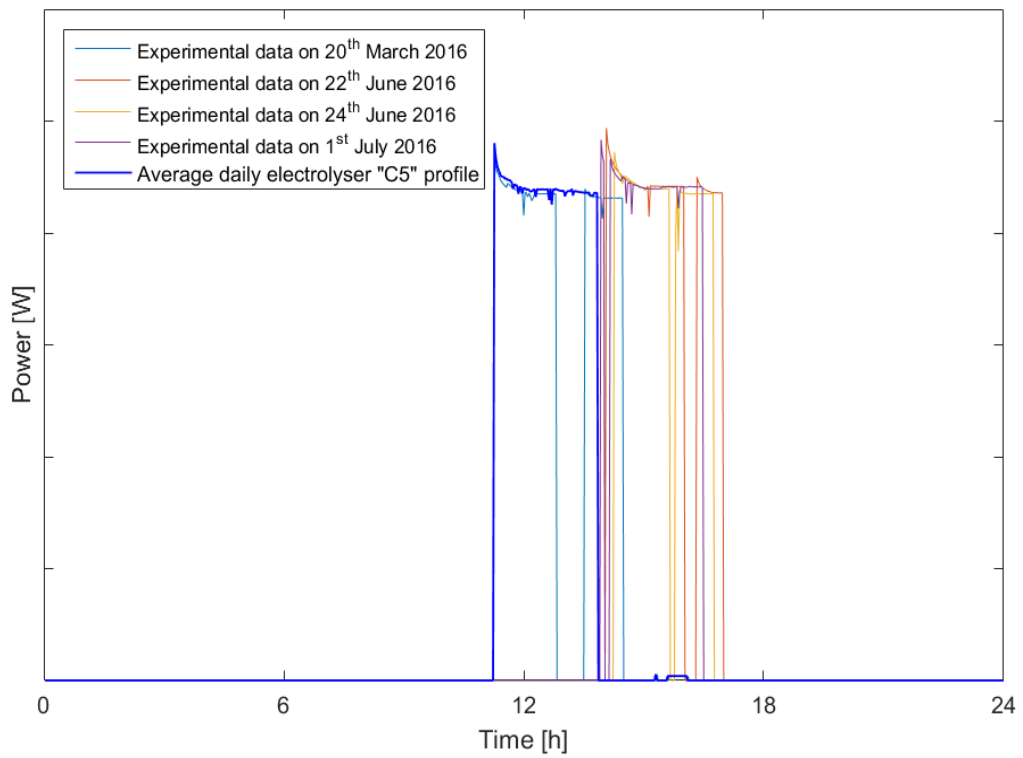


Figure 164 - Average electrolyser power profile "C5"

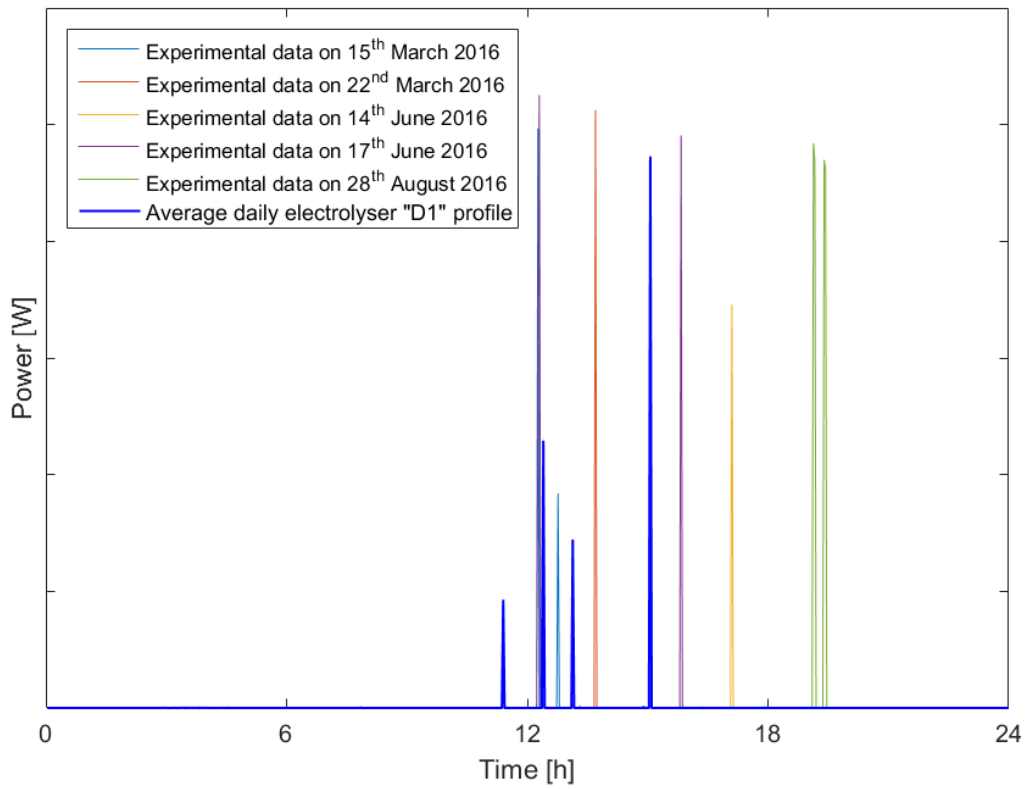


Figure 165 - Average electrolyser power profile "D1"

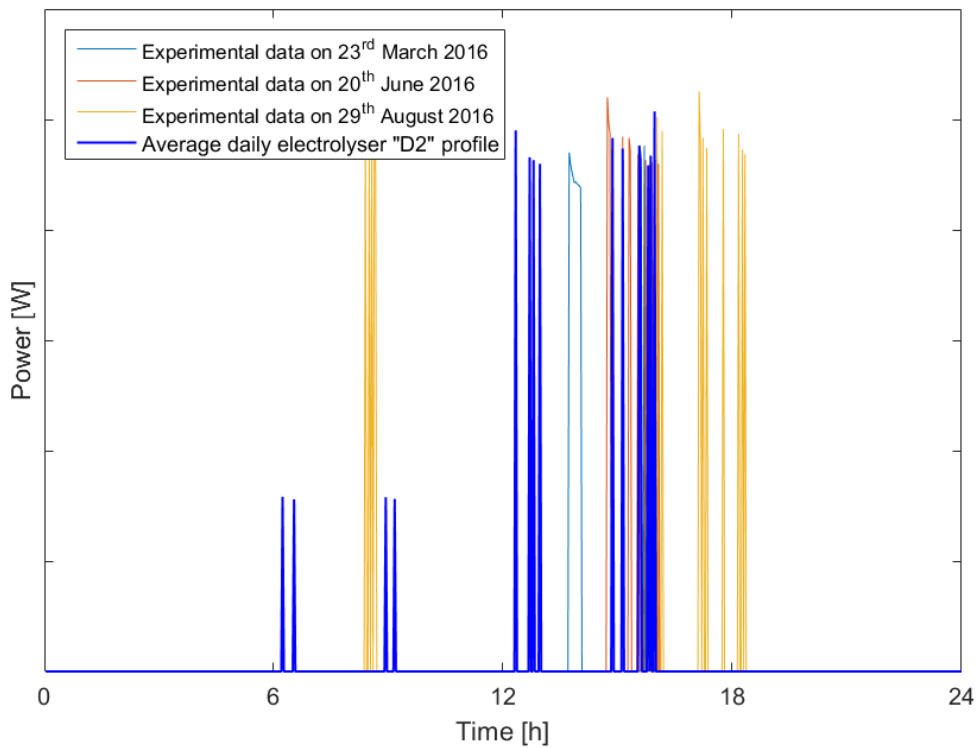


Figure 166 - Average electrolyser power profile "D2"

As already done for the fuel cell power profiles, quality evaluation of the average, the profiles were sorted, representing the power from the highest to the lowest value. Then, the

quality indicators were evaluated at each time, in order to build the error profiles, as shown in Figure 167 for the PRSD. The high values reached at the end of the error profiles are caused by the huge power difference occurring because of the different durations of the power profiles.

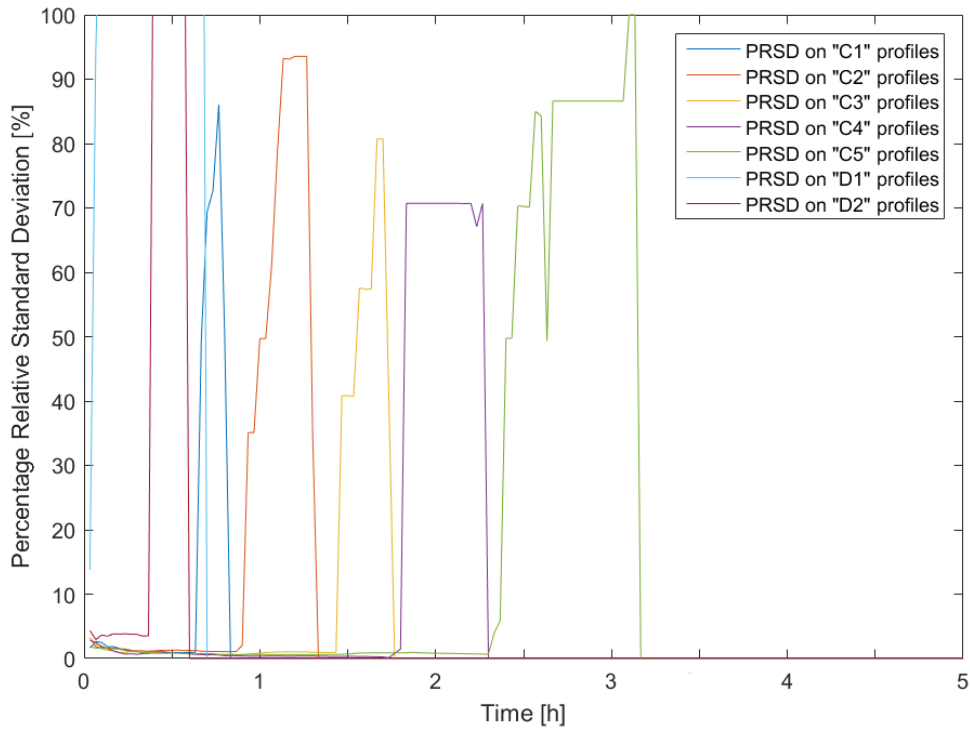


Figure 167 - PRSD for the electrolyser power profiles

For each class, the values of the MAPE and the PRSD, evaluated both on the whole profile and on the running hours are shown in Table 20.

Table 20: PSRD and MAPE on average electrolyser power profiles

Class	MAPE [%]	PRSD [%]	PRSD on running time [%]
C1	0.4 %	0.5 %	13.2 %
C2	0.9 %	1.2 %	21.8 %
C3	0.5 %	0.8 %	9.8 %
C4	1.0 %	1.4 %	14.2 %
C5	2.2 %	2.9 %	20.5 %
D1	4.0 %	5.0 %	39.0 %
D2	1.2 %	1.2 %	18.9 %

The absolute standard deviation is shown in Figure 168 and its values for each class are presented in Table 21.

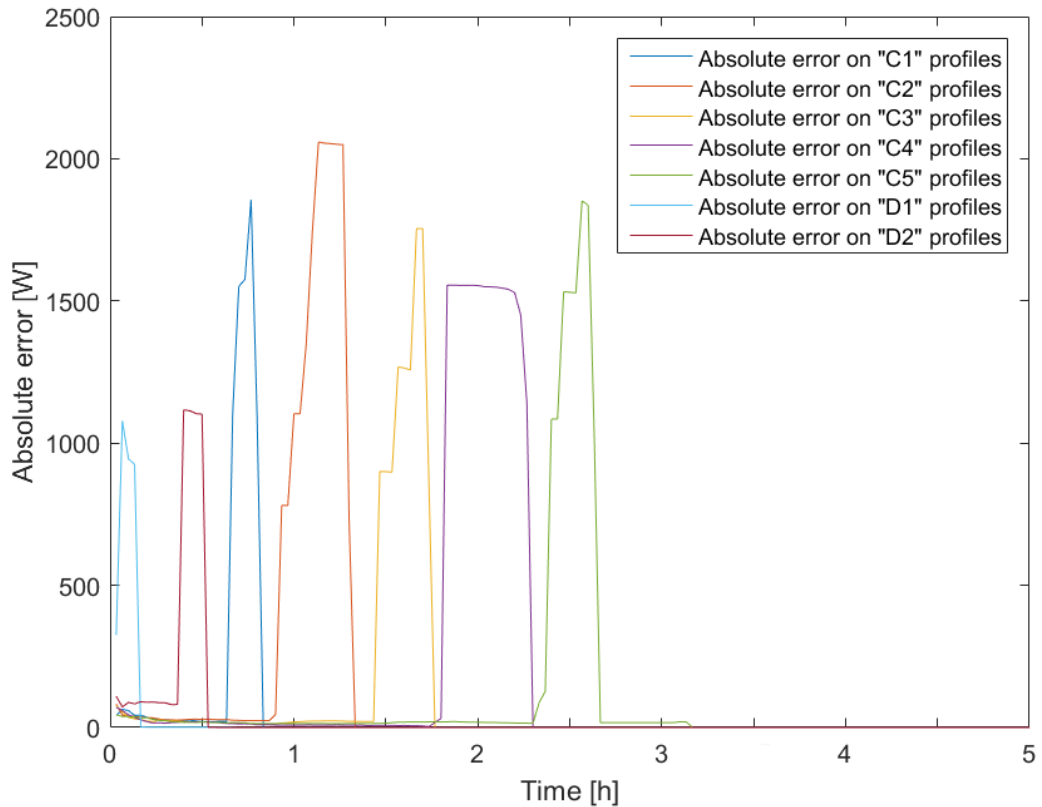


Figure 168 - Absolute error on electrolyser power profiles

Table 21: Absolute error on the electrolyser power profiles

Class	Difference of Energy [%]
C1	16.2 %
C2	26.2 %
C3	11.0 %
C4	16.2 %
C5	8.0 %
D1	69.9 %
D2	18.5 %

The difference of energy shows acceptable values for most classes, but bad results were obtained for the category “D1”, showing that at least one more class should be created in order to better represent the energy level of these profiles.

5.4.2 Year 2017 power data

The classification shown in Table 19 was applied to the 59 experimental profiles of the year 2017. All profiles are included in the “continuous” running mode classes, except one profile, belonging to the “D2” category. For each class, a comparison between the experimental profiles of the year 2017 and the average profiles built in 2016 was made, in

order to evaluate their fitting. The results are shown in the plots from Figure 169 to Figure 174.

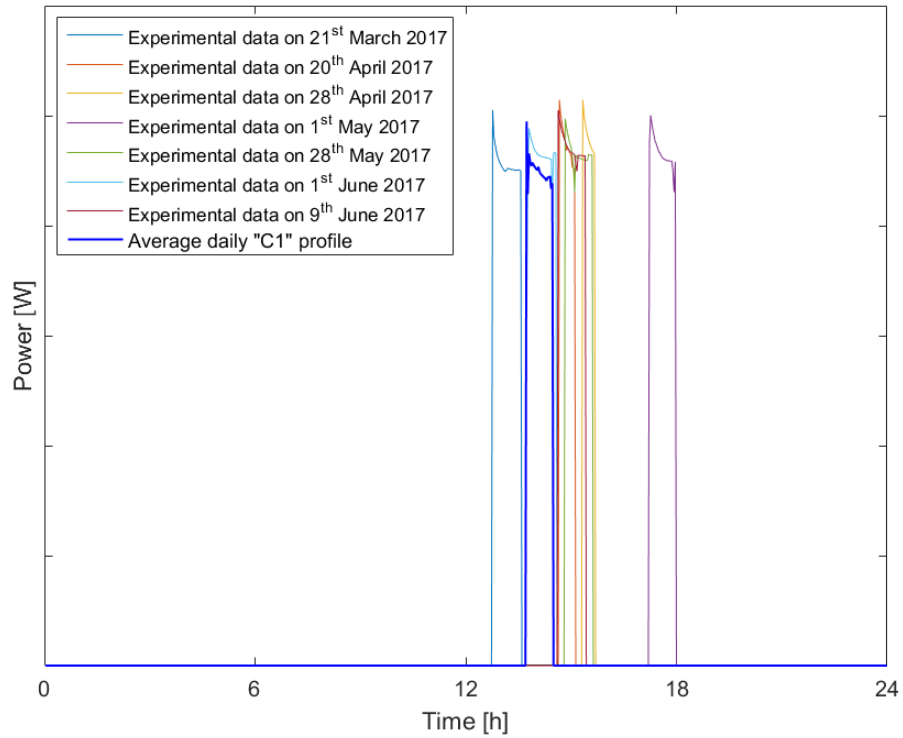


Figure 169 - Comparison between experimental electrolyser profile and average "C1"

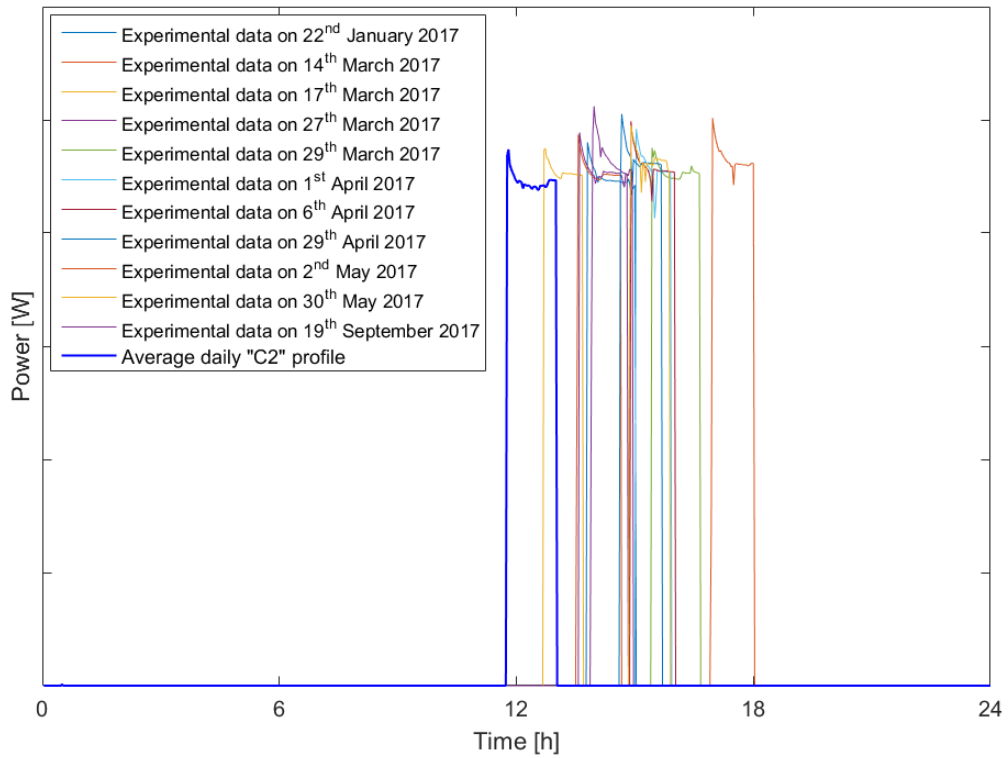


Figure 170 - Comparison between experimental electrolyser profile and average "C2"

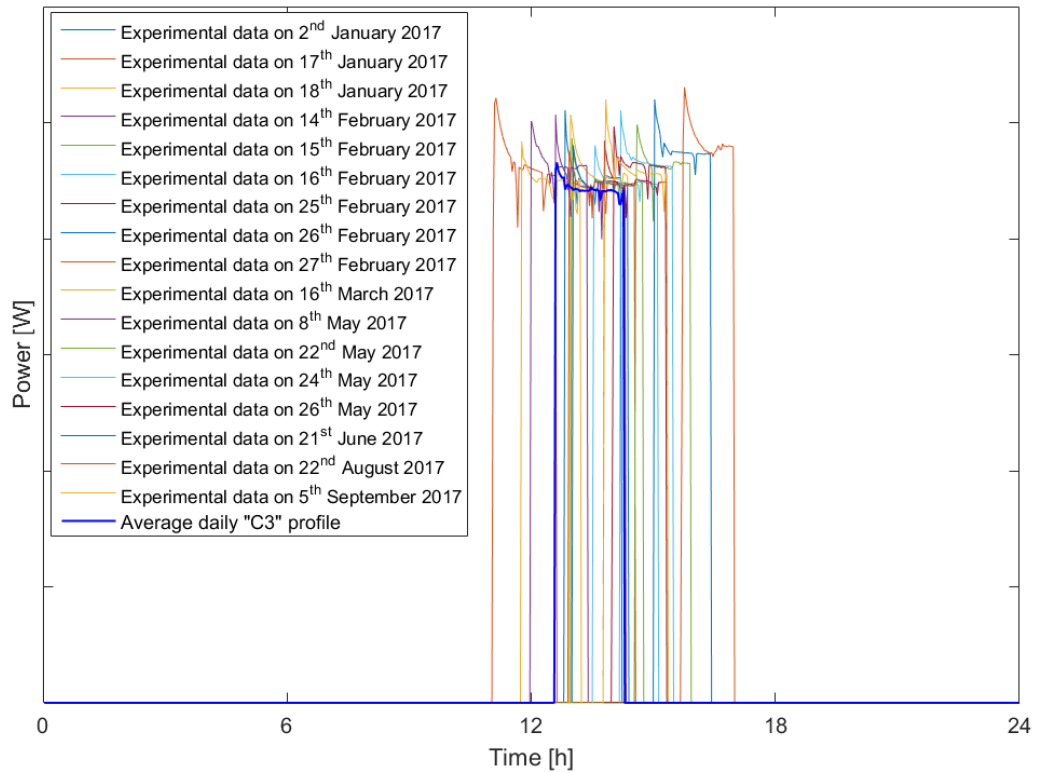


Figure 171 - Comparison between experimental electrolyser profile and average "C3"

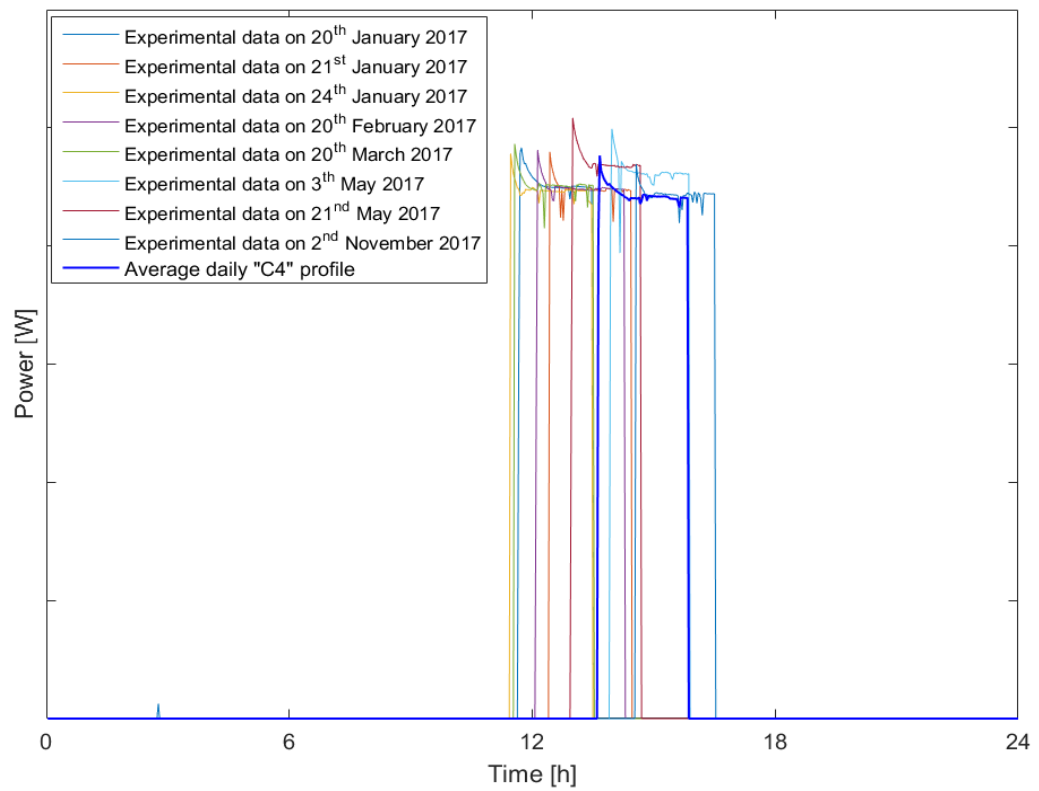


Figure 172 - Comparison between experimental electrolyser profile and average "C4"

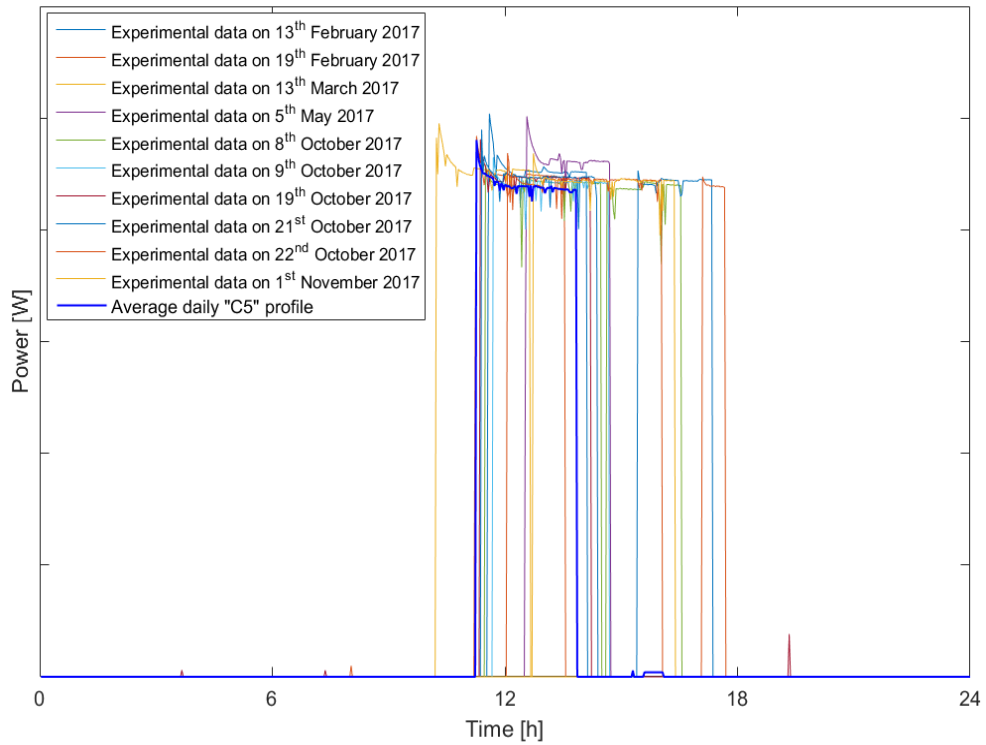


Figure 173 - Comparison between experimental electrolyser profile and average "C5"

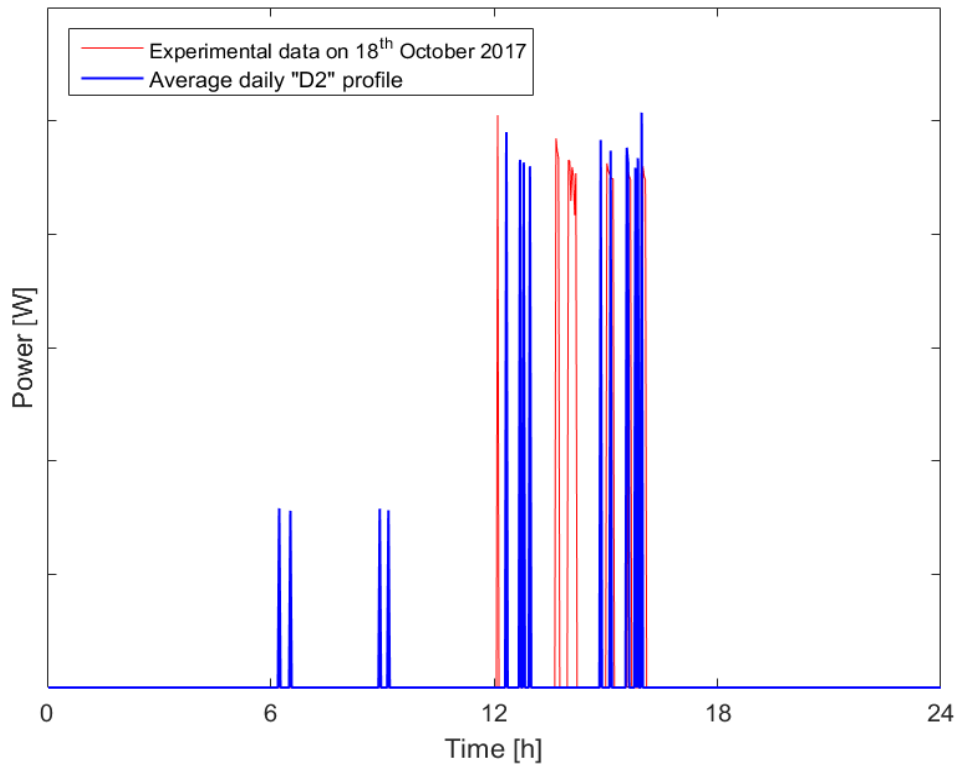


Figure 174 - Comparison between experimental electrolyser profile and average "D2"

The accuracy of the prognostics was evaluated with the absolute standard deviation, shown in Figure 175, for all the compared classes. The errors are high, in some cases, as shown also by the values of the Difference of energy, in Table 22. Indeed, even if the average profiles built in 2016 have a similar shape with respect to the experimental profiles of 2017, the energy associated to the profiles of the second year can be different. For this reason, the

new profiles do not fit very well to the classification created for the first year data (especially for the classes “C5” and “D2”), showing again that if the events are not repeated in the time the prognosis is not able to give good results.

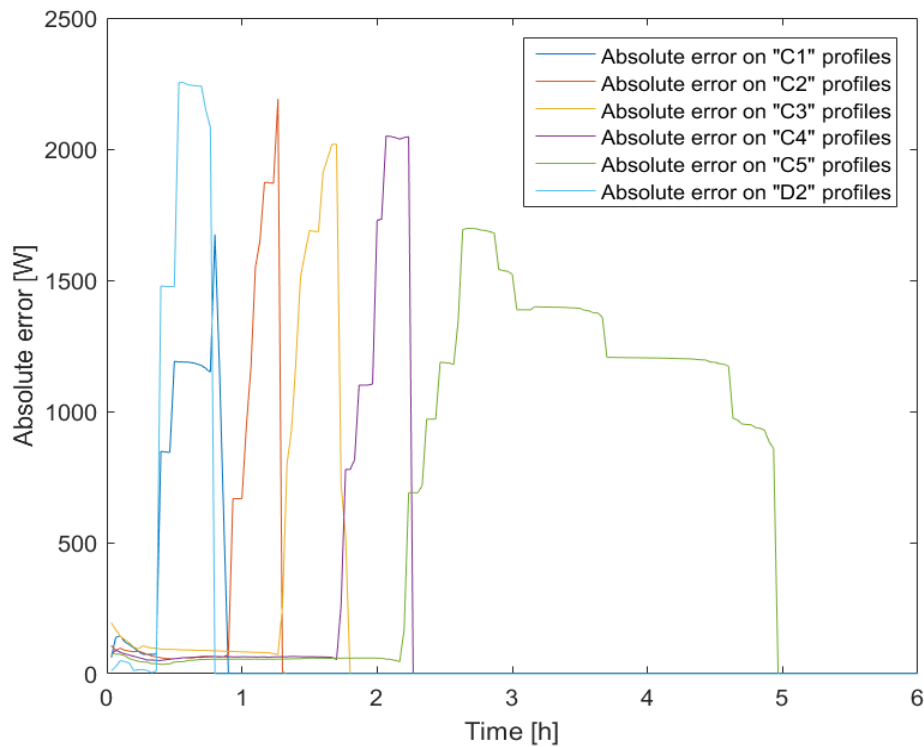


Figure 175 - Absolute error on electrolyser power profiles

Table 22: Difference of energy on the compared electrolyser power profiles

Class	Difference of Energy [%]
C1	36.0 %
C2	22.6 %
C3	23.8 %
C4	19.5 %
C5	47.2 %
D2	45.4 %

5.5 Battery power profiles

In this Section, the analysis of the experimental data about the battery power is presented. Also in this case, the daily power data were analysed, profiled and, finally, averaged. The average profiles were built by using the data collected during 2016 and, then, they were compared with the data measured in 2017, to evaluate the fitting between the average and the real daily profiles.

The battery is running everyday, so the number of daily profiles is equal to the total number of monitored days, that is 640, divided in 346 in 2016 and 294 in 2017. The indicator chosen for the classification was the daily energy, that is the sum in absolute value of the power produced or consumed by the battery. Fifteen classes were generated after a preliminary analysis of the data, in order to group in the same class profiles with similar features. The classes are shown in Table 23, together with the percentage of occurrence of each profile during the first year of operation.

Table 23: Battery power profiles classes

Class	Daily Energy (DE) [kWh]	Percentage on year 2016 [%]
P1	$0 < DTP < 2.5$	8.4 %
P2	$2.5 < DTP < 3.0$	9.8 %
P3	$3.0 < DTP < 3.3$	9.8 %
P4	$3.3 < DTP < 4.2$	12.1 %
P5	$4.2 < DTP < 5.1$	6.4 %
P6	$5.1 < DTP < 5.7$	5.8 %
P7	$5.7 < DTP < 6.3$	5.8 %
P8	$6.3 < DTP < 7.3$	7.5 %
P9	$7.3 < DTP < 8.3$	5.8 %
P10	$8.3 < DTP < 9.0$	4.0 %
P11	$9.0 < DTP < 9.7$	6.4 %
P12	$9.7 < DTP < 10.3$	4.0 %
P13	$10.3 < DTP < 11.0$	3.8 %
P14	$11.0 < DTP < 11.6$	5.2 %
P15	$DTP > 11.6$	5.2 %

The average profile for each class was built following the general averaging algorithm, described in Section 3.3.

5.5.1 Year 2016 power data

The averaging procedure was applied to the 346 experimental profiles of the year 2016. Figure 176 to Figure 190 show the generated average profiles, compared with one of the experimental profiles of each class.

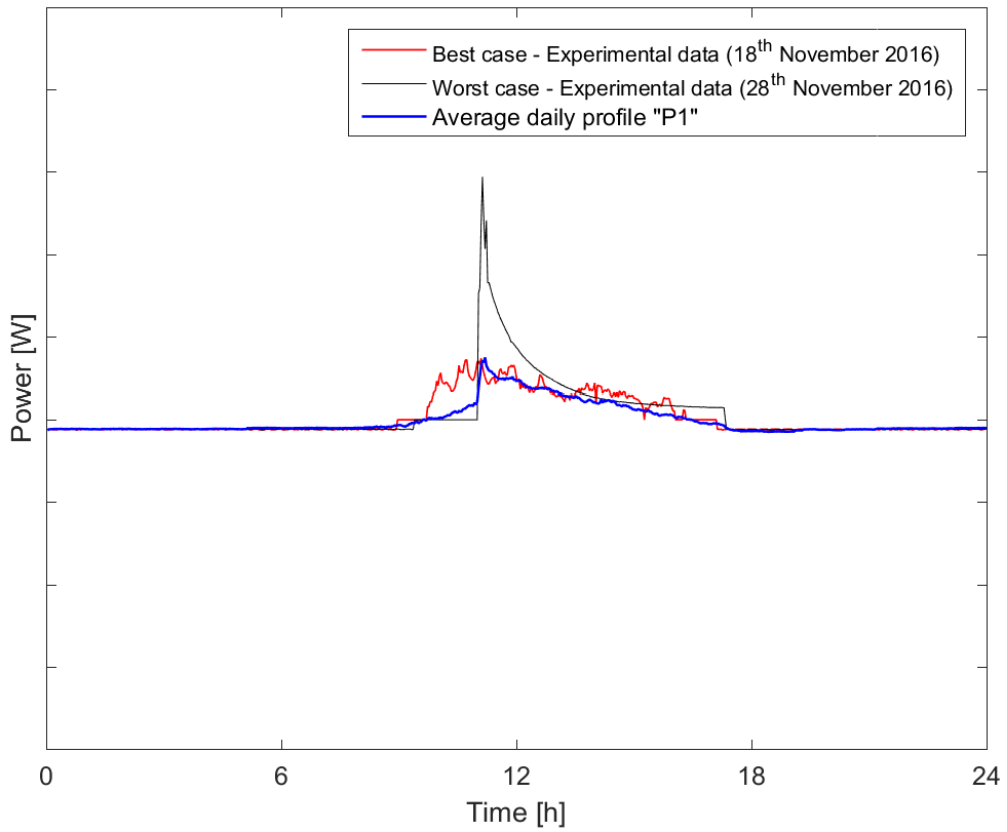


Figure 176 - Average battery power profile "P1"

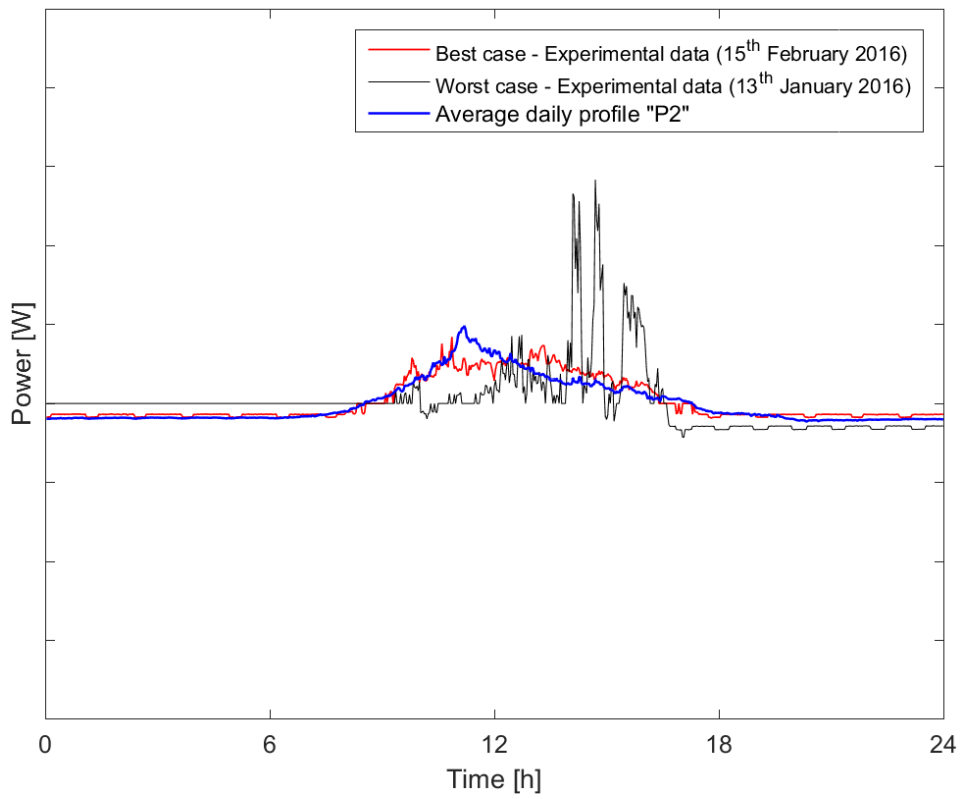


Figure 177 - Average battery power profile "P2"

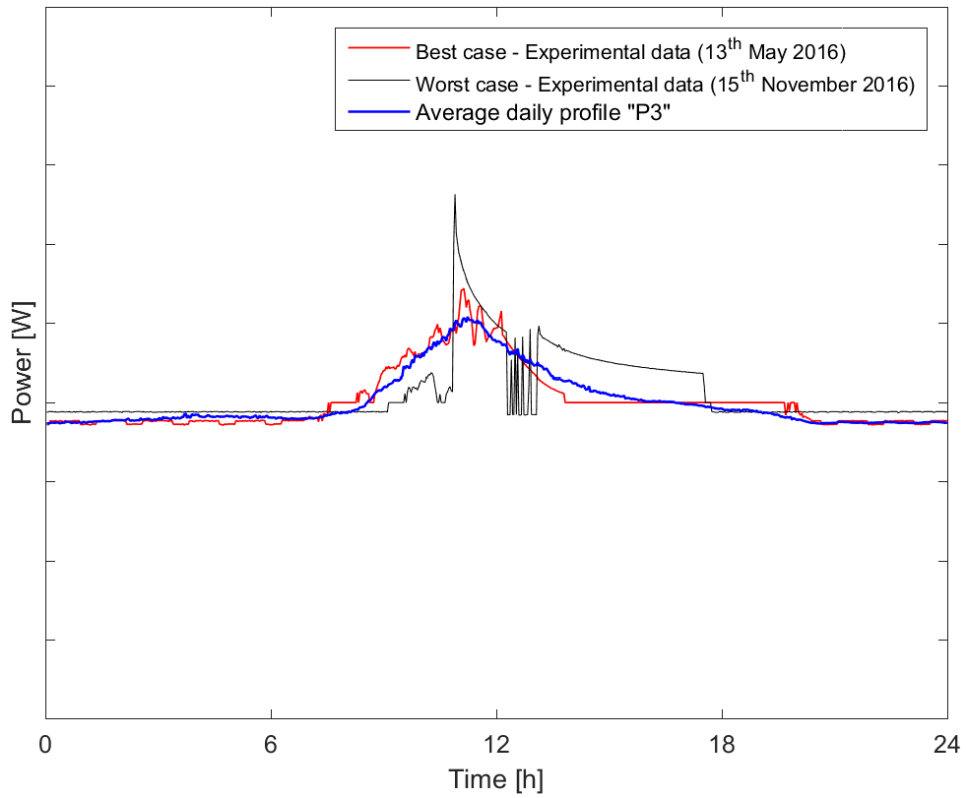


Figure 178 - Average battery power profile "P3"

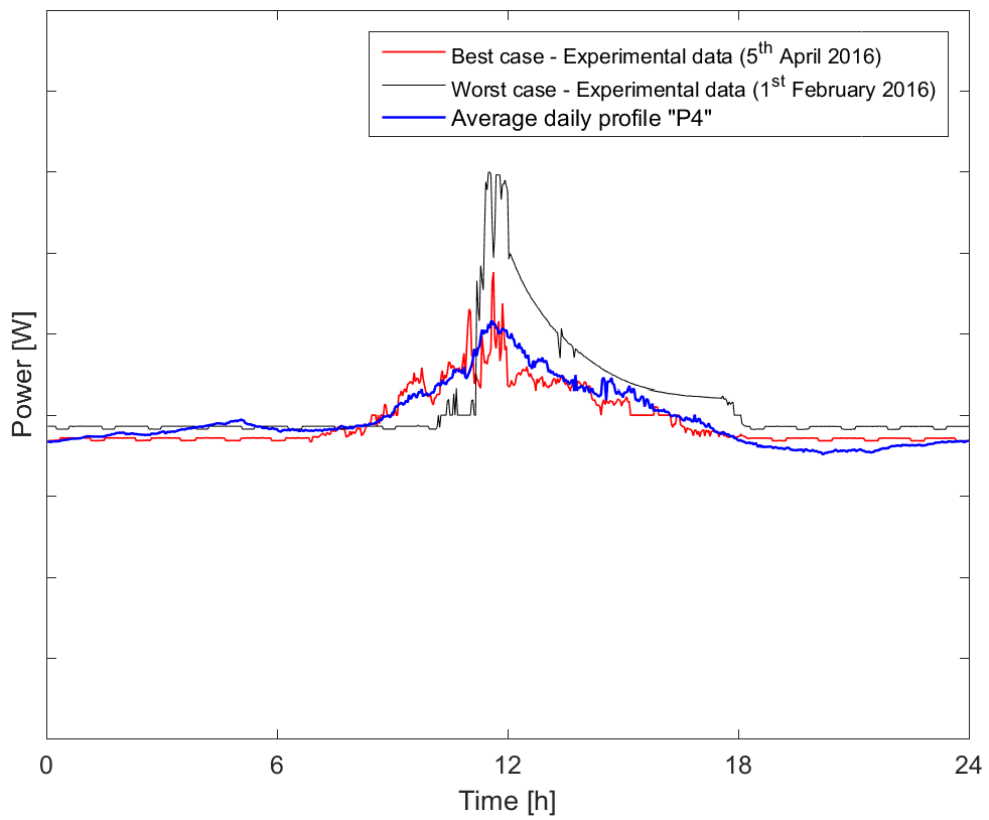


Figure 179 - Average battery power profile "P4"

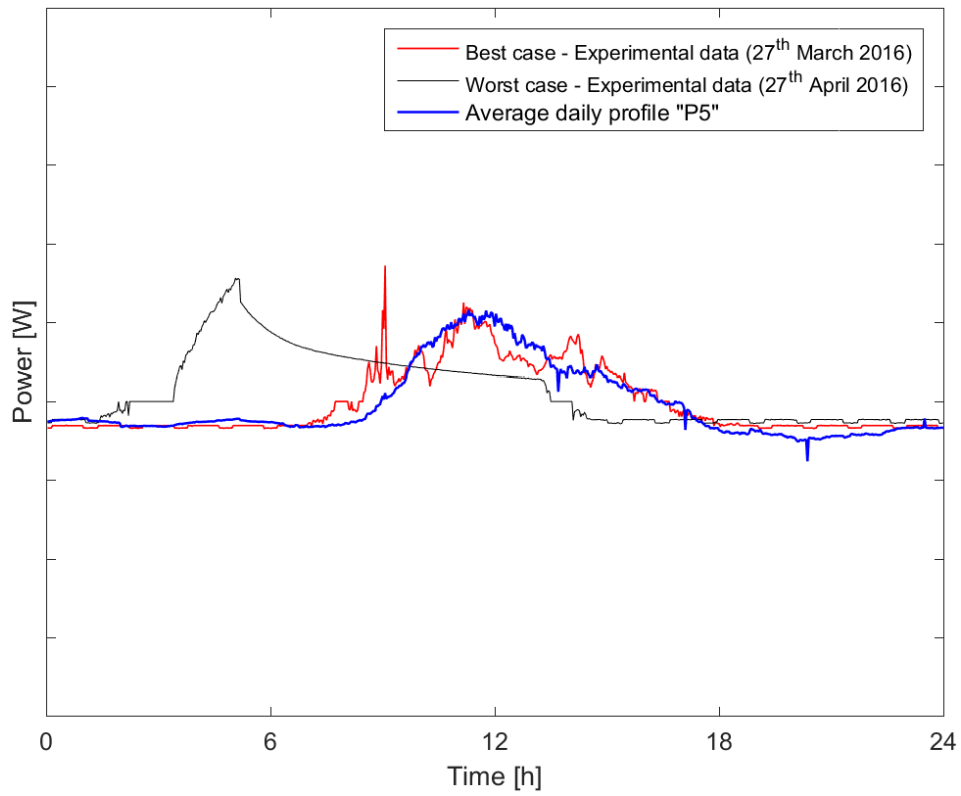


Figure 180 - Average battery power profile "P5"

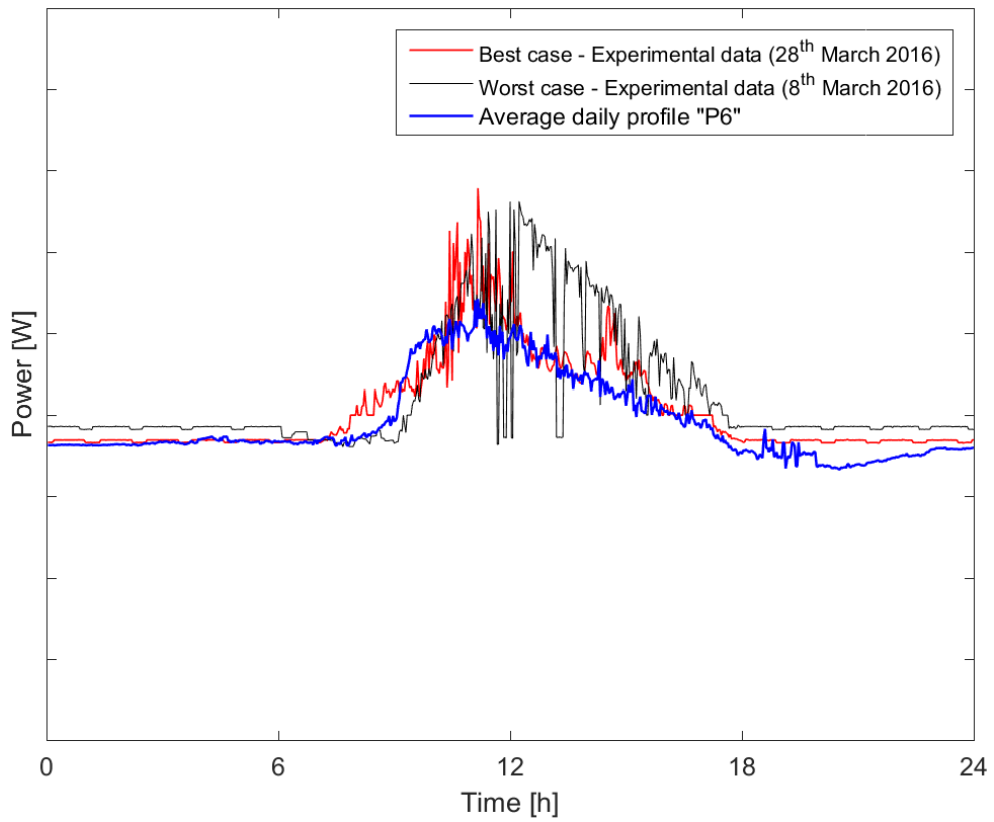


Figure 181 - Average battery power profile "P6"

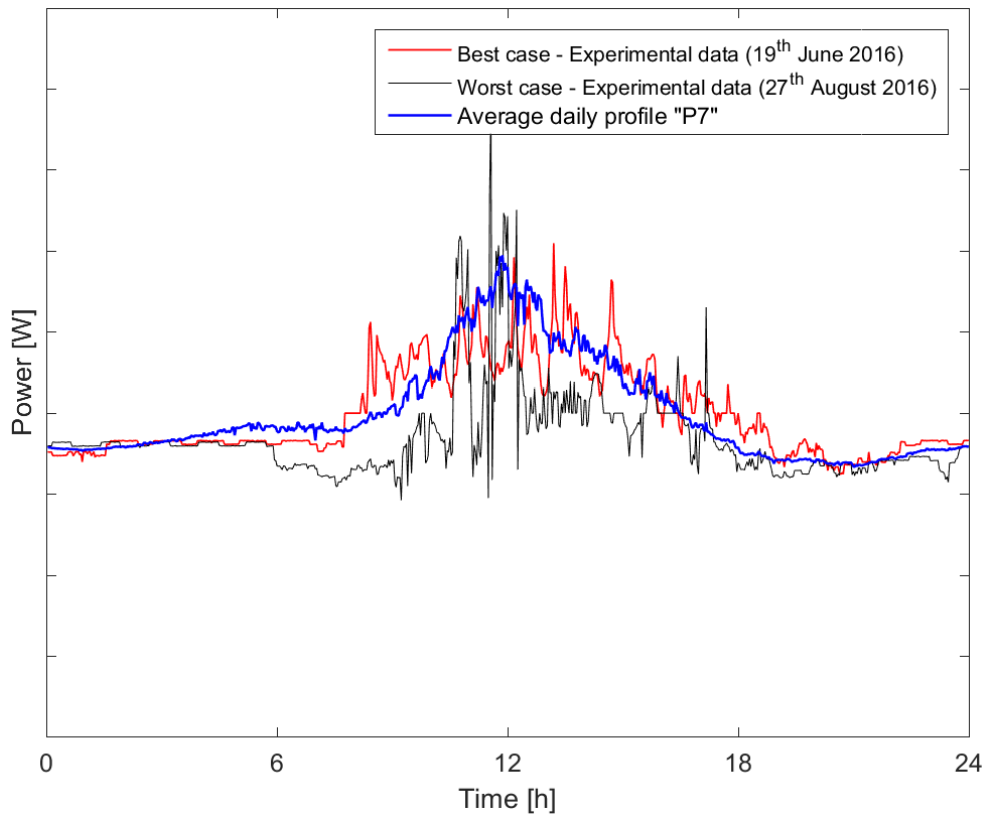


Figure 182 - Average battery power profile "P7"

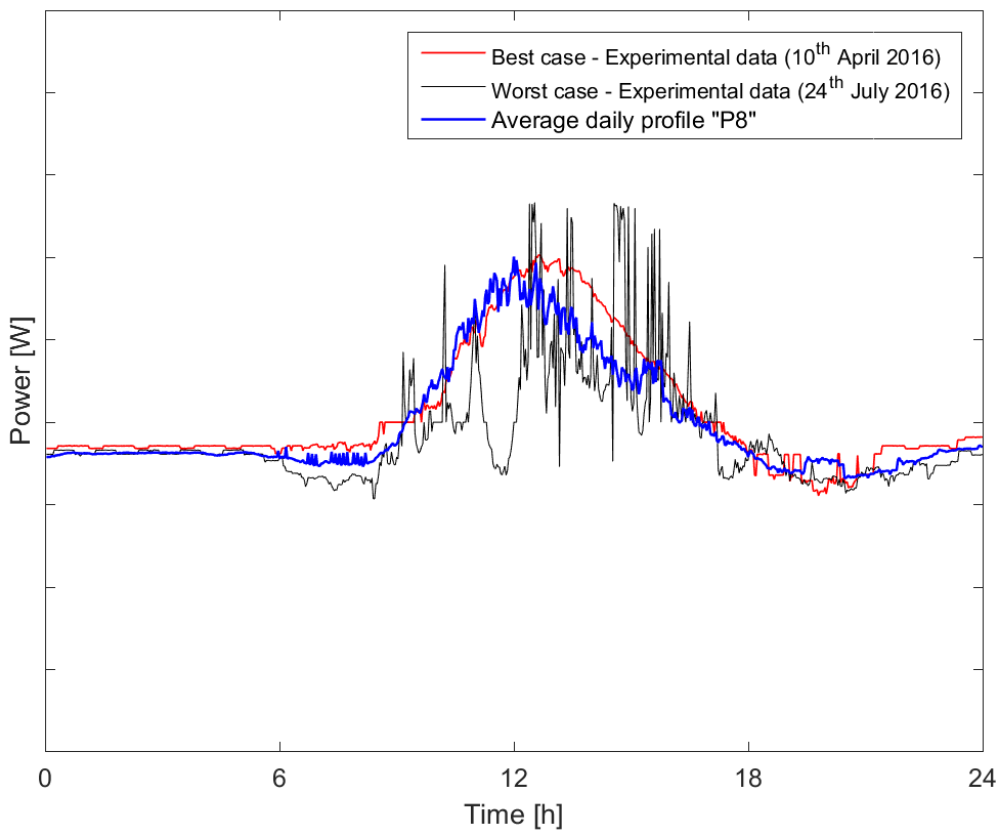


Figure 183 - Average battery power profile "P8"

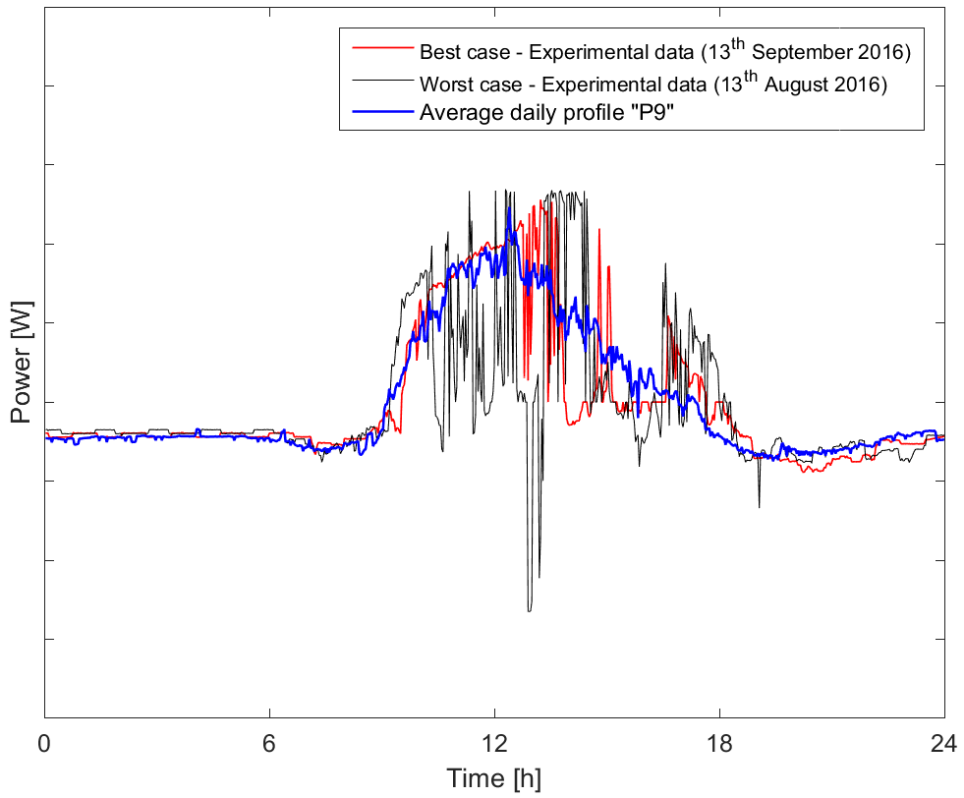


Figure 184 - Average battery power profile "P9"

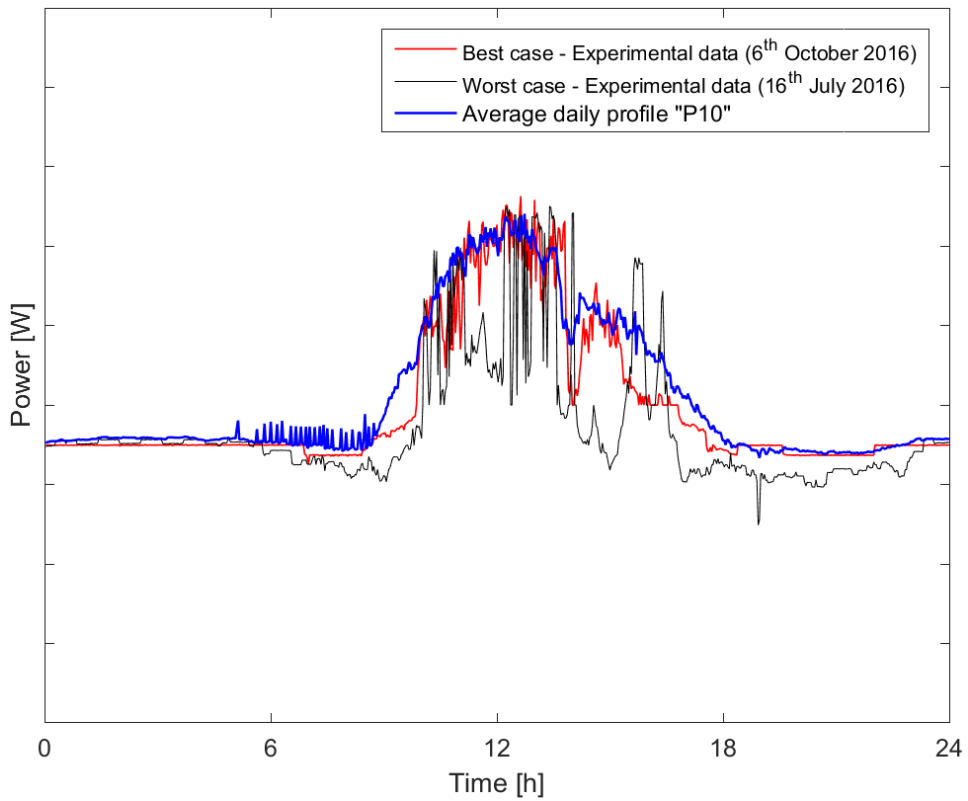


Figure 185 - Average battery power profile "P10"

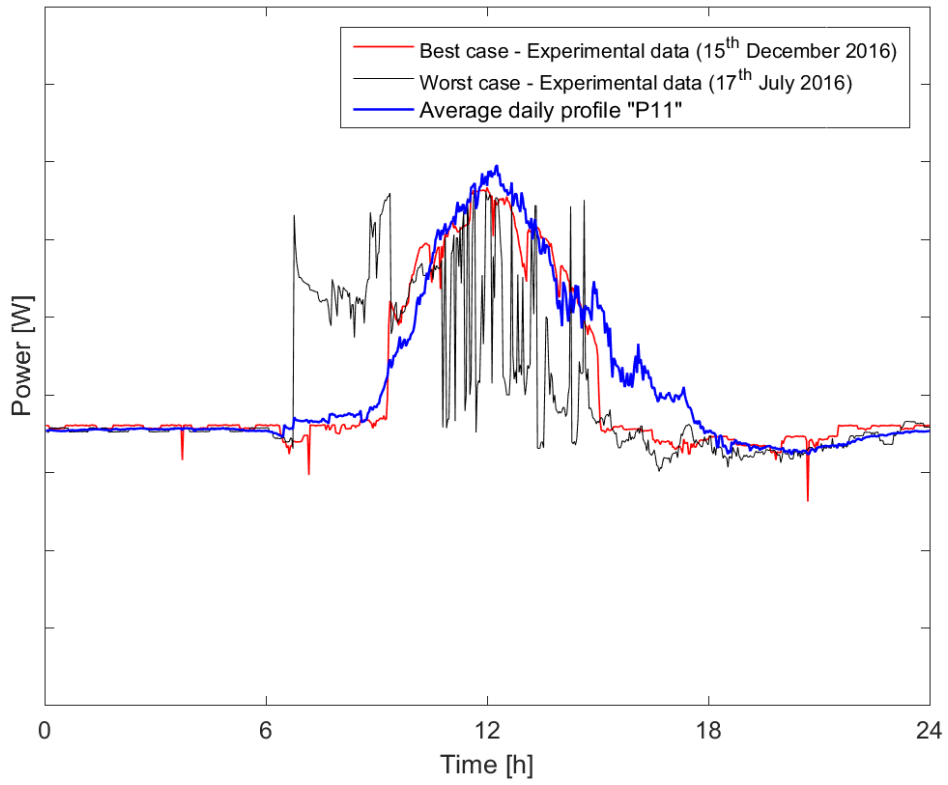


Figure 186 - Average battery power profile "P11"

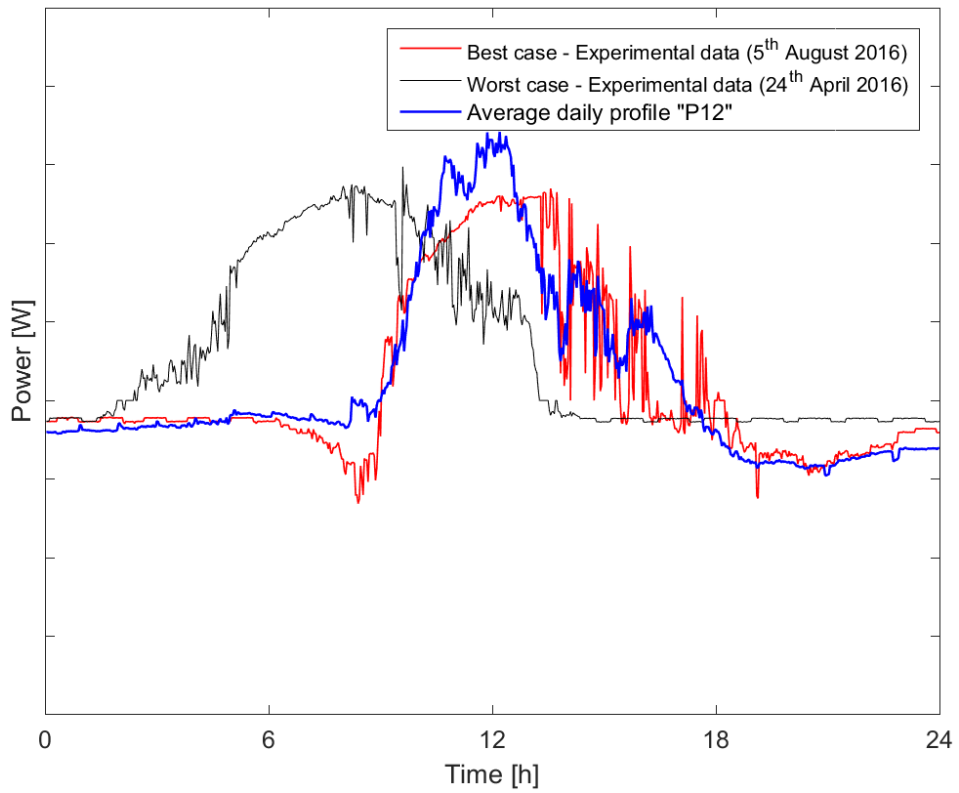


Figure 187 - Average battery power profile "P12"

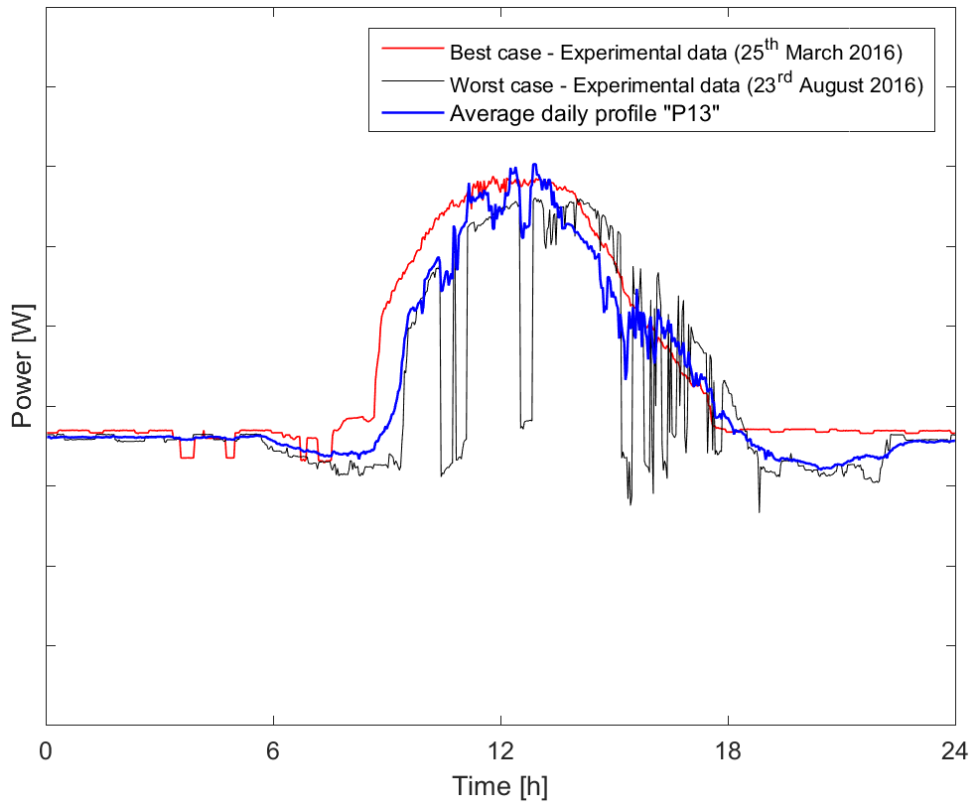


Figure 188 - Average battery power profile "P13"

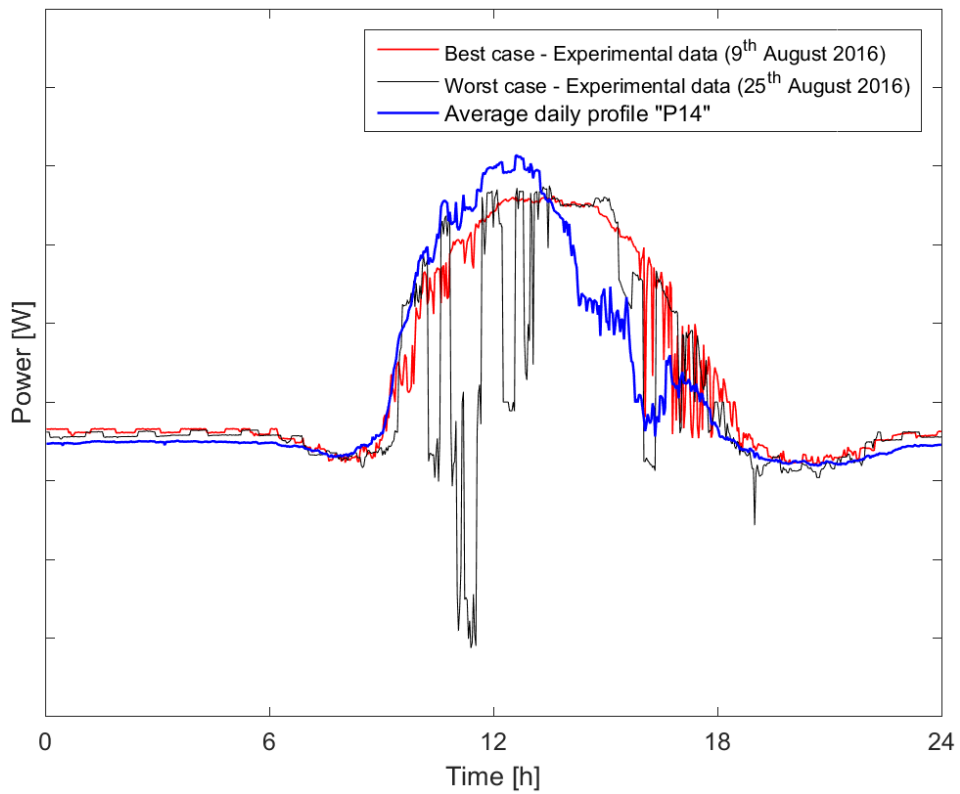


Figure 189 - Average battery power profile "P14"

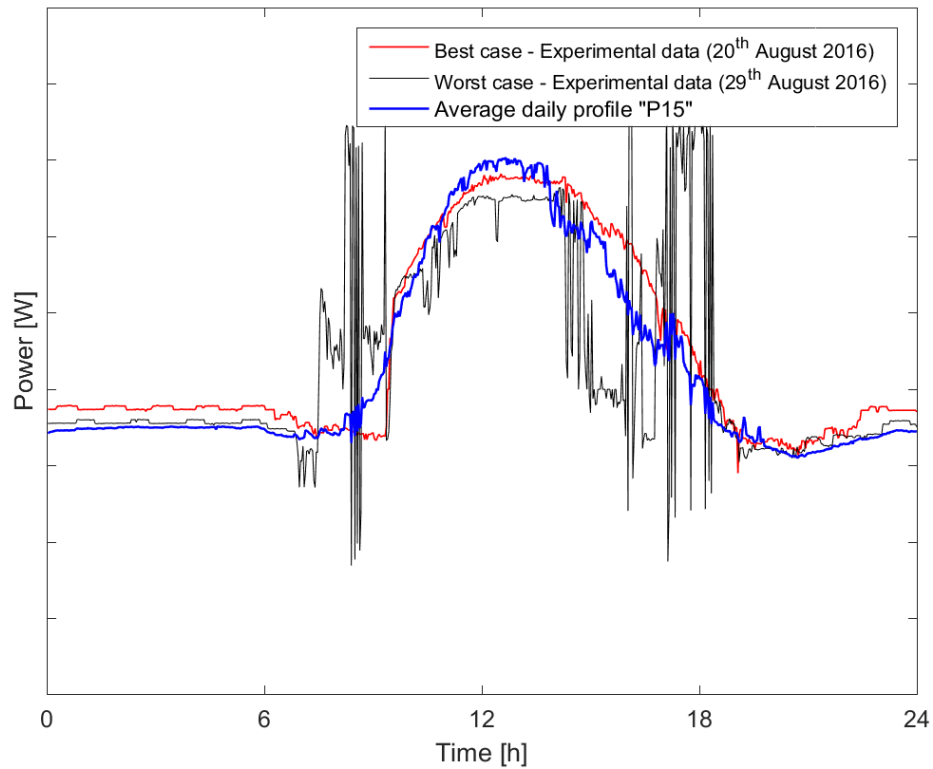


Figure 190 - Average battery power profile "P15"

The errors between the experimental and the average profiles were evaluated with the MAPE and the PRSD, whose values, for each class, are shown in Table 24.

Table 24: PSRD and MAPE on average battery profiles

Class	MAPE [%]	PRSD [%]
P1	26.7 %	34.4 %
P2	21.9 %	26.9 %
P3	16.3 %	20.5 %
P4	23.4 %	29.6 %
P5	24.6 %	29.8 %
P6	26.3 %	31.2 %
P7	26.8 %	32.7 %
P8	25.1 %	28.4 %
P9	25.5 %	31.8 %
P10	24.0 %	24.3 %
P11	22.4 %	24.2 %
P12	24.1 %	29.1 %
P13	22.7 %	24.8 %
P14	22.3 %	22.9 %
P15	22.0 %	23.3 %

The values of the errors are quite high. This is because the battery power profiles can have very different and irregular shapes, as they are easily influenced by the random variations of the user load or of the solar irradiance. The absolute error is shown in Figure 191 and the values of the Difference of Energy, for each class, are listed in Table 25. The increase of the error in the last part of the plots occurs because the average profile is not able to properly represent the negative peaks that, in the sorted vectors, are located in the final part of the profile.

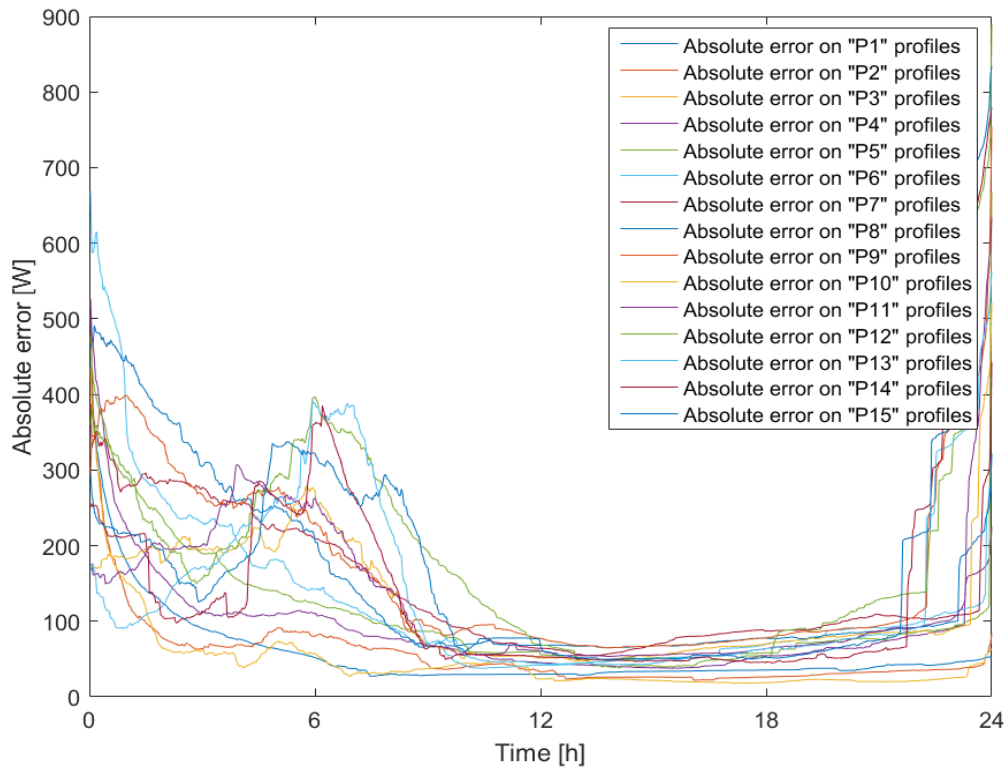


Figure 191 - Absolute error on battery power profiles

Table 25: Difference of Energy on the battery power profiles

Class	Difference of Energy [%]
P1	80.1 %
P2	48.2 %
P3	34.1 %
P4	56.8 %
P5	56.7 %
P6	54.9 %
P7	57.2 %
P8	53.5 %
P9	50.9 %

P10	33.2 %
P11	33.0 %
P12	42.2 %
P13	31.2 %
P14	30.4 %
P15	32.5 %

The values of the quality indicator based on the energy are high, too. Indeed, the classification of the battery profiles should be improved as the daily energy only is not a sufficient criterion to group the profiles according to their features. Therefore, some additional criteria should be considered to better categorize the power profiles and also the number of classes could be increased.

5.5.2 Year 2017 power data

The 294 experimental power profiles collected in the year 2017 were divided in classes, according to the classification of Table 23. Then, they were compared with the corresponding average profiles built in 2016, as shown in the plots from Figure 192 to Figure 206, in order to evaluate their fitting.

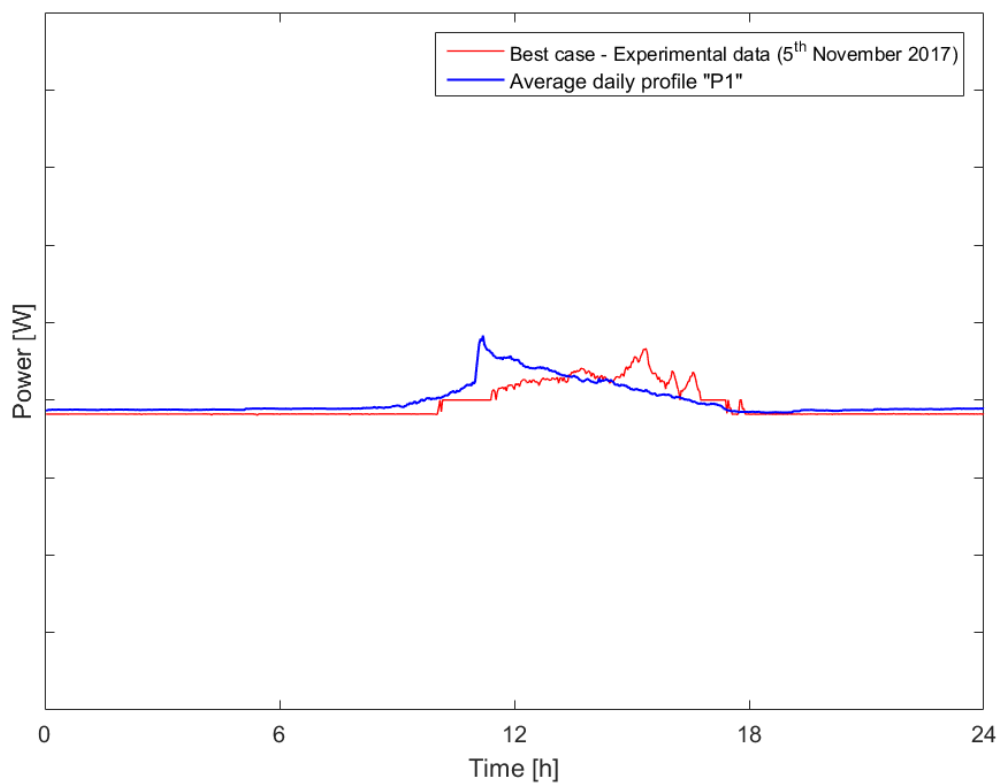


Figure 192 - Comparison between experimental battery profile and average "P1"

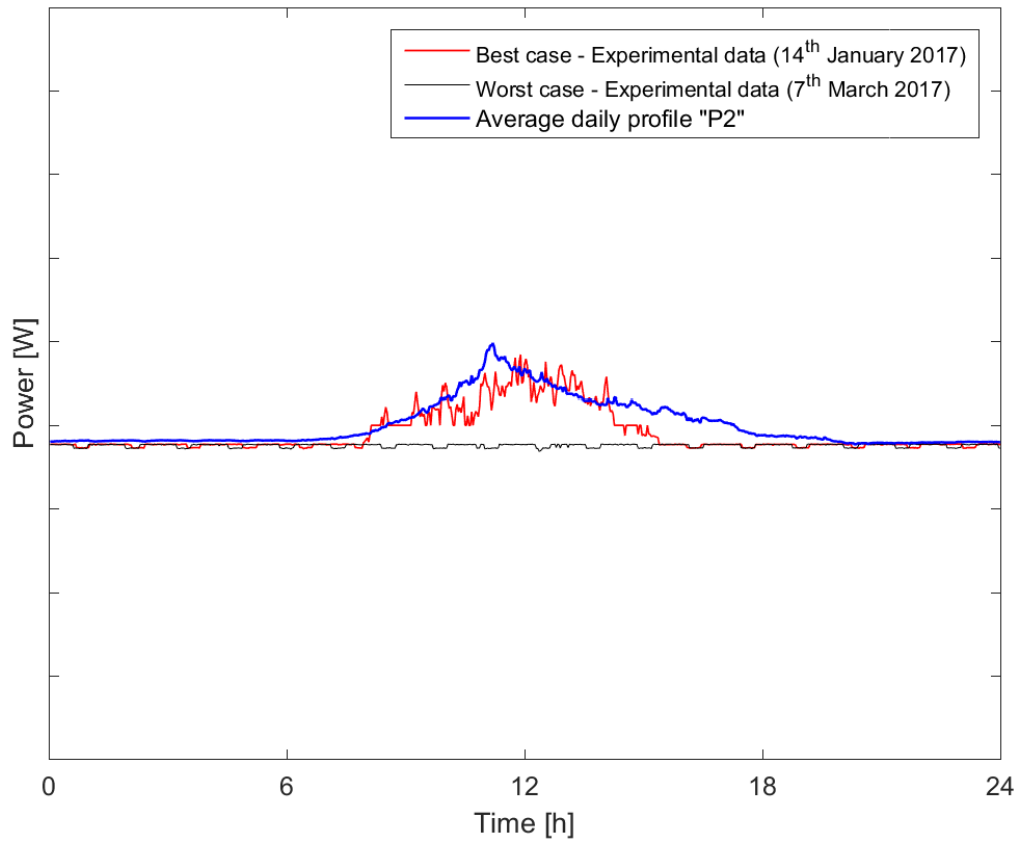


Figure 193 - Comparison between experimental battery profile and average "P2"

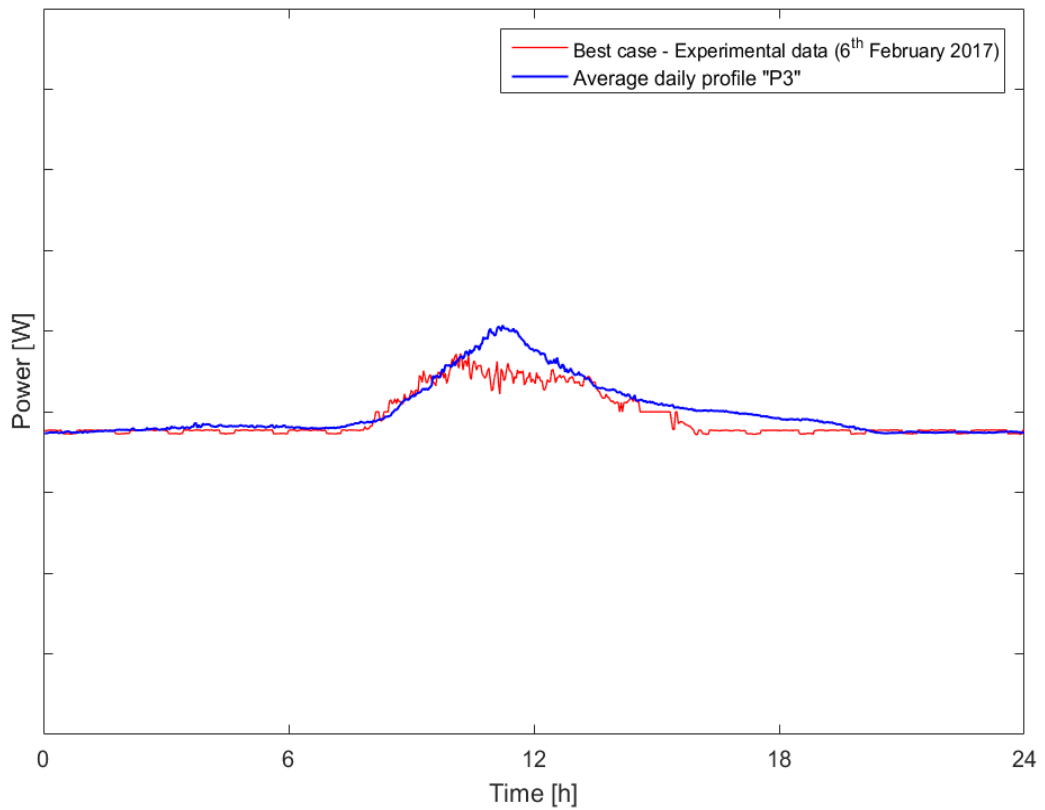


Figure 194 - Comparison between experimental battery profile and average "P3"

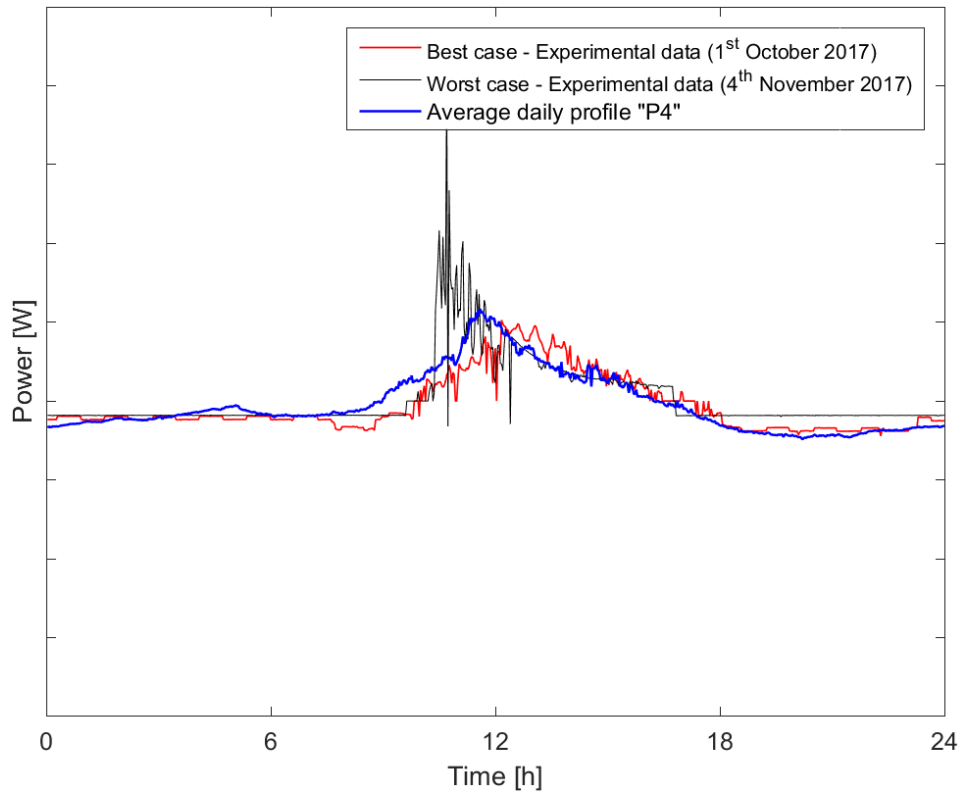


Figure 195 - Comparison between experimental battery profile and average "P4"

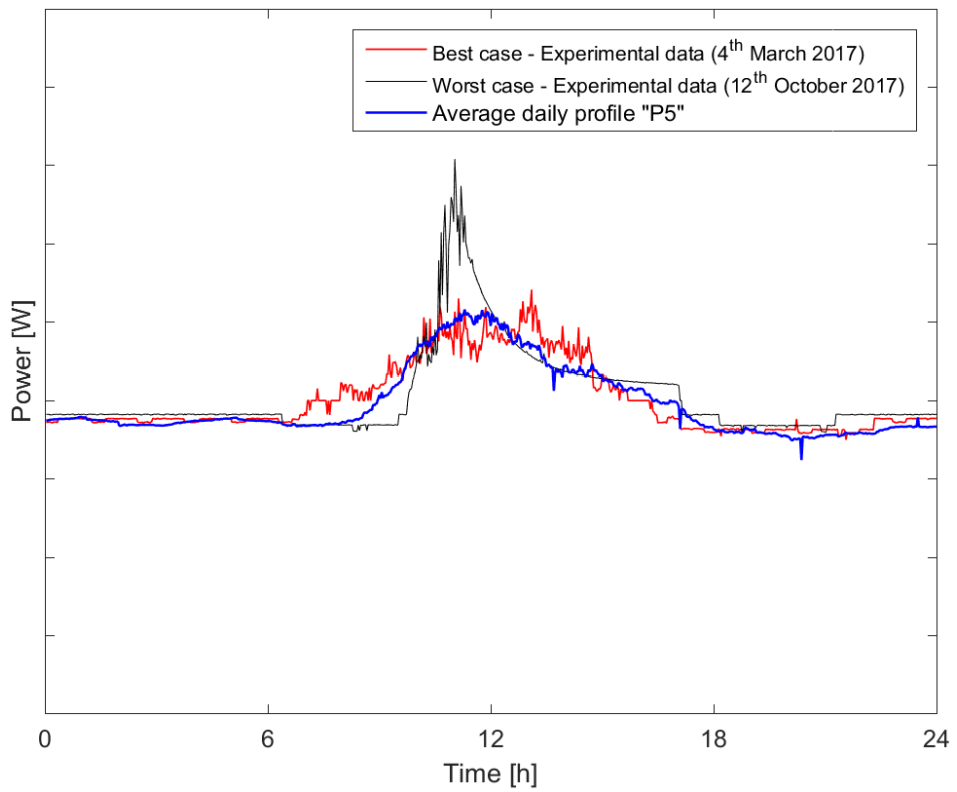


Figure 196 - Comparison between experimental battery profile and average "P5"

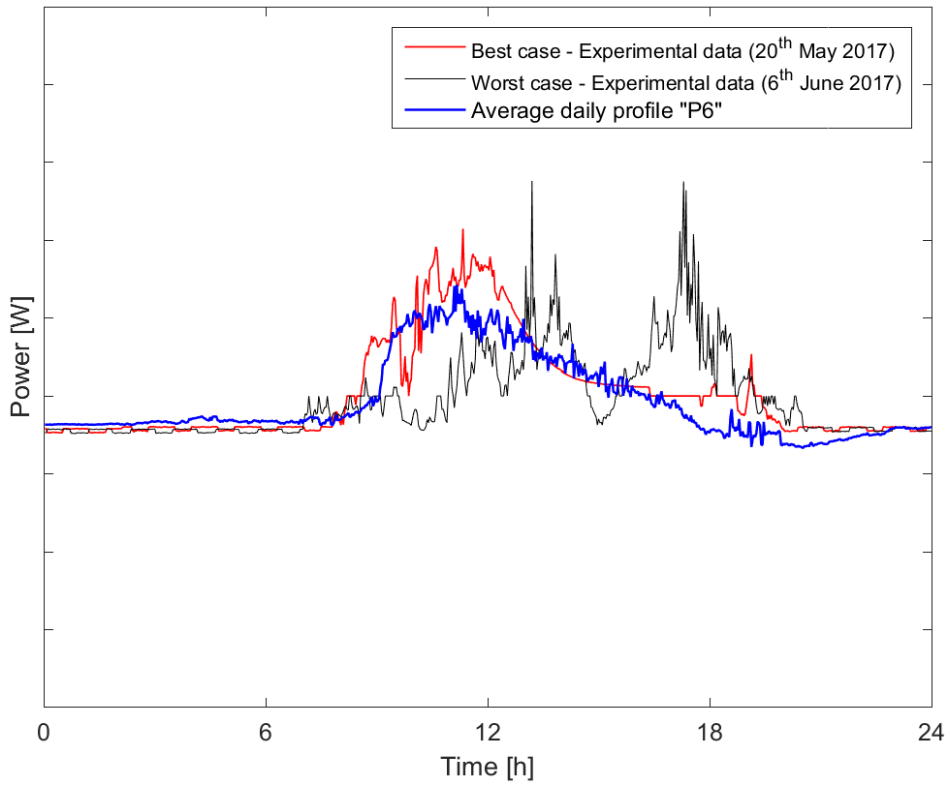


Figure 197 - Comparison between experimental battery profile and average "P6"

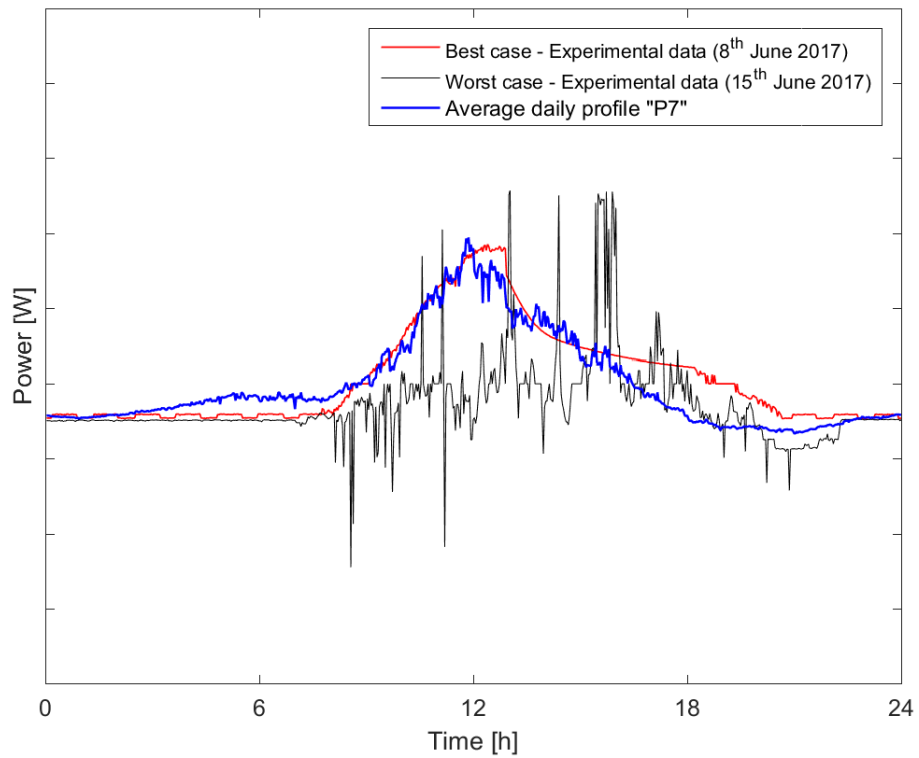


Figure 198 - Comparison between experimental battery profile and average "P7"

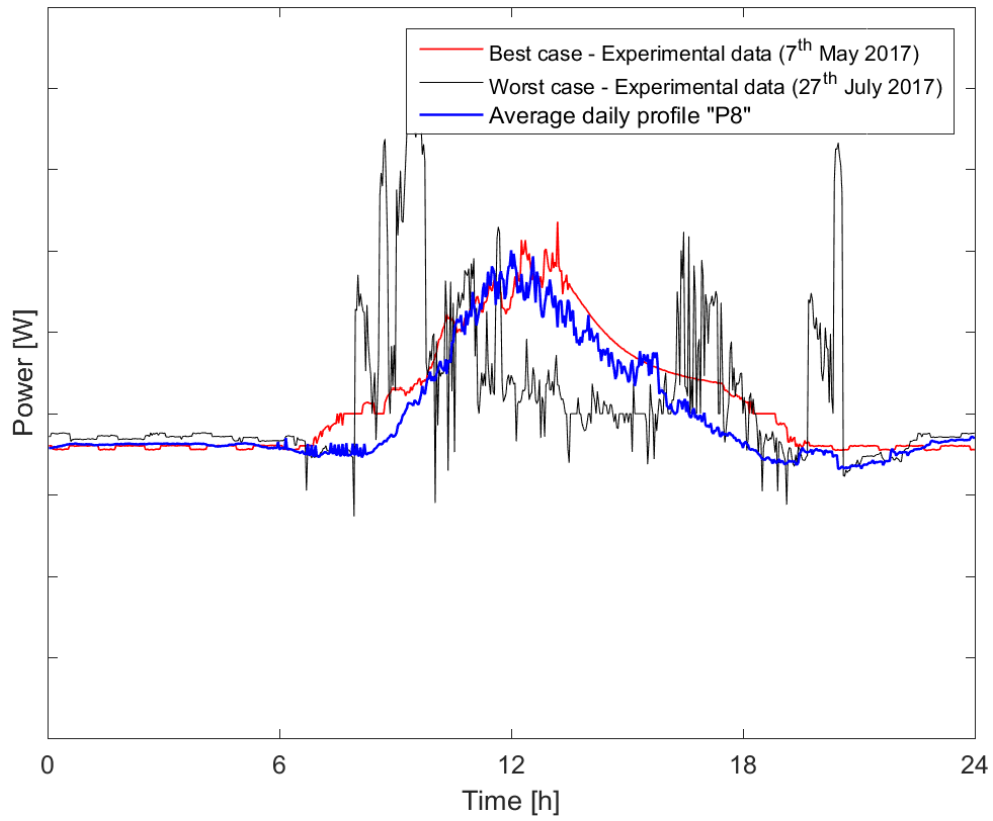


Figure 199 - Comparison between experimental battery profile and average "P8"

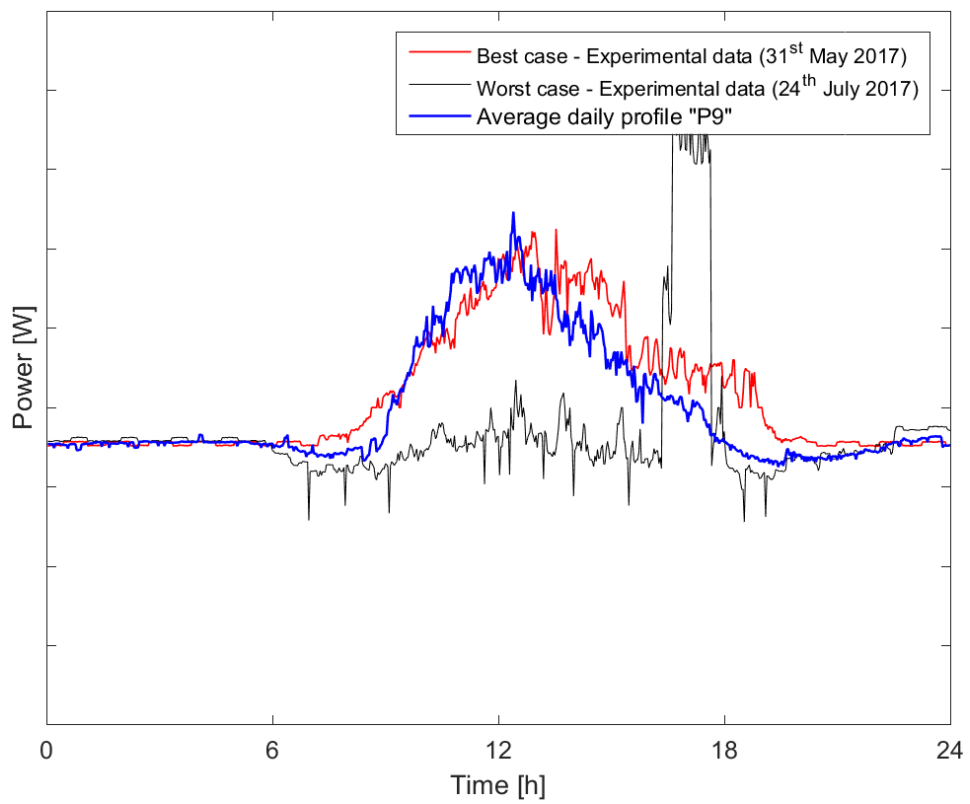


Figure 200 - Comparison between experimental battery profile and average "P9"

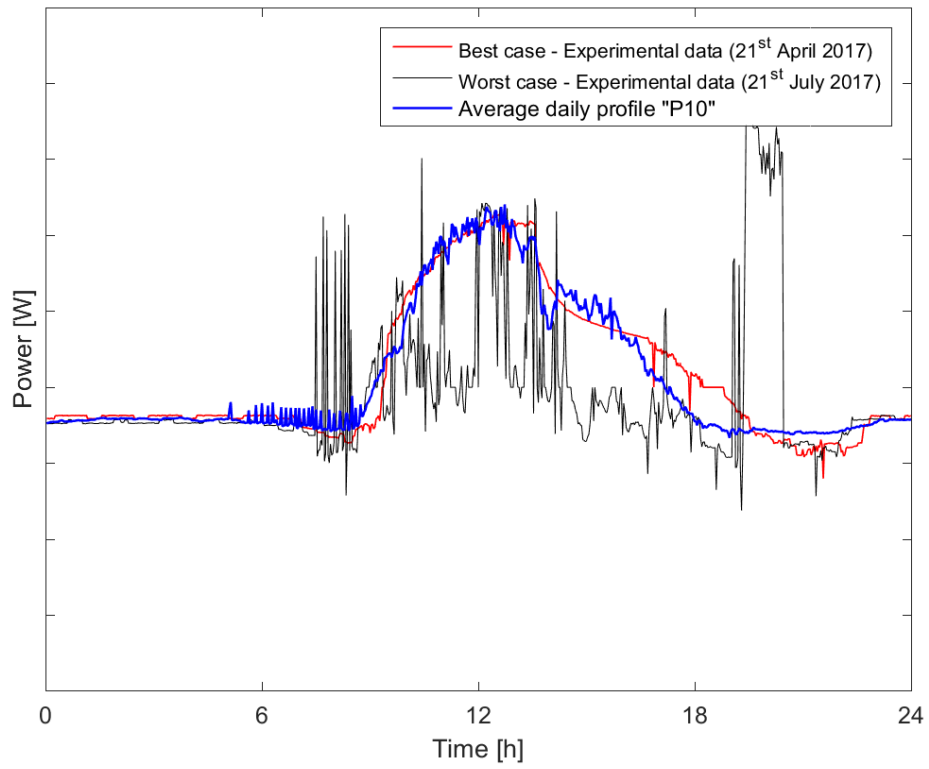


Figure 201 - Comparison between experimental battery profile and average "P10"

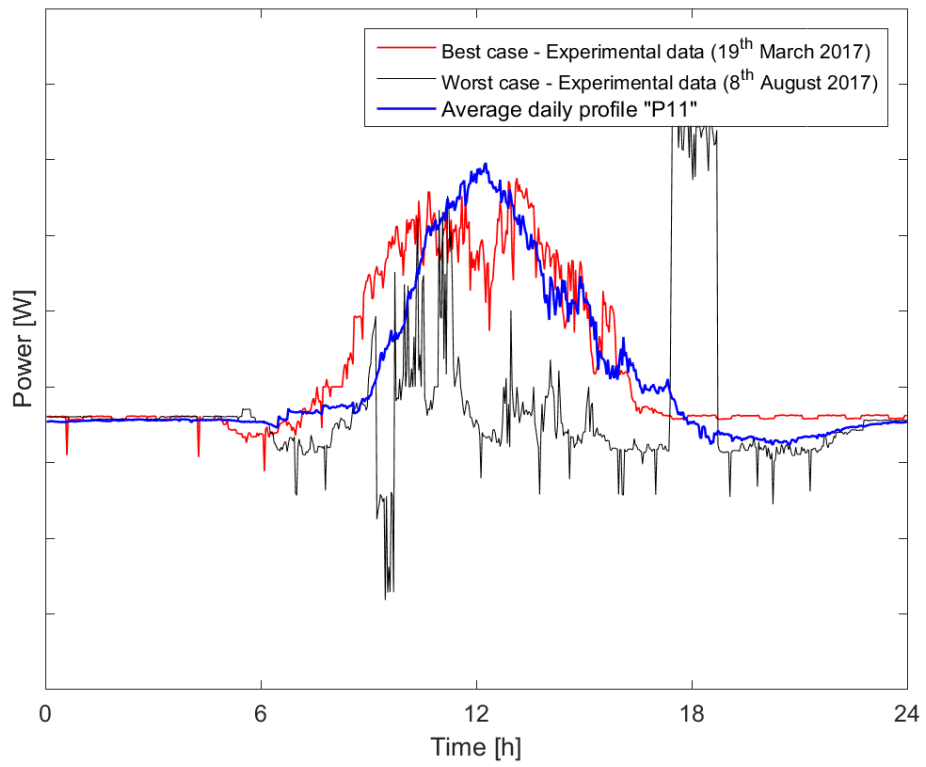


Figure 202 - Comparison between experimental battery profile and average "P11"

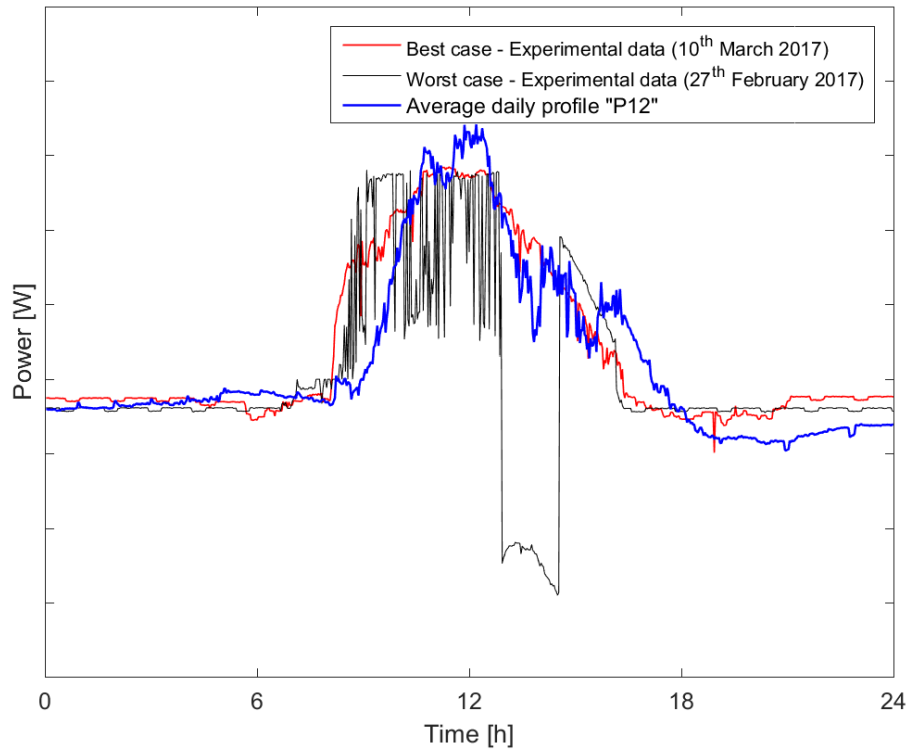


Figure 203 - Comparison between experimental battery profile and average "P12"

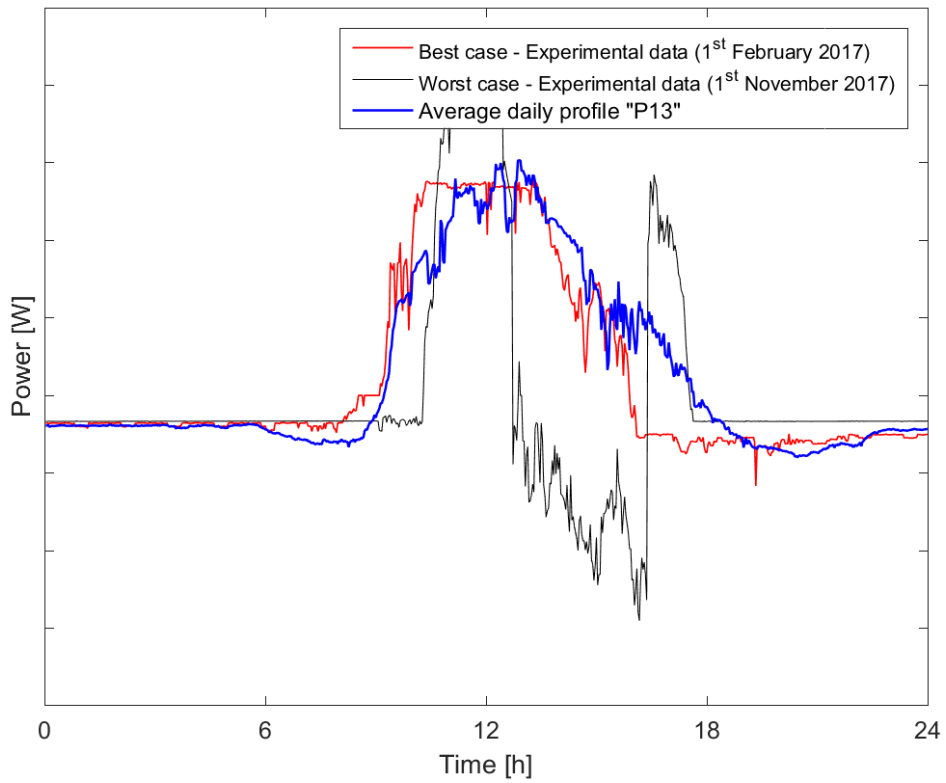


Figure 204 - Comparison between experimental battery profile and average "P13"

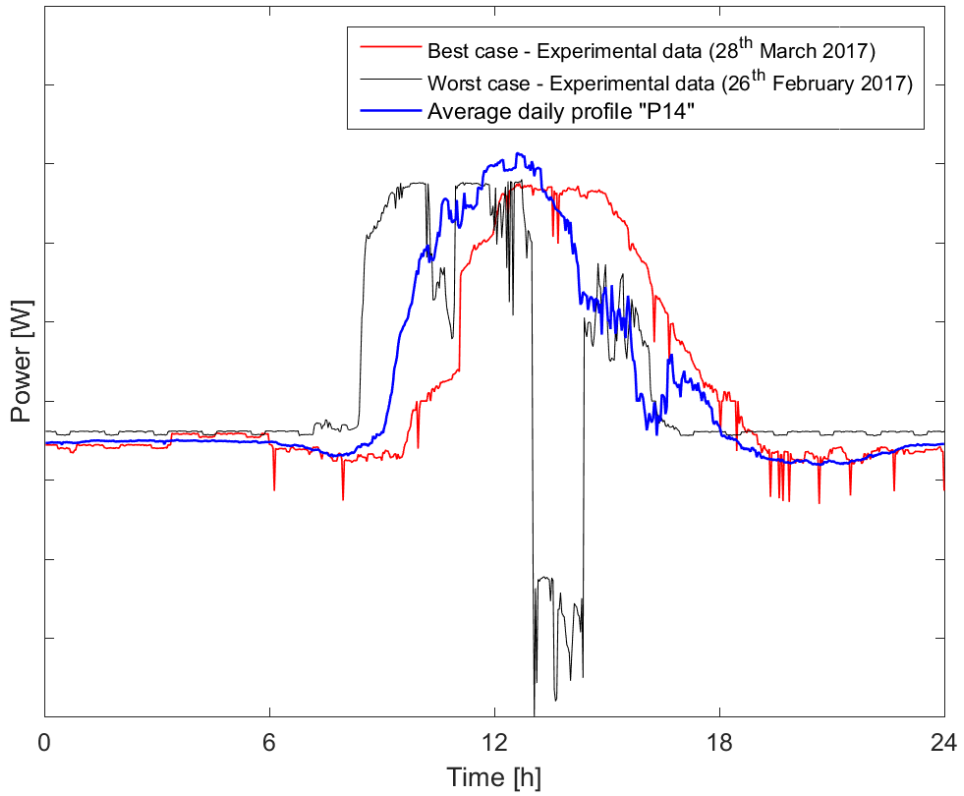


Figure 205 - Comparison between experimental battery profile and average "P14"

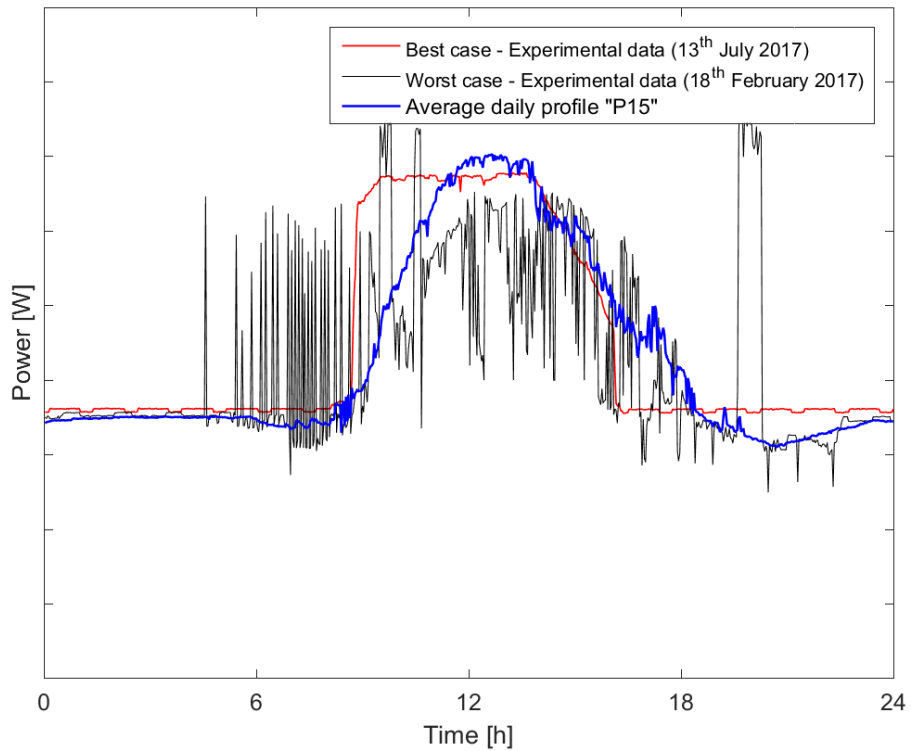


Figure 206 - Comparison between experimental battery profile and average "P15"

The accuracy of the prognostics was evaluated with the absolute standard deviation, shown in Figure 207. The errors are quite high, as shown also by the values of the Difference

of energy, in Table 26. In some cases, the average profiles built with the data of the first year of operation seem to be able to approximate in a quite good way the experimental battery power profiles of the second year. However, in most cases, the battery profiles of 2017 are different from those observed in the previous year and they are, anyway, characterized by the most various and irregular shapes. Therefore, due to the strong irregularity of this kind of profiles and to the non-repeatability of the behaviour, the prognosis was not able to achieve good results.

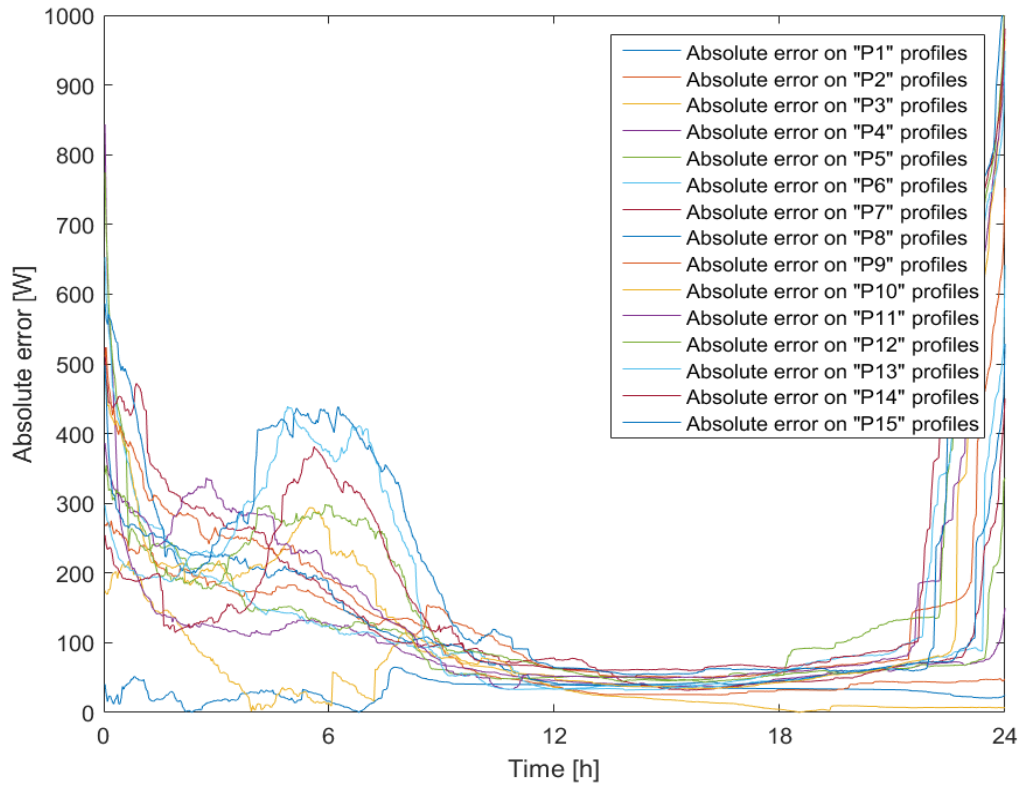


Figure 207 - Absolute error on the compared battery power profiles

Table 26: Difference of energy on the compared battery power profiles

Class	Difference on Energy [%]
P1	33.3 %
P2	76.7 %
P3	37.7 %
P4	54.9 %
P5	55.4 %
P6	49.4 %
P7	54.8 %
P8	44.6 %
P9	47.0 %
P10	40.7 %

P11	43.0 %
P12	46.4 %
P13	44.0 %
P14	41.2 %
P15	47.2 %

5.6 Conclusions

In this chapter, the analysis of the experimental data monitored on the system that produces power for the Col du Palet mountain retreat, in Peisey-Nancroix, was presented. After a short system description, an overall analysis of the sources of power production and consumption was performed; the experimental data were examined season by season, in order to identify some possible periodical behaviours of the components, which was the case of the fuel cell only.

The averaging procedure was applied on the daily power profiles of each component (fuel cell, electrolyser and battery). First, taking into account the dataset from the first year of operation (2016), the power profiles were classified in some categories according their daily energy and, for each class, an average was built. These average profiles were, then, compared with the 2017 experimental profiles in order to evaluate their fitting and if they could be assumed to represent the expected power operational profile of the device.

The profile prediction is not an easy task, as the operational profile of a device can exhibit significant variations from a year to another. Therefore, even if the assumption that the power profile measured on a device will be repeated in the future in a similar way is reasonable, this is not always true because the behaviour of the devices in different years can be characterized by significant variations, leading to high errors in the prediction phase.

This was the case of the dataset analysed in this chapter. Indeed, the prognostics results obtained for the three electrochemical devices of the system, were not good, as they were characterized by very high errors. The cause is that their behaviour recorded in the first year of operation is completely different from the one measured in the second year. Therefore, as the unexpected events, which have not been previously analysed by the algorithm, cannot be forecasted, the prognosis led to inaccurate results.

For instance, the fuel cell showed, in 2017, a very different behaviour with respect to the preceding year, starting to exhibit a more discontinuous and intermittent running. Indeed, while in 2016 most daily profiles belonged to the categories of the “Continuous” running, in 2017 the daily profiles were almost all included in the “Discontinuous” classes. Moreover, this change in the operational profile could probably lead to a more severe aging of the fuel cell, as a frequent on-off switching can affect the degradation of the device more than an operation in continuous mode.

Conclusions

Electrochemical devices, such as Proton Exchange Membrane Fuel Cells (PEMFC) and Lithium-ion (Li-ion) batteries, are among the most promising technologies to be applied in stationary and transportation applications, in the scenario of energy transition from fossil fuels to alternative power sources [12].

As these devices suffer from fast aging and degradation, Prognostics and Health Management (PHM), and in particular its Prognostics phase, can be used in order to predict the future health conditions and the Remaining Useful Lifetime (RUL), to define when maintenance should be performed and avoid system failure [6].

In this framework, the present work was presented as a part of the research made by EIFER for the development of a new prognostics algorithm, aiming at estimating the RUL of different types of electrochemical devices. The algorithm is based on the concept that, depending on its operating mode (or operational point), a system can suffer degradation in different ways. Therefore, it is important to know the past and future operational profiles of the device and its behaviour at different operating conditions, so that the right aging rate can be evaluated for each operational point.

For this purpose, the experimental data monitored on the two power production systems of the Cirque de Mafate and Col du Palet were analysed and classified in categories in order to obtain some average profiles, able to represent the different operating modes of each device.

Concerning the on-field data of Mafate energy system, the daily profiling analysis was performed on five variables: the power produced by the fuel cell, the power consumed by the electrolyser, the power of the batteries, the end user power consumption and the solar irradiance. These quantities were analysed on a daily time window and their daily profiles were divided in different classes, according to their specific features. Then, for each of these classes, an average profile was defined, in order to approximate and represent the specific features of the profiles of each class. The best results were obtained on the fuel cell power, as the absolute Standard Deviation and the Difference of Energy evaluated between the average profiles and the experimental ones reached not too high values. Moreover, the results obtained on the user load profiles with the profiling procedure, developed in this work, were also better than those achieved with the application of the ANFIS methodology. However, it was not possible to perform a true prognostics analysis on the data, as the available measurements covered a too short time horizon (few months).

The same profiling and averaging procedure was applied to the on-field data gathered at the Col du Palet energy system to determine the daily average profiles of the power of the fuel cell, the electrolyser and the batteries. However, no data about the solar irradiance or

the end user consumptions were available. In this case, the profiling was made only on the data related to the first year of operation (2016) and, then, the obtained average profiles were compared with the experimental daily profiles of the second year of operation (2017), in order to verify if they could be used to approximate and predict the future operating profile in each specific operation mode. It was difficult to perform good prognosis on these data, as the behaviour of the analysed devices during the two years of operation exhibited remarkable differences. The best results were obtained on the electrolyser power data, as the shape of the average profiles was able to reproduce in a good way the experimental ones, but in all cases the error reached were quite high.

The results achieved in this work could be used in the future as an input for the prognostics algorithm developed by EIFER. The evaluated average profiles representing the daily power of the fuel cell, the electrolyser and the batteries could represent a kind of database for the algorithm, containing the features of each operating point for each device. These features could indeed be useful for evaluating the aging rate associated with each operating mode, that is needed for the prediction of the final RUL of each device.

On the other hand, the average profiles of the other analysed variables, such as the solar irradiance and the end user load, could be used to build an expected future operating profile of the devices, that is needed for the forecasting of their future state of health. Indeed, if the future solar irradiance or the user power request are not known, a way to overcome the problem would be to suppose that these quantities will have a future profile similar to the one observed in the past through the monitored data.

The prognosis procedure could be refined and extended in the next years, first of all by improving the classification. This could be done by adding new criteria, beside the daily energy, that could be useful to identify the specific features that define the shapes of the profiles, allowing to group them in a better way. Then, an automatization of the classification procedure could be interesting to make faster the application of the algorithm; indeed, in this way, the classes would be defined automatically, without the need of a preliminary analysis performed by the user.

Moreover, as the experimental data on the two power systems are continuously monitored and recorded, with more data available it will be possible to perform wider and deeper analysis with different purposes:

- to identify periodical behaviours of the devices, linked for instance to the specific season of the year, in order to predict in a more accurate way the future operational profile;
- to better observe the aging phenomenon, which can be better identified on long time horizons, especially on those devices that are not used in a continuous way all over the year, as in this case the fuel cells and the electrolysers of both power plants.

Nomenclature

ANFIS	Adaptive Neuro Fuzzy Inference System
ANN	Artificial Neural Network
ANOVA	Analysis of Variance
AR	Auto Regressive model
DDR	Different Discharge Rates
DE	Daily Energy
EIFER	European Institute For Energy Research
EIS	Electrochemical Impedance Spectroscopy
ELM	Extreme Learning Machine
EOL	End Of Life
ESN	Echo State Network
FFNN	Feed-Forward Neural Network
FIS	Fuzzy Inference System
FL	Fuzzy Logic
FT	Failure Threshold
GD	Gradient Descent
GMDH	Group Method of Data Handling
IEA	International Energy Agency
IND-AR	Iterative Nonlinear Degradation – Auto Regressive model
MAPE	Mean Absolute Percent Error
MF	Membership Function
MIMO	Multiple Input Multiple Output model
MISMO	Multiple Input Several Multiple Output approach
NARNN	Nonlinear Auto Regressive Neural Network
NMC	Nickel Manganese Cobalt
OCV	Open Circuit Voltage
PDF	Probability Density Function
PEMFC	Proton Exchange

PF	Particle Filter
PHM	Prognostic and Health Management
PL	Peak Load
R²	Coefficient of determination
RLSE	Recursive Least Square Estimator
RMSE	Root Mean Square Error
RNN	Recurrent Neural Network
RUL	Remaining Useful Life
SOC	State Of Charge
SOH	State Of Health
SW-ELM	Summation Wavelet – Extreme Learning Machine
UKF	Unscented Kalman Filter
UPF	Unscented Particle Filter
UT	Unscented Transformation
W-GMDH	Wavelet analysis – Group Method of Data Handling

List of symbols

y_t	Observed value of the health indicator from the system at time t
\hat{y}_t	Predicted value of the health indicator at time t
\bar{y}_t	Average of observed values of the health indicator at time t
m	Number of observed value of the health indicator
X	Input data set of a data-driven method
Y	Output data set of a data-driven method
\hat{Y}	Estimated values of the output data set of a data-driven method
$La(.)$	Learning algorithm
H	Prediction horizon
RUL_{os}	Remaining Useful Life Online Steadiness
\widehat{RUL}_t	Remaining Useful Life estimation at time t
U	Voltage [V]
E_n	Nernst potential [V]
R_{mem}	Area specific resistance of the electrolyte [$\Omega \cdot m^2$]
j	Current density [A/m^2]
b_a, b_c	Tafel parameters for the anode and the cathode
j_{0a}, j_{0c}	Exchange current density at the anode and at the cathode [A/m^2]
j_{Lc}	Limit current density at the cathode [A/m^2]
x_k	State variable of a Bayesian problem
y_k	Observation value of a Bayesian problem
$f(.)$	State function of a Bayesian problem
$g(.)$	Observation function of a Bayesian problem

R	Universal gas constant [J/mol·K]
F	Faraday constant [C/mol]
j_n	Internal current density [A/m ²]
m_{trans}, n_{trans}	Mass transport loss coefficients
Q	Battery capacity [Ah]
t	Time instant
A, B	Membership functions of an ANFIS network
x, y	Inputs of an ANFIS network
f	Output of an ANFIS network
p, q, r	Consequent parameters of a fuzzy rule
O	Output of each layer of an ANFIS network
a, b, c	Premise parameters of a bell-shaped membership function
w	Firing strength of a fuzzy rule
\bar{w}	Normalized firing strength
E_p	Error measure on each data sample
P	Number of training samples of an ANFIS network
M	Number of nodes in the first layer of an ANFIS network
T	Target output of an ANFIS
E	Sum of the error measures for all data samples of an ANFIS
C	Vector of unknown consequent parameters of an ANFIS
I	Matrix of inputs from the training dataset of an ANFIS

GREEK SYMBOLS

$\Gamma(\cdot)$	Real function that links the input and the output data set of a data-driven method
-----------------	--

$\hat{f}(\cdot)$	Approximated function that links the input and the estimated output data set
σ	Standard deviation
α	Charge transfer coefficient
θ_k	Unknown parameters of the state function of a Bayesian problem
ν_k	Noise of the state function of a Bayesian problem
μ_k	Noise of the observation function of a Bayesian problem
τ	Generic premise parameter of an ANFIS
μ	Membership function
η	Learning rate

Figure index

Figure 1 - PHM architecture [14]	10
Figure 2 - Classification of prognostics approaches [13]	11
Figure 3 - Example of an ANFIS structure [16]	16
Figure 4 - ESN structure [19]	17
Figure 5 - Voltage prediction results with ESN [19]	18
Figure 6 - RUL prediction with ESN [19]	18
Figure 7 – ANOVA-optimized ESN: voltage results [1].....	19
Figure 8 – ANOVA-optimized ESN: RUL results [1]	19
Figure 9 - Comparison of SW-ELM, ELM and ESN on RUL estimation for two different FTs [4]	20
Figure 10 - RUL estimation at frequent intervals for the three approaches [4].....	21
Figure 11 - Accuracy results for the three approaches [4].....	21
Figure 12 - GMDH prediction results on Stack 1 [6]	22
Figure 13 - W-GMDH results on Stack 1 for each waveform [6]	23
Figure 14 - Overall W-GMDH results on Stack 1 [6]	23
Figure 15 - Scheme of the model-based approach [14]	23
Figure 16 - Dynamic model electrical equivalency [14]	24
Figure 17 - Equivalent circuit for Warburg impedance [14]	24
Figure 18 - Current profile and prediction results of the model-based method [14]	25
Figure 19 - Principle of particle filtering [13]	26
Figure 20 - Prediction results from particle filtering on Stack 1 (left) and Stack 2 (right) [20]	27
Figure 21 - RUL prediction results of the three models for Stack 1 [13]	28
Figure 22 - RUL prediction results of the three models for Stack 2 [13]	28
Figure 23 - Structure of a NARNN model [5]	29
Figure 24 - Moving window method applied on both approaches [5].....	29
Figure 25 - Flowchart of the overall hybrid method [5]	30
Figure 26 - Prediction results of the hybrid method [5]	31
Figure 27 - Error comparison at different moving window lengths [5].....	31
Figure 28 - PF prediction results at 32 cycles [10]	32
Figure 29 - UPF prediction results at 32 cycles [10]	32
Figure 30 - Discharge rate profile applied to the battery [22]	33
Figure 31 - DDR-dependent method RUL results [22]	33
Figure 32 - Not DDR-dependent method RUL results [22]	33
Figure 33 - Flowchart of the hybrid method [23]	34
Figure 34 - Capacity prediction results of the IND-AR model [23].....	35
Figure 35 - Example of a generic ANN architecture [2]	38
Figure 36 - Basic structure of a FIS [26]	39
Figure 37 - Basic structure of an ANFIS [27]	41
Figure 38 - Bell-shaped function [28].....	41
Figure 39 - PEMFC voltage prediction in training and testing phase [18].....	44
Figure 40 - Stack 1: RMSE vs training time [16]	45
Figure 41 - Stack 2: RMSE vs training time [16]	45

Figure 42 - Voltage prediction for Stack 1 [16].....	45
Figure 43 - Voltage prediction for Stack 2 [16].....	45
Figure 44 - Current profile applied to the PEMFC [28]	46
Figure 45 - Voltage prediction results using ANFIS [28]	46
Figure 46 - Flowchart of the profiling algorithm.....	50
Figure 47 - Flowchart of the averaging procedure	51
Figure 48 - System scheme in case of lack of PV power	55
Figure 49 - System scheme in case of excess PV power produced	55
Figure 50 - System energy balance.....	56
Figure 51 - Batteries state of charge (SOC).....	57
Figure 52 - Fuel cell power production	58
Figure 53 - Electrolysers power consumption	58
Figure 54 - Sources of power consumption (sunny day)	59
Figure 55 - Sources of power consumption (cloudy day).....	59
Figure 56 - Average fuel cell power profile "FC1"	61
Figure 57 - Average fuel cell power profile "FC2"	61
Figure 58 - Average fuel cell power profile "FC3"	62
Figure 59 - Average fuel cell power profile "FC4"	62
Figure 60 – Sorted profiles of the class “FC4”	63
Figure 61 – PRSD on fuel cell power profiles of the class “FC4”	64
Figure 62 - PRSD on fuel cell power profiles	64
Figure 63 - Absolute error on fuel cell power profiles	65
Figure 64 - Average electrolyser power profile "EL1".....	67
Figure 65 - Average electrolyser power profile "EL2"	67
Figure 66 - Average electrolyser power profile "EL3".....	68
Figure 67 - Average electrolyser power profile "EL4".....	68
Figure 68 - Sorted profiles of the class "EL3".....	69
Figure 69 - PRSD of the electrolyser power profiles.....	69
Figure 70 - Absolute standard deviation on the electrolyser power profiles	70
Figure 71 - Average battery power profile "P1"	72
Figure 72 - Average battery power profile "P2"	72
Figure 73 - Average battery power profile "P3"	73
Figure 74 - Average battery power profile "P4"	73
Figure 75 - Average battery power profile "P5"	74
Figure 76 - Average battery power profile "P6"	74
Figure 77 - Average battery power profile "P7"	75
Figure 78 - Average battery power profile "P8"	75
Figure 79 - PRSD on battery power profiles	76
Figure 80 - Absolute standard deviation on battery power profiles	76
Figure 81 - Sorted profiles of the class "P8".....	77
Figure 82 - Sorted profiles of the class "P4".....	77
Figure 83 - Average solar irradiance profile "S1"	79
Figure 84 - Average solar irradiance profile "S2"	79
Figure 85 - Average solar irradiance profile "S3"	80
Figure 86 - Average solar irradiance profile "S4"	80
Figure 87 - Average solar irradiance profile "S5"	81
Figure 88 - Average solar irradiance profile "S6"	81

Figure 89 - Average solar irradiance profile "S7"	82
Figure 90 - Average solar irradiance profile "S8"	82
Figure 91 - Average solar irradiance profile "S9"	83
Figure 92 - Average solar irradiance profile "S10"	83
Figure 93 - PRSD on solar irradiance profiles.....	84
Figure 94 - Absolute error on solar irradiance profiles	84
Figure 95 - Average load profile "Low 1"	88
Figure 96 - Average load profile "Low 2"	89
Figure 97 - Average load profile "Low 3"	89
Figure 98 - Average load profile "Medium 1"	90
Figure 99 - Average load profile "Medium 2"	90
Figure 100 - Average load profile "Medium 3"	91
Figure 101 - Average load profile "Medium 4"	91
Figure 102 - Average load profile "Medium 5"	92
Figure 103 - Average load profile "Medium 6"	92
Figure 104 - Average load profile "Medium 7"	93
Figure 105 - Average load profile "Medium 8"	93
Figure 106 - Average load profile "Medium 9"	94
Figure 107 - Average daily "High" load profile	95
Figure 108 - Average load profile "High 1"	95
Figure 109 - Average load profile "High 2"	96
Figure 110 - Neuro-Fuzzy MATLAB toolbox with training data plotted	97
Figure 111 - Structure of the generated FIS	97
Figure 112 - Plot of ANFIS results vs training data	98
Figure 113 - Plot of ANFIS results vs testing data	98
Figure 114 - ANFIS results vs test data for the "Low 1" profile.....	99
Figure 115 - ANFIS results vs test data for the "Low 2" profile.....	99
Figure 116 - ANFIS results vs test data for the "Low 3" profile.....	100
Figure 117 - ANFIS results vs test data for the "Medium 1" profile.....	101
Figure 118 - ANFIS results vs test data for the "Medium 2" profile.....	101
Figure 119 - ANFIS results vs test data for the "Medium 3" profile.....	102
Figure 120 - ANFIS results vs test data for the "Medium 4" profile.....	102
Figure 121 - ANFIS results vs test data for the "Medium 5" profile.....	103
Figure 122 - ANFIS results vs test data for the "Medium 6" profile.....	103
Figure 123 - ANFIS results vs test data for the "Medium 7" profile.....	104
Figure 124 - ANFIS results vs test data for the "Medium 8" profile.....	104
Figure 125 - ANFIS results vs test data for the "Medium 9" profile.....	105
Figure 126 - ANFIS results (with one input) vs testing data for the "High 1" profile .	105
Figure 127 - ANFIS results (with one input) vs testing data for the "High 2" profile .	106
Figure 128 - Absolute error on "Low" load profiles obtained with analytic (a) and ANFIS (b) algorithm.....	107
Figure 129 - Absolute error on "Medium" load profiles obtained with analytic (a) and ANFIS (b) algorithm	107
Figure 130 - Absolute error on "High" load profiles obtained with analytic (a) and ANFIS (b) algorithm.....	108
Figure 131 - System scheme in case of lack of PV power	112
Figure 132 - System scheme in case of excess PV power produced	112

Figure 133 - System energy balance (year 2016)	113
Figure 134 - System energy balance (year 2017)	114
Figure 135 - Battery power production and consumption	115
Figure 136 - Electrolyser power consumption.....	115
Figure 137 - Fuel cell power production	116
Figure 138 - Fuel cell power production in summer 2016 and 2017.....	117
Figure 139 – Comparison between the fuel cell profiles of 2016 and 2017.....	117
Figure 140 - Absolute standard deviation between the fuel cell profiles of 2016 and 2017	117
.....	
Figure 141 - Average fuel cell power profile "C1".....	119
Figure 142 - Average fuel cell power profile "C2"	119
Figure 143 - Average fuel cell power profile "C3".....	120
Figure 144 - Average fuel cell power profile "D1"	120
Figure 145 - Average fuel cell power profile "D2"	121
Figure 146 - Sorted profiles of the class "C1"	121
Figure 147 - PRSD on fuel cell power profiles of the class “C1”	121
Figure 148 - PRSD of the fuel cell power profiles	122
Figure 149 - Absolute error on fuel cell power profiles	123
Figure 150 - Comparison between experimental fuel cell profile and average "C1" ...	124
Figure 151 - Comparison between experimental fuel cell profile and average "C2" ...	124
Figure 152 - Comparison between experimental fuel cell profile and average "D1" ...	125
Figure 153 - Absolute error on the compared fuel cell power profiles.....	125
Figure 154 - Electrolyser power consumption in 2016 and 2017.....	126
Figure 155 – Comparison between the electrolyser profiles of 2016 and 2017	127
Figure 156 - Absolute standard deviation between the electrolyser profiles of 2016 and 2017	127
.....	
Figure 157 - Electrolyser power consumption in spring 2016 and 2017.....	127
Figure 158 - Electrolyser power consumption in summer 2016 and 2017.....	128
Figure 159 - Electrolyser power consumption in autumn 2016 and 2017.....	128
Figure 160 - Average electrolyser power profile "C1"	129
Figure 161 - Average electrolyser power profile "C2"	130
Figure 162 - Average electrolyser power profile "C3"	130
Figure 163 - Average electrolyser power profile "C4"	131
Figure 164 - Average electrolyser power profile "C5"	131
Figure 165 - Average electrolyser power profile "D1".....	132
Figure 166 - Average electrolyser power profile "D2".....	132
Figure 167 - PRSD for the electrolyser power profiles	133
Figure 168 - Absolute error on electrolyser power profiles.....	134
Figure 169 - Comparison between experimental electrolyser profile and average "C1"	135
.....	
Figure 170 - Comparison between experimental electrolyser profile and average "C2"	135
.....	
Figure 171 - Comparison between experimental electrolyser profile and average "C3"	136
.....	
Figure 172 - Comparison between experimental electrolyser profile and average "C4"	136
.....	

Figure 173 - Comparison between experimental electrolyser profile and average "C5"	137
.....	
Figure 174 - Comparison between experimental electrolyser profile and average "D2"	137
.....	
Figure 175 - Absolute error on electrolyser power profiles.....	138
Figure 176 - Average battery power profile "P1"	140
Figure 177 - Average battery power profile "P2"	140
Figure 178 - Average battery power profile "P3"	141
Figure 179 - Average battery power profile "P4"	141
Figure 180 - Average battery power profile "P5"	142
Figure 181 - Average battery power profile "P6"	142
Figure 182 - Average battery power profile "P7"	143
Figure 183 - Average battery power profile "P8"	143
Figure 184 - Average battery power profile "P9"	144
Figure 185 - Average battery power profile "P10"	144
Figure 186 - Average battery power profile "P11"	145
Figure 187 - Average battery power profile "P12"	145
Figure 188 - Average battery power profile "P13"	146
Figure 189 - Average battery power profile "P14"	146
Figure 190 - Average battery power profile "P15"	147
Figure 191 - Absolute error on battery power profiles	148
Figure 192 - Comparison between experimental battery profile and average "P1"	149
Figure 193 - Comparison between experimental battery profile and average "P2"	150
Figure 194 - Comparison between experimental battery profile and average "P3"	150
Figure 195 - Comparison between experimental battery profile and average "P4"	151
Figure 196 - Comparison between experimental battery profile and average "P5"	151
Figure 197 - Comparison between experimental battery profile and average "P6"	152
Figure 198 - Comparison between experimental battery profile and average "P7"	152
Figure 199 - Comparison between experimental battery profile and average "P8"	153
Figure 200 - Comparison between experimental battery profile and average "P9"	153
Figure 201 - Comparison between experimental battery profile and average "P10" ..	154
Figure 202 - Comparison between experimental battery profile and average "P11" ..	154
Figure 203 - Comparison between experimental battery profile and average "P12" ..	155
Figure 204 - Comparison between experimental battery profile and average "P13" ..	155
Figure 205 - Comparison between experimental battery profile and average "P14" ..	156
Figure 206 - Comparison between experimental battery profile and average "P15" ..	156
Figure 207 - Absolute error on the compared battery power profiles	157

Tables index

Table 1: Fuel cell power profiles classes	60
Table 2: PSRD and MAPE on average fuel cell power profiles.....	65
Table 3: Difference of energy for fuel cell profiles	66
Table 4: Electrolysers power profiles classes	66
Table 5: PSRD and MAPE on average electrolyser power profiles	70
Table 6: Difference of energy on the electrolyser power profiles	70
Table 7: Batteries power profiles classes.....	71
Table 8: PSRD and energy error on average battery power profiles	77
Table 9: Solar irradiance profiles classes	78
Table 10: PSRD, MAPE and Difference of Energy on the average solar irradiance profiles	85
.....	
Table 11: End user power profiles classes.....	86
Table 12: Percentage of occurrence of the end user consumption profiles	87
Table 13: Comparison of the Absolute Error for the analytic and the ANFIS methods	108
.....	
Table 14: Comparison of the PRSD for the analytic and the ANFIS methods	109
Table 15: Fuel cell power profiles classes	118
Table 16: PRSD and MAPE on fuel cell average profiles.....	122
Table 17: Difference of Energy on fuel cell average power profiles.....	123
Table 18: Difference of energy on the compared fuel cell power profiles	126
Table 19: Electrolyser power profiles classes.....	129
Table 20: PSRD and MAPE on average electrolyser power profiles	133
Table 21: Absolute error on the electrolyser power profiles	134
Table 22: Difference of energy on the compared electrolyser power profiles	138
Table 23: Battery power profiles classes	139
Table 24: PSRD and MAPE on average battery profiles.....	147
Table 25: Difference of Energy on the battery power profiles	148
Table 26: Difference of energy on the compared battery power profiles	157

References

- [1] S. Morando, S. Jemei, D. Hissel, R. Gouriveau and N. Zerhouni, "ANOVA method applied to proton exchange membrane fuel cell ageing forecasting using an echo state network," *Mathematics and Computers in Simulation*, no. 131, pp. 283-294, 2017.
- [2] S. Becker and V. Karri, "Predictive models for PEM-electrolyzer performance using adaptive neuro-fuzzy inference systems," *International journal of hydrogen energy*, no. 35, pp. 9963-9972, 2010.
- [3] M. Jouin, M. Bressel, S. Morando, R. Gouriveau, D. Hissel, M.-C. Péra, N. Zerhouni, S. Jemei, M. Hilairet and B. O. Bouamama, "Estimating the end-of-life of PEM fuel cells: Guidelines and metrics," *Applied Energy*, no. 177, pp. 87-97, 2016.
- [4] K. Javed, R. Gouriveau, N. Zerhouni and D. Hissel, "Prognostics of Proton Exchange Membrane Fuel Cells stack using an ensemble of constraints based connectionist networks," *Journal of Power Sources*, no. 324, pp. 745-757, 2016.
- [5] D. Zhou, F. Gao, E. Breaz, A. Ravey and A. Miraoui, "Degradation prediction of PEM fuel cell using a moving window based hybrid prognostic approach," *Energy*, no. 138, pp. 1175-1186, 2018.
- [6] H. Liu, J. Chen, M. Hou, Z. Shao and H. Su, "Data-based short-term prognostics for proton exchange membrane fuel cells," *International Journal of Hydrogen Energy*, no. 42, pp. 20791-20808, 2017.
- [7] N. Herr, J.-M. Nicod, C. Varnier, L. Jardin, A. Sorrentino, D. Hissel and M.-C. Péra, "Decision process to manage useful life of multi-stacks fuel cell systems under service constraint," *Renewable Energy*, no. 105, pp. 590-600, 2017.
- [8] C. Sbarufatti, M. Corbetta, M. Giglio and F. Cadini, "Adaptive prognosis of lithium-ion batteries based on the combination of particle filters and radial basis function neural networks," *Journal of Power Sources*, no. 344, pp. 128-140, 2017.
- [9] F. Yang, D. Wang, Y. Xing and T. Kwok-Leung, "Prognostics of Li(NiMnCo)O₂-based lithium-ion batteries using a novel battery degradation model," *Microelectronics Reliability*, no. 70, pp. 70-78, 2017.
- [10] Q. Miao, L. Xie, H. Cui, W. Liang and M. Pecht, "Remaining useful life prediction of lithium-ion battery with unscented particle filter technique," *Microelectronics Reliability*, no. 53, pp. 805-810, 2013.

- [11] S. Morando, S. Jemei, D. Hissel, R. Gouriveau and N. Zerhouni, "Proton exchange membrane fuel cell ageing forecasting algorithm based on Echo State Network," *International Journal of Hydrogen Energy*, no. 42, pp. 1472-1480, 2017.
- [12] D. Wang, F. Yang, Y. Zhao and K.-L. Tsui, "Prognostics of Lithium-ion batteries based on state space modeling with heterogeneous noise variances," *Microelectronics Reliability*, no. 75, pp. 1-8, 2017.
- [13] M. Jouin, R. Gouriveau, D. Hissel, M.-C. Péra and N. Zerhouni, "Prognostics of PEM fuel cell in a particle filtering framework," *International Journal of Hydrogen Energy*, no. 39, pp. 481-494, 2014.
- [14] E. Lechartier, E. Laffly, M.-C. Péra, R. Gouriveau, D. Hissel and N. Zerhouni, "Proton exchange membrane fuel cell behavioral model suitable for prognostics," *International Journal of Hydrogen Energy*, no. 40, pp. 8384-8397, 2015.
- [15] T. Sutharssan, D. Montalvao, Y. K. Chena, W.-C. Wangb, C. Pisac and H. Elemara, "A review on prognostics and health monitoring of proton exchange membrane fuel cell," *Renewable and Sustainable Energy Reviews*, no. 75, pp. 440-450, 2017.
- [16] R. Silva, R. Gouriveau, S. Jemei, D. Hissel, L. Boulon, K. Agbossou and N. Yousfi Steiner, "Proton exchange membrane fuel cell degradation prediction based on Adaptive Neuro-Fuzzy Inference Systems," *International Journal of Hydrogen Energy*, no. 39, pp. 11128-11144, 2014.
- [17] R. Gouriveau and N. Zerhouni, "Connexionist-Systems-Based Long Term Prediction Approaches for Prognostics," *IEEE Transactions on Reliability, Institute of Electrical and Electronics Engineers*, no. 61, pp. 909-920, 2012.
- [18] S. Morando, S. Jemei, R. Gouriveau, N. Zerhouni and D. Hissel, "Fuel Cells Remaining Useful Lifetime forecasting using Echo State Network," *Vehicle Power and Propulsion Conference*, 2014.
- [19] L. Mao, L. Jackson and T. Jackson, "Investigation of polymer electrolyte membrane fuel cell internal behaviour during long term operation and its use in prognostics," *Journal of Power Sources*, no. 362, pp. 39-49, 2017.
- [20] J. Dunik, M. Simandl and O. Straka, "Unscented Kalman Filter: Aspects and Adaptive Setting of Scaling Parameter," *IEEE Transaction on Automatic Control*, no. 57, 2012.
- [21] D. Wang, F. Yang, Y. Zhao and K.-L. Tsui, "Battery remaining useful life prediction at different discharge rates," *Microelectronics Reliability*, no. 78, pp. 212-219, 2017.
- [22] Y. Song, D. Liu, C. Yang and Y. Penga, "Data-driven hybrid remaining useful life estimation approach for spacecraft lithium-ion battery," *Microelectronics Reliability*, no. 75, pp. 142-153, 2017.

- [23] J. Jang, C. Sun and E. Mizutani, *Neuro-Fuzzy and Soft Computing*, Upper Saddle River NJ: Prentice-Hall, 1997.
- [24] X.-P. Zhang, “Adaptive-Network-Based Fuzzy Inference System for Short Term Load Forecasting,” *IFAC Control of Power Systems and Power Plants*, 1997.
- [25] W. Suparta and K. Alhasa, *Modeling of Tropospheric Delays Using ANFIS*, Springer International Publishing, 2016.
- [26] J.-S. R. Jang, “ANFIS: Adaptive-Network-Based Fuzzy Inference System,” *IEEE Transaction on Systems, Man, and Cybernetics*, vol. 23, no. 3, 1993.
- [27] Y. Vural, D. B. Ingham and M. Pourkashanian, “Performance prediction of a proton exchange membrane fuel cell using the ANFIS model,” *International Journal of Hydrogen Energy*, no. 34, pp. 9181-9187, 2009.
- [28] L. Mao and L. Jackson, “Comparative study on prediction of fuel cell performance using machine learning approaches,” in *Proceedings of The International Multi-Conference of Engineers and Computer Scientists*, Hong Kong, 2016.
- [29] S. Haykin, *Neural Networks and Learning Machines*, Prentice Hall, 2009.

Acknowledgements

First of all, I would like to thank the mentor of this thesis, Professor Pierluigi Leone, for his availability, professionalism and the support given to me during the writing of this work.

I would like also to thank my supervisors during the period spent at the European Institute for Energy Research, in Karlsruhe (Germany), where this work was developed and where I had the opportunity to live a stimulating experience for a personal and professional growth.

Heartfelt thanks to my family, who supported me with love during this journey, especially in the hardest moments.

A sincere thanks to Mario, with whom I shared the joys and satisfactions of these years, overcoming together worries and difficulties with mutual help.

Finally, thanks to all my friends, near and far, which accompanied me in some way along this path.

Ringraziamenti

Desidero, innanzitutto, ringraziare il relatore di questa tesi, il professor Pierluigi Leone, per la sua disponibilità e il supporto datomi durante la stesura del lavoro.

Ringrazio, inoltre, i miei supervisori durante il periodo trascorso presso l'European Institute For Energy Research, a Karlsruhe (Germania), dove questo lavoro di tesi è stato sviluppato e dove ho avuto l'opportunità di vivere un'esperienza stimolante dal punto di vista formativo e personale.

Un grazie di cuore alla mia famiglia, che mi ha sostenuto con amore durante questo percorso, soprattutto nei momenti più difficili.

Un sincero grazie a Mario, con il quale ho condiviso le gioie e le soddisfazioni di questi anni, superando insieme con il reciproco aiuto preoccupazioni e difficoltà.

Infine, un grazie a tutti gli amici, vicini e lontani, che in un modo o nell'altro mi hanno accompagnato in questo percorso.